

University of Southampton Research Repository ePrints Soton

Copyright © and Moral Rights for this thesis are retained by the author and/or other copyright owners. A copy can be downloaded for personal non-commercial research or study, without prior permission or charge. This thesis cannot be reproduced or quoted extensively from without first obtaining permission in writing from the copyright holder/s. The content must not be changed in any way or sold commercially in any format or medium without the formal permission of the copyright holders.

When referring to this work, full bibliographic details including the author, title, awarding institution and date of the thesis must be given e.g.

AUTHOR (year of submission) "Full thesis title", University of Southampton, name of the University School or Department, PhD Thesis, pagination

UNIVERSITY OF SOUTHAMPTON

FACULTY OF NATURAL AND ENVIRONMENTAL SCIENCES

Chemistry

**Mechanistic and structural characterisation of
HydG catalysed L-tyrosine cleavage**

by

Rebecca Christine Driesener

Thesis for the degree of Doctor of Philosophy

April 2014

Diese Arbeit ist meinen Eltern gewidmet,
für ihre stetige Unterstützung.

Our greatest glory is not in never falling, but in rising every time we fall.

Confucius

UNIVERSITY OF SOUTHAMPTON

ABSTRACT

FACULTY OF NATURAL AND ENVIRONMENTAL SCIENCES

Chemistry

Thesis for the degree of Doctor of Philosophy

MECHANISTIC AND STRUCTURAL CHARACTERISATION OF HYDG CATALYSED L-TYROSINE CLEAVAGE

Rebecca Christine Driesener

The *S*-adenosyl-L-methionine (AdoMet) dependent enzyme HydG is one of three maturase enzymes involved in [FeFe]-hydrogenase cofactor assembly. It catalyses L-tyrosine cleavage to yield the cofactor cyanide and carbon monoxide ligands as well as *p*-cresol. *Clostridium acetobutylicum* HydG contains the conserved CX₃CX₂C motif coordinating the AdoMet binding [4Fe-4S] cluster and a C-terminal CX₂CX₂₂C motif proposed to coordinate a second [4Fe-4S] cluster. To improve the understanding of the roles of each of these iron-sulfur clusters in catalysis, HydG variants lacking either the N- or C-terminal cluster have been generated and examined using spectroscopic and kinetic methods. Quantification of coordinated iron, UV-Vis spectroscopy and electron paramagnetic resonance (EPR) spectroscopy of an N-terminal C96/100/103A triple HydG mutant which cannot coordinate the radical AdoMet cluster was used to unambiguously show that the C-terminal cysteine motif coordinates an auxiliary [4Fe-4S] cluster. Spectroscopic comparison with

a C-terminally truncated HydG (Δ CTD) harbouring only the N-terminal cluster demonstrates that both clusters have similar UV-Vis and EPR spectral properties, but that AdoMet binding and cleavage can only occur at the N-terminal radical AdoMet cluster. The latter observation was also confirmed by initial structural characterisation of a thermostable *Thermoanaerobacter italicus* HydG. To elucidate which steps in the catalytic cycle of HydG require the auxiliary [4Fe-4S] cluster, Michaelis-Menten constants for AdoMet and L-tyrosine for reconstituted wild-type, C386S, and Δ CTD *Clostridium acetobutylicum* HydG were determined and demonstrate that these C-terminal modifications do not strongly affect the affinity for AdoMet, but that the affinity for L-tyrosine is drastically reduced compared to that of wild-type HydG. A definite tyrosine binding site could unfortunately not be established in the *Thermoanaerobacter italicus* HydG crystal structure. Further kinetic characterisation of the above *Clostridium acetobutylicum* HydG mutants suggests that the C-terminal cluster and residues are not essential for L-tyrosine cleavage to *p*-cresol but are necessary for conversion of a tyrosine derived intermediate to cyanide and CO.

Contents

Abstract	v
Contents	vii
List of tables.....	xi
List of figures	xv
List of schemes	xxi
List of accompanying materials	xxv
Declaration of authorship	xxvii
Acknowledgements	xxix
Definitions and Abbreviations	xxxii
Chapter 1 Introduction	1
1.1 Hydrogenases.....	1
1.1.1 [FeFe]–hydrogenase active site	2
1.1.2 [FeFe]–hydrogenase active site assembly.....	4
1.2 The superfamily of radical AdoMet enzymes	8
1.2.1 Electron transfer during AdoMet cleavage.....	12
1.2.2 Structural characterisation of radical AdoMet enzymes	15
1.2.2.1 The triose–phosphate isomerase barrel core	15
1.2.2.2 AdoMet binding	17
1.2.2.3 Substrate binding.....	19
1.2.3 Strategies for controlled radical generation	20
1.2.3.1 Thermodynamic control	21
1.2.3.2 Structural control.....	23
1.2.4 Roles of auxiliary [4Fe–4S] clusters in AdoMet enzymes	25

1.2.5	HydG belongs to a C α -C β lyase subclass	32
1.2.6	Role of HydE in [FeFe]-hydrogenase active site assembly	40
1.3	Aims of thesis	43
Chapter 2 Spectroscopic characterisation of wild-type and mutant		
<i>C. acetobutylicum</i> HydG		45
2.1	Introduction.....	45
2.2	Expression and purification of <i>C. acetobutylicum</i> HydG variants.....	51
2.3	UV-Vis characterisation and iron content analyses	54
2.4	EPR characterisation.....	60
2.5	Summary and conclusions.....	69
Chapter 3 Mechanistic insights into HydG catalysed tyrosine cleavage 71		
3.1	Introduction.....	71
3.2	Initial kinetic characterisation of wild-type and mutant <i>C. acetobutylicum</i> HydG.....	77
3.3	Improving HydG in vitro activity and methodology	82
3.3.1	Optimisation of in vitro assay buffer.....	82
3.3.2	Optimisation of glyoxylate derivatisation procedure	84
3.4	Investigating substrate affinity of wild-type and mutant <i>C. acetobutylicum</i> HydG.....	87
3.4.1	HPLC optimisation for quantification of nanomolar <i>p</i> -cresol	93
3.4.2	Enzymatic synthesis and purification of (<i>S,S</i>)-AdoMet	95
3.4.3	Determination of AdoMet and tyrosine Michaelis-Menten constants.....	101
3.5	Optimised kinetic characterisation of wild-type and mutant <i>C. acetobutylicum</i> HydG.....	108
3.6	Factors influencing wild-type HydG activity.....	113
3.6.1	Activity in the presence of tyrosine substrate analogues	113
3.6.2	HydG catalysed <i>p</i> -cresol formation is pH dependent.....	120
3.7	Summary and conclusions.....	125

Chapter 4 Towards structural characterisation of HydG..... 131

4.1	Introduction	131
4.2	Genetic context of <i>hydG</i>	134
4.3	Preparation of <i>hydG</i> expression plasmids	137
4.4	Expression and purification of <i>T. lettingae</i> HydG.....	140
4.4.1	Ni-Affinity purification of <i>T. lettingae</i> HydG	140
4.4.2	Superdex 75 gel filtration of <i>T. lettingae</i> HydG	142
4.5	Expression and purification of <i>T. maritima</i> HydG	145
4.5.1	Ion exchange chromatography of <i>T. maritima</i> HydG	147
4.5.2	Superdex 75 gel filtration of <i>T. maritima</i> HydG.....	150
4.6	Expression and purification of <i>Th. italicus</i> HydG	152
4.7	Screening crystallisation conditions	153
4.7.1	C-terminally 6His tagged <i>T. maritima</i> HydG	153
4.7.2	N-terminally 6His tagged <i>T. lettingae</i> HydG	159
4.8	Data collection on <i>T. lettingae</i> HydG crystals	168
4.8.1	Basic theory	168
4.8.2	Practice	171
4.9	Crystal structure of <i>Th. italicus</i> HydG.....	175
4.9.1	Overall fold and AdoMet binding	175
4.9.2	C-terminal domain and tyrosine binding	180
4.10	Summary and conclusions	185

Chapter 5 Investigating cyanide transfer between *C. acetobutylicum*

HydG and HydF

5.1	Introduction	189
5.2	Expression and purification of <i>C. acetobutylicum</i> HydF and HydF ^E ..	192
5.3	Characterisation of <i>C. acetobutylicum</i> HydF and HydF ^E	201
5.4	Expression, purification and characterisation of <i>C. acetobutylicum</i> HydE	204
5.5	Strep tag pull-down assays for characterisation of activated HydF ..	209
5.6	Modification of the cyanide detection method.....	215

5.7	Summary and conclusions.....	217
Chapter 6 Conclusions and future work		219
6.1	Conclusions.....	219
6.2	Future experiments.....	227
Chapter 7 Experimental		231
7.1	Materials.....	231
7.2	Equipment	234
7.3	General microbiology methods	238
7.4	Preparation of plasmids	247
7.5	Expression and purification of proteins.....	250
7.6	Protein reconstitution and activity assays	257
7.7	Protein spectroscopy.....	263
7.8	Preparation of enzymatically synthesised AdoMet	264
7.9	HPLC methods	269
7.10	Protein crystallography	276
References		279
Appendices		297
Appendix 1 – Phylogenetic analyses.....		297
Appendix 2 – Plasmid maps		300
Appendix 3 – Liquid media		313
Appendix 4 – EPR simulations		314
Appendix 5 – HydG, ThiH sequence alignment.....		315

List of tables

Table 1.1	Representative radical AdoMet enzymes containing two or more iron–sulfur clusters.	26
Table 2.1	Spectroscopic characteristics of ferredoxin–like iron–sulfur clusters.	46
Table 2.2	Summary of iron content for HydG variants.	55
Table 2.3	EPR parameters for N- and C-terminal HydG [4Fe–4S] clusters.	63
Table 3.1	Kinetic analysis of AdoMet and tyrosine cleavage by HydG variants.	80
Table 3.2	Examples of substrate K_d and K_M constants for radical AdoMet enzymes.	88
Table 3.3	AdoMet dependent kinetic parameters for <i>p</i> -cresol formation by WT and mutant HydG.	107
Table 3.4	Tyrosine dependent kinetic parameters for <i>p</i> -cresol formation by WT and mutant HydG.	107
Table 3.5	Kinetic analysis of AdoMet and tyrosine cleavage by HydG variants.	111
Table 3.6	HydG dependent AdoMet cleavage in the presence of tyrosine analogues.	118

Table 4.1	<i>C. acetobutylicum</i> hydrogenase genes and protein references.	134
Table 4.2	Prepared plasmids encoding <i>hydG</i> .	138
Table 4.3	Molecular weights and isoelectric points of ISC proteins.	142
Table 4.4	Initial leads for crystallisation of <i>T. maritima</i> HydG with AdoMet.	154
Table 4.5	Crystallisation of <i>T. maritima</i> HydG.	155
Table 4.6	Crystallisation of <i>T. lettingae</i> HydG with AdoMet.	160
Table 4.7	Crystallisation of <i>T. lettingae</i> HydG with tyrosine.	163
Table 4.8	Overview of different crystal forms obtained with reduced <i>T. lettingae</i> HydG in the presence of tyrosine.	166
Table 4.9	Crystallisation of <i>T. lettingae</i> HydG with AdoMet and tyrosine.	167
Table 4.10	Data processing statistics for M7S13.	172
Table 4.11	Data processing statistics for M8S1.	174
Table 4.12	Data processing statistics for <i>Th. italicus</i> HydG.	176
Table 5.1	Modifications to Strep II tagged HydF, HydF ^{FE} purifications.	195
Table 5.2	Overview of activity assays carried out to establish reaction conditions for cyanide transfer from HydG to HydF.	211
Table 5.3	Comparative investigations of cyanide derivatisation procedure.	216
Table 7.1	Overview of materials used in this study.	231

Table 7.2	Composition of TFB buffer solutions.	238
Table 7.3	Composition of SOC medium.	240
Table 7.4	Analytical digest mixture.	241
Table 7.5	Composition of 6x gel-loading buffer.	241
Table 7.6	Composition of 50x TAE running buffer.	241
Table 7.7	Composition of Bradford reagent.	242
Table 7.8	Composition of 15% SDS-PAGE resolving and stacking gel.	243
Table 7.9	Composition of SDS-PAGE buffers.	244
Table 7.10	Composition of SDS-PAGE imaging solutions.	244
Table 7.11	Composition of Western blotting buffers.	246
Table 7.12	Components for mutagenesis PCR.	248
Table 7.13	Optimised PCR cycling parameters.	249
Table 7.14	Parameters for expression of proteins from <i>C. acetobutylicum</i> .	251
Table 7.15	Dilution series for Fe ²⁺ calibration curve.	258

List of figures

Figure 1.1	[FeFe]-hydrogenase active site.	3
Figure 1.2	X-ray crystal structures of representative radical AdoMet enzymes.	16
Figure 1.3	Representative AdoMet binding in BioB.	18
Figure 1.4	Energetics of reductive AdoMet cleavage as estimated in LAM.	22
Figure 1.5	Substrate binding forces AdoMet into a catalytically active conformation.	24
Figure 1.6	Partial sequence alignment of HydG from selected organisms.	34
Figure 2.1	Basic EPR principles.	48
Figure 2.2	Schematic of prepared <i>C. acetobutylicum</i> HydG mutants.	50
Figure 2.3	Purification of WT and mutant HydG.	52
Figure 2.4	Analytical gel filtration of HydG variants.	53
Figure 2.5	UV-Vis characterisation of HydG variants.	55
Figure 2.6	UV-Vis characterisation of BSA.	57
Figure 2.7	Separation efficiency of Nap-10 and PD-10 Sephadex G25 columns.	58
Figure 2.8	X-band EPR spectra of WT HydG.	61

Figure 2.9	X-band EPR spectra of Δ CTD and C96/100/103A HydG.	62
Figure 2.10	Simulation of WT HydG X-band EPR spectra.	64
Figure 2.11	X-band EPR spectra (10 – 12 K) of WT HydG in the presence of substrate and/or substrate analogues.	66
Figure 2.12	X-band EPR spectra of C386S HydG.	68
Figure 3.1	Time dependent AdoMet and tyrosine cleavage by HydG variants.	79
Figure 3.2	HydG catalysed tyrosine cleavage in different buffers.	83
Figure 3.3	Fluorescence of glyoxylate derivatisation product in the presence of HydG assay components.	85
Figure 3.4	Quantification of <i>p</i> -cresol in the presence of tyrosine.	93
Figure 3.5	<i>p</i> -Cresol quantification by HPLC with fluorescence detection.	94
Figure 3.6	SDS-PAGE analysis of AdoMet synthetase expression study.	97
Figure 3.7	Enzymatic synthesis of (<i>S,S</i>)-AdoMet with time.	98
Figure 3.8	Enzymatic synthesis of (<i>S,S</i>)-AdoMet and purification by cation exchange chromatography.	100
Figure 3.9	Representative AdoMet dependent <i>p</i> -cresol formation.	102
Figure 3.10	Representative tyrosine dependent <i>p</i> -cresol formation.	103
Figure 3.11	Substrate dependent <i>p</i> -cresol formation by HydG variants.	106
Figure 3.12	Time dependent AdoMet and tyrosine cleavage by HydG variants with near saturating substrate concentrations.	110

Figure 3.13	HydG catalysed <i>p</i> -cresol formation is pH dependent.	121
Figure 3.14	Differing pK _a values in an enzyme active site.	123
Figure 4.1	Principles of protein crystallisation by vapour diffusion.	133
Figure 4.2	Phylogenetic tree based on primary sequences of HydG from different (hyper)thermophilic organisms.	135
Figure 4.3	Genetic context of <i>hydG</i> from selected organisms.	136
Figure 4.4	Analytical restriction digest of pRD003.	139
Figure 4.5	Ni-Affinity purification of <i>T. lettingae</i> HydG.	141
Figure 4.6	UV-Vis characterisation of <i>T. lettingae</i> HydG.	143
Figure 4.7	Gel filtration of <i>T. lettingae</i> HydG.	144
Figure 4.8	Ni-Affinity purification of C-terminally tagged <i>T. maritima</i> HydG.	145
Figure 4.9	SDS-PAGE analysis of heat treated <i>T. maritima</i> HydG.	146
Figure 4.10	Anion exchange purification of C-terminally 6His tagged <i>T. maritima</i> HydG.	148
Figure 4.11	Cation exchange purification of C-terminally 6His tagged <i>T. maritima</i> HydG.	149
Figure 4.12	Gel filtration purification of C-terminally 6His tagged <i>T. maritima</i> HydG.	151
Figure 4.13	Small scale expression of <i>Th. italicus</i> HydG.	152

Figure 4.14	Small crystal of non-reduced C-terminally 6His tagged <i>T. maritima</i> HydG with AdoMet and tyrosine.	157
Figure 4.15	Data collection of M7S13.	171
Figure 4.16	Data collection of M8S1.	173
Figure 4.17	Crystal structure of <i>Th. italicus</i> HydG homodimer.	177
Figure 4.18	AdoMet binding in the <i>Th. italicus</i> HydG active site.	179
Figure 4.19	A tunnel links both [4Fe-4S] clusters of <i>Th. italicus</i> HydG.	181
Figure 4.20	Proposed proton-coupled electron transfer pathway in <i>E. coli</i> RNR.	183
Figure 5.1	Partial sequence alignment of HydF from selected organisms.	190
Figure 5.2	Strep-Tactin affinity purification of HydF.	194
Figure 5.3	Strep-Tactin affinity purification of HydF ^E .	197
Figure 5.4	Strep-Tactin affinity co-purification of HydF ^E .	198
Figure 5.5	UV-Vis analysis of early eluting HydF ^E fractions.	199
Figure 5.6	UV-Vis characterisation of HydF and HydF ^E .	202
Figure 5.7	GTPase activity of reconstituted HydF and HydF ^E .	203
Figure 5.8	Partial sequence alignment of HydE from selected organisms.	204
Figure 5.9	Ni-Affinity purification of HydE.	205
Figure 5.10	UV-Vis characterisation of HydE.	206

Figure 5.11	Activity studies with HydE.	208
Figure 5.12	UV-Vis spectra of HydG and HydF before and after affinity chromatography.	209
Figure 5.13	Analysis of HydF ^(E) , HydG and HydE interaction assays.	213
Figure 5.14	Optimisation of cyanide derivatisation procedure.	216
Figure 7.1	Analytical 1% agarose gel analyses of mutagenesis PCR mix towards pCDFDuet-1 containing <i>hydG_ΔCTD</i> .	249
Figure 7.2	Calibration curve of FeSO ₄ ·7H ₂ O standards.	259
Figure 7.3	¹ H NMR spectrum of enzymatically synthesised and purified AdoMet.	267
Figure 7.4	High resolution mass spectrum of enzymatically synthesised and purified AdoMet.	268
Figure 7.5	HPLC quantification of 5'-dAH and <i>p</i> -cresol.	270
Figure 7.6	HPLC quantification of cyanide.	272
Figure 7.7	HPLC quantification of glyoxylate.	274
Figure 7.8	HPLC elution chromatogram of GTP.	275

List of schemes

Scheme 1.1	Proposed [FeFe]-hydrogenase cofactor biosynthesis.	6
Scheme 1.2	Representative reactions catalysed by radical AdoMet enzymes.	9
Scheme 1.3	Proposed mechanism for reductive AdoMet cleavage.	11
Scheme 1.4	Reversible and irreversible AdoMet cleavage.	13
Scheme 1.5	Uncoupled AdoMet cleavage.	20
Scheme 1.6	Proposed mechanism of BioB catalysed biotin formation.	29
Scheme 1.7	Proposed mechanism of BtrN catalysed amino-DOI formation.	31
Scheme 1.8	Catalysed reactions by radical AdoMet C α -C β lyase subfamily.	33
Scheme 1.9	Proposed mechanism for ThiH catalysed in vitro tyrosine cleavage.	36
Scheme 1.10	Proposed fate of HydG derived dehydroglycine to a dithiomethylamine bridge.	38
Scheme 1.11	Reaction products identified during HydG catalysed tyrosine cleavage.	39
Scheme 1.12	Proposed role of radical AdoMet enzyme HydE.	42

Scheme 3.1	Proposed reaction pathway of HydG catalysed tyrosine cleavage.	72
Scheme 3.2	Proposed HydG catalysed collapse of a C-centred glycine radical to cyanide and CO.	74
Scheme 3.3	Proposed HydG catalysed collapse of dehydroglycine to cyanide and CO.	76
Scheme 3.4	Racemisation and degradation of (<i>S,S</i>)-AdoMet.	89
Scheme 3.5	Enzyme catalysed reaction following Michaelis-Menten kinetics.	90
Scheme 3.6	Enzymatic (<i>S,S</i>)-AdoMet synthesis.	96
Scheme 3.7	Tyrosine analogues employed in ThiH and HydG activity assays.	114
Scheme 3.8	Proposed antiperiplanar arrangement for L-tyrosine binding.	115
Scheme 3.9	Additional tyrosine analogues investigated as HydG substrates.	117
Scheme 3.10	Action of 5'-methylthioadenosine nucleosidase.	120
Scheme 3.11	Electron transfer roles of the HydG auxiliary [4Fe-4S] cluster.	128
Scheme 4.1	Flow chart summarising the efforts to crystallise <i>T. maritima</i> HydG.	154
Scheme 4.2	Flow chart summarising the efforts to crystallise <i>T. lettingae</i> HydG.	161

Scheme 6.1	HydG catalysed tyrosine cleavage to <i>p</i> -cresol.	223
Scheme 6.2	HydG catalysed dehydroglycine cleavage to cyanide and CO.	225

List of accompanying materials

A CD containing the following two Excel files belong to this thesis:

- Tm_HydG_Crystallisation_Electronic_Appendix
- Tlet_HydG_Crystallisation_Electronic_Appendix

The contained spreadsheets list the screening conditions used throughout the crystallisation experiments.

DECLARATION OF AUTHORSHIP

I, Rebecca Christine Driesener declare that the thesis entitled 'Mechanistic and structural characterisation of HydG catalysed L-tyrosine cleavage' and the work presented in the thesis are both my own, and have been generated by me as the result of my own original research.

I confirm that:

- this work was done wholly or mainly while in candidature for a research degree at this University;
- where any part of this thesis has previously been submitted for a degree or any other qualification at this University or any other institution, this has been clearly stated;
- where I have consulted the published work of others, this is always clearly attributed;
- where I have quoted from the work of others, the source is always given. With the exception of such quotations, this thesis is entirely my own work;
- I have acknowledged all main sources of help;
- where the thesis is based on work done by myself jointly with others, I have made clear exactly what was done by others and what I have contributed myself;

- parts of this work have been published as:

Hiscox, M. J., Driesener, R. C., and Roach, P. L. (2012) Enzyme catalyzed formation of radicals from *S*-adenosylmethionine and inhibition of enzyme activity by the cleavage products, *Biochim. Biophys. Acta: Proteins and Proteomics* 1824, 1165–1177

Challand, M. R., Salvadori, E., Driesener, R. C., Kay, C. W. M., Roach, P. L., and Spencer, J. (2013) Cysteine methylation controls radical generation in the Cfr radical AdoMet rRNA methyltransferase, *PLoS ONE* 8, e67979

Driesener, R. C., Duffus, B. R., Shepard, E. M., Bruzas, I. R., Duschene, K. S., Coleman, N. J.–R., Marrison, A. P. G., Salvadori, E., Kay, C. W. M., Peters, J. W., Broderick, J. B., and Peter L, R. (2013) Biochemical and kinetic characterization of radical *S*-adenosyl–L–methionine enzyme HydG, *Biochemistry* 52, 8696–8707

Signed:

Date:

Acknowledgements

The work presented here is the culmination of extended laboratory work and endless sleepless nights. Help and support during this time was coming from a variety of people, whom I would like to thank and acknowledge here.

First of all, I would like to thank my supervisor, Peter Roach for his continued guidance and patience throughout all stages of my PhD, for letting me to attend a bioinorganic training workshop in the USA and for his professional advice to improve this thesis.

Further thanks goes to Martyn Hiscox for demonstrating how things can be done to a point, for eventful EPR trips and for always seeing the bright side of things.

I would like to thank Enrico Salvadori, Chris Kay and Richard Cammack at University College London for recording the EPR spectra presented herein. I would also like to acknowledge my collaborators Benjamin Duffus and Eric Shepard from Montana State University for characterisation of the N-terminal HydG mutant and especially like to thank them for their endless support and insightful discussions regarding simulation of the EPR spectra.

Special thanks goes to Jenny Harmer for introducing me to the 'world of crystals' and for proof reading and advancing the crystallisation chapter with her expert advice. I further like to acknowledge that Pedro Dinis has proof read early drafts of the spectroscopic and kinetic HydG characterisation chapters and further like to thank him for his continued efforts to solve the HydG crystal structure. Jen, Pedro and Alice Loasby made Synchrotron trips the more fun.

Thanks also goes to past and present Roach group members who all played their part during my PhD. These include, in order of 'appearance', Martin Challand, Jenny McKelvie, Laura Batten, Rachael Wilkinson, Mari Giurrandino and Daren Fearon.

As life is nothing without the correct balance, I thank my many friends in the University Hillwalking Club for making weekend trips lasting memories with extraordinary adventures off the beaten track. My 'Avenue' housemates, I like to thank for film and dinner evenings and for distributing an uplifting spirit. I wish to express my gratitude to Rebecca Longley and Paul Ramsay for help and support in planning the thesis writing process.

Last but not least, I like to thank my parents and grandparents for their emotional support and independent advice.

Definitions and Abbreviations

Gene names are written in italics, starting with a lower case letter, e.g. *hydA*, *hydG*. Gene products are capitalised and written in normal type style, e.g. HydA, HydG. Unless indicated by an accompanying superscript, protein notations represent proteins expressed on their own. The superscript 'EG' in HydF^{EG} indicates that HydF was expressed in the presence of HydE and HydG, whereas HydF^(E) refers to 'HydF or HydF^E'.

This thesis refers to L-tyrosine as tyrosine, the D-tyrosine enantiomer will be explicitly referred to.

Unless otherwise stated, S-adenosyl-L-methionine refers to commercial preparations.

ACP•	3-Amino-3-carboxypropyl radical
AdoHcy	S-Adenosyl-L-homocysteine
AdoMet	S-Adenosyl-L-methionine (unless other stereochemistry is specifically indicated)
Amino-DOI	Amino-dideoxy- <i>scyllo</i> -inosose
anSME	Anaerobic sulfatase maturation enzyme
ATP	Adenosine-5'-triphosphate
BioB	Biotin synthase
BSA	Bovine serum albumin

<i>C. acetobutylicum</i>	<i>Clostridium acetobutylicum</i>
CBI	1-Cyanobenz[f]isoindole
<i>Chl. reinhardtii</i>	<i>Chlamydomonas reinhardtii</i>
Cluster I	AdoMet binding [4Fe-4S] cluster
Cluster II	Auxiliary [4Fe-4S] cluster
<i>C. pasteurianum</i>	<i>Clostridium pasteurianum</i>
Δ CTD	C-terminal deletion mutant
5'-dAH	5'-Deoxyadenosine
5'-dA•	5'-Deoxyadenosyl radical
<i>D. desulfuricans</i>	<i>Desulfovibrio desulfuricans</i>
DMHA	N,N-Dimethylhexylamine
DMSO	Dimethyl sulfoxide
DNA	Deoxyribonucleic acid
DOIA	2-deoxy- <i>scyllo</i> -inosamine
DTB	Dethiobiotin
DTT	Dithiothreitol
ϵ_{xxx}	Extinction coefficient at specified wavelength
E	Enzyme
<i>E. coli</i>	<i>Escherichia coli</i>
EDTA	Ethylenediaminetetraacetic acid

ES	Enzyme–substrate complex
ESEEM	Electron spin echo envelope modulation
ENDOR	Electron nuclear double resonance
EPR	Electron paramagnetic resonance
FTIR	Fourier–transform infrared
GDP	Guanosine–5′–diphosphate
GTP	Guanosine–5′–triphosphate
HABA	2–(4′–Hydroxy–benzeneazo)benzoic acid
Hb	Deoxyhaemoglobin
HbCO	Carboxyhaemoglobin
HPLC	High pressure liquid chromatography
HYSCORE	Hyperfine sublevel correlation
IPTG	Isopropyl β–D–1–thiogalactopyranoside
ISC	Iron–sulfur cluster assembly proteins
k_{cat}	Turnover number
$k_{\text{cat}}^{\text{app}}$	Apparent turnover number
K_{d}	Dissociation constant
K_{M}	Michaelis–Menten constant
$K_{\text{M}}^{\text{AdoMet}}$	Michaelis–Menten constant for AdoMet
$K_{\text{M}}^{\text{TYR}}$	Michaelis–Menten constant for tyrosine

LAM	Lysine 2,3-aminomutase
LCP	Lipoyl carrier protein
LipA	Lipoyl synthase
MAD	Multiwavelength anomalous dispersion
MTA	5'-Methylthioadenosine
MTAN	5'-Methylthioadenosine/ <i>S</i> -adenosyl-L-homocysteine nucleosidase
MWCO	Molecular weight cut-off
NA	Not applicable
NADPH	Nicotinamide adenine dinucleotide phosphate hydrogen
NaDT	Sodium dithionite
NDA	Naphthalene-2,3-dicarboxaldehyde
NHE	Normal hydrogen electrode
NMR	Nuclear magnetic resonance
OD ₆₀₀	Optical density at 600 nm
PCR	Polymerase chain reaction
PEG	Polyethylene glycol
PES	Polyethersulfone
PFL	Pyruvate formate lyase
PFL-Ae	Pyruvate formate lyase activating enzyme

P _i	Inorganic phosphate
PLP	Pyridoxal phosphate
PP	PACT Premier screen
QM/MM	Quantum mechanical/molecular mechanical
R ²	Measure for goodness of fit
rmsd	Root-mean-square deviation
RNA	Ribonucleic acid
RNR	Ribonucleotide reductase
rpm	Revolutions per minute
r. t.	Room temperature
S	Substrate
6His	Six histidine tag
SAD	Singlewavelength anomalous dispersion
SDS-PAGE	Sodium dodecyl sulfate polyacrylamide gel electrophoresis
<i>Sh. oneidensis</i>	<i>Shewanella oneidensis</i>
<i>S. solfataricus</i>	<i>Sulfolobus solfataricus</i>
<i>Th. italicus</i>	<i>Thermoanaerobacter italicus</i>
<i>Th. tengcongensis</i>	<i>Thermoanaerobacter tengcongensis</i>
TIM	Triose-phosphate isomerase

TFA	Trifluoroacetic acid
TLC	Thin-layer chromatography
<i>T. lettingae</i>	<i>Thermotoga lettingae</i>
<i>T. maritima</i>	<i>Thermotoga maritima</i>
<i>T. neapolitana</i>	<i>Thermotoga neapolitana</i>
UV-Vis	UV-Visible
WT	Wild-type

Chapter 1

Introduction

1.1 Hydrogenases

Hydrogenases are complex anaerobic metalloenzymes which catalyse the reversible reduction of protons to form molecular hydrogen ($2\text{H}^+ + 2\text{e}^- \rightleftharpoons \text{H}_2$) and play a key role in energy metabolism in all kingdoms of life. In clostridial fermentative bacteria for example, excess electrons produced during oxidative metabolism are removed by forming hydrogen, whereas hydrogenases in nitrogen-fixing prokaryotes recycle the hydrogen which was formed during endogenous nitrogenase activity^{1,2}. Three phylogenetically unrelated hydrogenases are differentiated based on their metal content of the active site. These include [NiFe]–hydrogenases found in bacteria and archaea, [FeFe]–hydrogenases restricted to bacteria and eukaryotes and [Fe]–hydrogenases in hydrogenotrophic methanogenic archaea^{2,3}. Especially [FeFe]–hydrogenases have recently attracted much attention as a source for biohydrogen^{4,5}.

Chapter 1 – Introduction

1.1.1 [FeFe]–hydrogenase active site

The X–ray crystal structures of the [FeFe]–hydrogenase from the anaerobic soil bacterium *Clostridium pasteurianum* (*C. pasteurianum*)⁶ and the sulfate–reducing bacterium *Desulfovibrio desulfuricans* ATCC 7757 (*D. desulfuricans*)⁷ have been solved (Figure 1.1). Based on these crystal structures, it was identified that the active site cofactor 1, also termed the H–cluster, is buried inside the protein but linked to the protein surface by ferredoxin like [4Fe–4S] clusters⁸. The H–cluster itself consists of a cubane [4Fe–4S] cluster which is connected via a protein derived cysteine residue to a [2Fe] subcluster (Figure 1.1). The iron atoms in this subcluster are linked by a bridging CO and a dithiolate ligand and furthermore coordinate a CO and cyanide ligand each^{6,7,9}. A vacant⁷, water⁶ or inhibitor¹⁰ coordinated site at the distal iron atom of the [2Fe] subcluster is thought to be the hydrogen binding site. Based on the X–ray crystal structure of the *D. desulfuricans* [FeFe]–hydrogenase⁷, the dithiolate bridge was initially modelled as 1,3 propane–dithiolate, but later assigned as a dithiomethylether bridge¹¹. In agreement with mechanistic proposals of hydrogen activation as well as experimental evidence^{12,13}, the linkage has more recently been modelled to be a dithiomethylamine^{9,14,15}.

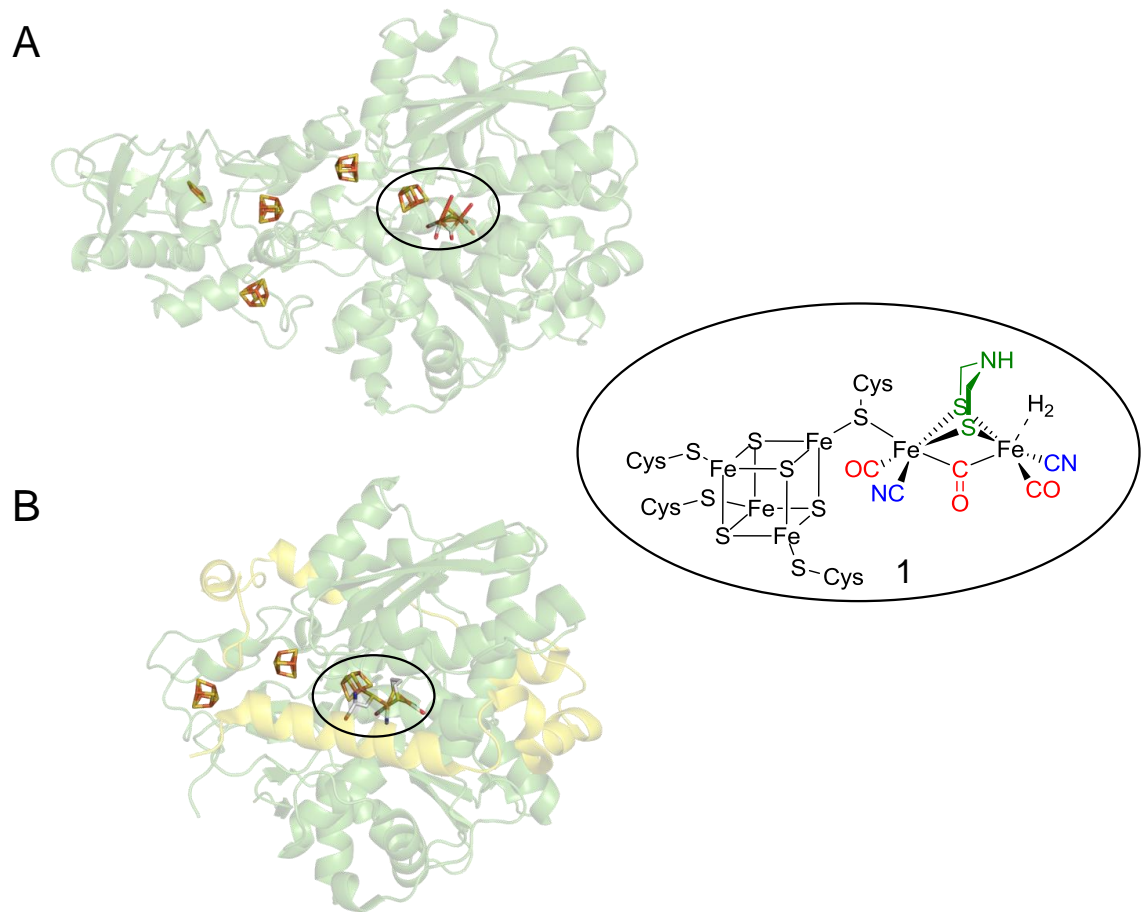


Figure 1.1 [FeFe]-hydrogenase active site.

Illustration of the [FeFe]-hydrogenase active site from (A) *C. pasteurianum* (PDB 1FEH) and (B) *D. desulfuricans* (PDB 1HFE; chain M, T) with the protein subunits coloured in green and yellow. The cofactor and [4Fe-4S] clusters are shown as sticks in the following colour scheme; iron – orange, sulfur – yellow, carbon – grey, oxygen – red, nitrogen – blue. The chemical structure of the highlighted H-cluster cofactor is depicted on the right, where the cyanide and CO ligands are coloured in blue and red, respectively, while the dithiomethylamine bridge is shown in green.

1.1.2 [FeFe]–hydrogenase active site assembly

While the assembly of the [NiFe]–hydrogenase cofactor, especially the incorporation of the cyanide and CO ligands has been studied in great detail^{16–21}, the understanding of [FeFe]–hydrogenase assembly has only recently been advanced. The currently proposed roles of the [FeFe]–hydrogenase maturation enzymes during H–cluster assembly are summarised in Scheme 1.1 and described below.

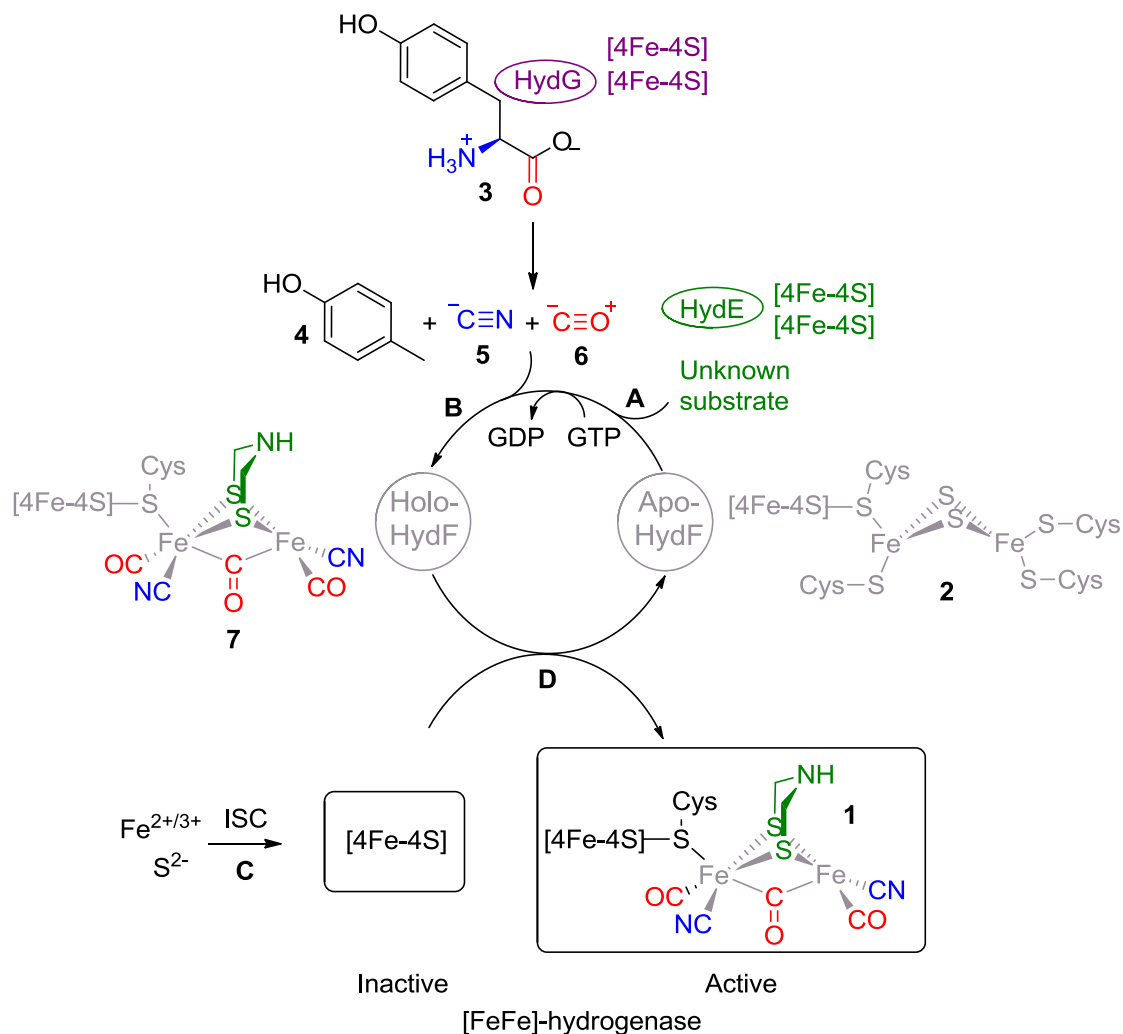
In 2004, the maturation enzymes essential for hydrogenase activity were identified when an insertional mutagenesis library was screened in *Chlamydomonas reinhardtii* (*Chl. reinhardtii*) for the ability to produce hydrogen²². Clones lacking the *hydEF* gene (found separately as *hydE* and *hydF* in prokaryotes) were found not to display hydrogenase activity²². Interestingly, heterologous expression of the *hydEF* and the adjacent *hydG* gene with the hydrogenase *hydA* resulted in hydrogen production, while expression of either *hydEF* or *hydG* with *hydA* yielded no hydrogenase activity²². This strongly suggested that the HydEF and HydG enzymes are responsible for assembly of a functional [FeFe]–hydrogenase²². Biochemical characterisations of the gene products identified that all coordinate iron–sulfur clusters. HydE and HydG are radical *S*–adenosyl–L–methionine (AdoMet) enzymes proposed to contain two [4Fe–4S] clusters^{23–25}. HydF on the other hand catalyses the hydrolysis of guanosine–5′–triphosphate (GTP) and is thought to coordinate one [4Fe–4S] cluster which is bridged to a [2Fe–2S] subcluster^{26–28}.

Demonstration that purified *Clostridium acetobutylicum* (*C. acetobutylicum*) HydF heterologously expressed in the background of HydE and HydG (HydF^{EG}) was sufficient for activation of the *C. pasteurianum* hydrogenase heterologously expressed in the absence of the maturase

enzymes led to the proposal of HydF as a scaffold protein^{29,30}. This functional assignment was further supported by the observation of cyanide and CO characteristic features in the HydF^{EG} Fourier–transform infrared (FTIR) spectrum^{31,32}, suggesting that HydE and HydG may act on a HydF [2Fe–2S] cluster to assemble the [2Fe] subcluster (Scheme 1.1, 2→7).

HydG has been shown to catalyse L-tyrosine (tyrosine hereafter, **3**) cleavage to produce *p*-cresol **4**³³, cyanide **5**³⁴ and CO **6**²⁵, which suggests that HydG may synthesise the [FeFe]–hydrogenase diatomic ligands. Experimental evidence that the above diatomic molecules are incorporated into the H–cluster came from characteristic FTIR shifts in the vibrational cyanide and CO energies of the *C. pasteurianum* [FeFe]–hydrogenase produced in vitro with either natural abundance or isotopically labelled tyrosine³⁵.

With the function of HydF and HydG being assigned, the remaining maturation enzyme HydE was hypothesised to play a role in the biosynthesis of the dithiomethylamine bridge or translocation of the [2Fe] subcluster^{31,36}. Despite the crystal structure of HydE being available³⁷, the substrate and reaction products are unknown. The μ_2 -sulfide atoms are the most reactive and electron deficient centres in a classical [2Fe–2S] cluster due to their electron donation towards the iron atoms^{38–40}. This observation led to the proposal that HydE acts first on a HydF [2Fe–2S] cluster to install the dithiolate bridge (Scheme 1.1, step A), thereby shifting the reactivity towards the iron atoms for incorporation of the cyanide and CO ligands by HydG^{31,40} (Scheme 1.1, step B). This hypothesis is in agreement with the approximately 10-fold higher affinity of HydE over HydG for HydF and the inability of HydF to interact with both radical AdoMet enzymes simultaneously⁴¹, suggesting a sequential binding of the maturation partners.



Scheme 1.1 Proposed [FeFe]-hydrogenase cofactor biosynthesis.

HydG and HydE assemble the [2Fe] subcluster on HydF before it is transferred to the [FeFe]-hydrogenase HydA. The identified iron-sulfur clusters in each enzyme are indicated and are proposed to be inserted by the host iron-sulfur cluster assembly proteins. Whether the H-cluster ligands synthesised by HydE and HydG are directly incorporated into a HydF [2Fe-2S] cluster or transferred as cluster bound intermediates to HydF is currently unknown.

HydF catalysed GTP hydrolysis was found not to be important for activation of HydA³¹ nor for interaction of HydF with HydA⁴¹. GTP hydrolysis was however increased in the presence of HydE or HydG³¹. While neither GTP binding nor hydrolysis was required for HydF interacting with these maturation enzymes, binding of GTP (or a non-hydrolysable GTP analogue) to a HydF–HydE or HydF–HydG complex triggered dissociation of the maturation partners⁴¹. This would provide a means to regulate HydE and HydG binding.

Comparison of the iron–sulfur cluster(s) of the HydF^{EG} and HydA^{EG} enzymes with regards to the metal oxidation state, geometry and first sphere ligands identified that HydF^{EG} likely coordinates a H–cluster like cofactor **7**⁴². The presence of a [4Fe–4S] cluster in individually expressed HydA suggests that H–cluster assembly may be a stepwise process, where insertion of the [4Fe–4S] cluster into HydA by the host iron–sulfur cluster assembly proteins (ISC) precedes insertion of the [2Fe] subcluster by HydF^{43,44} (Scheme 1.1, steps C, D).

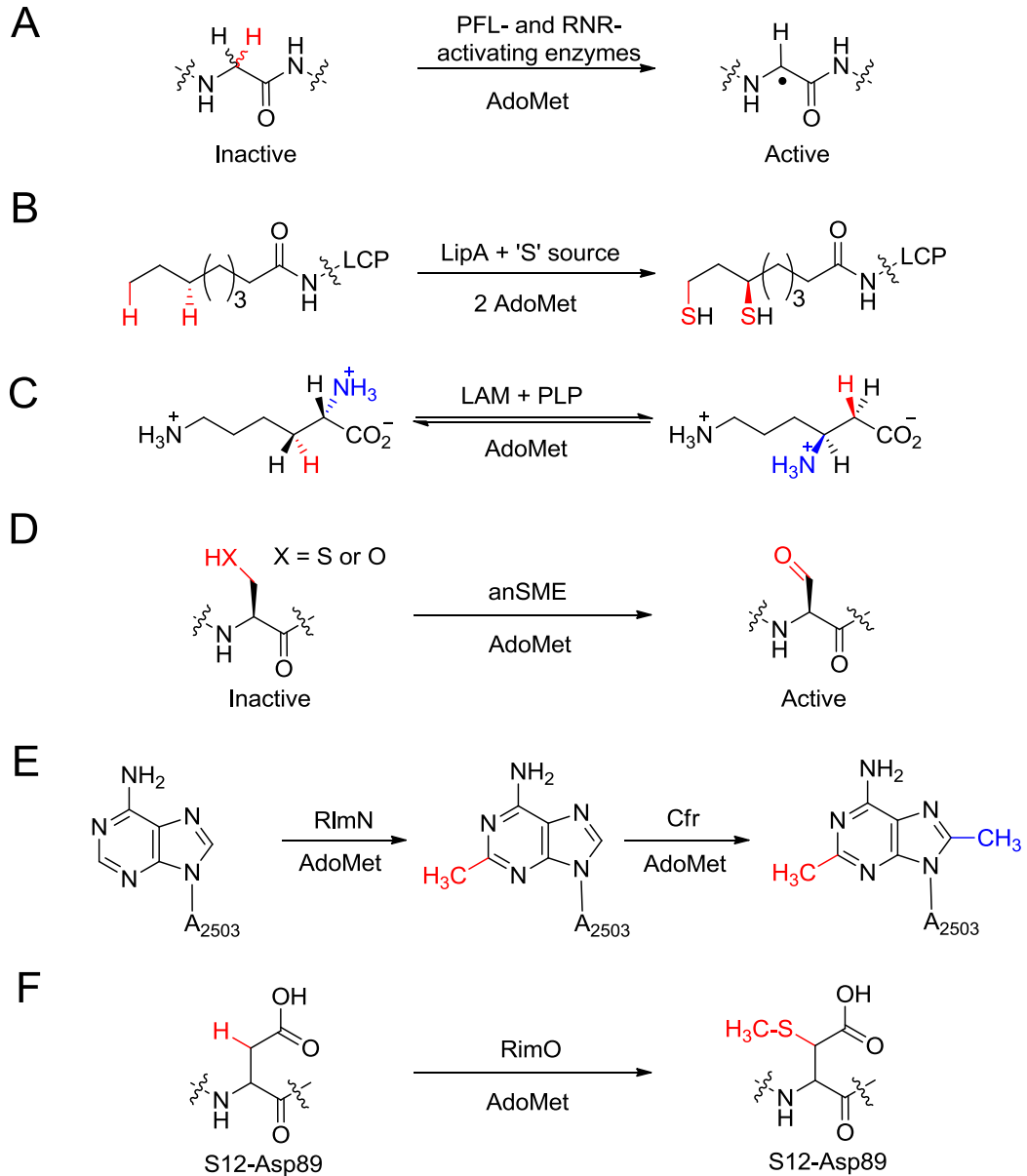
The observation by Mansure and Hallenbeck that *Desulfovibrio vulgaris* (Hildenborough) HydE and HydG but not HydF interact with the putative hydrogenase HydA⁴⁵ indicates that the proposed action of HydF as a scaffold protein may not be conserved among all [FeFe]–hydrogenases. Similarly, *Shewanella oneidensis* (*Sh. oneidensis*) HydG and not HydF was the only maturase necessary for *C. pasteurianum* HydA activation in the presence of a desalted *Escherichia coli* (*E. coli*) lysate and the HydG substrates³⁶.

Despite further knowledge becoming available regarding H–cluster assembly, detailed mechanistic insight into ligand syntheses, incorporation into a HydF [2Fe–2S] cluster and subsequent linkage with the HydA [4Fe–4S] cluster are still lacking.

1.2 The superfamily of radical AdoMet enzymes

The [FeFe]–hydrogenase maturation proteins HydE and HydG belong to the radical AdoMet superfamily of enzymes²⁴. This family catalyses a remarkably diverse set of more than 40 distinct biochemical transformations as highlighted in a special issue in *Biochimica et Biophysica Acta – Proteins and Proteomics* (2012, vol 1824, issue 11). Catalysed reactions include, but are not limited to glyceryl radical formation, isomerisation, sulfation, methylation, thiomethylation, hydroxylation, dehydrogenation and decarboxylation (Scheme 1.2). All reactions are essential during posttranscriptional and posttranslational modifications as well as biosynthesis of complex cofactors.

The radical AdoMet superfamily is currently estimated to contain more than 44000 individual sequences⁴⁶ and was initially characterised by a conserved N–terminal cysteine CX₃CX₂C motif and the requirement for a reduced [4Fe–4S]¹⁺ cluster and AdoMet for activity⁴⁷. Three iron atoms of the essential [4Fe–4S] cluster are coordinated by the conserved cysteine residues⁴⁷ whereas the free, unique iron is coordinated by the α –amino and α –carboxy groups of AdoMet **8**^{48–51} (Scheme 1.3 A). In recent years, AdoMet dependent enzymes with variant cysteine motifs have however been discovered which highlights some flexibility in the [4Fe–4S] cluster coordination environment. Examples include ThiC (CX₂CX₄C)⁵², HmdB (CX₅CX₂C)⁵³ and Elp3 (CX₄CX₂C)⁵⁴.

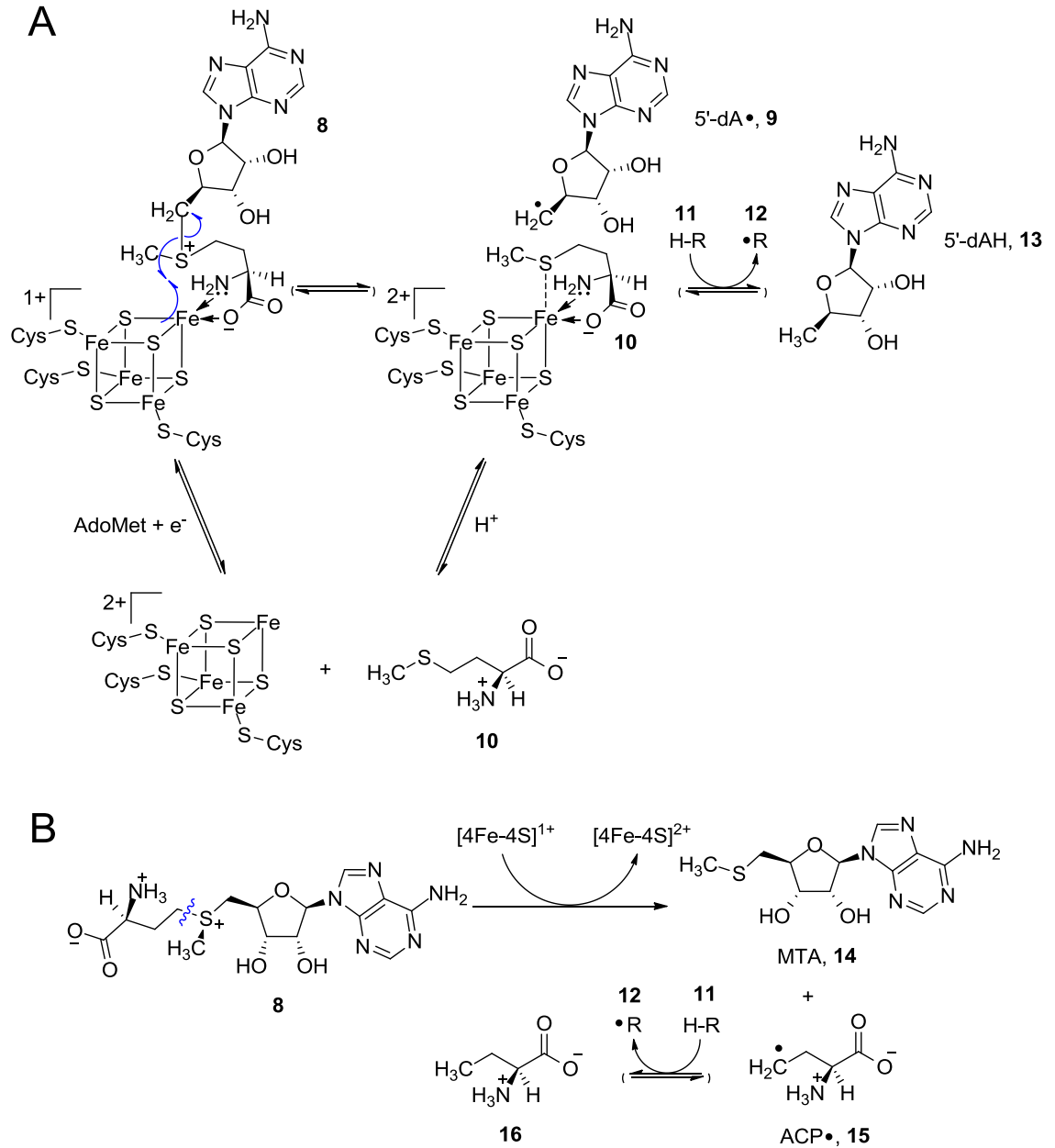


Scheme 1.2 Representative reactions catalysed by radical AdoMet enzymes.

(A) Activation of glycyl radical enzymes such as pyruvate formate lyase (PFL) and ribonucleotide reductase (RNR), (B) sulfur atom insertion into unactivated C–H bonds of the lipoyl carrier protein (LCP) by lipoyl synthase, (C) interconversion of L- α -lysine to L- β -lysine by lysine 2,3-aminomutase in the presence of the pyridoxal phosphate cofactor, (D) formation of formylglycine by Cys- and Ser-type anaerobic sulfatase maturation enzymes, (E) methylation of rRNA substrates by RlmN and Cfr and (F) thiomethylation of ribosomal proteins by RimO.

Chapter 1 – Introduction

Single electron transfer from the reduced $[4\text{Fe}-4\text{S}]^{1+}$ cluster to AdoMet **8** initiates homolytic 5'-C-S bond cleavage to form a highly reactive C-centred 5'-deoxyadenosine radical (5'-dA•, **9**) and methionine **10**^{55,56} (Scheme 1.3 A). Subsequent hydrogen atom abstraction by 5'-dA• from the enzyme's substrate **11** generates the experimentally observed 5'-deoxyadenosine (5'-dAH, **13**). The concomitantly formed substrate radical **12** subsequently undergoes enzyme specific reactions. Observation of AdoMet dependent formation of 5'-methylthioadenosine (MTA, **14**) and 2-aminobutyric acid **16** by the B₁₂-independent glycerol dehydratase activating enzyme during activation of the glycerol dehydratase⁵⁷ and by Dph2 during diphthamide biosynthesis⁵⁸ suggests that an alternative AdoMet Cγ-S bond cleavage pathway via an 3-amino-3-carboxypropyl radical (ACP•, **15**) may exist (Scheme 1.3 B).



Scheme 1.3 Proposed mechanism for reductive AdoMet cleavage.

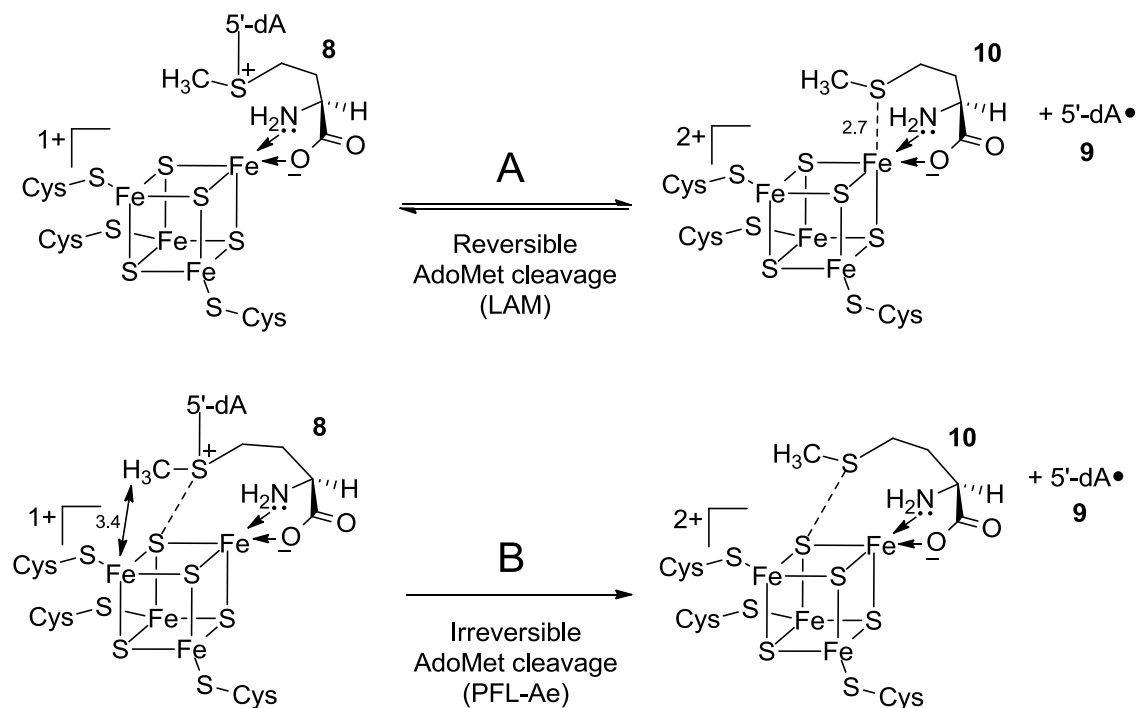
AdoMet cleavage is postulated to yield (A) a 5'-deoxyadenosine radical **9** or (B) a 3-amino-3-carboxypropyl radical **15**. Adapted from Hiscox et al.⁵⁹.

1.2.1 Electron transfer during AdoMet cleavage

While AdoMet coordination to the [4Fe–4S] cluster via its α -amino and α -carboxy groups was unambiguously demonstrated^{48–51}, two slightly different mechanisms of electron transfer from the [4Fe–4S]¹⁺ cluster to AdoMet were proposed, depending on whether AdoMet is used as a cofactor or as a substrate (Scheme 1.4). Lysine 2,3-aminomutase (LAM) cleaves AdoMet reversibly to 5'-dA• **9** and methionine **10**. Spectroscopic analysis of the cleavage complex resulting from LAM turnover with seleno-AdoMet (AdoMet where the sulfur atom is replaced with selenium) and a lysine analogue identified a short 2.7 Å Se-Fe distance⁶⁰, suggesting that selenomethionine coordinates directly to the unique [4Fe–4S] cluster iron (Scheme 1.4 A). This coordination behaviour was further interpreted to suggest that inner sphere electron transfer from the [4Fe–4S] cluster to AdoMet originates from the unique iron and not from a cluster sulfur atom⁶⁰. Methionine coordination to the [4Fe–4S] cluster would also ensure facile recombination with the 5'-dA• to reform AdoMet for the next catalytic cycle.

Pyruvate formate lyase-activating enzyme (PFL-Ae) is an example for radical AdoMet enzymes which use AdoMet as a substrate. Short distances between the AdoMet methyl group and the [4Fe–4S] cluster (3–5 Å) led to the proposal that the AdoMet sulfonium interacts with a cluster sulfide and not a cluster iron⁶¹ (Scheme 1.4 B). This was supported by electrostatic calculations which showed that the electron density on the cluster sulfides increases upon cluster reduction⁶², favouring interactions with a positively charged sulfonium group. The observation that neither productive turnover of PFL-Ae with seleno-AdoMet nor addition of selenomethionine, 5'-dAH and the reaction product triggered observable Se-Fe interactions in PFL-Ae⁵¹ indicates that, at

least for PFL–Ae, the methionine sulfur is located further away from the unique cluster iron compared to LAM (Scheme 1.4 B). Alternatively, methionine dissociates from the cluster after AdoMet cleavage such that a new molecule of AdoMet can bind.



Scheme 1.4 Reversible and irreversible AdoMet cleavage.

The role of AdoMet as a cofactor or substrate was proposed to be governed by distinct coordination modes to the radical AdoMet [4Fe–4S] cluster and electron transfer via a cluster iron or sulfide, respectively. The experimentally observed Fe–S–methionine and Fe–CH₃–AdoMet distances are indicated in Å.

The concept of iron or sulfide based electron transfer to AdoMet depending on its functional role is not supported by the X-ray crystal structures of LAM⁶³, PFL–Ae⁶⁴ and other AdoMet bound radical AdoMet enzymes⁶⁵. All structures highlight a shorter cluster iron to AdoMet sulfonium than sulfide to sulfonium distance⁶⁵, suggesting that the AdoMet sulfonium

Chapter 1 – Introduction

always binds closer to the cluster iron as indicated in Scheme 1.4 A. Seemingly contradicting, and therefore of particular interest, is the PFL–Ae structure in the absence of the PFL substrate. It demonstrates a relatively long 6.1 Å distance between the AdoMet sulfonium and the cluster iron⁶⁴ (Figure 1.5 A). However, the presence of a substrate peptide analogue induces conformational changes which ensure that AdoMet coordinates to the [4Fe–4S] cluster in a catalytically active form⁶⁴, as described for LAM. This is discussed in more detail in section 1.2.3.

Further support for the unique iron as the origin for electron transfer from the [4Fe–4S] cluster to the AdoMet sulfonium came from hybrid quantum mechanical/molecular mechanical (QM/MM) calculations based on the high resolution crystal structure of *Thermotoga maritima* (*T. maritima*) HydE⁵⁵. These investigations suggest that the highest occupied molecular orbitals in the ground (AdoMet bound) state are situated on the unique iron atom⁵⁵. In addition, the iron d orbital and AdoMet S σ^+ orbital were calculated to be of similar energy⁵⁵, as required for facile electron transfer.

1.2.2 Structural characterisation of radical AdoMet enzymes

1.2.2.1 The triose–phosphate isomerase barrel core

A survey of more than 20 crystal structures of radical AdoMet enzymes from different subfamilies identified that most family members adopt a barrel structure with parallel β -sheets surrounded on the outside by α -helices⁶⁶ (Figure 1.2). The radical AdoMet enzymes HydE³⁷ and biotin synthase (BioB)⁶⁷ are examples which adopt a full $\beta_8\alpha_8$ triose–phosphate isomerase (TIM) barrel (Figure 1.2 A), but partial $\beta_6\alpha_6$ and $\beta_5\alpha_4$ barrels have been identified in PFL–Ae⁶⁴ (Figure 1.2 B) and BtrN⁶⁸ (Figure 1.2 D), respectively. Structure–based sequence alignments suggest that this TIM barrel is common for most members of the radical AdoMet superfamily⁶⁹. This allows cautious predictions of TIM barrel residues for structurally uncharacterised radical AdoMet enzymes. However, well known exceptions are ThiC⁵² and Dph2⁵⁸. While both use AdoMet as a substrate and harbour a [4Fe–4S] cluster^{58,70–72}, their structural departure from the classical TIM barrel fold has sparked discussions regarding the identifiers for radical AdoMet enzymes⁵⁹.

While each monomer of the *Caulobacter crescentus* ThiC homodimer adopts a full $\beta_8\alpha_8$ TIM barrel, the C-terminal domain containing the conserved cysteine residues proposed to coordinate the radical AdoMet [4Fe–4S] cluster folds over the substrate binding site of the other monomer⁵² (Figure 1.2 E). This is unprecedented and implies that 5'-dA• generated in monomer A catalyses hydrogen atom abstraction from the substrate bound by monomer B. On the other hand, the conserved cysteine residues coordinating the [4Fe–4S] cluster in *Pyrococcus horikoshii* Dph2 are far apart in the primary sequence (CX₁₀₃CX₁₂₃C). In fact, they are located on three different protein domains (Figure 1.2 F).

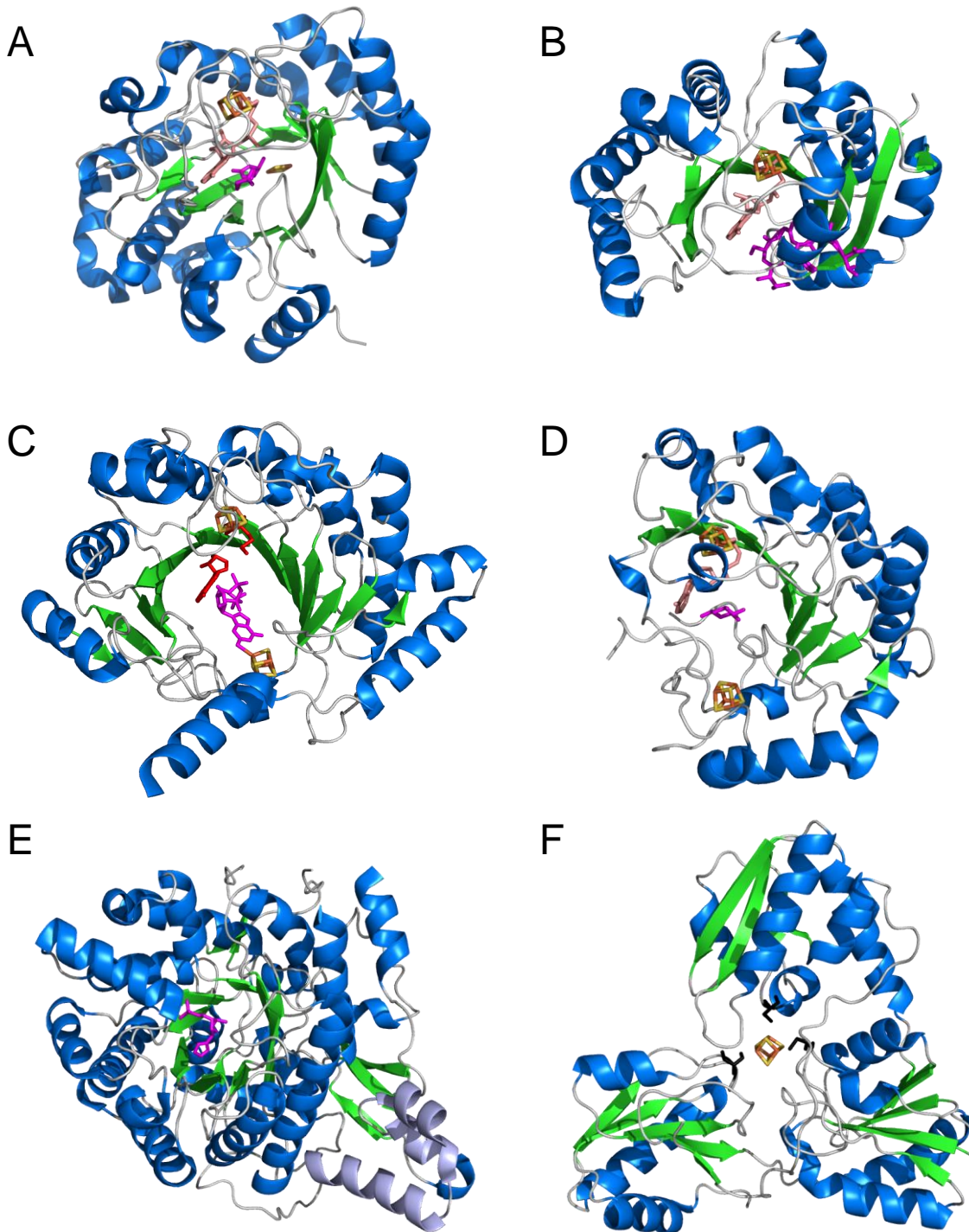


Figure 1.2 X-ray crystal structures of representative radical AdoMet enzymes.

(A) BioB with AdoMet and dethiobiotin (PDB 1R30, chain A), (B) PFL-Ae with AdoMet and RVSGYAV peptide substrate (PDB 3CB8), (C) MoaA with methionine, 5'-dAH and GTP (PDB 2FB3, chain A), (D) BtrN with AdoMet and 2-deoxy-*scyllo*-inosamine (PDB 4M7T), (E) ThiC monomer with imidazole ribonucleotide

and C-terminal cluster domain highlighted in light blue (PDB 3EPN, chain A), (F) Dph2 monomer with cluster coordinating cysteine residues in black (PDB 3LZD). Secondary structures are shown in blue (α -helices), green (β -sheets) and grey (loops) while substrates and cofactors (if present) are shown as sticks in the following colour scheme; AdoMet – salmon, methionine and 5'-dAH – red, substrate – magenta, cluster iron – orange, cluster sulfide – yellow.

1.2.2.2 AdoMet binding

For the structurally characterised members of the radical AdoMet superfamily, the radical AdoMet [4Fe-4S] cluster binding site is usually situated inside the TIM barrel, at the C-terminal end of the core β -strands, approximately 7-10 Å away from the protein surface⁶⁵ (Figure 1.2 A-D). Placement of this iron-sulfur cluster close to the surface allows interactions with other proteins, such as the host ISC proteins to facilitate cluster assembly⁶⁷ as well as redox partners like flavodoxin or ferredoxin for facile cluster reduction^{64,73}. The conserved cysteine residues coordinating three of the four cluster irons are situated on the 'cluster binding loop' which follows the first β -strand⁶⁵ (Figure 1.3, yellow). This loop protects the hydrophobic active site and the highly reactive radical intermediates generated upon turnover from solvent exposure. The unique iron of the radical AdoMet [4Fe-4S] cluster faces into the TIM barrel and is coordinated by the AdoMet α -amino and α -carboxy groups⁴⁸⁻⁵¹ (Figure 1.2 A-D, Figure 1.3).

Five binding motifs to AdoMet have been observed among radical AdoMet family members⁶⁵, but are not identical with respect to their amino acid sequences. These signature motifs are highlighted in Figure 1.3 for BioB and include hydrophobic interactions of the penultimate residue in the classical

Chapter 1 – Introduction

CX₃CX ϕ C motif with the AdoMet adenine moiety (Figure 1.3, yellow), where ϕ is usually a tyrosine or phenylalanine residue. The adenine moiety is further recognised by hydrophobic residues on strand β 5, termed the ‘GXIXGXXE motif’ (Figure 1.3, cyan) and by backbone hydrogen bonding from a ‘structural motif’ on strand β 6 (Figure 1.3, green). A glycine rich ‘GGE motif’, referring to the sequence in PFL–Ae, is situated at the C–terminus of β 2 (Figure 1.3, orange) and backbone hydrogen bonds the AdoMet amino group to ensure correct orientation of the AdoMet methionine moiety.

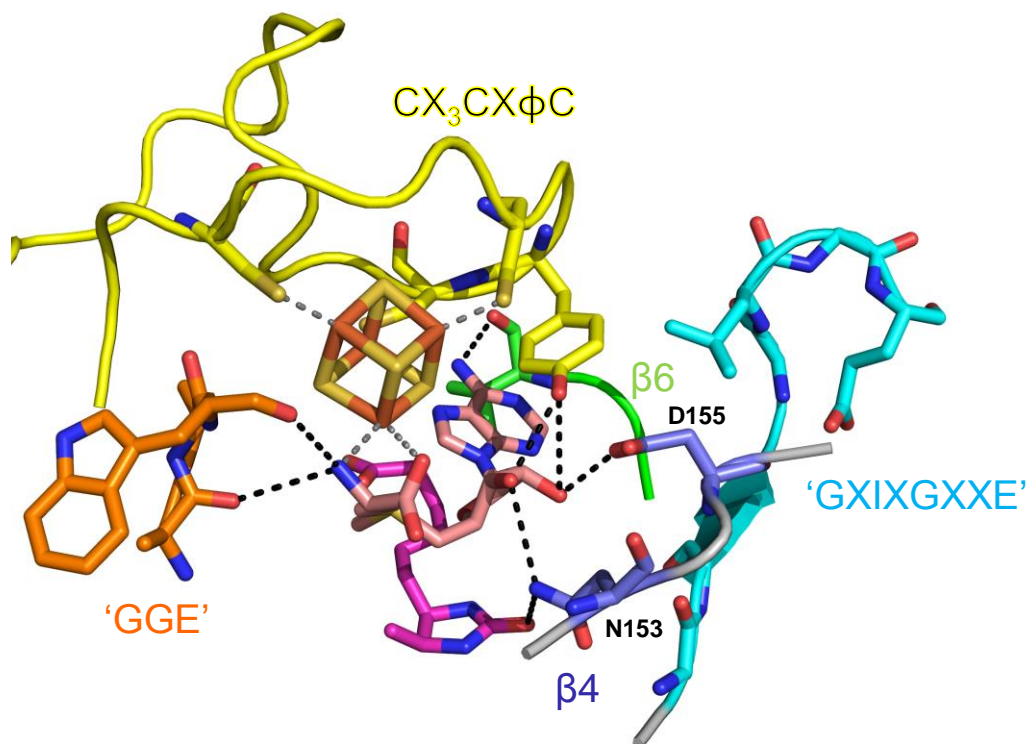


Figure 1.3 Representative AdoMet binding in BioB.

BioB active site (PDB 1R30) highlighting identified interactions with AdoMet (salmon) and the dethiobiotin substrate (magenta) as described in the text. Hydrogen bonding and coordination interactions are depicted as black and grey dashes, respectively.

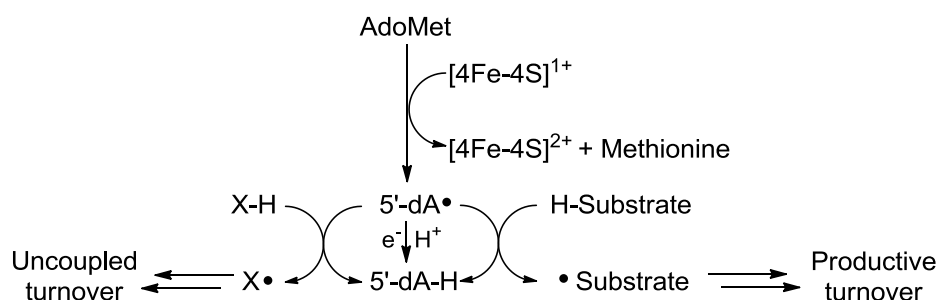
Interactions with the AdoMet ribose hydroxyl groups are less well conserved, but may include hydrogen bonding interactions from polar residues on strands β 4 and β 5. Interestingly, while BioB β 4 residues Asn153 and Asp155 were found to interact with the AdoMet ribose hydroxyls (Figure 1.3, blue), mutations of these residues do not strongly affect AdoMet cleavage or substrate binding, but decrease formation of the biotin product relative to 5'-dAH accumulation⁷⁴. This was interpreted by the authors to suggest that these residues not only have a role in AdoMet binding and orientation but potentially also in reaction catalysis to couple 5'-dA• generation with hydrogen atom abstraction⁷⁴. This interpretation may also explain the low conservation in the ribose binding motif between members of the radical AdoMet family as each substrate will require slightly different positioning relative to the 5'-dA•.

1.2.2.3 Substrate binding

Given the large variety of substrates accepted by radical AdoMet enzymes, it is not surprising that amino acid residues contacting the substrate are not conserved among family members⁶⁵. Consequently, no accurate predictions regarding substrate binding residues are possible without available structural information. A survey of available crystal structures of radical AdoMet enzymes in the presence of AdoMet and substrate has however identified that binding of the substrate always occurs inside the TIM barrel, proximal to the [4Fe-4S] cluster bound AdoMet⁶⁵ (Figure 1.2 A-D, Figure 1.3). This binding arrangement mostly involves inward facing β -sheet residues and leads to a short 4 Å distance between the AdoMet 5'-C and the substrate's hydrogen abstraction site⁶⁵.

1.2.3 Strategies for controlled radical generation

Some radical AdoMet enzymes are capable of cleaving AdoMet to 5'-dAH and methionine in the absence of the substrate⁷⁵⁻⁷⁸ and 5'-dAH formation rates ranging between $(0.7-4.2) \times 10^{-4} \text{ s}^{-1}$ have been observed^{24,79,80}. This phenomenon is termed uncoupled AdoMet cleavage and is likely due to premature quenching of the highly reactive 5'-dA• (Scheme 1.5), mostly observed when the non-natural reducing agents dithionite or 5'-deazariboflavin are used^{78,81}. Under the reducing conditions employed in activity assays, a possible mechanism for radical quenching may involve 5'-dA• reduction to the carbanion, followed by protonation to 5'-dAH (Scheme 1.5). Alternatively, non-specific hydrogen atom abstraction from protein backbone amino acids, similar to activation of glycy radical enzymes (Scheme 1.2 A), or attack on a [4Fe-4S] cluster sulfide⁷⁴ may occur. To limit these damaging side reactions, precise control and efficient coupling between 5'-dA• generation and hydrogen atom abstraction from the substrate is required.



Scheme 1.5 Uncoupled AdoMet cleavage.

The highly reactive 5'-dA• cannot only abstract hydrogen atoms from the enzyme's substrate but also from protein backbone amino acids (X-H). Alternatively, reduction of 5'-dA• followed by protonation may occur. Both events lead to uncoupled 5'-dAH formation.

1.2.3.1 Thermodynamic control

The redox potential of AdoMet in aqueous solution is estimated as -1600 mV (vs normal hydrogen electrode, NHE)⁸² while the protein bound $[4\text{Fe-4S}]^{2+}$ cluster has an estimated potential of -480 mV, as estimated in LAM⁸³. This potential energy gap (ΔE^\ddagger) of 1120 mV corresponds to an activation barrier (ΔG^\ddagger) of 108 kJ/mol (Equation 1.1, $F = 9.65 \times 10^4$ C/mol) and ensures that AdoMet cleavage does not occur spontaneously. The events leading to feasible AdoMet reduction are summarised in Figure 1.4 and described below.

$$\Delta G^\ddagger = -n F \Delta E^\ddagger \quad \text{Equation 1.1}$$

Initial AdoMet binding to the $[4\text{Fe-4S}]^{2+}$ cluster increases the cluster redox potential to -430 mV, presumably to allow cluster reduction to its $1+$ oxidation state⁸⁴. Coordination of AdoMet to the iron-sulfur cluster brings about the largest change in the potential difference as the redox potential of AdoMet itself is increased from -1600 mV to -990 mV⁸⁵. Only upon binding of the substrate (and cofactors if required) is the energy gap between the $[4\text{Fe-4S}]$ cluster and AdoMet redox potentials further decreased⁸⁵. The resulting activation barrier for reductive AdoMet cleavage of 390 mV (38 kJ/mol) allows facile electron transfer from the cluster to AdoMet. This small energy gap agrees well with computational QM/MM studies on the X-ray crystal structures of HydE bound with AdoMet or the cleavage products $5'$ -dAH and methionine which established an activation energy barrier of 54 kJ/mol⁵⁵.

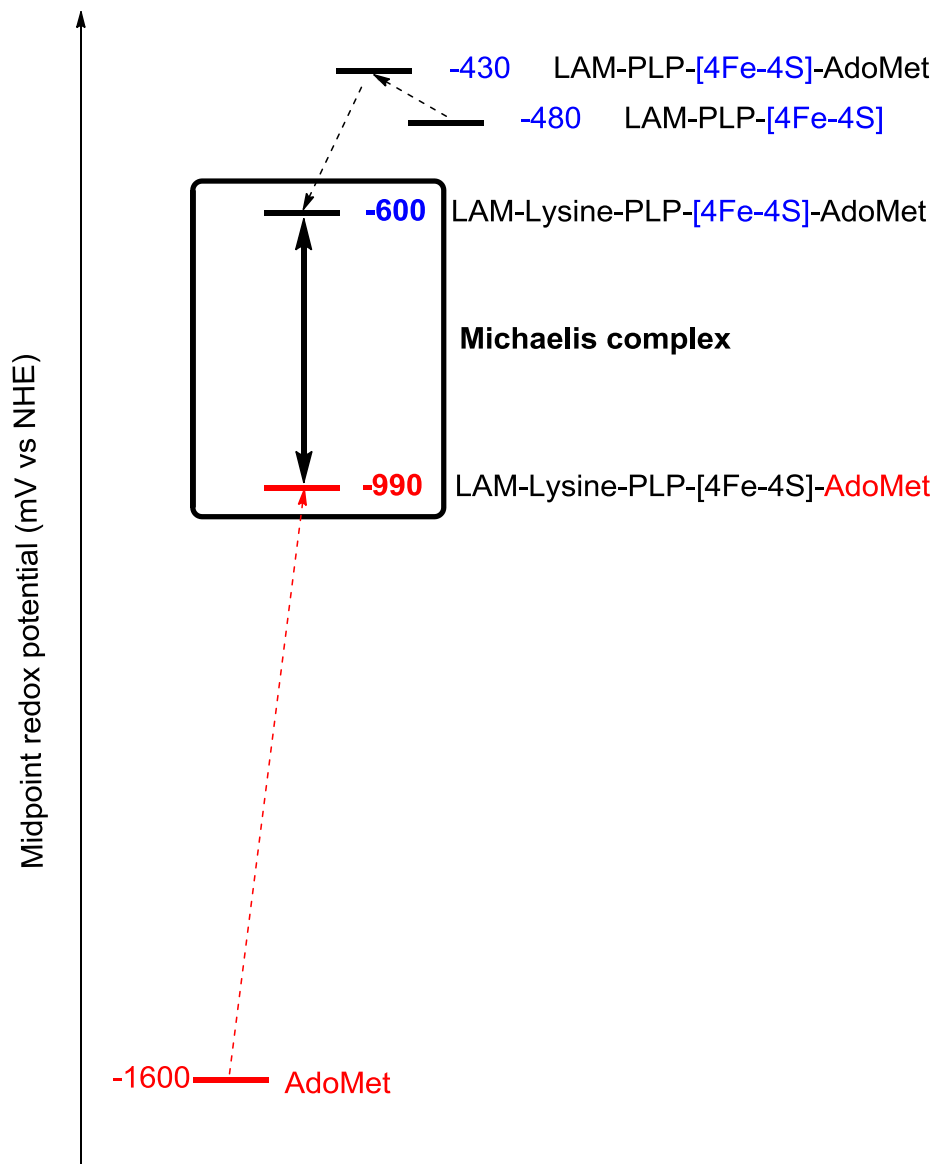


Figure 1.4 Energetics of reductive AdoMet cleavage as estimated in LAM. AdoMet related midpoint redox potentials are shown in red while [4Fe-4S] cluster potentials are highlighted in blue. The L- α -lysine substrate has been abbreviated to lysine. Adapted from Wang et al.⁸⁵.

1.2.3.2 Structural control

While X-ray crystal structures of the majority of AdoMet bound radical AdoMet enzymes^{37,73,86,87} show AdoMet coordinating to the [4Fe-4S] cluster as previously described for LAM (see section 1.2.1), the respective PFL-Ae structure⁶⁴ shows a disordered AdoMet with an AdoMet sulfonium to cluster iron distance of 6.1 Å (Figure 1.5 A). Only in the presence of a 7-residue substrate peptide (including the catalytically important G734) is AdoMet positioned such that the electron transfer distance reduces to 3.2 Å⁶⁴ (Figure 1.5 B). In addition, the hydrogen abstraction site at C α of Gly734 is situated only 4.1 Å away from the 5'-C of the incipient 5'-dA \bullet , an orientation which facilitates efficient coupling of radical generation and hydrogen atom abstraction. These comparative structures indicate how radical AdoMet enzymes may control AdoMet cleavage through unproductive AdoMet binding in the absence of substrate. Upon substrate binding, the conformational changes associated with the substrate binding loop (Figure 1.5, orange) furthermore protect the occurring radical chemistry from solvent exposure to prevent unnecessary radical quenching.

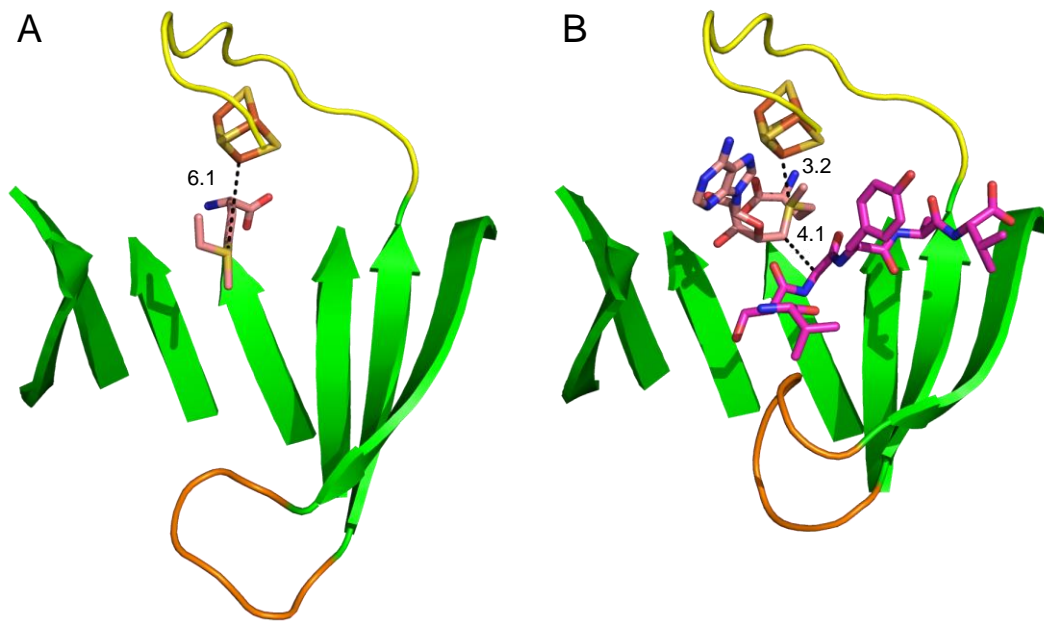


Figure 1.5 Substrate binding forces AdoMet into a catalytically active conformation.

X-ray crystal structures of (A) PFL-Ae with disordered AdoMet (salmon) (PDB 3C8F) and (B) PFL-Ae in the presence of AdoMet and a 7-peptide substrate (RVSGYAV, magenta) (PDB 3CB8). Note that only the methionine part of AdoMet is clearly visible in (A), while only the last 6 residues of the heptamer peptide could be refined in (B). β -Sheets are shown in green, helices and loops have been omitted for clarity. Only the [4Fe-4S] cluster binding loop (yellow) and the substrate binding loop (orange) are shown. Distances are shown in Å. Adapted from Dowling et al.⁶⁶.

1.2.4 Roles of auxiliary [4Fe–4S] clusters in AdoMet enzymes

There is an increasing number of radical AdoMet enzymes which require an auxiliary (mostly [4Fe–4S]) cluster for activity⁸⁸. Representative members of this growing subfamily are shown in Table 1.1 which highlights that neither the conserved cysteine sequence coordinating the auxiliary cluster, nor the relative position to the radical AdoMet cluster binding cysteine residues is conserved. A survey of available crystal structures of this radical AdoMet subfamily confirms that the spatial position of the auxiliary cluster with respect to the radical AdoMet cluster is not preserved. Distances between both [4Fe–4S] clusters vary between 8 Å and 17 Å, where the main substrate is often sandwiched between the cluster bound AdoMet and the auxiliary cluster (see also Figure 1.2 A, C, D). Different roles have been identified for the auxiliary iron–sulfur clusters as summarised in Table 1.1.

Table 1.1 Representative radical AdoMet enzymes containing two or more iron–sulfur clusters.

With the exception of BioB and HydE, all enzymes coordinate an auxiliary [4Fe–4S] cluster. The proposed role and distance of the auxiliary cluster to the radical AdoMet cluster is listed in column 2 if known. Column 3 highlights the sequence relationship of the additional cysteine motif to the radical AdoMet [4Fe–4S] cluster coordinating cysteine triad as being N- or C-terminal.

Enzyme (PDB)	Role of auxiliary cluster	Auxiliary cluster coordinating sequence	References
<i>Complex cofactor biosynthesis</i>			
MoaA (1TV8, 2FB3)	GTP binding (17 Å)	C::CX ₂ CX ₁₃ C	86,89,90
TYW1 (2YX0, 2Z2U)	Pyruvate binding	N::CX ₁₂ CX ₁₂ C	91,92
HydE ^a (3IIZ)	Currently unknown (20 Å)	C::CX ₇ CX ₂ C	37
<i>Dehydrogenases</i>			
BtrN (4M7T)	Electron acceptor (16 Å)	C::CX ₁₇ CX ₄₄ CX ₂ C	68,93
anSME ^b (4K36, 4K39)	Electron acceptor (17 Å)	C::CX ₅ CX ₁₄ CX ₅₃ C	94

Table 1.1 cont.

<i>Methylthiotransferases</i>			
MiaB	Binding of sulfur source	N::CX ₃₅ CX ₃₂ C	95,96
RimO (4JC0)	Binding of sulfur source (8 Å)	N::CX ₃₅ CX ₂₈ C	96,97
<i>Sulfur insertion</i>			
LipA ^c	Sacrificial sulfur source (13 Å)	N::CX ₄ CX ₅ CX ₂₂₈ S	98-100
BioB (1R30)	Sacrificial sulfur source (12 Å)	C::CX ₃₀ CX ₅₉ CX ₇₁ R	67,101-104

a – The cysteine motif is not fully conserved and not essential for HydE activity³⁷.

b – *Clostridium perfringens* anSME contains two additional [4Fe-4S] clusters, details are described for auxiliary cluster I¹⁰⁵.

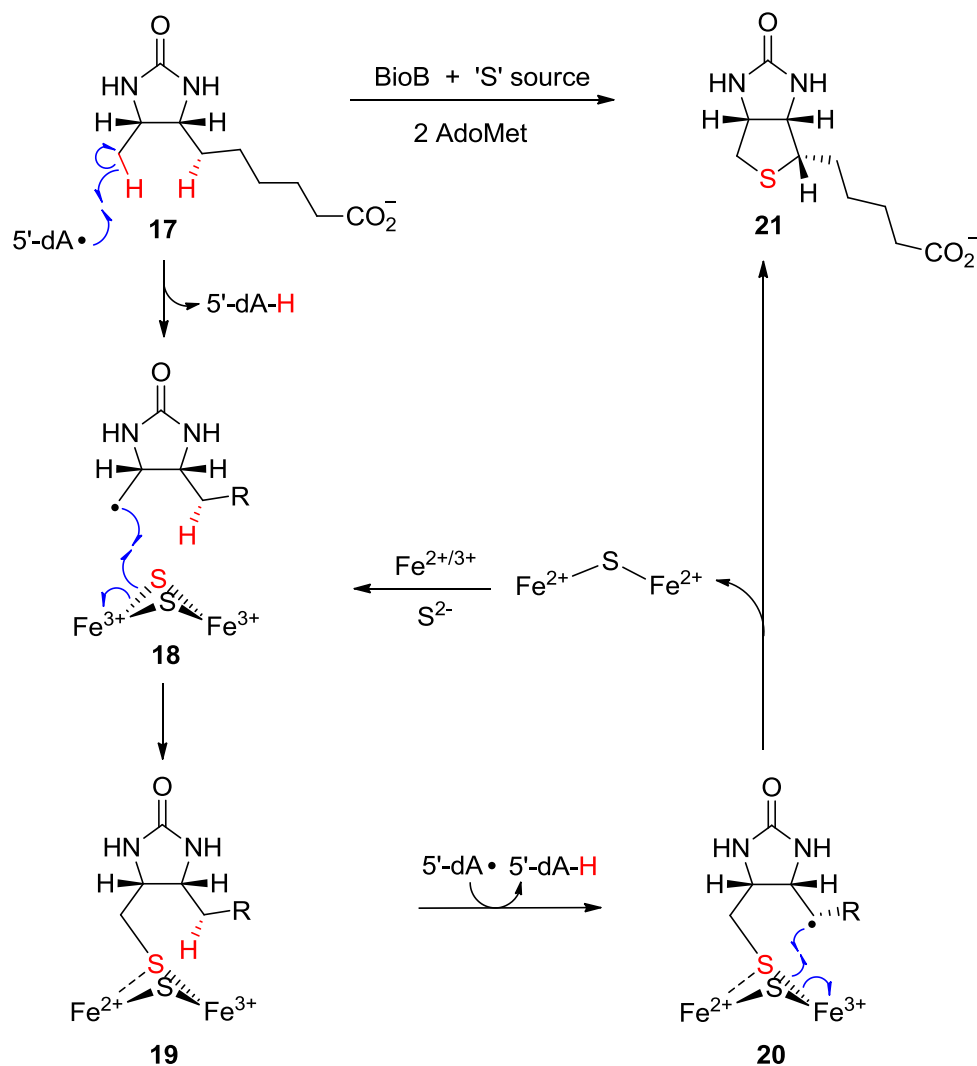
c – The cluster distances and ligation of a conserved serine residue to the auxiliary cluster have been identified in the X-ray crystal structure of *Thermosynechococcus elongates* LipA by Jenny E. Harmer¹⁰⁶.

Chapter 1 – Introduction

The auxiliary [2Fe–2S] cluster in BioB is thought to be a sacrificial sulfur source during the biosynthesis of biotin **21** from dethiobiotin (DTB, **17**)^{102,107–110} (Scheme 1.6). Sulfur insertion is proposed to be a stepwise process which requires two equivalents of AdoMet^{78,111}. It is thought that hydrogen atom abstraction by 5'-dA• occurs first at the C9 methyl group of DTB **17**. The resulting radical then attacks the [2Fe–2S]²⁺ cluster μ_2 -sulfide to form 9-mercaptodethiobiotin **19** with concomitant cluster reduction^{104,112,113}. Similarly, abstraction of the C6 *pro-S* hydrogen from **19**¹¹⁴ and C–S bond formation with retention of stereochemistry (**20**) results in biotin **21** and cluster degradation. Reassembly of the [2Fe–2S] cluster is thought to occur by the ISC assembly machinery in vivo¹¹⁵. Fugate and co-workers¹¹⁶ have provided a detailed review of the evidence regarding the mechanism of biotin formation.

The auxiliary [4Fe–4S] cluster of lipoyl synthase LipA is ascribed a similar (sulfur donating) role during sequential thiolation of the octanoyl chain of a lipoyl carrier protein^{99,100,117} (Scheme 1.2 B).

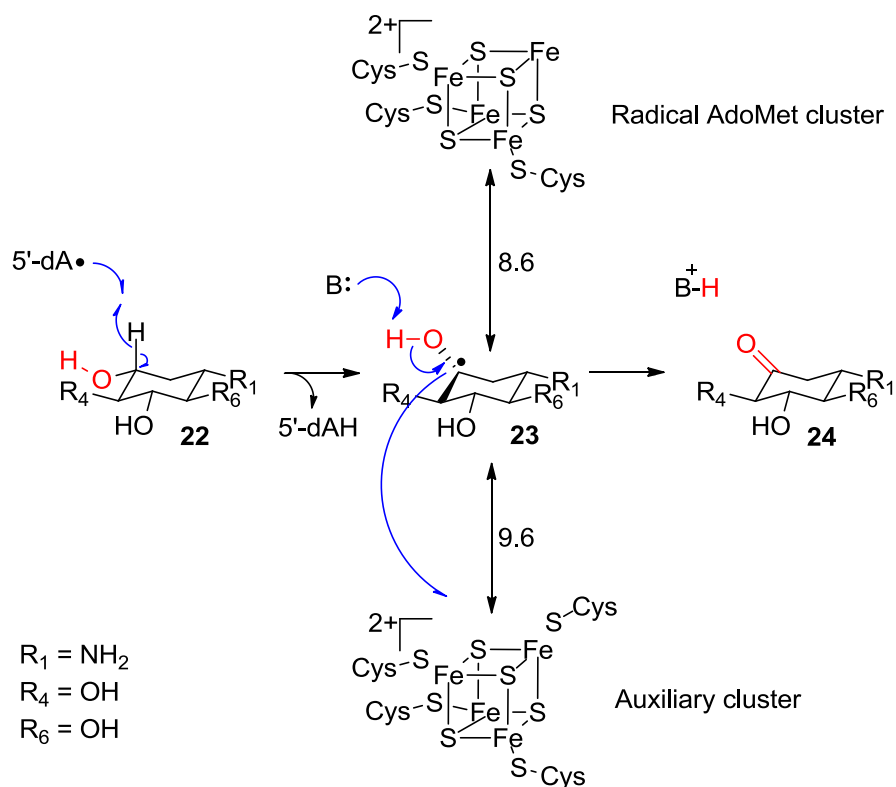
While the auxiliary clusters in BioB and LipA are coordinated by three cysteine and one non-cysteine residue, the auxiliary [4Fe–4S] cluster in MoaA, TYW1 and the methylthiotransferases MiaB and RimO has one uncoordinated, unique iron atom, very similar to the radical AdoMet [4Fe–4S] cluster. There is unambiguous experimental evidence for MoaA^{90,118} and RimO⁹⁶ that the non-ligated iron is facing into the TIM barrel active site and that it furthermore anchors the enzyme's substrate for correct positioning relative to AdoMet.



Scheme 1.6 Proposed mechanism of BioB catalysed biotin formation.

Biotin formation involves two consecutive hydrogen atom abstraction and thiolation steps. The auxiliary [2Fe-2S] cluster is the sacrificial sulfur source and requires reassembly after turnover. Adapted from Fugate et al.¹¹⁶. For clarity, the [2Fe-2S] cluster ligating amino acids have been omitted, R = (CH₂)₄-CO₂⁻.

A third subclass of radical AdoMet enzymes containing an auxiliary [4Fe–4S] cluster is comprised by the dehydrogenases BtrN and anSME. Both enzymes oxidise a respective carbohydrate hydroxyl group or a Cys/Ser residue to a ketone (Scheme 1.2 D) and are thought to follow identical mechanisms⁹³. Their auxiliary clusters have originally been proposed to be involved in substrate binding^{93,119} but their recently solved X-ray crystal structures demonstrate that the [4Fe–4S] cluster is coordinated by a full set of cysteine ligands^{68,105}. The auxiliary cluster in BtrN has now been postulated to act as an electron acceptor during oxidation of 2-deoxy-*scyllo*-inosamine (DOIA, **22**) to amino-dideoxy-*scyllo*-inosose (amino-DOI, **24**)⁶⁸ as outlined in Scheme 1.7. The AdoMet derived 5'-dA• abstracts a hydrogen atom from the C3 position of DOIA **22**⁶⁸. Deprotonation of the resulting C-centred hydroxyalkyl radical **23** is proposed to occur by Arg152 (*Bacillus circulans* sequence), activated by a nearby carboxylate⁶⁸. The oxidised auxiliary [4Fe–4S]²⁺ cluster⁹³ at a distance of 9.6 Å is poised to accept an electron to complete oxidation of **23** to amino-DOI **24**⁶⁸. Re-oxidation of the auxiliary [4Fe–4S]¹⁺ cluster has been proposed to occur by electron transfer to the radical AdoMet cluster⁹³. This is however unlikely due to the 16 Å separation between both clusters, too large a distance for facile electron transfer (4–14 Å are common¹²⁰). Instead, transfer to an external redox partner may occur⁶⁸.

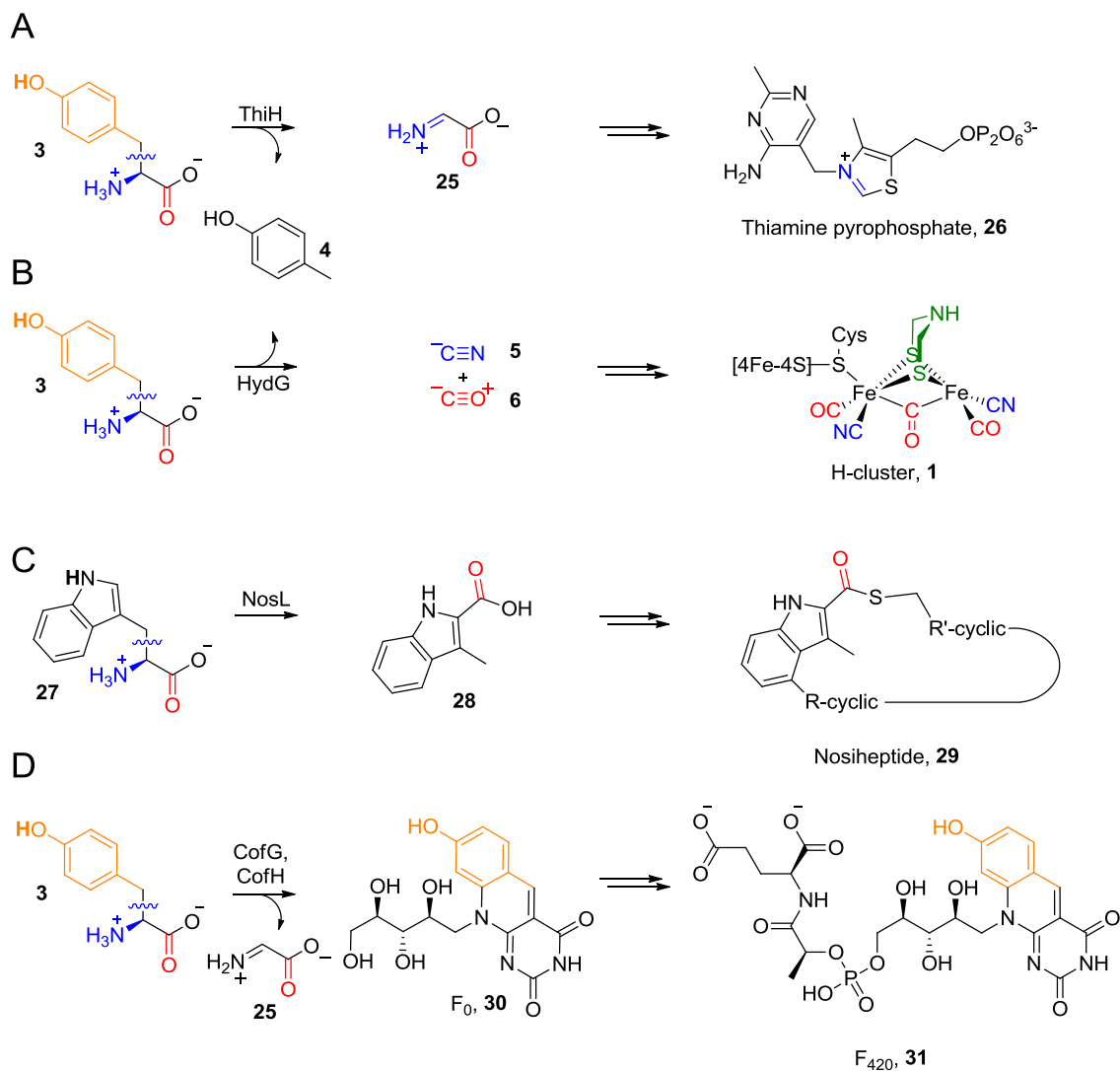


Scheme 1.7 Proposed mechanism of BtrN catalysed amino-DOI formation.

The auxiliary [4Fe-4S] cluster in BtrN acts as an electron acceptor during oxidation of DOIA **22** to amino-DOI **24**. The outlined mechanism was proposed by Goldman and co-workers based on their spectroscopic characterisation of BtrN^{68,93} and previous mechanistic studies by Yokoyama and colleagues¹²¹. The approximate separation between the substrate and the [4Fe-4S] clusters is indicated in Å; B represents a catalytic base, likely Arg152⁶⁸.

1.2.5 HydG belongs to a C α -C β lyase subclass

Sequence analyses (Appendix 1) suggest that the radical AdoMet enzymes HydG, ThiH and NosL form a subfamily^{34,122} in which members cleave the C α -C β bond of aromatic amino acids. Specifically, ThiH and HydG cleave tyrosine **3** during biosynthesis of the thiamine pyrophosphate cofactor **26**^{123,124} and the [FeFe]-hydrogenase H-cluster **1**³³⁻³⁵, respectively (Scheme 1.8 A, B). NosL on the other hand catalyses the rearrangement of L-tryptophan **27** to 3-methyl-2-indolic acid **28** during nosiheptide **29** biosynthesis^{125,126} (Scheme 1.8 C). An additional family member should be the recently identified F₀ synthase, as it cleaves the tyrosine C α -C β bond towards F₀ **30** during biosynthesis of the F₄₂₀ cofactor **31**¹²⁷ (Scheme 1.8 D). Despite the apparent functional homology, sequence alignments suggest that the CofG/CofH subunits of the F₀ synthase are more similar to the radical AdoMet enzyme HydE than to HydG or ThiH (Appendix 1).



Scheme 1.8 Catalysed reactions by radical AdoMet C α -C β lyase subfamily.

The hydrogen atom most likely abstracted by the 5'-dA \bullet is shown in bold.

While all enzymes in the radical AdoMet C α -C β lyase subfamily contain the conserved radical AdoMet CX₃CX₂C motif, HydG is the only member which contains an additional cysteine triad as exemplified in Figure 1.6. While the C-terminal CX₂CX₂₂C motif in *C. acetobutylicum* HydG was shown to be essential during [FeFe]-hydrogenase activation²³, CX₅CX₁₉C and CX₂CX₁₁C variants exist¹²⁸ (Figure 1.6 B). Only the first and last cysteine residue were found to be conserved among 301 HydG homologues investigated¹²⁸. The proposal that the C-terminal cysteine motif may coordinate an auxiliary [4Fe-4S] cluster²³ was supported by initial iron quantifications and electron paramagnetic resonance (EPR) characterisations of *T. maritima*²⁴ and *C. acetobutylicum*²⁵ HydG.

A *Clostridium acetobutylicum* SNY CVNG CVY CPYHHKNKH IARKKLSQEDVKRETI AL
Thermotoga maritima GND C I NDCVY CGFRVSNKVVERRTL TEEQLKEEVKAL
Shewanella oneidensis SNH CANS CSY CGFNADNHELKRKTLKQDE IRQEVA I L
Thermoanaerobacter tengcongensis SNL CVNN CVY CGFRRENTV I KRRRLTLEEVRREA EVL

B *Clostridium acetobutylicum* N - Y I P S F C T A C Y R E G R T G D R F M S L V K S G Q I A N C C Q P N
Thermotoga maritima G - F V P S F C T A C Y R A G R T G E H F M E F A I P G F V K N F C T P N
Shewanella oneidensis S D A I P S F C T G C Y R K G R T G D H F M G L A K Q Q F I G K F C Q P N
Thermoanaerobacter tengcongensis G - Y I T S F C T A G Y R C G R T G K H I M T L L K T G R E A V F C K L N

Figure 1.6 Partial sequence alignment of HydG from selected organisms.

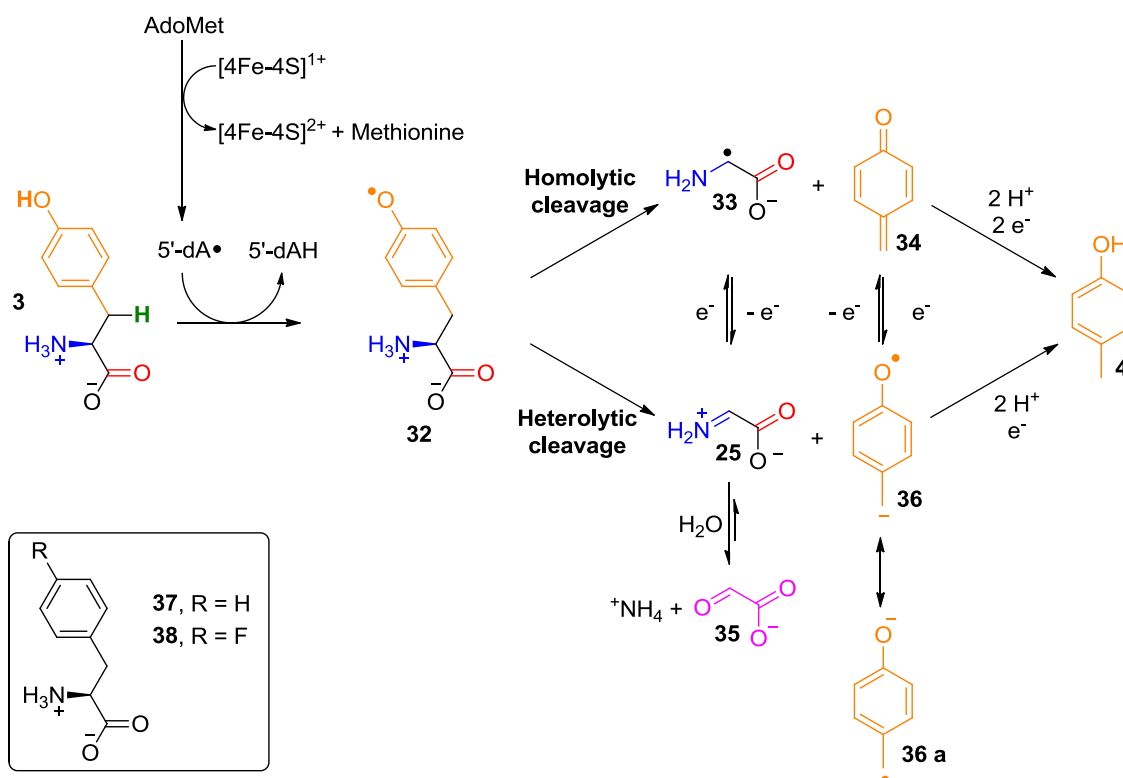
(A) Conserved N-terminal radical AdoMet CX₃CX₂C motif and (B) partially conserved C-terminal CX₂CX₂₂C motif of HydG from selected organisms.

HydG shares 27% sequence homology with ThiH³³ and both enzymes have been shown to cleave the tyrosine C α -C β bond in an AdoMet dependent fashion to yield *p*-cresol **4**^{33,124} (Scheme 1.8 A, B). During ThiH assays, glyoxylate **35** accumulated in a stoichiometric ratio with respect to *p*-cresol **4** and is thought to be the *in situ* hydrolysis product of dehydroglycine **25**¹²⁴ (Scheme 1.9). Hydrogen atom abstraction from the tyrosine hydroxyl group by 5'-dA• was hypothesised by Kriek and co-workers to initiate homolytic or heterolytic C α -C β bond cleavage of tyrosine **3** to yield a C-centred glycine radical **33** and quinone methide **34** or dehydroglycine **25** and a phenyl radical **36**, respectively¹²⁴ (Scheme 1.9).

Abstraction of an exchangeable hydrogen atom is less common among radical AdoMet enzymes and attack on the benzylic hydrogen atom of tyrosine **3** could also lead to a C-centred glycine radical **33** and *p*-cresol **4**. In fact, abstraction of the hydroxyl hydrogen is not predicted based on the bond dissociation energies¹²⁹ of the phenolic O-H (364 kJ/mol) compared to the benzylic C-H (355 kJ/mol) bond. The importance of the phenolic hydrogen for tyrosine cleavage was however inferred by ThiH activity studies where neither L-phenylalanine **37** nor *p*-fluoro-L-phenylalanine **38** were able to promote AdoMet cleavage relative to the natural substrate **3**¹³⁰. Fluorine occupies 97% of the van der Waals radius of oxygen¹³¹, suggesting that **38** may have been a ThiH substrate if the benzylic hydrogen were abstracted.

Although homolytic tyrosine cleavage is thermodynamically favoured¹²⁴, neither of the cleavage intermediates **33** and **34** have yet been observed. The C-centred glycine radical **33** may however be converted into the experimentally inferred dehydroglycine product **25** by a one electron oxidation step (Scheme 1.9). Although glycine radical oxidation seems unlikely under the

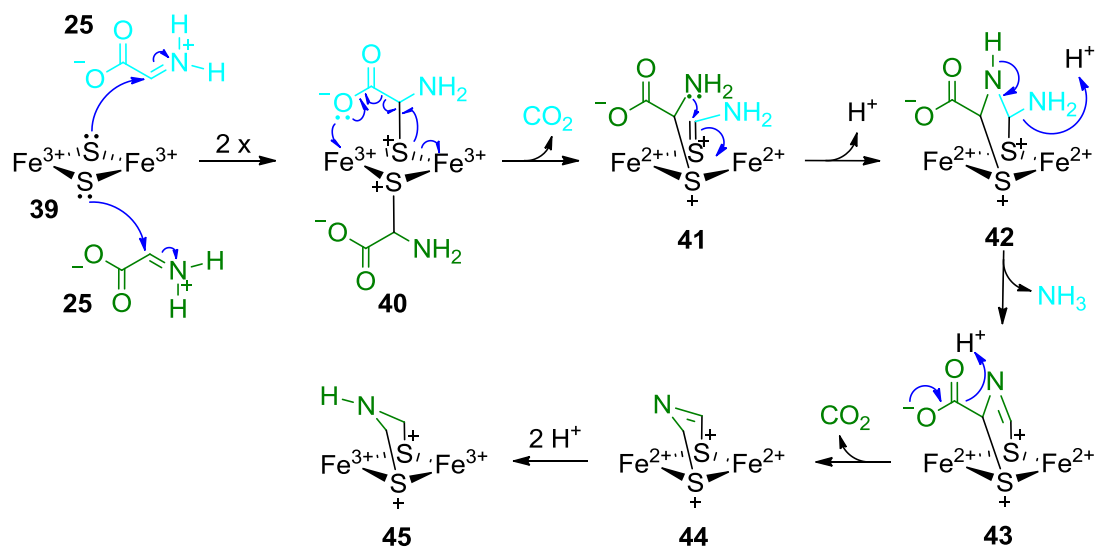
reducing assay conditions, it could theoretically be achieved by electron transfer to the quinone methide **34**, resulting in **25** and radical **36**. In either case, electrons for subsequent reduction steps to *p*-cresol **4** are likely provided by the added reductant.



Scheme 1.9 Proposed mechanism for ThiH catalysed in vitro tyrosine cleavage.

Although abstraction of the benzylic hydrogen (bold green) over the phenolic hydrogen (bold orange) is favoured based on bond dissociation energies, the 5'-dA• attacks the latter. The resulting tyrosyl radical **32** can cleave homolytically or heterolytically to form *p*-cresol **4**. Adapted from Kriek et al.¹²⁴.

The functional similarity between ThiH and HydG with regards to tyrosine **3** cleavage to *p*-cresol **4** led Pilet and co-workers to propose that HydG catalysed tyrosine cleavage also yields stoichiometric quantities of dehydroglycine **25**³³. At the time, this reactive intermediate was postulated to be the precursor to the [FeFe]-hydrogenase H-cluster **1** dithiolate bridge³³ (Scheme 1.8 B, green). Two equivalents of dehydroglycine **25** were thought to undergo concomitant decarboxylation to condense on a presumed C-terminal [2Fe-2S] cluster of HydG³³ (Scheme 1.10, **40**→**41**, **43**→**44**). This mechanism is initiated by nucleophilic attack of the cluster sulfides (**39**) towards the iminium carbon of **25**³³, a reactivity inconsistent with the observation that the μ_2 -sulfides of a classical [2Fe-2S] centre contain little spin density^{38,39}. In addition, *in silico* evaluation by Grigoropoulos and co-workers found that dehydroglycine **25** or a glycine radical **33** are thermodynamically unfavourable precursors for the formation of the dithiomethylamine bridge⁴⁰. For these reasons, the reaction in Scheme 1.10 is unlikely to occur.



Scheme 1.10 Proposed fate of HydG derived dehydroglycine to a dithiomethylamine bridge.

Two equivalents of dehydroglycine condense on the presumed C-terminal [2Fe-2S] cluster of HydG to form a dithiomethylamine bridge. The electrons for the final, two electron reduction step are proposed to derive from the cluster irons. For clarity, the two dehydroglycine molecules have been coloured in light blue and green while [2Fe-2S] cluster ligating amino acids have been omitted.

Adapted from Pilet et al.³³.

An alternative fate of the tyrosine derived dehydroglycine **25** or the C-centred glycine radical **33** may involve collapse to the H-cluster cyanide **5** and CO **6** ligands (Scheme 1.8 B). The hypothesis of HydG catalysed cyanide formation was experimentally supported by negligible formation of glyoxylate **35** in HydG activity assays, but accumulation of equimolar quantities of cyanide **5**³⁴ as well as sub-stoichiometric amounts of CO **6**²⁵ with respect to *p*-cresol **4**. Analysis methods based on high pressure liquid chromatography (HPLC) with UV-Vis and fluorescence detection were used to quantify the HydG catalysis products³⁴ as summarised in Scheme 1.11. The products 5'-dAH **13**

Nicolet and co-workers prepared a *C. acetobutylicum* SX₂SX₂₂C HydG double mutant and a C-terminal truncated HydG mutant (Δ CTD), which lacked the entire C-terminal domain, including the cysteine motif¹³³. Both mutants showed a decreased coordination of iron compared to wild-type (WT) HydG, suggesting that the proposed auxiliary [4Fe-4S] cluster may not be coordinated. Furthermore, the respective double and Δ CTD HydG mutants formed approximately 50% and 100% less cyanide with respect to the WT enzyme¹³³, inferring a functional importance of the HydG auxiliary [4Fe-4S] cluster during cyanide synthesis. Based on these observations, detection of sub-stoichiometric amounts of HbCO in HydG in vitro assays²⁵ was postulated to arise from formation of a stable cluster-carbonyl complex¹³³.

Unambiguous evidence for the auxiliary [4Fe-4S] cluster in HydG as well as detailed mechanistic information regarding cyanide and CO formation or the transfer and incorporation of these ligands into the [FeFe]-hydrogenase H-cluster has not been fully described and requires substantial future research.

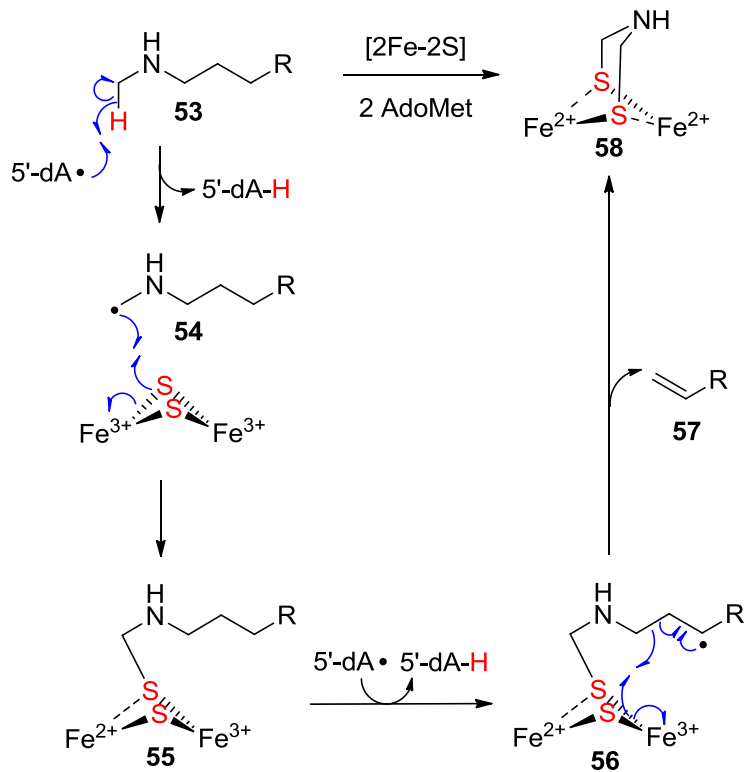
1.2.6 Role of HydE in [FeFe]-hydrogenase active site assembly

Based on the observation that *T. maritima* HydE and HydG likely coordinate two [4Fe-4S] clusters, Rubach and co-workers proposed that either enzyme may synthesise the H-cluster dithiolate bridge using BioB and LipA related chemistry²⁴ (Scheme 1.6, Scheme 1.2 B). By identifying that HydG likely catalyses the formation of the H-cluster cyanide and CO ligands^{25,34,35}, HydE is, by exclusion, likely responsible for the synthesis of the dithiomethylamine^{31,36}. Sequence analyses confirm a close relationship of HydE with BioB and LipA^{34,128}

(Appendix 1) and a radical AdoMet dependent mechanism for installation of the dithiomethylamine bridge has been proposed by Grigoropoulos and Szilagyi⁴⁰ (Scheme 1.12). This mechanism assumes the presence of a [2Fe–2S] cluster instead of a [4Fe–4S] cluster on HydE and involves abstraction of a hydrogen atom from the methyl group of a secondary amine precursor **53** by 5'-dA•. The resulting C-centred radical **54** attacks the [2Fe–2S] cluster μ_2 -sulfide with concomitant cluster reduction to yield **55**. A second molecule of 5'-dA• then abstracts a hydrogen atom from the C5 position of **55** before collapse of radical **56** via homolytic C3–C4 scission and attack on the other cluster μ_2 -sulfide. The ultimate alkylated all ferrous iron–sulfur cluster **58** is formed with release of alkene **57**. The cysteine sulfur to iron bonds of this diferrous cluster are labile and thus poised for ligand exchange reactions of the cysteine thiolate and/or incorporation of the cyanide and CO ligands⁴⁰. The exact identity of the proposed alkane precursor **53** is currently unknown, but it is likely that it is an *E. coli* metabolite. This conclusion comes from the observation that HydA heterologously expressed in *E. coli* can be activated by the heterologously expressed and purified HydF^{EG} maturase^{29,30}.

Despite the described plausible reaction mechanism, it is unlikely that the dithiolate bridge is assembled on a HydE based auxiliary iron–sulfur cluster^{24,37}, because the cluster coordinating CX₇CX₂C sequence identified in *T. maritima* HydE is not fully conserved³⁷. Furthermore, mutating these cysteine residues did not abolish the ability of HydE to activate HydA³⁷, suggesting that they are functionally not important.

Chapter 1 – Introduction



Scheme 1.12 Proposed role of radical AdoMet enzyme HydE.

For clarity, cluster ligating residues have been omitted. Adapted from Grigoropoulos et al.⁴⁰.

1.3 Aims of thesis

In collaboration with the Joan B. Broderick and John W. Peters laboratories (Montana State University), the project aim was to address the following questions:

- Does *C. acetobutylicum* HydG coordinate an auxiliary [4Fe–4S] cluster via the C-terminal CX₂CX₂₂C motif?
- Is the binding of the tyrosine substrate facilitated by the HydG C-terminal [4Fe–4S] cluster?
- What is the role of the HydG C-terminal [4Fe–4S] cluster and/or amino acid residues during tyrosine cleavage to cyanide and CO?
- What mechanism drives cyanide and CO formation?

Chapter 2

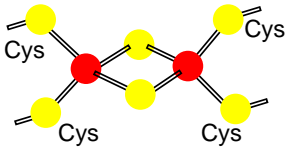
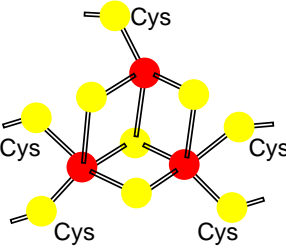
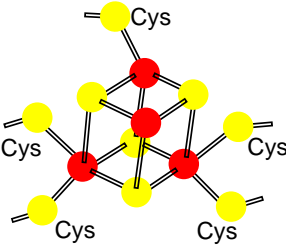
Spectroscopic characterisation of wild-type and mutant *C. acetobutylicum* HydG

2.1 Introduction

UV-Vis spectroscopy can be used to characterise iron-sulfur cluster containing proteins due to the iron to sulfur charge transfer giving rise to distinct absorption bands¹³⁴ where $[4\text{Fe-4S}]^{2+}$ and $[2\text{Fe-2S}]^{2+}$ clusters can be differentiated (Table 2.1). While the former absorb strongly at 400 nm ($\epsilon_{400} = 16 \text{ mM}^{-1} \text{ cm}^{-1}$)¹³⁴, $[2\text{Fe-2S}]^{2+}$ clusters show several characteristic peaks at 330 nm, 460 nm and 550 nm (in order of decreasing extinction coefficients, see Table 2.1). Although UV-Vis spectra can give an indication of the iron-sulfur cluster type and may be sufficient for 'simple', single cluster containing proteins, unambiguous conclusions regarding the composition in proteins containing several clusters cannot be drawn due to broad and overlapping absorption bands.

Table 2.1 Spectroscopic characteristics of ferredoxin-like iron-sulfur clusters.

Adapted from Lippard et al.¹³⁵ with information from references ^{134,136,137}. The cluster iron and sulfur atoms are coloured red and yellow, respectively.

Cluster type	Oxidation state	Spin state	EPR g values	ϵ per iron (mM ⁻¹ cm ⁻¹)
	2+	$S = 0$	Inactive	$\epsilon_{325} = 6.4$ $\epsilon_{420} = 4.8$ $\epsilon_{465} = 4.9$ $\epsilon_{550} = 2.5$
	1+	$S = \frac{1}{2}$	2.05, 1.95, 1.89	Absorbance reduces by 50%
	1+	$S = \frac{1}{2}$	2.02, 2.00, 1.79	$\epsilon_{305} = 7.7$ $\epsilon_{415} = 5.2$ $\epsilon_{455} = 4.4$
	0	$S = 0$	Inactive	$\epsilon_{425} = 3.2$
	3+	$S = \frac{1}{2}$	2.12, 2.04, 2.04	$\epsilon_{325} = 8.1$ $\epsilon_{385} = 5.0$ $\epsilon_{450} = 4.6$
	2+	$S = 0$	Inactive	$\epsilon_{305} = 4.9$ $\epsilon_{400} = 4.0$
	1+	$S = \frac{1}{2}$	2.06, 1.92, 1.88	Absorbance reduced

A good technique to distinguish between [4Fe-4S], [3Fe-4S] and [2Fe-2S] clusters however is EPR spectroscopy, which characterises the spin of unpaired electrons ($S = \frac{1}{2}$). While both [4Fe-4S] and [2Fe-2S] clusters in their oxidised 2+ state are EPR inactive, reduction to the 1+ state leads to a paramagnetic cluster¹³⁸ (Table 2.1). Similar to nuclear magnetic resonance (NMR), the energy levels of the electron spin will split in an applied magnetic field B_0 , where the spin magnetic moment m_s aligns parallel or antiparallel to the magnetic field (Figure 2.1 A). For X-band EPR experiments, the magnetic field is varied in the presence of constant microwave radiation ($\nu = 9\text{--}10$ GHz) which may result in transitions between these Zeeman levels. The net absorption of energy constitutes the isotropic EPR spectrum, often plotted as the first derivative¹³⁹ (Figure 2.1 A). The shape of the EPR spectrum is described by g tensor values and depends strongly on the electronic environment of the paramagnetic species. This is due to interactions between the electron spin and the magnetic moment of surrounding nuclei¹³⁹ (Figure 2.1 B). The coordination environment of the reduced iron-sulfur cluster is therefore of great importance and cysteine ligated [4Fe-4S]¹⁺ and [2Fe-2S]¹⁺ clusters usually exhibit similar rhombic or near axial line shapes, with an average g value of 1.94¹³⁶. These clusters can however be differentiated based on the faster relaxation rates of [4Fe-4S]¹⁺ over [2Fe-2S]¹⁺ clusters¹³⁶, making [4Fe-4S]¹⁺ clusters detectable at temperatures between 10–35 K¹³⁴.

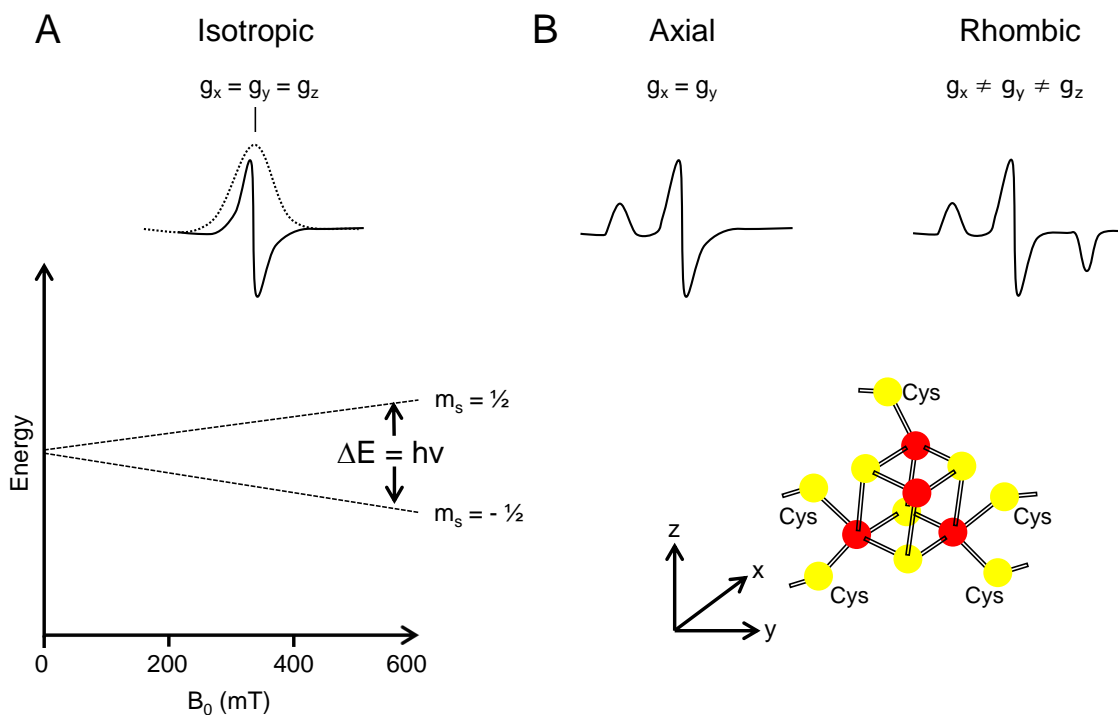


Figure 2.1 Basic EPR principles.

(A) Energy levels of an electron spin in an isotropic environment showing the idealised absorption (---) and first derivative (—) EPR spectra. (B) An anisotropic ligand field, as exemplified by a cartoon [4Fe-4S] cluster in the g tensor principal axis system, changes the shape of the EPR spectrum. Shown are idealised axial and rhombic first derivative EPR spectra. Iron and sulfur atoms of the cluster are coloured red and yellow, respectively. Adapted from Brückner et al.¹³⁹.

The primary sequence of *C. acetobutylicum* HydG contains two cysteine triads (Figure 1.6), giving the potential to coordinate two iron-sulfur clusters. The N-terminal CX₃CX₂C sequence likely coordinates the radical AdoMet [4Fe-4S] cluster, whereas the C-terminal CX₂CX₂₂C motif is thought to coordinate an auxiliary [4Fe-4S] cluster^{24,140}. Initial spectroscopic characterisation of chemically reconstituted *T. maritima* HydG indicated the presence of one and

possibly two [4Fe–4S] clusters²⁴. The EPR spectrum of reconstituted *C. acetobutylicum* HydG, photochemically reduced in the presence of 5'-deazaflavin, displayed g values of 2.03, 1.92 and 1.90 and was comparable to the axial spectrum displayed in Figure 2.1 B. Similar spectra were also observed for other radical AdoMet enzymes, containing either one (ThiG¹²³, NoCL¹²², viperin¹⁴¹) or two [4Fe–4S] clusters (LipA⁹⁸, BtrN⁹³, TYW1⁹²).

Addition of AdoMet to the photoreduced HydG sample resulted in two distinct rhombic EPR signals ($g_1 = 2.02, 1.93, 1.91$; $g_2 = 2.00, 1.87, 1.83$)²⁵, similar to the idealised spectrum in Figure 2.1 B. At the time, this was proposed to arise from two site-differentiated [4Fe–4S]¹⁺ clusters, the radical AdoMet [4Fe–4S] cluster and an auxiliary [4Fe–4S] cluster. The observation of similar signal splitting upon AdoMet addition to reduced radical AdoMet enzymes containing only a single [4Fe–4S] cluster^{141,142} suggests however that these signals may be attributed to differing ratios of an AdoMet bound and non-bound radical AdoMet [4Fe–4S] cluster. As such, the two signals observed for *C. acetobutylicum* HydG in the presence of AdoMet²⁵ are not unambiguous evidence for the presence of a second [4Fe–4S] cluster.

Potential intramolecular as well as intermolecular spin-spin interactions between two paramagnetic iron-sulfur clusters in WT HydG would complicate the EPR spectrum significantly^{143,144} and would make it almost impossible to unambiguously distinguish between the N-terminal and the inferred C-terminal [4Fe–4S] cluster. To isolate the spectral component of the C-terminal [4Fe–4S] cluster and therefore unambiguously demonstrate its presence, an N-terminal C96/100/103A *C. acetobutylicum* HydG mutant, unable to coordinate the radical AdoMet [4Fe–4S] cluster was prepared (Figure 2.2). Preparation and characterisation of this mutant was carried out by our collaborators Benjamin

Chapter 2 – Spectroscopy

R. Duffus and Eric M. Shepard at Montana State University. To establish the functional role of the proposed auxiliary [4Fe–4S] cluster as well as C-terminal residues during tyrosine cleavage, *C. acetobutylicum* C386S and Δ CTD HydG mutants were additionally prepared (Figure 2.2) and comparatively characterised.

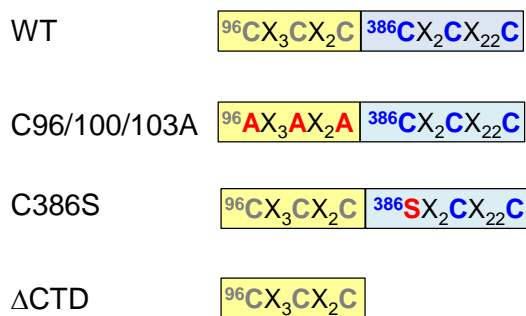


Figure 2.2 Schematic of prepared *C. acetobutylicum* HydG mutants.

The cysteine residues coordinating the radical AdoMet binding [4Fe–4S] cluster are coloured in grey, while the cysteine residues proposed to ligate an auxiliary [4Fe–4S] cluster are coloured in blue. The HydG N- and C-terminal domains are simplified as light yellow and blue boxes, respectively. The Δ CTD HydG mutant lacks amino acids after and including Cys386, single amino acid mutations are highlighted in red.

2.2 Expression and purification of *C. acetobutylicum* HydG variants

N-terminally 6His tagged *C. acetobutylicum* HydG (55 kDa) was expressed in *E. coli* BL21(DE3) using a modification of an established procedure³⁴ (Method 11). The mutant genes *hydG_C386S*, *hydG_C96/100/103A* and *hydG_ΔCTD* were prepared by site directed mutagenesis using the *hydG_WT* DNA³⁰ as a template and is described in Method 10. The corresponding plasmid maps can be found in Appendix 2. Mutant proteins were expressed using the same method used for expression of WT HydG and yielded on average 4 g/L beige cell pastes. All HydG proteins were purified from the soluble cells by anaerobic Ni-affinity chromatography (Method 13) to obtain 30–50 mg/L of protein. The purity was estimated between 80% and 94% by SDS-PAGE analysis (Figure 2.3). The prominent bands just under 66 kDa represent WT and C386S HydG (55 kDa), while the band close to the 42 kDa molecular weight marker corresponds to the truncated Δ CTD HydG variant (45 kDa). Analytical gel filtration (Figure 2.4) of WT and mutant HydG using Superdex 200 resin (Method 14) revealed that all HydG variants eluted with a calculated molecular weight of 53 kDa, corresponding to a monomeric state for these proteins in solution.

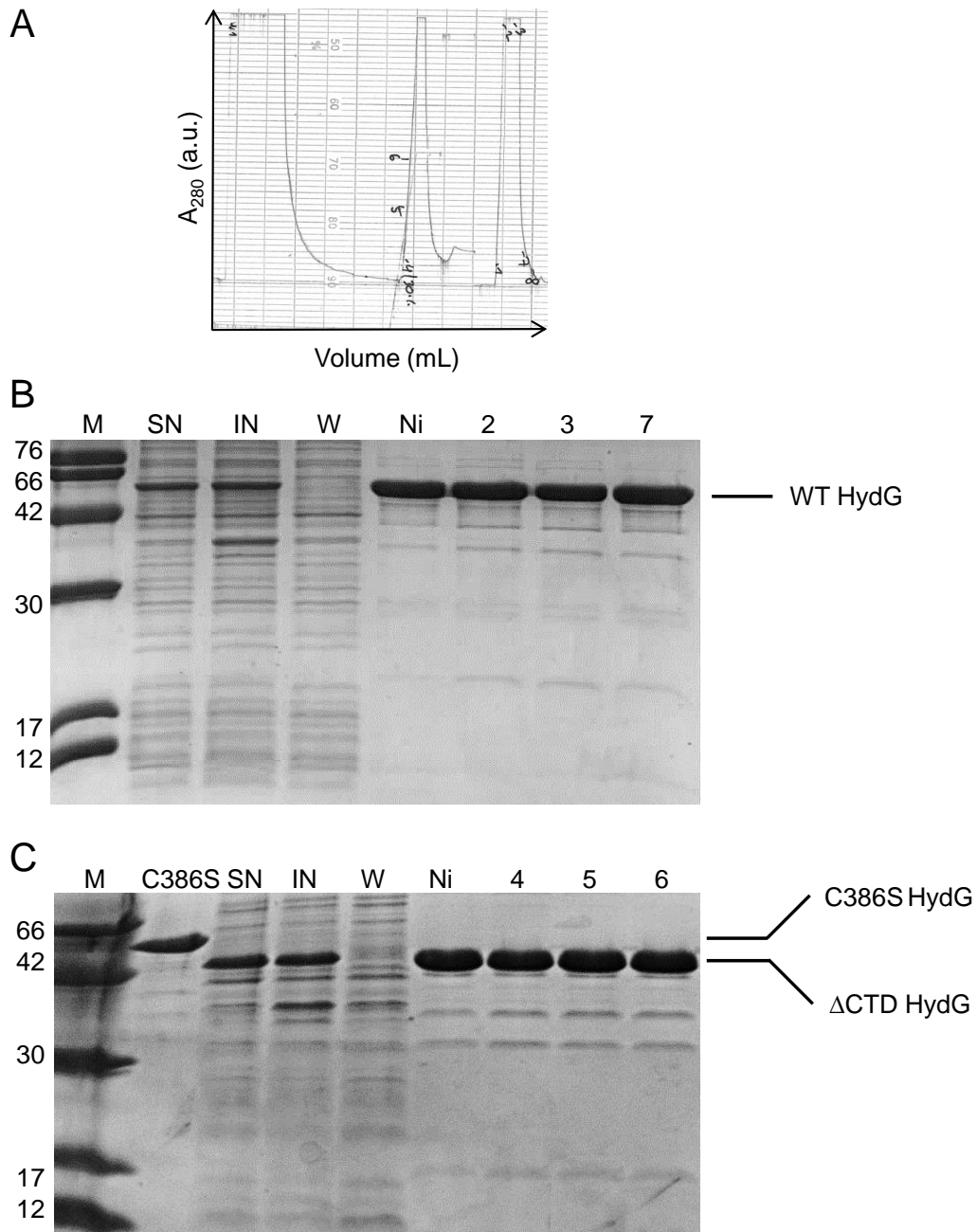


Figure 2.3 Purification of WT and mutant HydG.

(A) Elution profile and 15% SDS-PAGE analysis of (B) WT HydG and (C) Δ CTD HydG fractions eluted from a Ni-affinity column. Mutant C386S HydG behaves like WT HydG and a purified fraction is analysed in lane 2 of panel C. M – molecular weight marker (kDa), IN – insoluble, SN – lysate supernatant, W – wash fractions, Ni – pooled fractions after Ni-affinity chromatography, numbers – Superdex 75 gel filtration fractions.

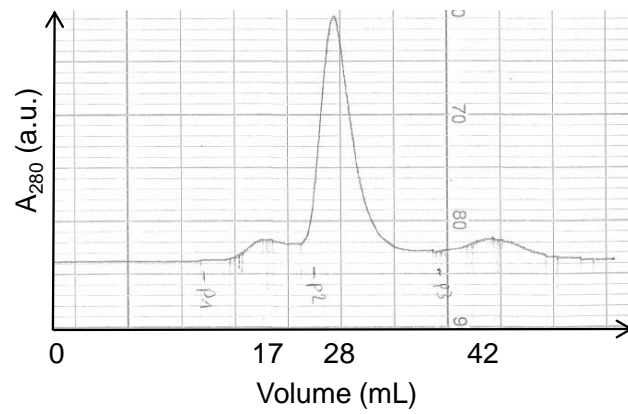


Figure 2.4 Analytical gel filtration of HydG variants.

Representative elution profile of reconstituted WT, C386S and Δ CTD HydG from a Superdex 200 gel filtration column.

2.3 UV-Vis characterisation and iron content analyses

Using the method of Fish¹⁴⁵ (Method 19), purified WT HydG was found to contain on average 0.85 ± 0.04 iron equivalents per protein. The C386S and Δ CTD HydG mutants coordinated even less iron (Table 2.2). Although these proteins contain at least the radical AdoMet [4Fe-4S] cluster, the observed substoichiometric amount of iron is not uncommon for purified radical AdoMet enzymes¹⁴⁶ and suggests inefficient iron-sulfur cluster assembly in vivo and/or oxidative cluster degradation during protein purification. In addition to the protein absorbance at 280 nm, the UV-Vis spectra of as-isolated WT and C386S HydG exhibited a broad absorbance at 410 nm, characteristic for [4Fe-4S]²⁺ clusters¹³⁴ as well as shoulders at 330 nm and 550 nm, suggesting the presence of [2Fe-2S]²⁺ clusters¹³⁷ (Figure 2.5 A, black, green). These absorbance features are less pronounced if not altogether absent for the C96/100/103A and Δ CTD HydG mutants (Figure 2.5 A, blue, red), supporting the hypothesis that less iron is coordinated compared to the WT and C386S HydG proteins.

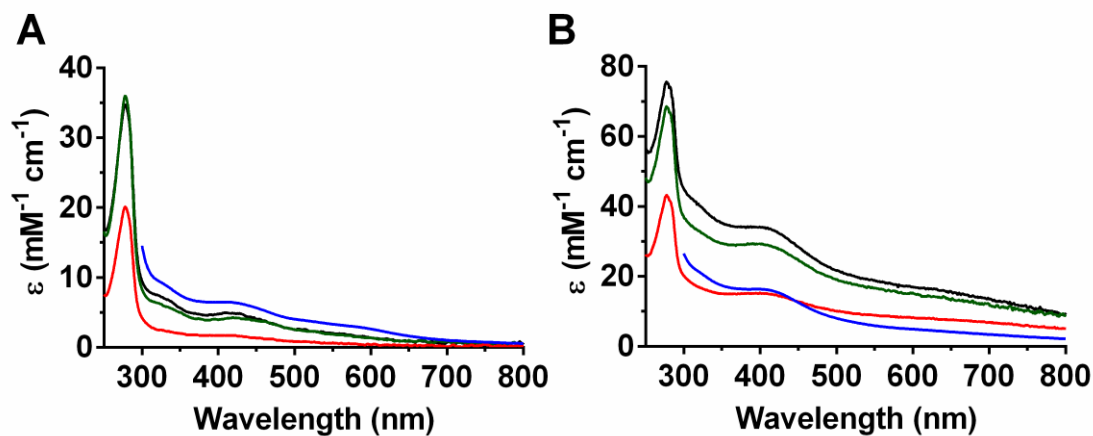
After chemical reconstitution of WT HydG with 8-10 molar equivalents of iron and sulfide in the presence of dithiothreitol (DTT) (Method 18), WT HydG contained on average 7.1 ± 1.1 irons per protein and showed a broad UV-Vis absorption band around 410 nm (Figure 2.5 B, black) confirming successful iron-sulfur cluster reconstitution. Based on the protein concentration determined using the Bradford assay¹⁴⁷, the extinction coefficient at 400 nm was calculated to be $34 \text{ mM}^{-1} \text{ cm}^{-1}$. This is in agreement with the presence of two [4Fe-4S]²⁺ clusters assuming a cluster extinction coefficient¹³⁴ of $16 \text{ mM}^{-1} \text{ cm}^{-1}$.

Table 2.2 Summary of iron content for HydG variants.

Iron content was determined in triplicate¹⁴⁵, where the first two columns correspond to protein samples analysed in Figure 2.5. The last column represents an average of 5 distinct reconstitutions.

HydG variant	Fe/unreconstituted	Fe/reconstituted	Fe/reconstituted
	protein	protein	protein
WT	0.8 ± 0.1	8.0 ± 0.9	7.1 ± 1.1
C96/100/103A	0.5 ± 0.1	3.4 ± 0.1	ND
Δ CTD	0.3 ± 0.2	3.6 ± 0.2	3.1 ± 0.4
C386S	0.4 ± 0.1	6.4 ± 0.8	4.9 ± 1.1

ND - not determined.

**Figure 2.5 UV-Vis characterisation of HydG variants.**

Representative UV-Vis spectra of (A) unreconstituted and (B) reconstituted WT (—), C96/100/103A (—), Δ CTD (—) and C386S HydG (—). Corresponding iron numbers are summarised in Table 2.2.

Iron analyses after in vitro reconstitution of C96/100/103A and Δ CTD HydG with 5 to 6 molar equivalents of iron and sulfide indicated that these mutants coordinate on average 3.4 ± 0.1 and 3.1 ± 0.4 irons per protein, respectively (Table 2.2). The calculated extinction coefficient at 400 nm of approximately $16 \text{ mM}^{-1} \text{ cm}^{-1}$ for both mutant proteins is consistent with the presence of a single $[4\text{Fe}-4\text{S}]^{2+}$ cluster (Figure 2.5 B, red, blue). This confirms the presence of the radical AdoMet $[4\text{Fe}-4\text{S}]$ cluster (cluster I) in Δ CTD HydG as well as the likely coordination of an auxiliary $[4\text{Fe}-4\text{S}]$ cluster (cluster II) by the C-terminal $\text{CX}_2\text{CX}_{22}\text{C}$ motif in C96/100/103A HydG.

The C386S HydG mutant was reconstituted with 10 molar equivalents of iron and sulfide to investigate whether the single amino acid change and the similarity of the ability of serine and cysteine to act as cluster ligands¹⁴⁸⁻¹⁵⁰ is sufficient for partial or full assembly of the C-terminal auxiliary cluster. Reconstituted C386S HydG contained between 3.7 and 6.4 irons per protein and showed a slightly decreased absorbance at 400 nm compared to reconstituted WT HydG (Table 2.2, Figure 2.5 B, green). This suggests that cluster II might only be present in a fraction of C386S HydG, or alternatively, may only be partially assembled, for example as a $[3\text{Fe}-4\text{S}]$ cluster⁸⁹. The UV-Vis spectrum supports the absence of $[2\text{Fe}-2\text{S}]$ clusters¹³⁷.

A high background absorbance in the UV-Vis spectra of reconstituted compared to as-isolated HydG samples was observed (Figure 2.5), which nearly doubled the protein absorbance at 280 nm. As a result, the extinction coefficients determined for the iron-sulfur clusters may not be very accurate and thus limit the quantitative estimation of coordinated $[4\text{Fe}-4\text{S}]$ clusters. This background absorbance could be due to non-specifically bound iron and sulfide, suggesting inefficient removal of excess iron and sulfide during the

desalting step of the reconstitution procedure. In fact, reconstitution of bovine serum albumin (BSA), a protein of similar size to WT HydG but which does not coordinate iron–sulfur clusters, resulted in a UV–Vis spectrum vaguely similar to reconstituted HydG (Figure 2.6).

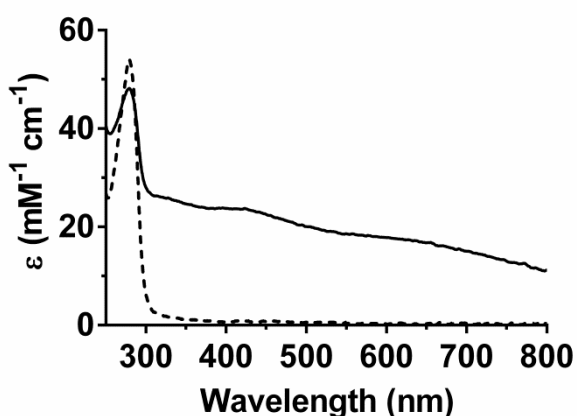


Figure 2.6 UV–Vis characterisation of BSA.

UV–Vis spectrum of BSA before (---) and after ‘chemical reconstitution’ with 10 molar equivalents of iron and sulfide (—).

It was attempted to remove excess iron by incubating the HydG proteins with the iron–chelator ethylenediaminetetraacetic acid (EDTA) but the strong absorbance decrease at 400 nm indicated additional loss of the protein bound [4Fe–4S] clusters (data not shown). This was also observed for reconstituted samples of the radical AdoMet enzymes MiaB⁹⁵ and BtrN^{93,151} and makes EDTA unsuitable for the selective removal of non–specifically bound iron.

The separation efficiency of large (i.e. HydG) and small (i.e. free iron and sulfide) molecules using a Nap-10 column packed with Sephadex G25 was then investigated instead. In this experiment, BSA (66 kDa) and fluorescein (332 Da), representing the large and small compounds, respectively were individually applied to a Nap-10 column. Elution fractions were collected and analysed for BSA recovery using the Bradford method¹⁴⁷ and fluorescein using fluorescence spectroscopy. It was found that approximately 50% fluorescein eluted within the recommended 1.5 mL elution volume (Figure 2.7 A), reflecting the poor separation of free iron and sulfide from reconstituted HydG samples.

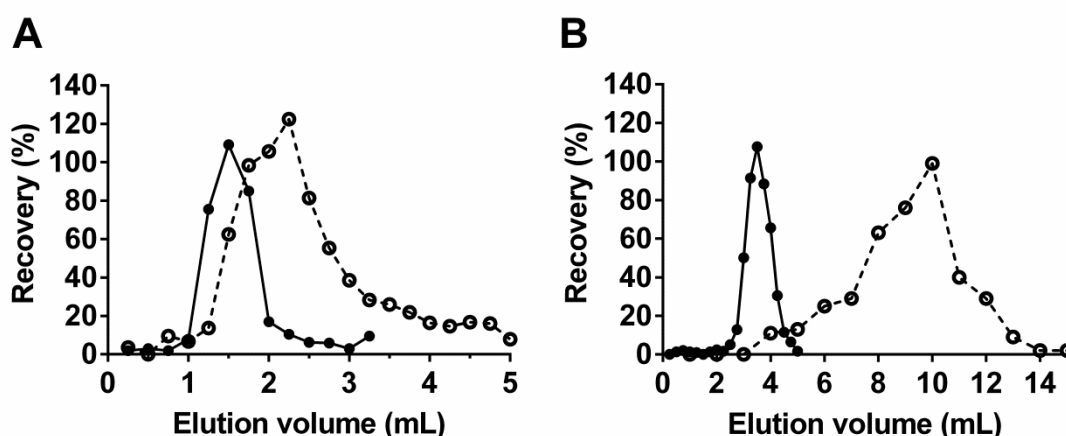


Figure 2.7 Separation efficiency of Nap-10 and PD-10 Sephadex G25 columns. Equal volumes (1 mL) and concentrations of BSA (—●—) were applied to a (A) Nap-10 or (B) PD-10 column and eluted fractions were analysed for the protein recovery. The small molecule fraction (---○---) was represented by the dyes (A) fluorescein and (B) bromophenol blue applied similarly to the column.

A similar separation was carried out using a PD-10 column of the same material. This column is slightly longer than Nap-10 columns and should allow better separation. Despite a 2.5 fold increased loading capacity of PD-10 over Nap-10 columns, an identical sample regarding concentration and volume was loaded. Bromophenol blue was used as the dye and it was found that the separation efficiency is enhanced, only approximately 10% of the dye co-eluted with BSA (Figure 2.7 B). For future small scale desalting steps, only the PD-10 column was used and the last 0.5 mL of the elution fraction was discarded with the goal to obtain reconstituted HydG proteins with minimal non-specifically bound iron and sulfide.

Work by Jenny E. Harmer¹⁵² as well as by Lanz and co-workers¹⁵³ later identified that iron and sulfide which bound non-specifically to protein surface residues can trigger protein aggregation. The protein-iron-sulfur aggregate increased the overall background absorbance as well as the specific absorbance at 400 nm, similar to the UV-Vis spectrum of 'reconstituted' BSA (Figure 2.6). For accurate iron-sulfur cluster characterisation, the protein-iron-sulfur aggregate needs to be separated from the active protein and is discussed in more detail in section 4.4.

2.4 EPR characterisation

To characterise the coordinated iron–sulfur clusters of all HydG variants in more detail, these proteins were subjected to EPR analyses in the absence and presence of AdoMet (Method 25). Photoreduced, reconstituted WT *C. acetobutylicum* HydG has previously been characterised in the literature and a very similar EPR spectrum was observed here for reconstituted, dithionite reduced WT HydG (Figure 2.8 A, dashed). Minor differences to photoreduced spectra exist with regard to the overall line shape and g values (Appendix 4). The temperature dependence of the $S = \frac{1}{2}$ signal (Figure 2.8 B) was consistent with fast-relaxing $[4\text{Fe}-4\text{S}]^{1+}$ instead of $[2\text{Fe}-2\text{S}]^{1+}$ clusters. Addition of AdoMet resulted in the characteristic ‘signal splitting’ with g values of 2.00, 1.89, 1.83 and 2.03, 1.93, 1.87 (Figure 2.8 A, solid). The observation of 0.48 spins/protein in photoreduced WT HydG samples in the absence and 0.88 spins/protein in the presence of AdoMet indicates an increase in reduced $[4\text{Fe}-4\text{S}]^{1+}$ clusters and may suggest that binding of AdoMet to cluster I increases its redox potential. This is in accord with spectroelectrochemical results that the redox potential of the $[4\text{Fe}-4\text{S}]^{2+/1+}$ couple in the radical AdoMet enzyme LAM is raised from -480 mV to -430 mV in the presence of AdoMet⁸⁴ (see section 1.2.3.1).

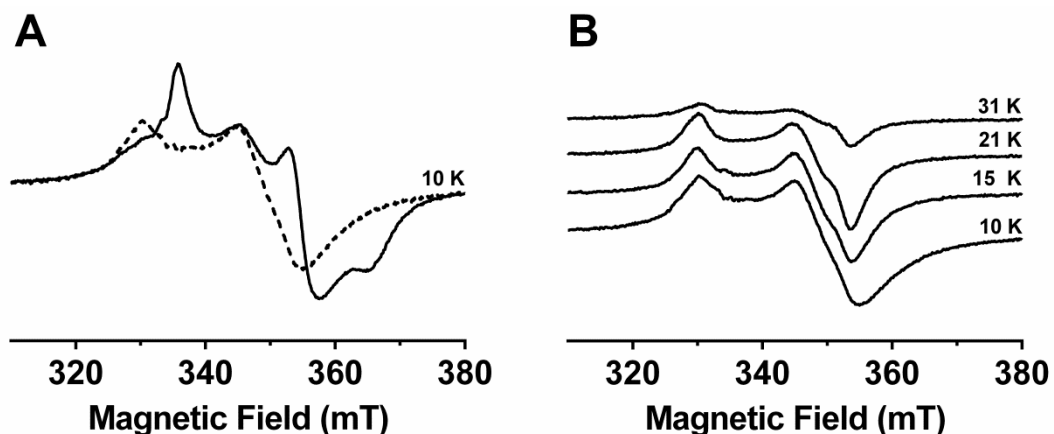


Figure 2.8 X-band EPR spectra of WT HydG.

(A) Dithionite reduced, reconstituted WT HydG (130 μ M, 5.3 ± 0.3 Fe/protein) in the absence (---) or presence (—) of AdoMet (1 mM). (B) WT HydG in the absence of AdoMet as in (A) at varying temperatures.

The $S = \frac{1}{2}$ signal in the EPR spectrum of dithionite reduced, reconstituted Δ CTD HydG (Figure 2.9 A, dashed) somewhat resembled the WT HydG resonance in the presence of AdoMet and suggests co-purification of AdoMet with Δ CTD HydG. Saturation of Δ CTD HydG with AdoMet generated a clear rhombic signal ($g = 2.00, 1.89, 1.84$) which suggests that AdoMet was coordinated to cluster I in the entire Δ CTD HydG sample (Figure 2.9 A, solid). By subtracting this cluster I-AdoMet resonance from the reduced Δ CTD HydG spectrum, g values for free cluster I have been determined as 2.03, 1.93 and 1.89 (Table 2.3).

Photoreduced, reconstituted C96/100/103A HydG displayed a broad EPR signal (Figure 2.9 B, dashed) which was similar to reduced, reconstituted WT HydG. The g values of 2.03, 1.92, 1.88 and the temperature dependence (not shown) are consistent with the presence of a $[4\text{Fe}-4\text{S}]^{1+}$ cluster,

unambiguously demonstrating that the *C. acetobutylicum* HydG C-terminal CX₂CX₂C motif coordinates a second [4Fe–4S] cluster. The observation of an EPR active cluster II with 0.41 spins/protein confirms that this cluster is redox-active. Although the similarity of the cluster I and cluster II EPR resonances points towards comparable electronic environments of each cluster, addition of AdoMet to the N-terminal mutant in greater than 10-fold molar excess did not cause a significant signal perturbation (Figure 2.9 B, solid). This suggests that cluster II cannot substitute for cluster I with regards to AdoMet binding.

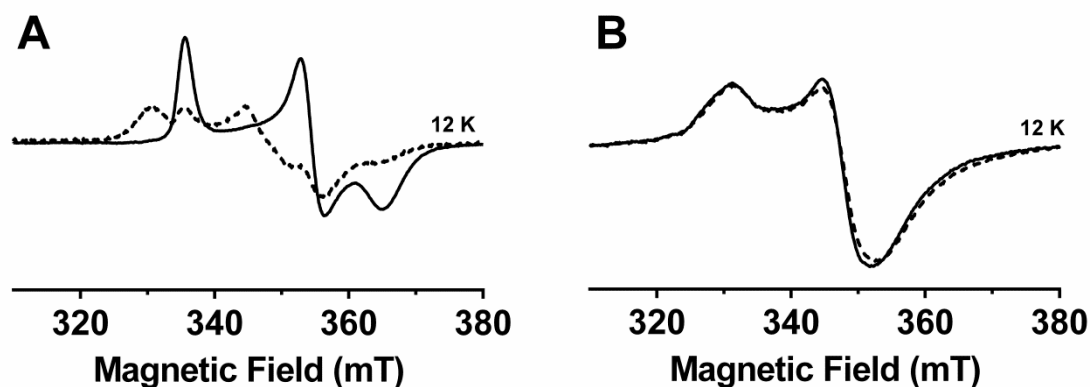


Figure 2.9 X-band EPR spectra of Δ CTD and C96/100/103A HydG.

(A) Dithionite reduced, reconstituted Δ CTD HydG (163 μ M, 3.3 ± 0.2 Fe/protein) and (B) photoreduced C96/100/103A HydG (90 μ M, 3.4 ± 0.1 Fe/protein) in the absence (---) or presence (—) of AdoMet (1 mM). The intensity of the dashed spectrum in (A) is increased threefold.

EPR analyses of the HydG variants lacking the N- or C-terminal [4Fe-4S] cluster allowed spectral simulations of the signals deriving from the individual clusters in the absence and presence of AdoMet (Table 2.3). As a result, the g values and quantitative contributions of the individual [4Fe-4S] clusters in WT HydG can be more accurately simulated (Appendix 4) compared to previous simulations²⁵.

Table 2.3 EPR parameters for N- and C-terminal HydG [4Fe-4S] clusters.

These g values have been obtained by simulating the experimental EPR spectra of the N- and C-terminal HydG variants in the absence and presence of AdoMet. A more thorough summary of the simulation parameters can be found in Appendix 4.

HydG Sample	g ₁	g ₂	g ₃
ΔCTD (Cluster I)	2.030	1.925	1.885
ΔCTD-AdoMet (Cluster I + AdoMet)	1.999	1.892	1.835
C96/100/103A (Cluster II)	2.027	1.922	1.880

The dithionite reduced WT HydG spectrum was approximated by summation of the N- and C-terminal cluster signals in a near 1:1 ratio (Figure 2.10 A), suggesting that both clusters may behave independently, with no observable coupling in the absence of AdoMet. The WT-AdoMet spectrum (Figure 2.10 B) was estimated to comprise 56% AdoMet bound cluster I signal, 39% contribution from cluster II and as little as 5% unbound cluster I.

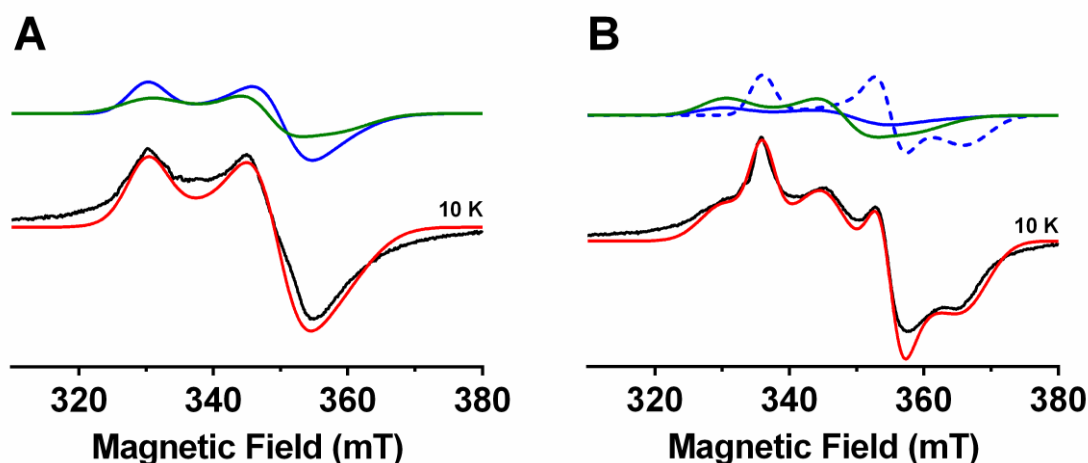


Figure 2.10 Simulation of WT HydG X-band EPR spectra.

Dithionite reduced, reconstituted WT HydG (130 μ M, 5.3 ± 0.3 Fe/protein) in (A) the absence or (B) presence of AdoMet (1 mM). Experimental spectra are depicted in black, while composite simulations are shown in red. Spectral components of the simulated signals are depicted in the upper part of each panel and include cluster I (—), cluster II (—) and AdoMet bound cluster I (---). Detailed simulation parameters can be found in Appendix 4.

Addition of the AdoMet analogues *S*-adenosyl-L-homocysteine (AdoHcy, **59**) or aza-AdoMet **60** to dithionite reduced WT HydG had no significant effect on the WT HydG spectrum (Figure 2.11 A, B), suggesting that neither analogue coordinates to cluster I. The C-terminal cysteine motif in WT HydG contains only three conserved cysteine residues which could leave one iron atom of cluster II available for tyrosine coordination in a mode similar to AdoMet binding to cluster I (Figure 2.11 C, **61**). Substrate coordination to the unique iron of the auxiliary [4Fe-4S] cluster was also observed in the crystal structure of MoaA¹¹⁸ and implicated for TYW1 by a combination of EPR and Mössbauer spectroscopy⁹². The presence of 1 mM tyrosine or 1 mM each of AdoHcy and tyrosine caused only subtle perturbations on the EPR spectrum of dithionite

reduced WT enzyme (Figure 2.11 B), indicating that tyrosine does not coordinate to cluster II or that its coordination does not substantially perturb cluster g values. In the absence of additional experimental evidence however, it is difficult to verify this. The lack of strong signal perturbation in the dithionite reduced WT spectrum on addition of AdoHcy **59** (Figure 2.11 A) suggests that it does not substitute successfully for AdoMet. As a result, it cannot be excluded that observable tyrosine binding would only occur in the presence of AdoMet. Cooperative substrate binding was also observed for the AdoMet dependent enzymes BioB¹⁵⁴ and AtsB¹⁵⁵.

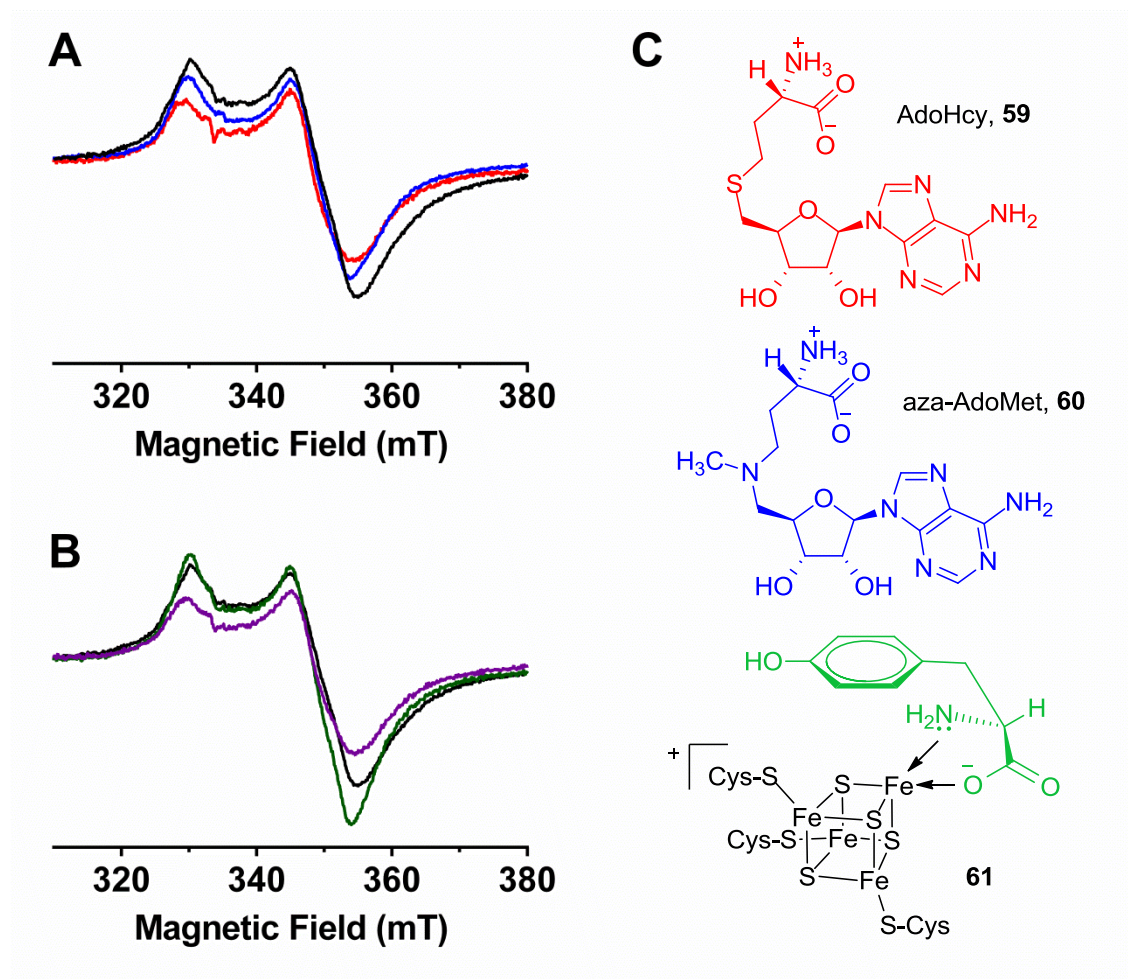


Figure 2.11 X-band EPR spectra (10 – 12 K) of WT HydG in the presence of substrate and/or substrate analogues.

Dithionite reduced, reconstituted WT HydG (130 μ M, 5.3 ± 0.3 Fe/protein, —) in the presence of (A) AdoHcy (—) or aza-AdoMet (—) (1 mM each) and (B) tyrosine (1 mM, —) or AdoHcy and tyrosine (1 mM each, —). (C) Structures of AdoHcy and aza-AdoMet and potential tyrosine coordination to the C-terminal [4Fe-4S] cluster of HydG.

EPR studies of dithionite reduced, reconstituted C386S HydG excluded the presence of $[2\text{Fe}-2\text{S}]^{1+}$ clusters as potential reasons for a decreased amount of iron quantified for C386S compared to WT HydG, as the $S = \frac{1}{2}$ signal was optimally observed below 35 K (similar to WT HydG, see Figure 2.8 B). The observed resonance (Figure 2.12, dashed) is more rhombic than WT HydG and was best simulated as 86% reduced cluster I ($g = 2.03, 1.93, 1.89$) and 14% reduced cluster II ($g = 2.02, 1.93, 1.86$). Addition of AdoMet gave rise to a clear rhombic signal ($g = 2.00, 1.89, 1.84$) (Figure 2.12, solid) for AdoMet bound cluster I, with approximately 10% contribution from the reduced C-terminal cluster II ($g = 2.04, 1.93, 1.87$). Independent of the presence of AdoMet, the spectral simulations suggest a consistently decreased EPR signal for cluster II, which may be due to incomplete assembly of the auxiliary $[4\text{Fe}-4\text{S}]$ cluster in most of the C386S HydG sample. Alternatively, the single cysteine to serine mutation may decrease the redox potential¹⁵⁶ of cluster II as to render it EPR inactive. In light of the reduced iron content observed for C386S HydG, the former hypothesis of incomplete cluster II assembly is more likely. Mössbauer spectroscopy as well as electrochemical measurements of the cluster II redox potential would however be required to confirm this proposal.

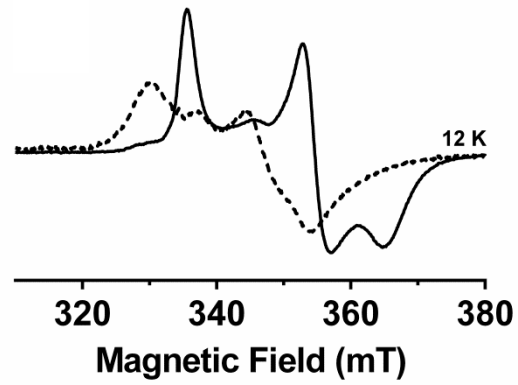


Figure 2.12 X-band EPR spectra of C386S HydG.

Dithionite reduced, reconstituted C386S HydG ($141 \mu\text{M}$, $4.3 \pm 0.4 \text{ Fe/protein}$) in the absence (---) or presence (—) of AdoMet (1 mM). The intensity of the dashed spectrum is increased threefold.

2.5 Summary and conclusions

Two *C. acetobutylicum* HydG mutants were prepared, lacking either the radical AdoMet [4Fe–4S] or the C-terminal [4Fe–4S] cluster. The observation of a prominent absorption band at 410 nm in the UV–Vis spectrum of the N-terminal C96/100/103A HydG mutant and its [4Fe–4S]¹⁺ characteristic EPR spectrum confirmed the coordination of a [4Fe–4S] cluster by the HydG C-terminal cysteine triad. The auxiliary [4Fe–4S] cluster can be reduced, but does not, contrary to cluster I, coordinate AdoMet. In light of this reducibility, cluster II may act as an electron donor during tyrosine cleavage and/or cyanide and CO formation.

The EPR spectrum of WT HydG was not strongly affected by the addition of tyrosine or AdoHcy and tyrosine, indicating that tyrosine does not bind to cluster II or that tyrosine coordination does not perturb the electronic environment of the [4Fe–4S] cluster. Bearing in mind the determined 300 μ M Michaelis–Menten constant of WT HydG for tyrosine (section 3.4.3) and the 1 mM tyrosine concentration employed during EPR analyses, it may be the case that higher tyrosine concentrations are required to achieve tyrosine binding in the absence of AdoMet. Determination of the tyrosine dissociation constant by isothermal titration calorimetry¹⁵⁷ or rapid equilibrium dialysis^{154,158} could confirm this hypothesis. Alternatively, coordination to cluster II might be reserved for the tyrosine cleavage intermediate dehydroglycine to allow metal catalysed cyanide and CO formation^{133,159}. Tyrosine binding could then occur through interactions with amino acids inside the TIM barrel, an active site arrangement which may mirror the ThiH active site.

Chapter 2 – Spectroscopy

Characterisation of N- and C-terminal *C. acetobutylicum* HydG mutants by EPR permitted extraction of the individual EPR parameters of the radical AdoMet and auxiliary [4Fe-4S] clusters. This allowed quantitative estimation of the [4Fe-4S] cluster signals contributing to WT and C386S HydG and identified that only a small proportion of cluster II (10-14%) contributed to the C386S HydG EPR signal in the absence or presence of AdoMet. In light of the reduced iron content of C386S compared to WT HydG, this suggests that little cluster II is coordinated by the C-terminal SX₂CX₂₂C motif.

The question of tyrosine binding to HydG was recently addressed through EPR characterisations of *Sh. oneidensis* HydG variants by Kuchenreuther and co-workers¹⁵⁹. Addition of tyrosine (3 mM) to reduced *Sh. oneidensis* WT but not SX₂SX₂₂C HydG generated a prominent new feature at $g = 1.9$, proposed to represent the tyrosine bound auxiliary [4Fe-4S] cluster¹⁵⁹. This high field signal was further characterised by electron nuclear double resonance (ENDOR) and hyperfine sublevel correlation (HYSCORE) spectroscopy of freeze quenched activity assays containing ¹³C and ¹⁵N labelled tyrosine¹⁵⁹. The observation of coupled ¹³C and ¹⁵N signals suggests close [4Fe-4S] cluster coordination by at least the amino group of tyrosine or of a non-aromatic tyrosine derivative (for example dehydroglycine).

Chapter 3

Mechanistic insights into HydG catalysed tyrosine cleavage

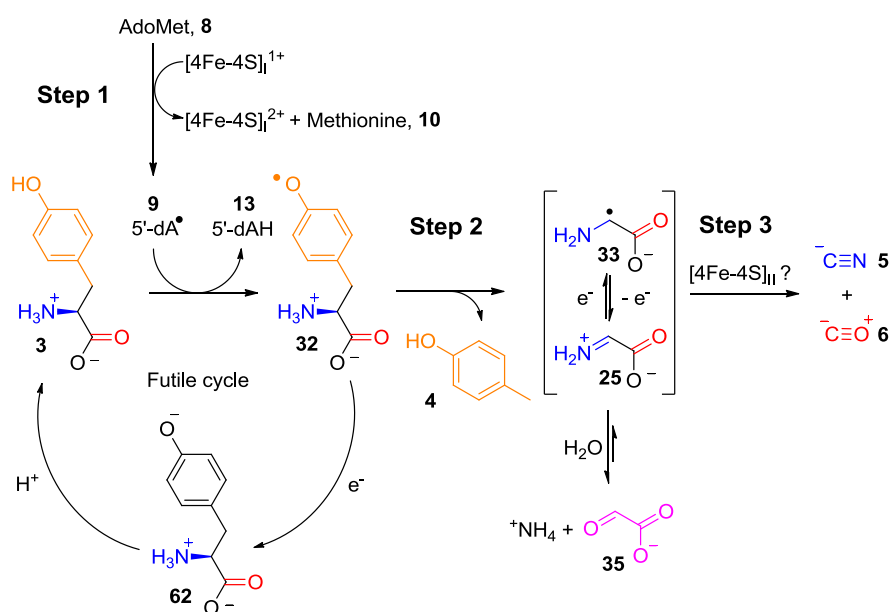
3.1 Introduction

Clostridium acetobutylicum HydG was shown to catalyse tyrosine cleavage with pseudo-first order kinetics³⁴, forming approximately 4 mol equivalents of *p*-cresol and cyanide with an average turnover number (k_{cat}) of $20 \times 10^{-4} \text{ s}^{-1}$. This rate of product formation is very comparable to ThiH catalysed *p*-cresol production with an k_{cat} value of $(32 \pm 8) \times 10^{-4} \text{ s}^{-1}$ under similar assay conditions¹³⁰. This may support the hypothesis that ThiH and HydG not only share tyrosine binding residues³³, but also mechanistic steps on the reaction path from tyrosine to *p*-cresol (Scheme 1.9).

The functional importance of the auxiliary [4Fe-4S] cluster of HydG was inferred in a mutagenesis study¹³³. An approximately 50% or 100% reduction in

Chapter 3 – Kinetics

cyanide formation was observed for a *C. acetobutylicum* SX₂SX₂₂C HydG double mutant and a ΔCTD mutant lacking the entire C-terminal domain including the cysteine motif, respectively¹³³. The authors did not quantify the formation of *p*-cresol **4** or glyoxylate **35** in parallel and as a consequence, it is not clear whether these mutations affected tyrosine **3** cleavage (Scheme 3.1, step 2) or the synthesis of cyanide **5** and CO **6** (Scheme 3.1, step 3). This question was further addressed by studies in which *C. acetobutylicum* and a respective *Thermoanaerobacter tengcongensis* (*Th. tengcongensis*) ΔCTD HydG mutant were shown to have a more than 98% reduced tyrosine cleavage activity with respect to the WT enzyme, forming only 0.04 molar equivalents (~1 μM) of *p*-cresol **4**¹⁶⁰. These very low levels of *p*-cresol **4** may indicate poor turnover of tyrosine **3** and this may explain the apparent absence of detected cyanide **5**. The additional lack of CO **6** formation by the SX₂SX₂₂C and ΔCTD HydG variants and the decreased iron content of both HydG variants compared to the WT enzyme were rationalised by the proposal that cluster II is not required for cyanide but is essential for CO **6** synthesis¹³³.

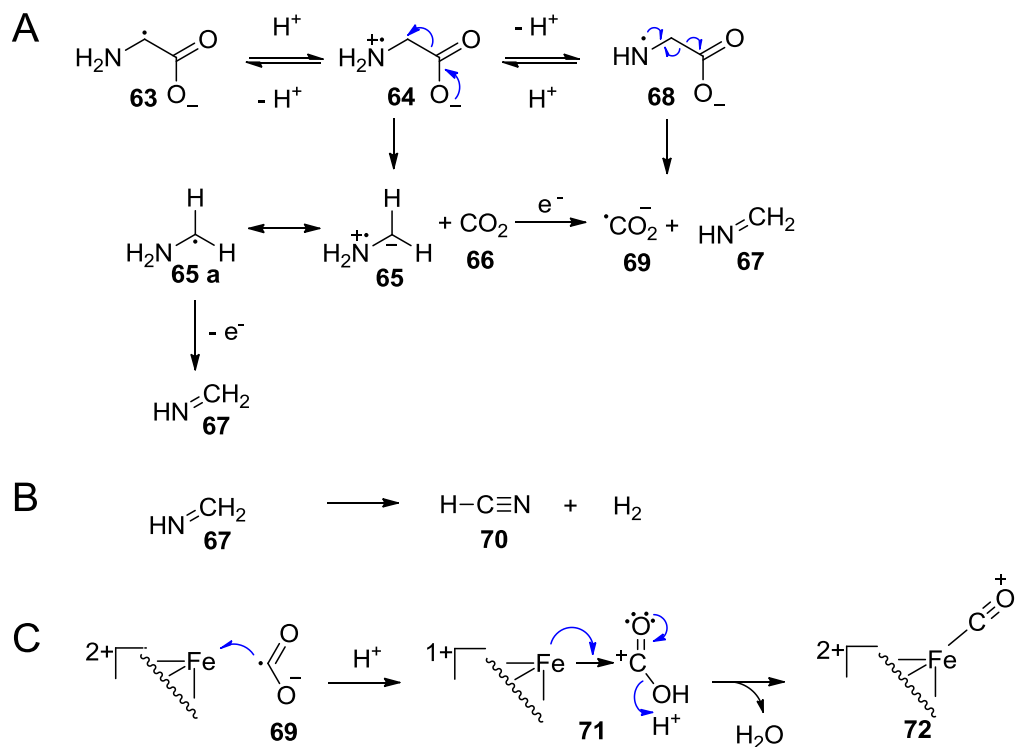


Scheme 3.1 Proposed reaction pathway of HydG catalysed tyrosine cleavage.

Potential mechanisms for step 3 are shown in Scheme 3.2 and Scheme 3.3.

Based on the above conclusions, Nicolet and co-workers suggested a mechanism in which an anionic C-centred glycine radical **63** initially undergoes protonation, followed by radical migration from carbon to nitrogen to form **64**^{133,161} (Scheme 3.2 A). Rather than decarboxylation of radical **64** to form an aminomethane radical **65**, the authors describe a direct collapse of the related N-centred glycine radical **68** to methane imine **67** and a carbon dioxide radical **69**¹³³. Furthermore, loss of hydrogen from methane imine **67** is proposed to result in hydrogen cyanide **70**¹³³ (Scheme 3.2 B), although the research literature does not reveal direct examples for this pathway. Nicolet and co-workers however argue that the intermediacy of methane imine during the pyrolysis of glycine to hydrogen cyanide¹⁶² may open the possibility of **67** also being an intermediate during HydG catalysed cyanide formation¹³³. Inspired by work of Grodkowski and Neta¹⁶³ on Cu-catalysed reduction of CO₂ to CO, they further propose that the carbon dioxide radical **69** initially reduces the HydG auxiliary [4Fe-4S]²⁺ cluster to form a dative cluster→CO₂⁻ complex **71**¹³³ (Scheme 3.2 C). This mechanism then requires protonation of the carboxylic acid in **71** and subsequent expulsion of water to arrive at an oxidised [4Fe-4S]²⁺ cluster carbonyl complex **72**¹³³.

The described mechanism is conceivable if the HydG cluster II is present in its oxidised 2+ state, but the current EPR spectroscopic observations that the cluster is reduced under assay conditions (section 2.4) somewhat weakens this proposal. The suggestion that cluster II is required for the formation of a stable iron-carbonyl complex¹³³ is however consistent with substoichiometric detection of CO in WT HydG assays²⁵, where the tight association of CO with WT HydG may prevent its detection with haemoglobin (Scheme 1.11).

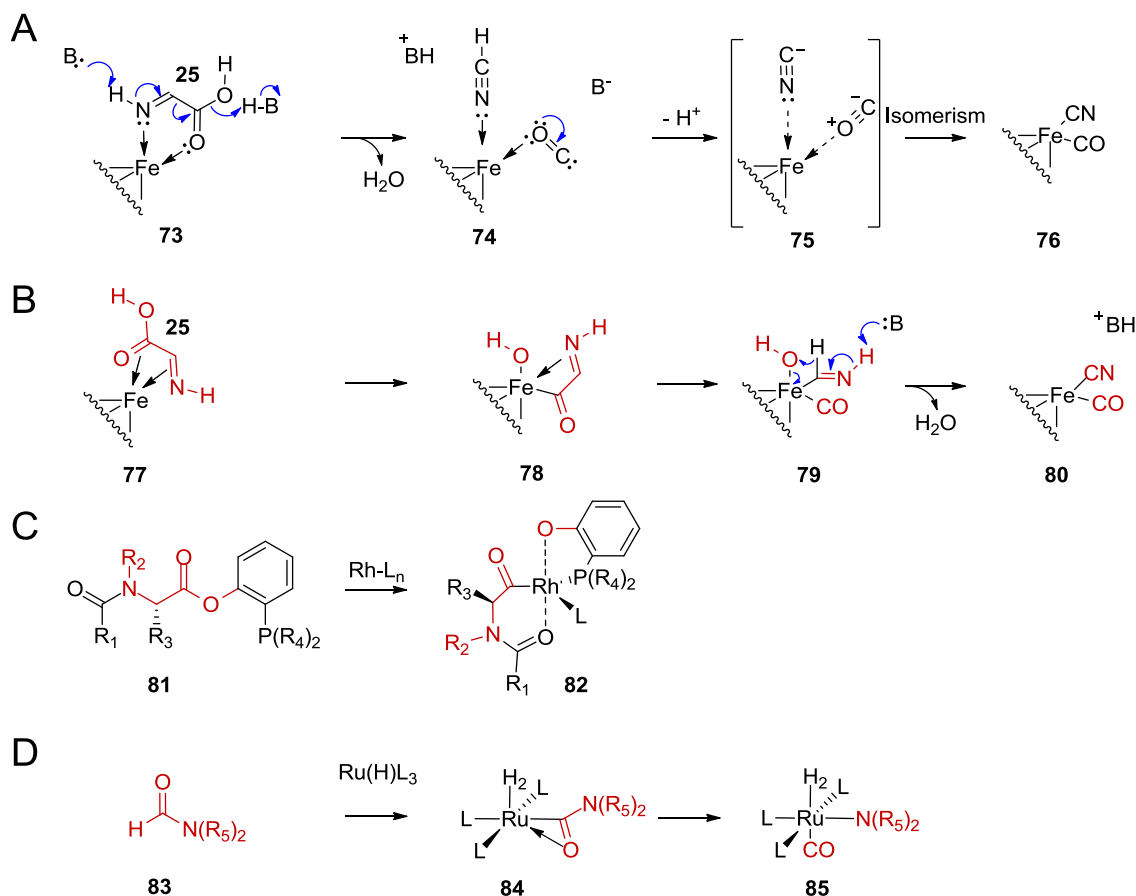


Scheme 3.2 Proposed HydG catalysed collapse of a C-centred glycine radical to cyanide and CO.

The shown mechanism was proposed by Nicolet and co-workers¹³³ and is discussed in the text. For clarity, only the cluster II unique iron is depicted.

The alternative tyrosine cleavage intermediate dehydroglycine **25** could undergo base catalysed decarbonylation to directly yield cyanide and CO³⁴ (Scheme 3.3 A). Although this E2 type elimination across an sp² hybridised system (**73**→**74**) is unfavourable due to poor orbital overlap¹⁶⁴, precedent N- and O-based chelation^{165,166} of dehydroglycine **25** to the HydG [4Fe-4S] cluster may help to overcome the energy barrier for electronic reorganisation. This mechanism of concerted decarbonylation would initially arrive at N- and O-centred coordination of hydrogen cyanide and CO (**74**) and requires isomerisation of the bonding character to give the experimentally inferred C-centred cyanide and CO ligands^{25,34,35,159} (**75**→**76**). This isomerism may

involve an oxidation state change of the unique iron atom of cluster II as ferric iron (Fe^{3+}) is considered a hard Lewis acid and prefers coordination of hard Lewis bases (oxygen). Ferrous iron (Fe^{2+}) on the other hand is a borderline soft Lewis acid which prefers soft bases such as carbon^{40,167}. Alternatively, coordination exploiting the double bond character of the ester and imine functionalities of dehydroglycine (**77**) could result in oxidative addition of the C–O bond to the unique iron (Scheme 3.3 B), where the resulting pseudo-octahedral coordination environment **78** might be a good driving force. Similar outcomes have been observed for the addition of amino acid esters (**81**) to rhodium¹⁶⁸ (Scheme 3.3 C) or addition of formates (**83**) to ruthenium¹⁶⁹. A second oxidative addition step (Scheme 3.3 B, **78**→**79**), preceded during decarbonylation of formamides¹⁶⁹ (Scheme 3.3 D, **84**→**85**), followed by base assisted imine dehydrogenation may result in [4Fe–4S] cluster bound, C-centred cyanide and CO ligands (Scheme 3.3 B, **79**→**80**). The feasibility of these oxidative addition reactions is however strongly dependent on the oxidation state of the unique iron, as mostly only Fe(0) complexes undergo oxidative additions¹⁷⁰.



Scheme 3.3 Proposed HydG catalysed collapse of dehydroglycine to cyanide and CO.

Cyanide and CO ligands may result from (A) base catalysed decarbonylation of dehydroglycine or (B) stepwise oxidative addition reactions as discussed in the text. For clarity, only the [4Fe-4S] cluster unique iron is shown, while the fate of the dehydroglycine-like functionalities in B to D are highlighted in red-brown. Arbitrary functional groups are indicated by R₁-R₅ and organic ligands by L.

3.2 Initial kinetic characterisation of wild-type and mutant *C. acetobutylicum* HydG

To elucidate which steps in the HydG catalysed tyrosine cleavage reaction require the auxiliary [4Fe–4S] cluster, AdoMet and tyrosine cleavage by *C. acetobutylicum* WT, C386S and Δ CTD HydG was investigated.

Unsurprisingly, the N-terminal C96/100/103A triple HydG mutant (100 μ M) was unable to cleave AdoMet to 5'-dAH when incubated with 1 mM AdoMet, 1 mM tyrosine and 5 mM sodium dithionite at 37 °C for 60 min due to lack of the AdoMet binding cluster I. Accordingly, this mutant was not included in the following study.

Reconstituted WT (48 μ M, 6.6 ± 0.2 Fe/protein), C386S HydG (48 μ M, 4.7 ± 0.1 Fe/protein) and Δ CTD HydG (48 μ M, 5.1 ± 0.1 Fe/protein) were incubated with AdoMet (1 mM), the substrate tyrosine (1 mM) and the reductant sodium dithionite (1 mM) at 37 °C in 100 mM potassium phosphate pH 7.5 buffer (Method 20). Assays were stopped at selected time points over a 60 min incubation period and analysed for the AdoMet **8** cleavage product 5'-dAH **13** and the tyrosine cleavage products *p*-cresol **4**, glyoxylate **35** and cyanide **5** as described in Scheme 1.11 and section 7.9.

Under the mentioned conditions, WT HydG catalysed formation of 5'-dAH, *p*-cresol and cyanide could be fitted to a first order process using Equation 3.1¹⁵⁸ (Figure 3.1 A), in which [P] and [P]_{max} refer to the observed and maximally predicted product concentrations respectively, while k is the observed first order rate constant. This equation was selected empirically, without theoretical kinetic modelling, because a relatively good fit was achieved (see Figure 3.1).

$$[P] = [P]_{\max} (1 - e^{-kt}) \quad \text{Equation 3.1}$$

$$k_{\text{cat}}^{(\text{app})} = \frac{[P]_{\max} k}{[E]} \quad \text{Equation 3.2}$$

The turnover number k_{cat} was calculated using Equation 3.2, which results from dividing the initial maximal velocity ($dP/dt = [P]_{\max} k = V_{\max}$) by the enzyme concentration employed. Due to the potential of non-saturating substrate concentrations in the experiment, this turnover number needs to be treated as an approximate value ($k_{\text{cat}}^{\text{app}}$).

The C386S and Δ CTD HydG mutants exhibited linear product formation over the investigated time period (Figure 3.1 A, B) and the data was best fitted to a linear function (Equation 3.3), where $k_{\text{cat}}^{\text{app}}$ was approximated by dividing the initial product formation rate k_0 by the enzyme concentration employed.

$$[P] = [P]_0 + k_0 t \quad \text{Equation 3.3}$$

The apparent turnover numbers of *p*-cresol and cyanide formation by WT HydG were calculated as $20 \times 10^{-4} \text{ s}^{-1}$ (Table 3.1), in very good agreement with previously published data³⁴ and product formation rates observed for other radical AdoMet enzymes¹⁷¹. The C-terminal C386S and Δ CTD HydG mutants were less active and 7- and 30-fold decreased *p*-cresol formation rates were observed, respectively (Table 3.1). This corresponds to accumulation of approximately 0.26 mol *p*-cresol by the Δ CTD HydG mutant compared to 0.04 mol equivalents observed by Tron and co-workers¹⁶⁰ under similar conditions. An obvious rationalisation for this difference is not apparent. All enzymes investigated displayed a small degree of uncoupled 5'-dAH over *p*-cresol formation which is routinely observed for radical AdoMet enzymes in the presence of sodium dithionite instead of the natural reducing system^{24,75,76,79,80} (see section 1.2.3).

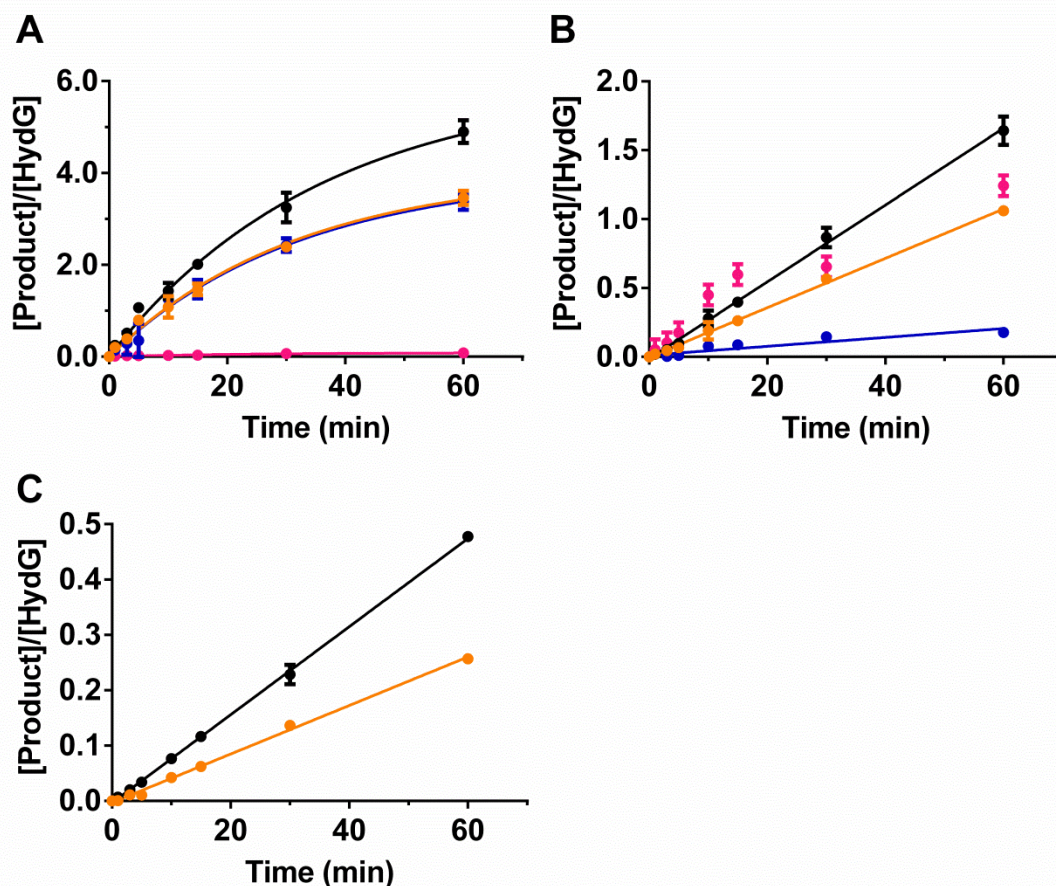


Figure 3.1 Time dependent AdoMet and tyrosine cleavage by HydG variants.

Formation of 5'-dAH (—●—), *p*-cresol (—●—), cyanide (—●—) and glyoxylate (—●—) by (A) WT (48 μ M, 6.6 ± 0.2 Fe/protein), C386S (48 μ M, 4.7 ± 0.1 Fe/protein) and (C) Δ CTD HydG (48 μ M, 5.1 ± 0.1 Fe/protein) in 100 mM potassium phosphate pH 7.5 buffer at 37 °C. Assays additionally contained tyrosine (1 mM), AdoMet (1 mM) and sodium dithionite (1 mM). The data represent the average of duplicate assays and are shown with standard deviations. Glyoxylate formation by Δ CTD HydG was not measured, while cyanide formation was not observed. The WT HydG data was fitted with first order kinetics (Equation 3.1), while the mutant data was modelled with linear kinetics (Equation 3.3). The fits resulted in R^2 values above 0.99, except for cyanide formation by C386S HydG (0.86) and glyoxylate formation by WT HydG (0.94). The corresponding turnover numbers are summarised in Table 3.1.

Table 3.1 Kinetic analysis of AdoMet and tyrosine cleavage by HydG variants.

The apparent turnover numbers for WT and mutant HydG activity shown in Figure 3.1 were calculated using Equation 3.2 or by dividing the initial product formation rate k_0 by the HydG concentration, respectively. Errors represent standard errors.

Product/HydG	$k_{\text{cat}}^{\text{app}}$ ($\times 10^{-4} \text{ s}^{-1}$)		
	WT	C386S	Δ CTD
5'-dAH	27.7 ± 3.9	4.6 ± 0.1	$1.3 \pm 0.0(1)$
<i>p</i> -Cresol	21.1 ± 2.7	3.0 ± 0.1	$0.7 \pm 0.0(1)$
Cyanide	20.8 ± 3.3	0.5 ± 0.1	NA ^b
Glyoxylate	0.6 ± 0.2	NA ^a	NA ^c

NA – Not applicable. Due to overestimation of glyoxylate (see text), (a) fitting or (c) measuring the formation of glyoxylate was not carried out, while (b) cyanide formation by Δ CTD was not detected.

The overall activity decrease of the C-terminally modified HydG mutants with respect to WT HydG 5'-dAH and *p*-cresol formation could indicate the involvement of the C-terminally coordinated [4Fe-4S] cluster and/or C-terminal residues in tyrosine C α -C β bond cleavage (Scheme 3.1, step 2). However, a decreased affinity of these mutants for tyrosine and/or AdoMet cannot be excluded. To accurately compare the (maximal) product formation rates between the HydG mutants, substrate saturation is required and to estimate the affinity of the AdoMet and tyrosine substrates to WT and mutant HydG, their Michaelis-Menten constants (K_M) need to be determined. This is discussed in detail in section 3.4.

Over the 60 min time course, the WT enzyme formed stoichiometric amounts of cyanide with respect to *p*-cresol. The rate of C386S HydG catalysed cyanide formation was however reduced to 17% relative to its *p*-cresol production, while no cyanide could be detected in Δ CTD HydG assays (Figure 3.1, Table 3.1). Assuming that the 83% reduction in cyanide formation by C386S HydG also applies to Δ CTD HydG, the absence of cyanide in Δ CTD HydG assays is not surprising. The very low *p*-cresol formation by the truncated HydG mutant predicts any formed cyanide to be below the current quantification limit of 5 μ M.

The observed decrease in cyanide formation by the C386S HydG mutant points towards a retarded reaction step on going from the dehydroglycine intermediate **25** (or the C-centred glycine radical **33**) to cyanide **5** (Scheme 3.1, step 3). As a consequence, the hydrolytically unstable dehydroglycine intermediate **25** rapidly reacts with water to form glyoxylate **35**. The sum of any formed glyoxylate **35** and cyanide **5** quantities should equal the total amount of *p*-cresol **4** formed. However, compared to *p*-cresol formation by C386S HydG, a consistently increased amount of glyoxylate was detected (Figure 3.1 B). Due to this discrepancy, the glyoxylate levels in Δ CTD HydG assays were not determined. *p*-Cresol **4** is detected directly by HPLC coupled to UV-Vis detection and elution of *p*-cresol as a single, well defined peak (Figure 7.5) argues against a significant inaccuracy in *p*-cresol quantification. Detection of glyoxylate **35** on the other hand is intrinsically more difficult and thus error prone as it requires chemical derivatisation with *o*-phenylene diamine **49** prior to HPLC quantification of the resulting 2-quinoxalinol derivative **50** by fluorescence spectroscopy (Scheme 1.11). The employed glyoxylate derivatisation procedure¹²⁴ was therefore reinvestigated (section 3.3.2).

3.3 Improving HydG in vitro activity and methodology

3.3.1 Optimisation of in vitro assay buffer

The initial HydG in vitro activity assays were carried out in 100 mM potassium phosphate pH 7.5 buffer (section 3.2). The HydG dependent detection of CO was however not successful in this buffer compared to using a HEPES or Tris based buffer system¹⁷². Previous HydG studies in our collaborating laboratory were carried out in buffer containing 50 mM HEPES, 0.5 M KCl, 5% glycerol at pH 7.4²⁵ or additionally containing 2 mM MgCl₂ when the HydG–HydF system was investigated³¹. To enhance the potential of parallel cyanide and CO detection and to increase the comparability between results from collaborating laboratories, HydG activity in different buffers was assessed by quantifying the amounts of *p*-cresol formed.

In vitro assays were carried out as described in section 3.2. Compared to HydG activity in 100 mM potassium phosphate pH 7.5 buffer, tyrosine cleavage was more than twofold enhanced in 50 mM HEPES pH 7.4 buffer (Figure 3.2 A, B). This activity improvement may be a result of phosphate's ability to chelate iron and promote autoxidation of Fe²⁺ to Fe³⁺ compared to HEPES¹⁷³. One could envision that the high concentration of phosphate (100 mM) successfully competes with AdoMet (1 mM) for binding to the unique iron of the radical AdoMet [4Fe–4S] cluster. This potential binding event may not only inhibit AdoMet coordination but may further lead to [4Fe–4S] cluster oxidation and subsequent decomposition, resulting in loss of HydG activity. Alternatively, the increased radical scavenging capacity of HEPES over phosphate buffer^{173,174} may protect the enzyme from excessive radical damage by 5'-dA•. A further 25% activity enhancement was observed in HEPES buffer additionally containing

0.5 M KCl and 2 mM MgCl₂ (Figure 3.2 C), which may be attributed to the high salt concentration stabilising the protein. In subsequent experiments, a buffer consisting of 50 mM HEPES, 0.5 M KCl at pH 7.4 was used. The presence of glycerol in assay buffers can decrease the resolution of the HPLC chromatogram and requires washing steps between successive sample runs to prevent pressure build-up in the HPLC column¹⁷⁵. For these reasons, glycerol was excluded from the assay buffer to facilitate more accurate and faster HPLC analyses.

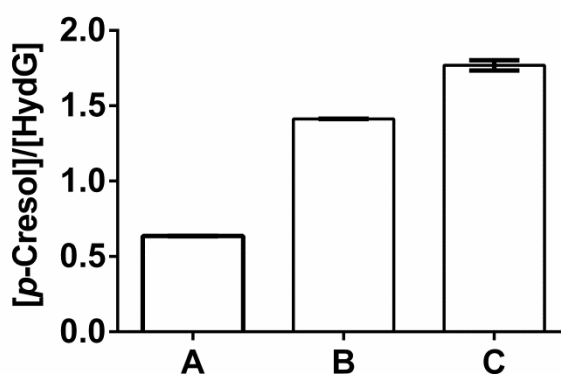


Figure 3.2 HydG catalysed tyrosine cleavage in different buffers.

WT HydG (20 μ M, 4.5 ± 0.1 Fe/protein) was incubated with tyrosine (0.5 mM), AdoMet (1 mM) and sodium dithionite (3 mM) for 30 min at 37 °C in (A) 100 mM potassium phosphate pH 7.5, (B) 50 mM HEPES pH 7.4 or (C) 50 mM HEPES, 0.5 M KCl, 2 mM MgCl₂, pH 7.4 buffer.

3.3.2 Optimisation of glyoxylate derivatisation procedure

Overestimation of glyoxylate was observed in C386S HydG time course assays (Figure 3.1 B). To investigate whether any of the HydG assay components (AdoMet, tyrosine or sodium dithionite) enhanced the derivatisation of glyoxylate **35** with *o*-phenylene diamine **49** (Scheme 1.11), a glyoxylate standard (50 μ M) in 100 mM potassium phosphate pH 7.5 buffer was incubated with each assay component, individually or all together, at 37 °C for 30 min before 'quenched' similar to activity assays (Method 20). The supernatant was then derivatised as outlined by Kriek and co-workers¹²⁴ and the fluorescent 2-quinoxalinol product **50** quantified using modified HPLC elution conditions (Method 33). Comparative quantification of **50** identified that the presence of dithionite enhances the fluorescence signal by approximately 25% (Figure 3.3). None of the other assay components affected the fluorescence response.

A study by Wu and co-workers indicated that the fluorescence of **50** remains stable for at least 30 min at room temperature¹⁷⁶, suggesting that the fluorescence may change any time thereafter. This prompted investigations into the fluorescence stability where the same derivatised glyoxylate standard was repeatedly subjected to HPLC analysis. It was identified that the fluorescence of the glyoxylate derivative **50** increased by approximately 10% over a 1.5 h time period (data not shown). To ensure accurate quantification of glyoxylate **35** in subsequent activity assays, glyoxylate standards were prepared in the presence of sodium dithionite. Derivatised samples were stored at -80 °C and were only thawed shortly (~1 min) before HPLC analysis to prevent time dependent fluorescence changes.

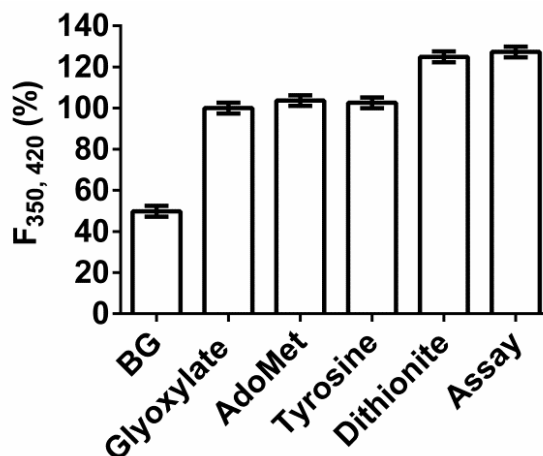


Figure 3.3 Fluorescence of glyoxylate derivatisation product in the presence of HydG assay components.

A glyoxylate standard (50 μM) in 100 mM potassium phosphate pH 7.5 buffer was incubated in the presence of AdoMet (1 mM), tyrosine (1 mM) or sodium dithionite (1 mM) or all components combined (Assay). The fluorescence of the glyoxylate derivatisation product 2-quinoxalinol is shown relative to the signal obtained from derivatisation of the glyoxylate standard in the absence of additives. The background fluorescence (BG) reflects the presence of AdoMet, tyrosine and sodium dithionite (1 mM each). Error bars represent 3% standard deviations observed on duplicate sample derivatisation.

Partial re-analysis of the initial C386S and ΔCTD HydG time course assays confirmed a more accurate quantification of glyoxylate (data not shown). The initial overestimation of glyoxylate most likely went unnoticed in the current WT HydG as well as published WT HydG assays³⁴ due to the naturally low concentrations of glyoxylate formed (<5 μM) compared to *p*-cresol (150 μM). No pre-treatment of glyoxylate standards was required for stoichiometric quantification with respect to *p*-cresol in ThiH activity assays¹²⁴. These assays contained the natural reducing system consisting of flavodoxin,

Chapter 3 – Kinetics

flavodoxin reductase and nicotinamide adenine dinucleotide phosphate hydrogen (NADPH) rather than dithionite¹²⁴, which presumably has no effect on the 2-quinoxalinol fluorescence. It was attempted to use this reducing system for HydG in vitro assays, but no turnover was observed over a 2 h incubation period (data not shown).

3.4 Investigating substrate affinity of wild-type and mutant *C. acetobutylicum* HydG

Binding of AdoMet to the radical AdoMet [4Fe-4S] cluster results in an absorbance decrease around 400 nm¹⁵⁴, likely due to changes in the coordination and electronic environment of the iron-sulfur cluster. These spectral changes have previously been employed to characterise AdoMet binding to BioB¹⁵⁴ and Cfr¹⁷⁷ in the absence or presence of the main substrates (Table 3.2). However, the low extinction coefficient of the absorption feature, as well as the observed scatter in the data¹⁵⁴, presumably due to increasing protein conformational changes introducing artificial spectroscopic features, makes this not a very accurate technique for measuring small substrate dissociation constants. However, the conformational changes associated with AdoMet binding were recently exploited by Crain and Broderick¹⁷⁸ to measure the PFL-Ae-(PFL)-AdoMet interactions using CD-spectroscopy.

Equilibrium dialysis is another technique commonly used to determine dissociation constants and was used for measurements on BioB, where similar AdoMet affinities compared to those obtained from AdoMet titrations were reported¹⁵⁴. Equilibrium dialysis is usually carried out over extended time periods, which makes it less suitable to study AdoMet binding due to its intrinsic instability. At 37 °C and pH 7.5, biologically active (*S,S*)-AdoMet **8** breaks down spontaneously to homoserine lactone **88** and MTA **14** and also readily racemises to the inactive (*R,S*)-AdoMet **89**¹⁷⁹. It may furthermore undergo hydrolysis to *S*-(5'-deoxyribosyl)-L-methionine **86** and adenine **87**¹⁷⁹ (Scheme 3.4). While only a 1% loss of AdoMet is expected over a 30 min time period, this relatively small decrease becomes more significant at lower AdoMet concentrations and may lead to overestimation of the AdoMet affinity.

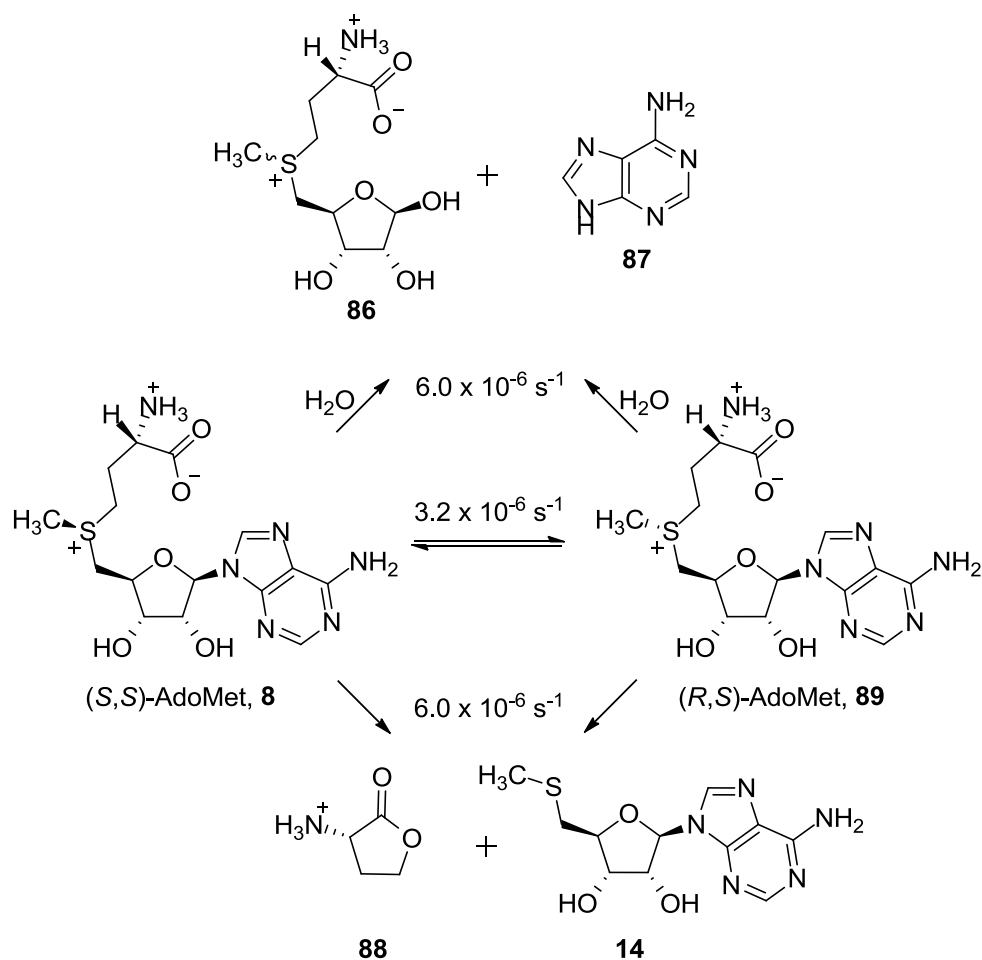
Table 3.2 Examples of substrate K_d and K_M constants for radical AdoMet enzymes.

Enzyme	Substrate(s) ^a	K_d (μM)	K_M (μM)	Reference
PFL–Ae	AdoMet	7.6 ± 1.9	2.8 ± 0.3	178,180
	AdoMet (PFL)	5.7 ± 1.7	--	178
	PFL	1.1–3.4	1.2 ± 0.4	178,180
BioB	AdoMet	~1000	--	154
	AdoMet (DTB)	0.2–5.0	--	
Cfr	AdoMet	12	--	177
BtrN	AdoMet	--	460 ± 100	121
	DOIA	--	22 ± 4	
QueE	AdoMet	--	45 ± 1	142
	CPH ₄ ^b	--	20 ± 7	
DesII	TDP–4–amino–4,6– dideoxy–D–glucose ^c	--	50 ± 2	181

a – All studies employed commercial AdoMet.

b – 6–Carboxy–5,6,7,8–tetrahydropterin.

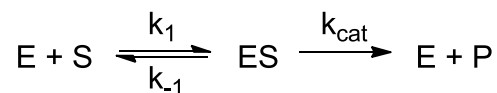
c – Thymidine diphosphate–4–amino–4,6–dideoxy–D–glucose.



Scheme 3.4 Racemisation and degradation of (S,S)-AdoMet.

AdoMet is intrinsically unstable under physiological conditions and racemisation and/or degradation may occur. Adapted from Iwig et al.¹⁷⁹.

An indirect estimation of the apparent AdoMet and tyrosine affinities for the variant HydG proteins can be obtained from Michaelis–Menten constants¹⁸². Michaelis–Menten kinetics provides an empirical model to describe the progress of enzyme reactions (Scheme 3.5), where a single substrate S reacts rapidly and reversibly with enzyme E to form an enzyme–substrate complex ES. Product formation then proceeds in an irreversible manner.



Scheme 3.5 Enzyme catalysed reaction following Michaelis–Menten kinetics.

E – enzyme, S – substrate, ES – enzyme–substrate complex.

Although the HydG catalysed reaction is a bi–substrate system, pseudo first order kinetics can be achieved by keeping one of the substrates in excess. This permits the approximation of the free substrate concentration with the initial substrate concentration. Further assuming steady–state conditions, the velocity of product formation can be described by the Michaelis–Menten equation^{183,184} (Equation 3.4), where v_0 and V_{max} are the initial and maximum rates of product formation respectively, K_M the apparent Michaelis–Menten constant and $[S]$ the substrate concentration.

$$v_0 = \frac{V_{\text{max}} [S]}{K_M^{\text{app}} + [S]} \quad \text{Equation 3.4}$$

In terms of rate constants, the apparent Michaelis–Menten constant is defined by Equation 3.5, which approximates the K_d (Equation 3.6) under rapid equilibrium conditions ($k_{-1} \gg k_{\text{cat}}$ in Scheme 3.5).

$$K_M^{\text{app}} = \frac{k_{-1} + k_{\text{cat}}}{k_1} \quad \text{Equation 3.5}$$

$$K_d = \frac{[E][S]}{[ES]} = \frac{k_{-1}}{k_1} \quad \text{Equation 3.6}$$

The assumption of rapid equilibrium is likely valid for HydG catalysed tyrosine cleavage due to the observed slow turnover of HydG³⁴ ($k_{\text{cat}} < 20 \times 10^{-4} \text{ s}^{-1}$, section 3.2) compared to estimated enzyme–substrate dissociation rates (10^9 – 10^{12} s^{-1})¹⁸⁵. These dissociation rates have been calculated using collision

theory and do not take into consideration the viscosity of the reaction medium, steric hindrance or conformational changes during interactions of the enzyme with substrate and consequently reflect an extreme upper limit. It is however unlikely that the energy required for any physical rearrangements in the HydG active site decreases the dissociation rate more than 10^{12} -fold. Consequently, chemical modification of the HydG substrates is still the rate limiting step.

To model product formation with Michaelis–Menten kinetics (Equation 3.4), significant substrate depletion has to be prevented. This would validate the assumption that the unbound substrate concentration equals the total quantity of substrate. As a result, the employed enzyme concentration has to be significantly lower than the smallest substrate concentration used. Based on the lowest previously determined K_M values for AdoMet and the substrates of other radical AdoMet enzymes (Table 3.2), HydG concentrations as low as $1 \mu\text{M}$ may be required. These K_M studies however employed commercial AdoMet preparations, which likely contained less than 50% biologically active (*S,S*)-AdoMet^{115,186}, therefore potentially underestimating the true affinity for AdoMet.

To determine the AdoMet Michaelis–Menten constant (K_M^{AdoMet}) experimentally, initial rates of 5'-dAH formation at varying AdoMet and saturating tyrosine concentrations have to be determined, while *p*-cresol formation would have to be measured at varying tyrosine and saturating AdoMet concentrations to determine the Michaelis–Menten constant for tyrosine (K_M^{TYR}). Bearing in mind (i) the previously determined HydG turnover rates of $\sim 20 \times 10^{-4} \text{ s}^{-1}$, (ii) the requirement for low enzyme concentrations ($\sim 1 \mu\text{M}$) and (iii) the necessity to measure initial rates of product formation during early time points ($\lesssim 5 \text{ min}$), very low concentrations of product ($\sim 1 \mu\text{M}$)

Chapter 3 – Kinetics

are expected to be formed by WT HydG, and even less by the C-terminal HydG mutants. These estimated concentrations are below the UV-Vis detection limit for 5'-dAH and *p*-cresol of approximately 5 μ M. This limitation was however overcome by employing the fluorescence rather than UV-Vis properties of *p*-cresol, decreasing its quantification limit to 15 nM as detailed in the next section. A similar strategy could not be employed for the AdoMet cleavage product 5'-dAH, but measuring initial *p*-cresol instead of 5'-dAH formation rates to also calculate K_M^{AdoMet} is considered more accurate due to the uncoupled turnover observed for WT as well as mutant HydG (section 3.2). Overestimation of initial 5'-dAH formation rates may otherwise result in erroneously small K_M^{AdoMet} values.

3.4.1 HPLC optimisation for quantification of nanomolar *p*-cresol

A more sensitive HPLC based *p*-cresol quantification method was obtained employing the fluorescent properties of *p*-cresol ($\lambda_{\text{ex}} = 274 \text{ nm}$, $\lambda_{\text{em}} = 312 \text{ nm}$)¹⁸⁷ (Method 31). Due to the near identical excitation and emission wavelengths of tyrosine and *p*-cresol and the high concentration of tyrosine present in HydG activity assays compared to the very small amounts of *p*-cresol being formed, it was initially difficult to accurately quantify *p*-cresol. The strong tailing of the earlier eluting tyrosine peak (Figure 3.4 A, $R_t = 3\text{--}6 \text{ min}$) obscured the signal for *p*-cresol ($R_t = 11.5 \text{ min}$) and a significant overestimation of nanomol quantities of *p*-cresol was observed in the presence of more than 500 μM tyrosine (Figure 3.4 B).

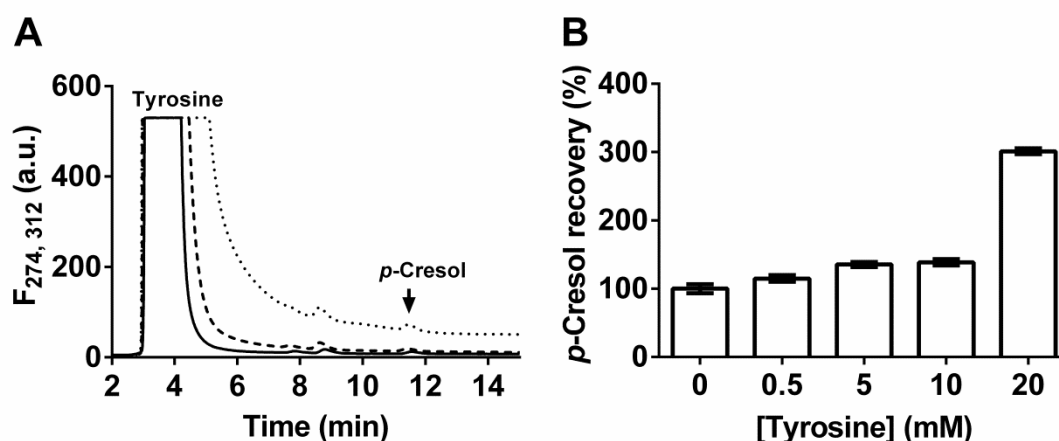


Figure 3.4 Quantification of *p*-cresol in the presence of tyrosine.

(A) HPLC chromatogram of a *p*-cresol standard (62.5 nM, $R_t = 11.5 \text{ min}$) analysed in the presence of increasing concentrations of tyrosine (0.5 mM, —; 10 mM, ---; 20 mM, ...; $R_t = 3\text{--}6 \text{ min}$). (B) The apparent recovery of *p*-cresol from (A) was quantified against a 62.5 nM *p*-cresol standard analysed in the absence of tyrosine.

By applying a long and shallow organic gradient, the HPLC elution conditions could be optimised to increase the separation between tyrosine and *p*-cresol. As a result, a linear *p*-cresol calibration curve was obtained with a quantification limit of 15 nM (Figure 3.5). This represents an approximate 1000-fold improvement over the 5 μ M quantification limit when using UV-Vis detection for *p*-cresol.

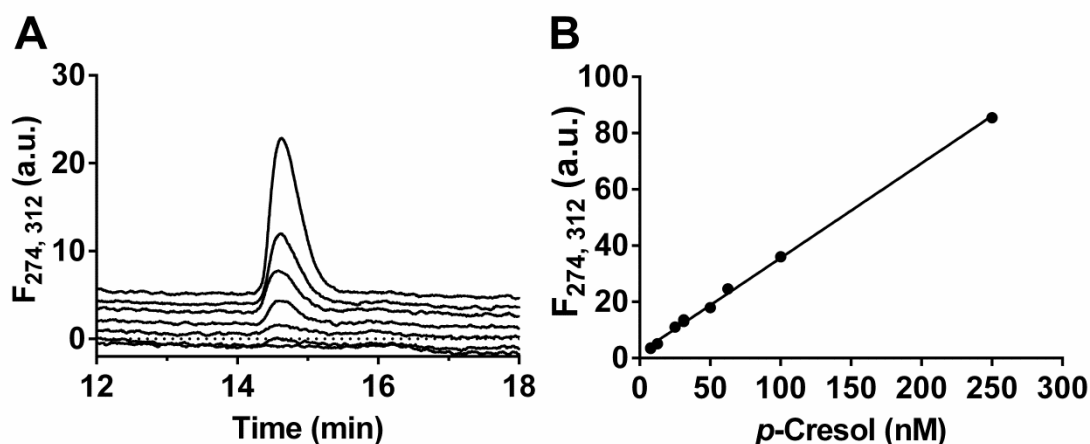


Figure 3.5 *p*-Cresol quantification by HPLC with fluorescence detection.

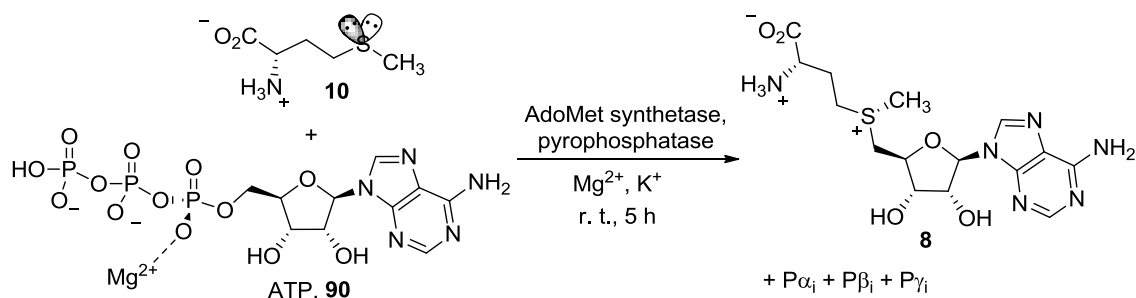
(A) HPLC chromatogram showing the fluorescence response ($\lambda_{\text{ex}} = 274 \text{ nm}$, $\lambda_{\text{em}} = 312 \text{ nm}$) for (bottom to top) water, 7.8, 15.6, 31.3, 62.5, 125 and 250 nM *p*-cresol. The data is offset for clarity. (B) Representative calibration curve for *p*-cresol standards in (A).

3.4.2 Enzymatic synthesis and purification of (*S,S*)-AdoMet

HPLC analysis of commercial AdoMet preparations has shown that they only contain approximately 43% biologically active (*S,S*)-AdoMet **8** and as much as 25% inactive (*R,S*)-AdoMet **89**¹¹⁵. Other impurities include MTA **14** and AdoHcy **59**, which have both been shown to inhibit BioB activity¹¹⁵ and may therefore also affect HydG. To overcome the likely inhibition effect of impurities in commercial AdoMet preparations¹¹⁵ in HydG activity assays and to accurately determine the concentrations of (*S,S*)-AdoMet added, enzymatically synthesised (*S,S*)-AdoMet is required.

AdoMet synthetase catalyses the conversion of *L*-methionine **10** and adenosine-5'-triphosphate (ATP, **90**) to (*S,S*)-AdoMet **8** (Scheme 3.6) in a reaction where Mg²⁺ and K⁺ ions are essential for substrate binding¹⁸⁸. The Mg²⁺ ion is thought to coordinate the *pro-S* oxygen of the β -phosphoryl group of ATP **90**^{188,189}. Stereospecific nucleophilic attack of the methionine sulfur *pro-S* lone pair onto the 5'-C of **90** leads to (*S,S*)-AdoMet **8** and triphosphate. The latter is hydrolysed to inorganic phosphate (P_i) and pyrophosphate by the enzyme's intrinsic triphosphatase activity¹⁸⁸. To overcome the non-competitive inhibition of the formed pyrophosphate for ATP **90**, inorganic pyrophosphatase is usually added¹⁸⁸, cleaving pyrophosphate to inorganic phosphates (P_i). The formed (*S,S*)-AdoMet exerts product inhibition on AdoMet synthetase, but β -mercaptoethanol and acetonitrile have both been used as additives to overcome this¹⁹⁰.

Chapter 3 – Kinetics



Scheme 3.6 Enzymatic (*S,S*)-AdoMet synthesis.

In the presence of Mg²⁺ and K⁺ ions, AdoMet synthetase catalyses the conversion of L-methionine **10** and ATP **90** to (*S,S*)-AdoMet **8** as well as the hydrolysis of tripolyphosphate to inorganic phosphate and pyrophosphate. The methionine sulfur *pro-S* and *pro-R* lone pair is highlighted in a grey and clear lobe, respectively.

The *E. coli* AdoMet synthetase (EC 2.5.1.6) overproducing strain DM22 (pK8) was previously used by other laboratories to prepare milligram quantities of pure (*S,S*)-AdoMet^{61,115,191} and was a kind gift from J. B. Broderick (Montana State University). AdoMet synthetase was expressed in *E. coli* BL21 (DE3) cells in LB media at 37 °C and the cells harvested after a 10 h or 17 h incubation period (Method 26). SDS-PAGE analysis confirmed the expression of AdoMet synthetase (45 kDa) as a major band close to the 42 kDa molecular weight marker (Figure 3.6), representing the monomer of the 180 kDa tetramer¹⁸⁸. Cells harvested after 17 h also contained a major impurity of approximately 20 kDa (Figure 3.6 E-H) which was less pronounced in the cells harvested after 10 h (Figure 3.6 A-D). Subsequent large scale expressions were therefore terminated after 10 h to give approximately 2 g/L light beige cell paste.

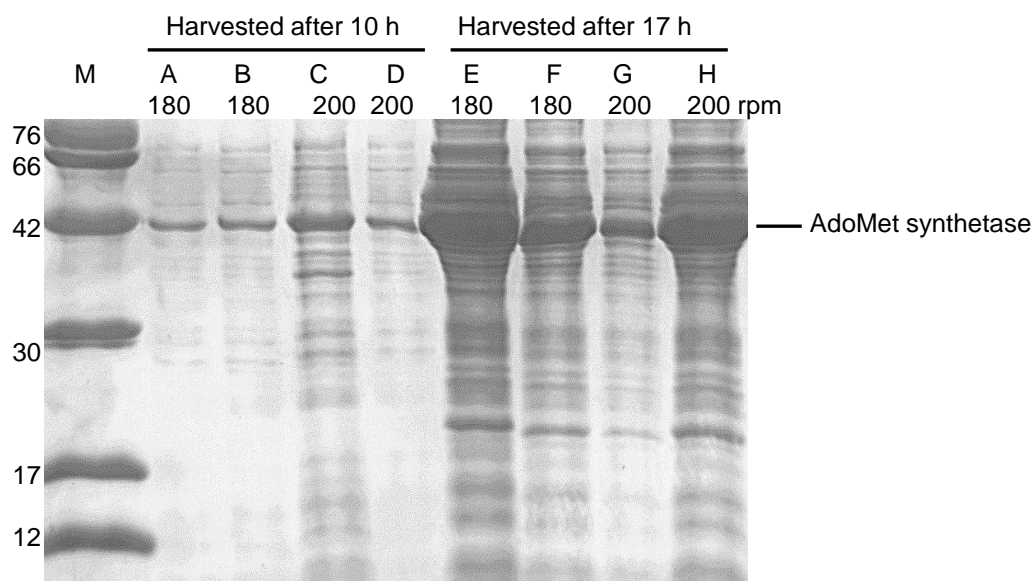


Figure 3.6 SDS–PAGE analysis of AdoMet synthetase expression study.

15% SDS–PAGE analysis of AdoMet synthetase containing cell lysates, which have been incubated for varying time periods and differing aeration rates.

To assess product inhibition of AdoMet synthetase, a crude synthetase lysate (~35 mg/mL) was incubated with L–methionine (10 mM), ATP (13 mM), 0.5 units of inorganic pyrophosphatase in the presence of 8% β–mercapto–ethanol or 20% acetonitrile (Method 27). At 1 h time intervals, small reaction aliquots were removed and any proteins precipitated with 1 M HCl. The resulting supernatant was then analysed by thin–layer chromatography (TLC) and HPLC (Method 30) to confirm the presence and quantity of the AdoMet formed. Synthesis of AdoMet reached a plateau after approximately 5 h (Figure 3.7 A, dashed), after which only in the presence of 20% acetonitrile small amounts of additional AdoMet was synthesised. This was on average equivalent to a synthesis yield between 40% and 60% and is in agreement with yields obtained by Gross and co–workers¹⁹². Surprisingly, using β–mercaptoethanol as the additive, AdoMet degradation was observed after the

5 h incubation period (Figure 3.7 A, dashed blue). While HPLC analyses confirmed the formation of increasing amounts of the AdoMet hydrolysis product adenine in all samples (Figure 3.7 B, dashed), MTA potentially resulting from intramolecular AdoMet cyclisation (Scheme 3.4) was not detected. The adenine quantities however did not account for the entire loss of AdoMet and another degradation pathway may exist. In the presence of AdoMet (1 mM), neither 20% acetonitrile nor β -mercaptoethanol could overcome product inhibition (Figure 3.7 A, solid). The presence or absence of inorganic pyrophosphatase was found not to have any effects on AdoMet synthesis (data not shown). Based on the AdoMet breakdown observed with β -mercaptoethanol, successive AdoMet syntheses were carried out in the presence of 20% acetonitrile.

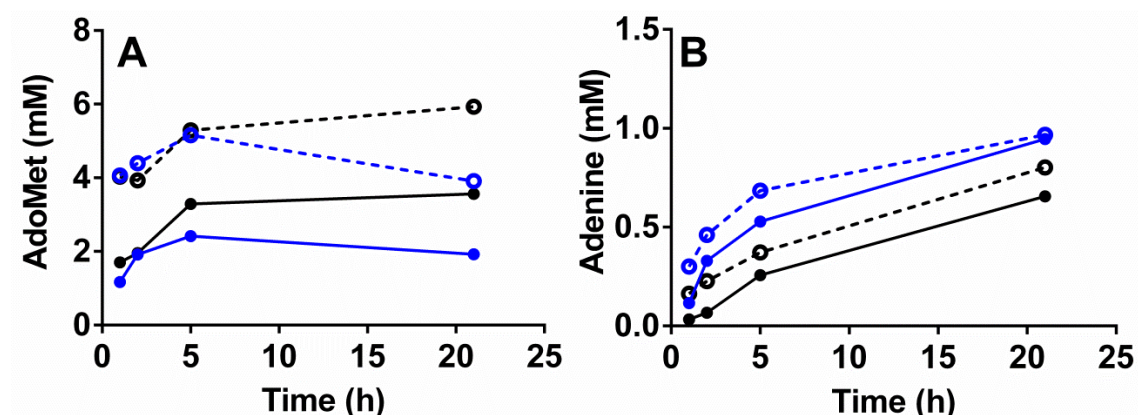


Figure 3.7 Enzymatic synthesis of (*S,S*)-AdoMet with time.

(A) AdoMet synthesis at 25 °C by AdoMet synthetase in the presence of L-methionine (10 mM), ATP (13 mM), 0.5 units of inorganic pyrophosphatase in 100 mM Tris, 50 mM KCl, 26 mM MgCl₂, 1 mM EDTA, pH 8.0 buffer and the additives β -mercaptoethanol (8%, blue) or acetonitrile (20%, black) in the absence (dotted) or presence (solid) of AdoMet (1 mM). (B) Respective formation of the AdoMet breakdown product adenine.

Exploiting the permanent positive charge on AdoMet, purification of the synthesised AdoMet by cation exchange chromatography using weakly acidic Amberlite IRC-50¹⁹² and Amberlite CG-50¹¹⁵ resins or strongly acidic Dowex 50¹⁹³ and Source 15S resins⁶¹ is documented. In this study, AdoMet purification using Amberlite IRC-50 (Method 28) was unsuccessful as AdoMet did not bind to the resin but eluted during the initial washing step. This was surprising as AdoMet has previously been purified using this type of resin, which is also known for its high exchange capacity¹⁹⁴. A protocol described by Walsby et al.⁶¹ for purification of AdoMet using Source 15S resin was then investigated instead. This involved that the AdoMet synthesis mixture was loaded onto a 1 M HCl charged but water equilibrated Source 15S column. Although AdoMet eluted over an applied 0–1 M HCl gradient, the subsequent lyophilisation step was highly inefficient. The AdoMet–HCl mixture did not stay frozen and repeated dilutions with water were required to overcome this problem. However, due to the instability of AdoMet¹⁷⁹, the repeated freeze–thawing cycles increased the amounts of adenine and especially MTA impurities as identified by HPLC. Using the more volatile trifluoroacetic acid (TFA) instead of HCl, AdoMet eluted as a single peak, typically between 0.7 M and 0.9 M TFA (Figure 3.8 A). Lyophilisation could be achieved over approximately two days without freeze–thawing. This purification protocol is detailed in Method 29.

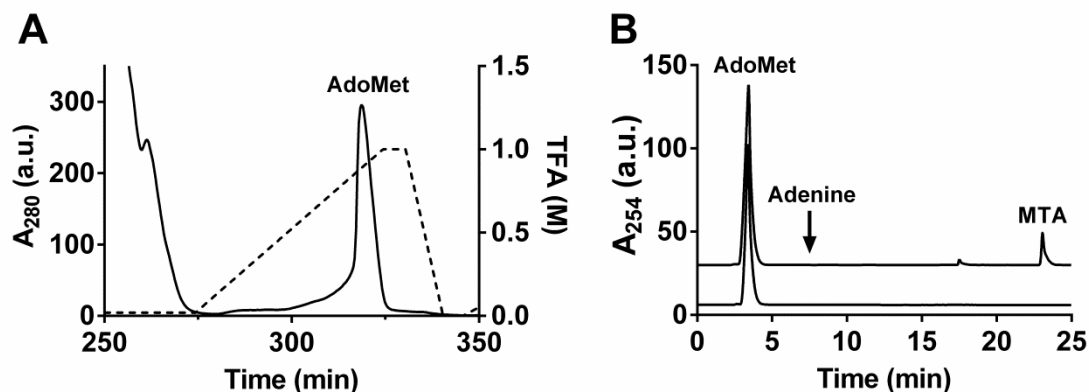


Figure 3.8 Enzymatic synthesis of (*S,S*)-AdoMet and purification by cation exchange chromatography.

(A) Elution chromatogram of AdoMet from a Source 15S column. (B) Representative HPLC traces of commercial (2 mM, top) and enzymatically synthesised AdoMet (2 mM, bottom) analysed using Method 30. The following retention times were observed, AdoMet – 3.1 min, adenine – 7.8 min, unknown impurity – 17.6 min and MTA – 22.9 min. For clarity, traces are displaced.

HPLC (Figure 3.8 B) and mass spectrometry (Figure 7.4) analysis of the pooled and lyophilised AdoMet fractions confirmed the purity of AdoMet. Compared to a commercial AdoMet standard, less than 0.1% adenine and 1.5% MTA was present. By integrating the respective proton resonances of the (*S,S*)-AdoMet and (*R,S*)-AdoMet methyl groups at 2.96 ppm and 2.92 ppm¹⁹⁵ in the AdoMet ¹H NMR spectrum (Figure 7.3), it was further confirmed that the enzymatically synthesised AdoMet contained on average 95% biologically active (*S,S*)-AdoMet. Unfortunately, the retention of AdoMet on the 15S cation exchange column was poor and a low 10–20% purification yield was observed, lowering the overall yield of pure, enzymatically synthesised (*S,S*)-AdoMet to an average of 5%.

3.4.3 Determination of AdoMet and tyrosine Michaelis–Menten constants

Non-specific binding of HydG to the plastic Eppendorf tubes during activity assays would decrease the apparent in vitro activity and would be most pronounced at low enzyme concentrations. The addition of bovine serum albumin (BSA) is routinely used to overcome this problem¹⁹⁶. Activity assays of WT and mutant HydG enzymes (1 μM) were carried out with AdoMet (1 mM), tyrosine (1 mM) and sodium dithionite (1 mM) in the absence or presence of 0.1% BSA. Based on the amount of *p*-cresol formed after 5 min, no differences regarding the presence of BSA were observed (data not shown).

To assess AdoMet dependent tyrosine cleavage, reconstituted HydG variants (5 μM) were incubated with varying concentrations of enzymatically synthesised AdoMet at constant, saturating tyrosine concentrations (400 μM or 3 mM for WT and mutant HydG, respectively). Tyrosine dependent *p*-cresol formation was assessed by incubation with constant, saturating enzymatically synthesised AdoMet concentrations (100 μM or 200 μM for WT and mutant HydG, respectively) at varying tyrosine concentrations (Method 21). Reactions were stopped between 1 min and 10 min and the formation of *p*-cresol quantified as exemplified in Figure 3.9 and Figure 3.10. The slow reaction catalysis of HydG limited the number of turnovers that could be measured. As a result, the initial rates of *p*-cresol formation may not have been determined under ideal steady state conditions. In addition, the employed enzyme concentration (5 μM) meant that the free ligand assumption for Michaelis–Menten kinetics, $[S]_{\text{total}} \sim [S]_{\text{free}}$, is not valid at the lowest substrate concentrations. For these two reasons, the determined Michaelis–Menten constants should be treated as approximate.

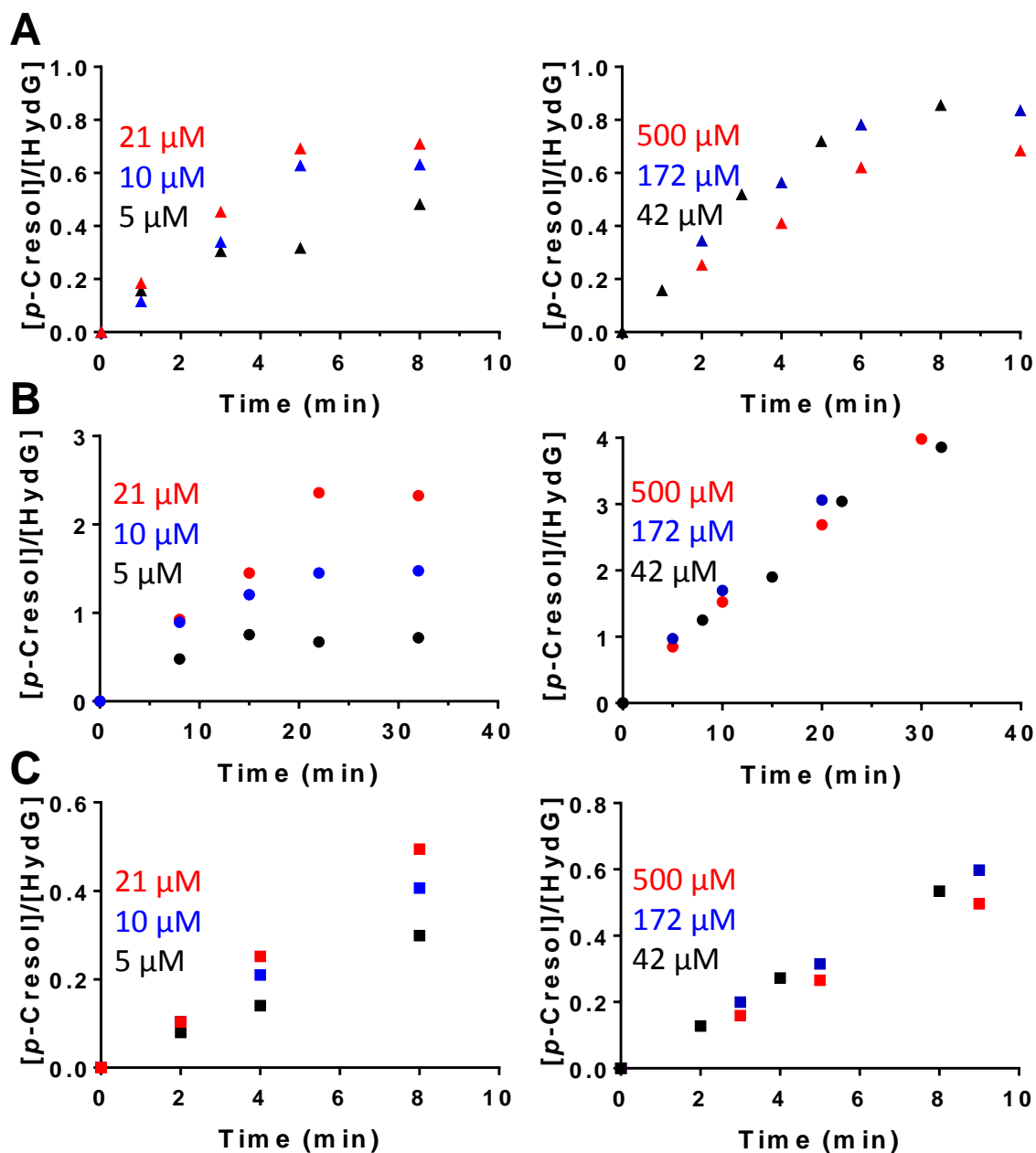


Figure 3.9 Representative AdoMet dependent *p*-cresol formation.

(A) WT (5 μM, 5.5 ± 0.4 Fe/protein), (B) C386S (5 μM, 4.8 ± 0.6 Fe/protein) and (C) Δ CTD HydG (5 μM, 3.0 ± 0.1 Fe/protein) was incubated at 37 °C in the presence of tyrosine (WT – 400 μM, mutants – 3 mM), sodium dithionite (1 mM) and varying concentrations of enzymatically synthesised AdoMet in 50 mM HEPES, 0.5 M KCl, pH 7.4 buffer. Respective AdoMet concentrations are indicated.

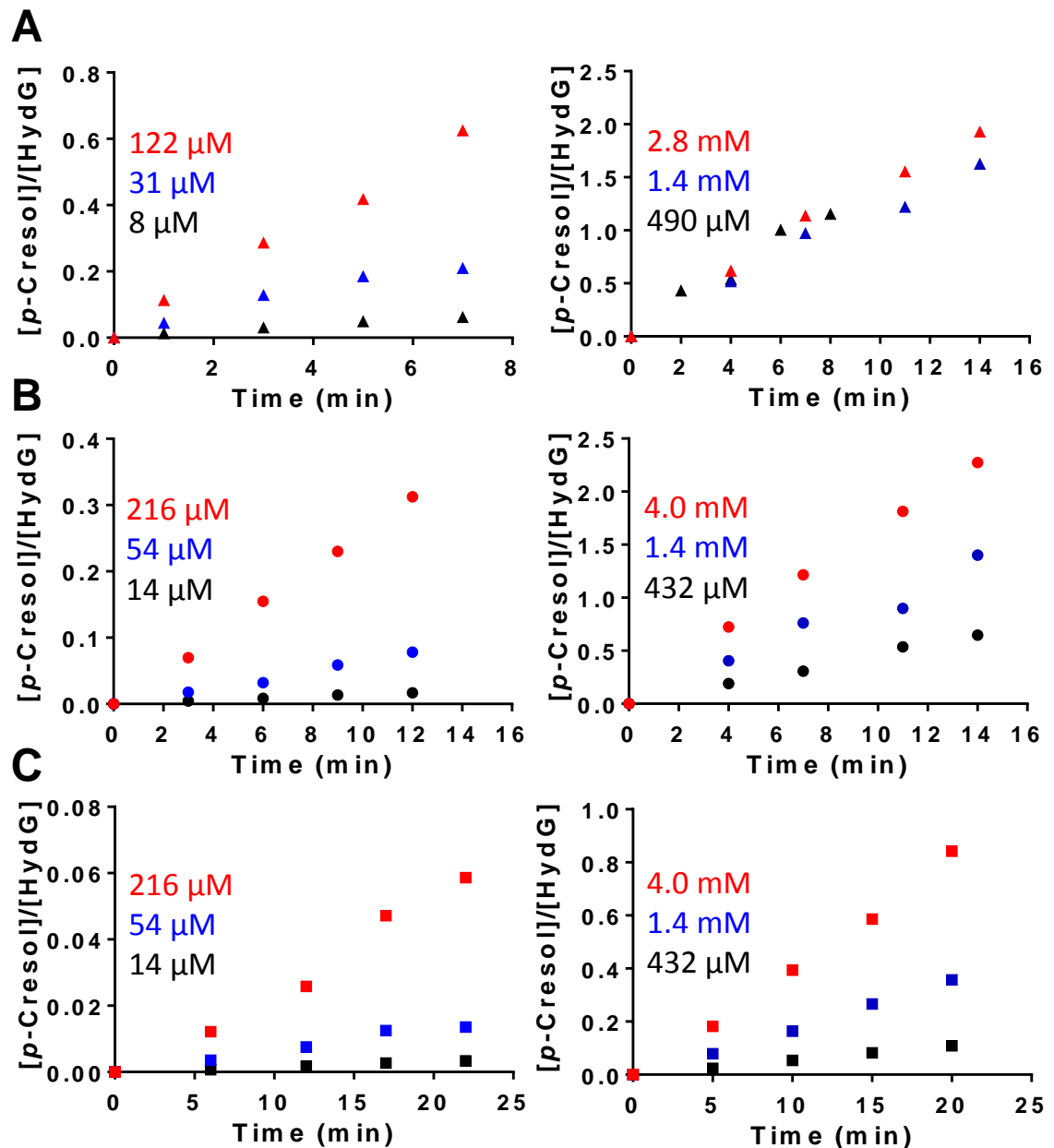


Figure 3.10 Representative tyrosine dependent *p*-cresol formation.

(A) WT (5 μ M, 7.6 ± 0.6 Fe/protein), (B) C386S (5 μ M, 4.9 ± 0.5 Fe/protein) and (C) Δ CTD HydG (5 μ M, 3.0 ± 0.2 Fe/protein) was incubated at 37 $^{\circ}$ C in the presence of enzymatically synthesised AdoMet (WT – 100 μ M, mutants – 200 μ M), sodium dithionite (1 mM) and varying tyrosine concentrations in 50 mM HEPES, 0.5 M KCl, pH 7.4 buffer. Respective tyrosine concentrations are indicated.

Chapter 3 – Kinetics

To obtain Michaelis–Menten plots, initial rates of *p*-cresol formation have been extracted from the linear portion of the *p*-cresol formation data (Figure 3.9, Figure 3.10) and plotted against the employed substrate concentrations. The AdoMet dependent velocity data of all HydG variants (Figure 3.11 A) was best fitted to classical Michaelis–Menten kinetics^{10,11} (Equation 3.4). The K_M^{AdoMet} for WT ($2.6 \pm 1.1 \mu\text{M}$) and ΔCTD HydG ($3.6 \pm 0.7 \mu\text{M}$) are identical within error, whereas the K_M^{AdoMet} for C386S HydG was calculated to be $17.4 \pm 2.6 \mu\text{M}$ (Table 3.3). These K_M^{AdoMet} values are within the range reported for other radical AdoMet enzymes^{154,180}. Given that AdoMet coordinates to cluster I and is additionally involved in well characterised hydrogen bonding interactions to residues not expected to be affected by the C386S mutation and C-terminal deletion^{48–50,65,197}, it is not surprising that the affinity for AdoMet is very similar for all HydG variants. It may further suggest that the introduced mutations do not affect the positioning of AdoMet binding residues, implying correct folding of the characteristic TIM barrel observed among radical AdoMet enzymes⁶⁶.

The decreased *p*-cresol formation rates at AdoMet concentrations above 200 μM (Figure 3.11 A), for especially WT HydG, was initially interpreted to reflect substrate inhibition. Recent pH measurements on a different set of assays however identified that assays containing more than 200 μM enzymatically synthesised AdoMet were up to 0.4 pH units more acidic than assays containing for example 50 μM AdoMet. This pH decrease is likely due to excess TFA in the enzymatically prepared AdoMet samples and may suggest a strong pH dependence of *p*-cresol formation by WT HydG compared to the C-terminal HydG variants. This is discussed in more detail in section 3.6.2.

Tyrosine dependent *p*-cresol formation (Figure 3.11) was also modelled with Michaelis–Menten kinetics^{183,184} (Equation 3.4, Table 3.4) and the K_M^{TYR} for WT HydG was calculated to be $278.9 \pm 34.0 \mu\text{M}$. This K_M value is one order of magnitude higher than most reported substrate K_M values of other radical AdoMet enzymes^{121,142,180} (Table 3.2), but it lies below the intracellular tyrosine concentration of *C. acetobutylicum* ATCC824 during acidogenesis ($640 \mu\text{M}$) and solventogenesis ($660 \mu\text{M}$)¹⁹⁸, ensuring that HydG would be able to respond to fluctuations in tyrosine concentration during both stages of cell growth. Bearing in mind the rapid equilibrium assumption required when treating a K_M as an apparent dissociation constant (section 3.4), the increased K_M^{TYR} constants for C386S and ΔCTD HydG of $1.6 \pm 0.2 \text{ mM}$ and $10.6 \pm 0.6 \text{ mM}$, respectively, clearly show that modifications to the C-terminal cluster decrease the apparent affinity for tyrosine. The determined K_M^{TYR} for ΔCTD HydG is approximately threefold higher than the highest tyrosine concentration employed during the initial rate determinations and is thus just an approximation. The similarity of the apparent turnover numbers for *p*-cresol formation between ΔCTD HydG ($30 \times 10^{-4} \text{ s}^{-1}$) and the respective WT and C386S values ($43 \times 10^{-4} \text{ s}^{-1}$) (Table 3.4) is consistent with a model in which the rate of 5'-dA• formation and tyrosine cleavage to *p*-cresol is unaffected in the variant proteins. This suggests that the reaction step leading to *p*-cresol (Scheme 3.1, step 2) can be rescued at higher tyrosine concentrations. Experimentally this is observed for C386S HydG, but it is experimentally difficult to fully saturate ΔCTD HydG because of the limited solubility of tyrosine in assay buffer at physiological pH¹⁹⁹.

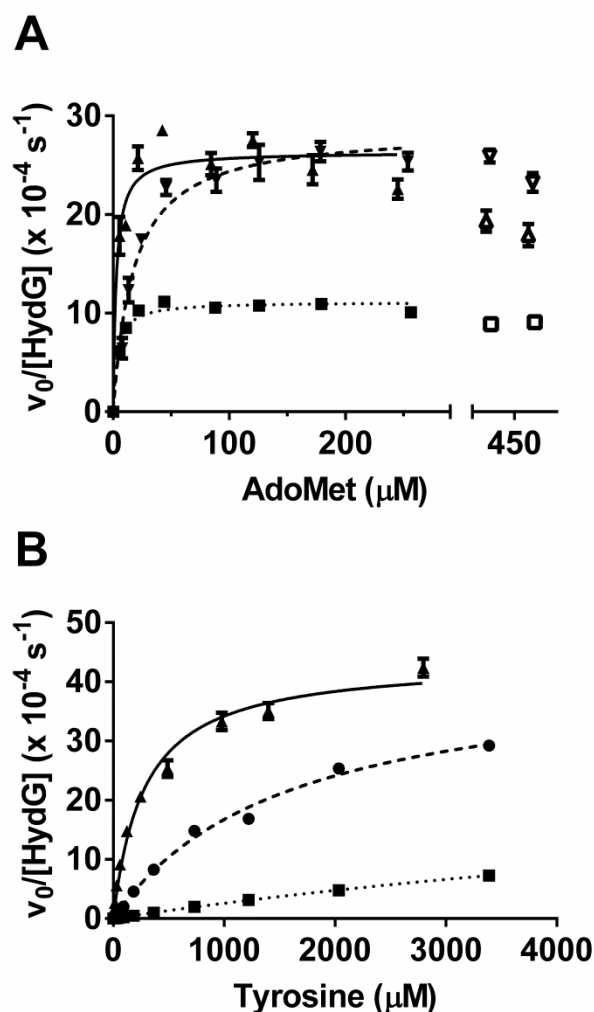


Figure 3.11 Substrate dependent *p*-cresol formation by HydG variants.

Initial *p*-cresol formation rates by HydG (5 μM) in 50 mM HEPES, 0.5 M KCl, pH 7.4 buffer at 37 °C. Assays additionally contained sodium dithionite (1 mM) and (A) tyrosine (WT – 400 μM , mutants – 3 mM) and varying concentrations of enzymatically synthesised AdoMet or (B) enzymatically synthesised AdoMet (WT – 100 μM , mutants – 200 μM) and varying tyrosine concentrations. The data is fitted to Michaelis–Menten kinetics (Equation 3.4). Calculated kinetic parameters for WT (—▲—), C386S (---●---) and Δ CTD HydG (···■···) are summarised in Table 3.3 and Table 3.4.

Table 3.3 AdoMet dependent kinetic parameters for *p*-cresol formation by WT and mutant HydG.

Initial *p*-cresol formation rates in Figure 3.11 A were fitted to Michaelis–Menten kinetics (Equation 3.4).

HydG sample	K_M^{AdoMet} (μM)	k_{cat} (10^{-4} s^{-1})	R^2	Fe/protein
WT	2.6 ± 1.1^a	26.3 ± 1.2^a	0.932	5.5 ± 0.4
C386S	17.4 ± 2.6	28.6 ± 1.0	0.982	4.8 ± 0.6
ΔCTD	3.6 ± 0.7	11.1 ± 0.3	0.978	3.0 ± 0.1

a – These values should be regarded as approximate because WT HydG displayed pH induced inhibition at higher AdoMet concentrations.

Table 3.4 Tyrosine dependent kinetic parameters for *p*-cresol formation by WT and mutant HydG.

Initial *p*-cresol formation rates in Figure 3.11 B were fitted to Michaelis–Menten kinetics (Equation 3.4).

HydG sample	K_M^{TYR} (mM)	k_{cat} (10^{-4} s^{-1})	R^2	Fe/protein
WT	$0.3 \pm 0.0(3)$	43.7 ± 1.6	0.991	7.6 ± 0.6
C386S	1.6 ± 0.2	43.2 ± 2.6	0.994	4.9 ± 0.5
ΔCTD	10.6 ± 0.6^a	30.1 ± 1.3^a	0.999	3.0 ± 0.2

a – These values should be regarded as approximate because the calculated K_M^{TYR} is higher than the highest tyrosine concentration experimentally investigated.

3.5 Optimised kinetic characterisation of wild-type and mutant *C. acetobutylicum* HydG

Taking advantage of the determined Michaelis–Menten constants for AdoMet and tyrosine (section 3.4.3), activity assays with WT, C386S and Δ CTD *C. acetobutylicum* HydG were repeated with near saturating substrate concentrations (40 μ M HydG, 0.5 mM enzymatically synthesised AdoMet, 4 mM tyrosine, 1 mM sodium dithionite) using the optimised 50 mM HEPES, 0.5 M KCl, pH 7.4 buffer (section 3.3.1). Time course data for all HydG variants were fitted to a first order function (Equation 3.1) and at least two full turnovers within the 60 min time period were observed (Figure 3.12). The fit to the data was good with R^2 values above 0.99, except for glyoxylate formation by WT HydG (0.97), C386S HydG (0.98) and cyanide formation by Δ CTD HydG (0.96). Observed *p*-cresol k_{cat} values ranged between $(10\text{--}46) \times 10^{-4} \text{ s}^{-1}$ (Table 3.5) for the three HydG variants investigated. This represents a 15-fold improvement for C386S and Δ CTD HydG catalysed *p*-cresol formation compared to initial time course investigations, while *p*-cresol formation by WT HydG has not much been affected (see section 3.2).

WT and C386S HydG demonstrated 1.3- and 1.5-fold uncoupled turnover, respectively, while Δ CTD HydG formed almost three times as much 5'-dAH **13** as *p*-cresol **4** after 60 min. This may suggest slight differences in AdoMet **8** and/or tyrosine **3** binding, which prevents facile hydrogen atom abstraction by 5'-dA• **9** from the tyrosine hydroxyl group (Scheme 3.1). Premature 5'-dA• quenching during Δ CTD HydG turnover likely results from a more solvent exposed active site. Alternatively, if the tyrosyl radical **32** was formed but C α –C β bond cleavage was impaired, reduction of the tyrosyl radical to **62** and protonation back to tyrosine **3** may be possible (Scheme 3.1).

The employed concentration of AdoMet (0.5 mM) represented a compromise between the observed inhibition of WT HydG (significant above 300 μM AdoMet; see Figure 3.11 A) and the problem of AdoMet becoming limiting upon multiple turnovers (increasingly a problem at low AdoMet concentrations). In fact, the inhibition of WT HydG remained a significant problem and a 60% reduction in *p*-cresol formation by WT compared to C386S HydG was observed (Figure 3.12 A, B). Respective turnover numbers were calculated as $(17.5 \pm 2.4) \times 10^{-4} \text{ s}^{-1}$ and $(45.8 \pm 1.9) \times 10^{-4} \text{ s}^{-1}$ (Table 3.5). This stark activity difference cannot alone be accounted for by the inhibition of WT HydG at higher AdoMet concentrations and may additionally be a result of poor reconstitution of the catalytically essential [4Fe-4S] clusters in WT HydG. The observed activity variations between different HydG batches of up to 30% support this hypothesis.

Over the 60 min time period investigated, ΔCTD HydG formed 100 μM *p*-cresol (Figure 3.12 C) with an apparent turnover number of $(10.5 \pm 1.1) \times 10^{-4} \text{ s}^{-1}$ (Table 3.5). Similar *p*-cresol quantities were formed by the WT enzyme, which, bearing in mind that ΔCTD HydG can experimentally not be saturated with tyrosine may suggest that neither the auxiliary cluster II nor the C-terminal residues (after C386) are essential for tyrosine cleavage to *p*-cresol (Scheme 3.1, step 2).

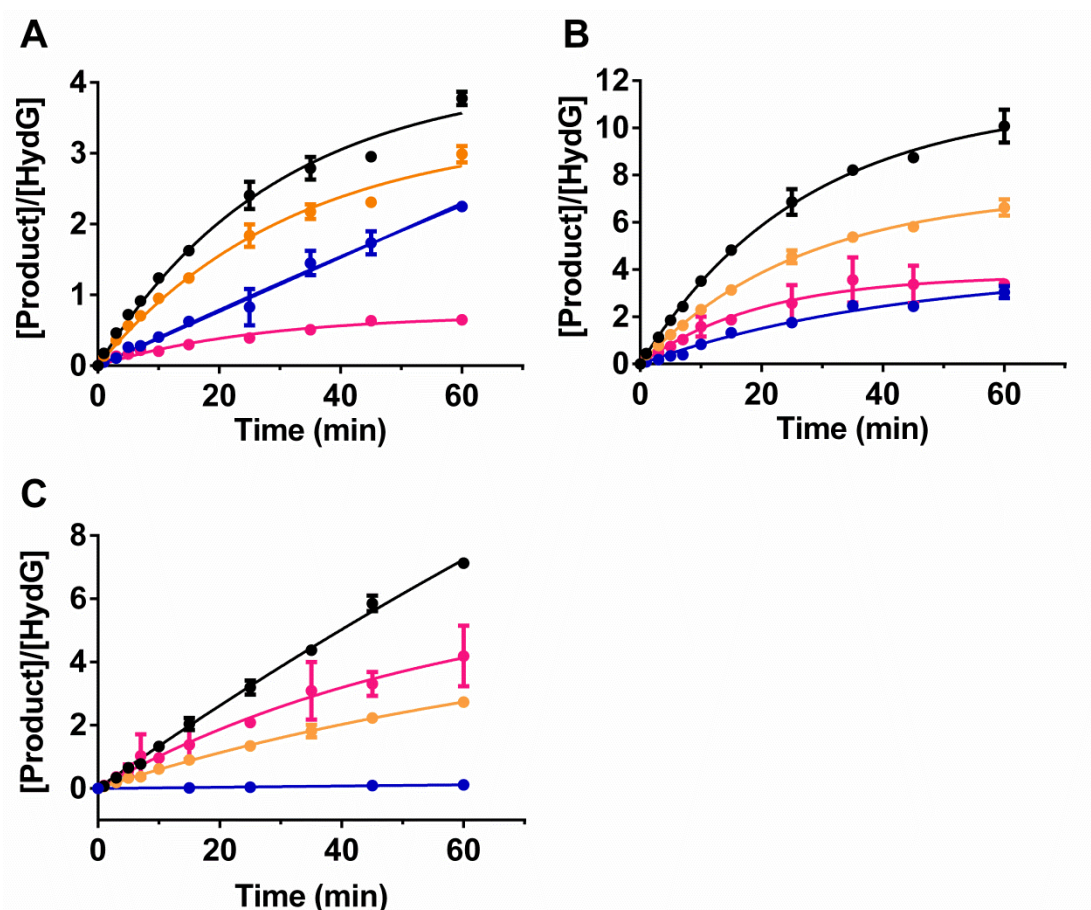


Figure 3.12 Time dependent AdoMet and tyrosine cleavage by HydG variants with near saturating substrate concentrations.

Formation of mol equivalents of 5'-dAH (—●—), *p*-cresol (—●—), cyanide (—●—) and glyoxylate (—●—) with respect to (A) WT (40 μ M, 8.0 ± 0.9 Fe/protein), (B) C386S (40 μ M, 6.4 ± 0.8 Fe/protein) and (C) Δ CTD HydG (40 μ M, 3.6 ± 0.2 Fe/protein) in the presence of enzymatically synthesised AdoMet (0.5 mM), tyrosine (4 mM) and sodium dithionite (1 mM) in 50 mM HEPES, 0.5 M KCl, pH 7.4 assay buffer. The data represent the average of duplicate assays incubated at 37 °C and are shown with standard deviations. The data was fitted with first order kinetics (Equation 3.1) to obtain respective turnover numbers summarised in Table 3.5. No satisfactory fit was obtained for cyanide formation by WT HydG which was instead modelled with linear kinetics (Equation 3.3). The intercept of panel C is adjusted to (0, -1).

Table 3.5 Kinetic analysis of AdoMet and tyrosine cleavage by HydG variants.

The apparent turnover numbers from the time course data in Figure 3.12 were extracted from the first order rate constant using Equation 3.2. Errors represent standard errors.

Product/HydG	$k_{\text{cat}}^{\text{app}}$ ($\times 10^{-4} \text{ s}^{-1}$)		
	WT	C386S	Δ CTD
5'-dAH	23.3 ± 2.9	69.4 ± 3.1	22.8 ± 11.3
<i>p</i> -Cresol	17.5 ± 2.4	45.8 ± 1.9	10.5 ± 1.1
Cyanide	6.4 ± 0.1	15.7 ± 3.6	NA ^a
Glyoxylate	4.6 ± 1.0	31.7 ± 4.3	18.4 ± 4.5

a – Cyanide quantities were too small to be fitted accurately.

Stoichiometric formation of cyanide with respect to *p*-cresol was observed for WT HydG during the initial time course investigations (Figure 3.1 A) and in the literature³⁴. In this particular study, some variation in the cyanide stoichiometry was observed for different WT HydG samples. At the 60 min time point for batch A for example, a *p*-cresol to cyanide ratio of 2.5:1 was observed (not shown), whereas for batch B, the ratio was 1.3:1 (Figure 3.12 A). The reduced cyanide formation compared to *p*-cresol was accounted for by detection of increased amounts of glyoxylate. WT HydG catalysed cyanide formation did not vary in the presence of tyrosine concentrations ranging between 0.5 mM and 4 mM (data not shown), confirming that the observed cyanide decrease was not due to the fourfold increase in tyrosine concentration employed compared to previous time course experiments in section 3.2. Although no significant differences in the iron content and UV-Vis spectra of the above HydG samples were observed (data not shown), the varying amounts

of cyanide formed were likely due to the previously mentioned batch to batch variation of reconstituted HydG samples. This strengthens the proposal that both [4Fe–4S] clusters are required for optimal cyanide formation. The variation in reconstituted protein samples makes it however particularly difficult to accurately assess the role of the C-terminal cysteine motif and coordinated cluster II with respect to cyanide formation by the C386S HydG mutant.

The turnover number for cyanide formation by C386S HydG was on average 66% lower than that of *p*-cresol (Table 3.5), which is equivalent to a *p*-cresol to cyanide ratio of 2.2:1 after 60 min (Figure 3.12 B). Again, the remaining tyrosine cleavage product was accounted for by glyoxylate. It is interesting to note that, while WT enzyme formed 1.5 to 2.3 molar equivalents of cyanide with respect to protein concentration, the C386S mutant catalysed formation of 2.8 molar equivalents.

Although Δ CTD HydG catalysed formation of 100 μ M *p*-cresol over a 60 min time period, representing a 60-fold activity improvement over observations by Tron¹⁶⁰, the amounts of detected cyanide were very low ($4.6 \pm 0.6 \mu$ M, 0.12 mol/mol protein). Instead, stoichiometric amounts of glyoxylate with respect to *p*-cresol were formed (Figure 3.12 C). The slight overestimation of glyoxylate likely reflects the fluorescence change of the glyoxylate derivatisation product as discussed in sections 3.2 and 3.3.2.

Collaborative studies by Benjamin R. Duffus (Montana State University) demonstrated that none of the C-terminally modified HydG variants formed CO, in agreement with findings by Nicolet and co-workers¹³³.

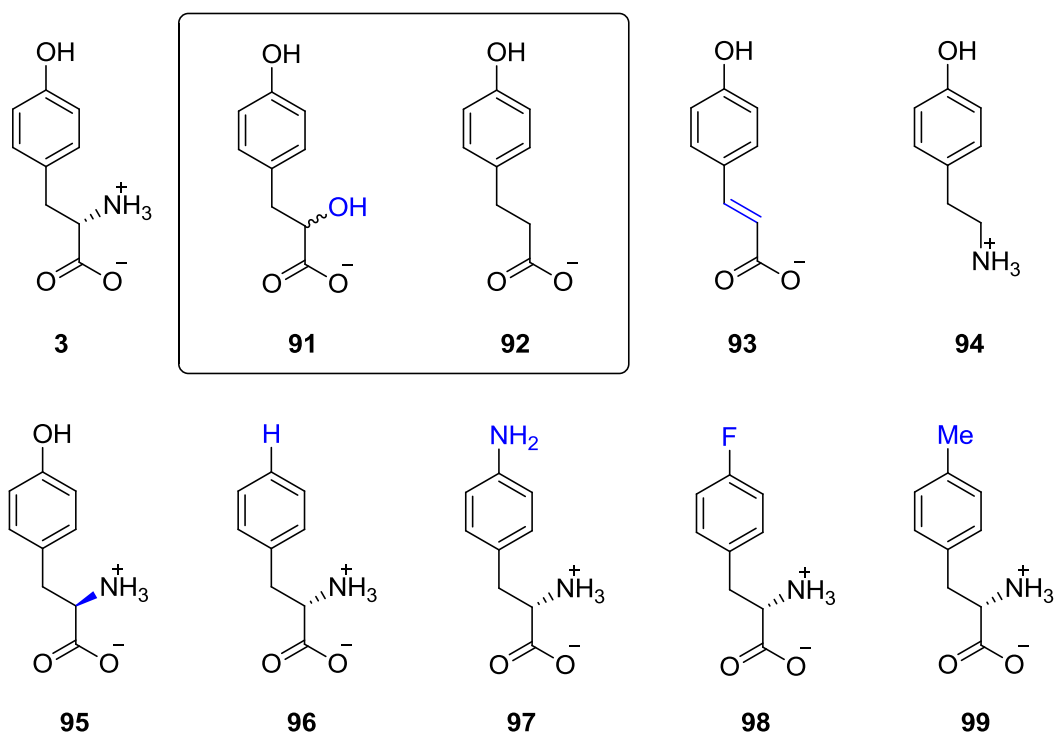
3.6 Factors influencing wild-type HydG activity

3.6.1 Activity in the presence of tyrosine substrate analogues

The phenomenon that substrate binding can tune the redox potential of the radical AdoMet [4Fe-4S] cluster to facilitate AdoMet cleavage (section 1.2.3.1) was exploited by Challand and co-workers to investigate which tyrosine functional groups may be required for its recognition and cleavage by ThiH¹³⁰. ThiH catalysed AdoMet cleavage was measured in the presence of varying tyrosine analogues (Scheme 3.7) and compared to activity assays with the natural substrate L-tyrosine¹³⁰. Relative to assays devoid of a tyrosine derivative, which reflect the background AdoMet cleavage capability of ThiH, AdoMet cleavage was increased by 50% in the presence of *p*-hydroxyphenyl- α -hydroxypropionic acid **91** or *p*-hydroxyphenylpropionic acid **92**¹³⁰. This may suggest that the L-tyrosine's carboxylic acid functionality is important for L-tyrosine recognition by ThiH, likely by establishing hydrogen bonding interactions with basic side chain residues in the active site (Scheme 3.8 B). Both substrate analogues supported less than 5% *p*-cresol formation, which may indicate that binding contacts are established to the carboxylate group for correct positioning of the hydroxyl functionality for hydrogen atom abstraction, but that initiation of C α -C β bond cleavage requires the amino group. The observed accumulation of 5'-dAH but lack of *p*-cresol formation is likely due to futile cycling of **91** and **92**, where the initially formed phenoxy radical is reduced and then protonated to reform the tyrosine analogue for the next cycle of hydrogen atom abstraction. This is exemplified for L-tyrosine in Scheme 3.1 (**32**→**62**→**3**). Interestingly, compared to *p*-hydroxyphenylpropionic acid **92**, *p*-hydroxyphenylcinnamic acid **93** was not successful in promoting AdoMet cleavage¹³⁰. This difference may suggest that L-tyrosine

Chapter 3 – Kinetics

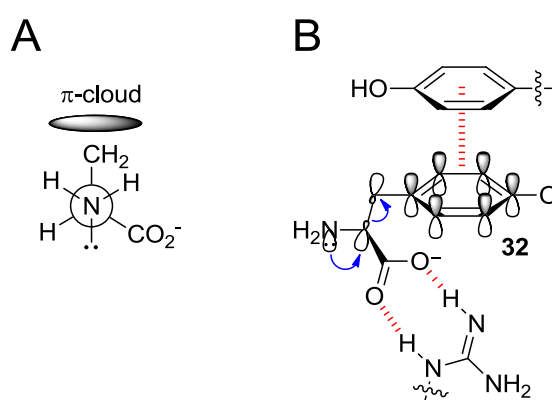
does not bind in one plane and that some flexibility in the non-aromatic carbon chain is required, such as free rotation around the C α -C β bond. Alternatively, the more electron deficient phenyl ring of **93** compared to **91** and **92** could weaken potential π - π or π -cation interactions with aromatic and positively charged side chain residues, respectively, which may normally correctly orient L-tyrosine in the active site (Scheme 3.8 B). None of the remaining tyrosine analogues in Scheme 3.7 significantly supported uncoupled AdoMet cleavage¹³⁰.



Scheme 3.7 Tyrosine analogues employed in ThiH and HydG activity assays.

The boxed tyrosine analogues stimulated ThiH dependent AdoMet cleavage by as much as 50% relative to assays containing L-tyrosine **3**¹³⁰.

The previous observations inspired Challand and co-workers to embark on a computational modelling study, which identified that the L-tyrosine C α -C β bond becomes elongated when the N-lone pair is positioned antiperiplanar to the π -cloud of the phenolic radical²⁰⁰ (Scheme 3.8 A). Challand proposes that this antiperiplanar arrangement may allow N-lone pair donation into the C α -C β σ^* bond for facile cleavage of the developing tyrosyl radical **32**²⁰⁰ (Scheme 3.8 B), which agrees with the absence of *p*-cresol in ThiH activity assays containing the (amino group lacking) tyrosine analogues **91** or **92**¹³⁰. Availability of the N-lone pair requires the tyrosine amino functionality to be neutral. However, under physiological conditions and in free solution, the majority of L-tyrosine molecules will contain an ammonium group (pK_a = 9.1). How the required change in the protonation state of the amino group in bound L-tyrosine may occur is discussed in the next section.



Scheme 3.8 Proposed antiperiplanar arrangement for L-tyrosine binding.

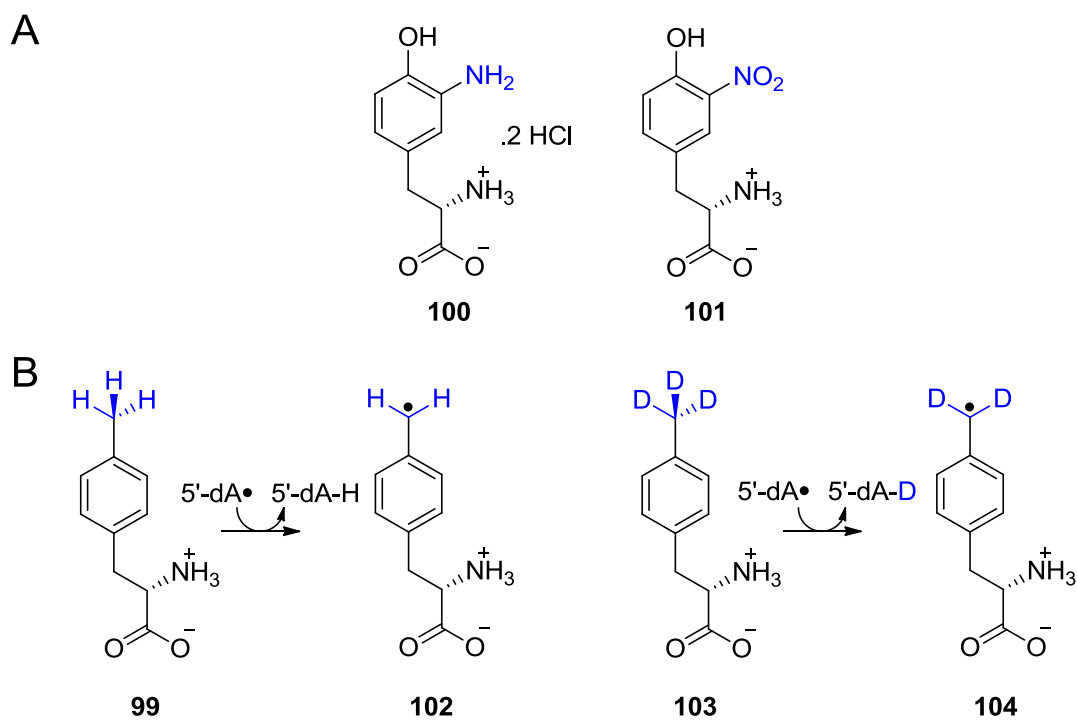
(A) Newman projection along the L-tyrosyl radical N-C α bond highlighting an antiperiplanar alignment of the N-lone pair with the phenolic π -cloud.

(B) Hypothetical arrangement of the developing L-tyrosyl radical in the ThiH active site to allow N-lone pair donation into the C α -C β σ^* bond. Red dotted lines represent potential H-bonding and π - π interactions with an arginine and tyrosine side chain, respectively. Adapted from Challand²⁰⁰.

In the absence of X-ray crystal structures for the ThiH and/or HydG enzyme, it is difficult to investigate the hypothesis by Pilet and co-workers that both enzymes may share conserved active site amino acid residues for L-tyrosine binding³³. Some insight may however be gained by comparing the structures of the tyrosine analogues which stimulated ThiH catalysed AdoMet cleavage with the analogues which stimulate HydG catalysed AdoMet cleavage. Reconstituted and reduced WT HydG (25 μ M) was therefore incubated with AdoMet (1 mM) and the individual tyrosine analogues (1 mM) shown in Scheme 3.7 and Scheme 3.9 A (Method 22). All assays were analysed for 5'-dAH and an aromatic by-product derived from AdoMet and tyrosine analogue C α -C β bond cleavage, respectively. Only **91** and **100** observably stimulated reductive AdoMet cleavage (Table 3.6), but the respective aromatic cleavage products *p*-cresol and 2-amino-*p*-cresol could not be detected. Taking into account the small amounts of 5'-dAH formed in the absence of substrate, only approximately 4% of 5'-dAH was formed in the presence of these analogues (**91**, **100**) with respect to 5'-dAH formation with L-tyrosine. This is in contrast to the observations with ThiH¹³⁰, but may indicate that HydG adopts a 'more defined' active site, in which additional interactions must be satisfied before AdoMet cleavage can occur.

None of the tyrosine analogues substituted at the phenolic position supported AdoMet cleavage, in agreement with the hypothesis that the phenolic hydroxyl group is the site for hydrogen atom abstraction¹³⁰. The outcome with *p*-methyl-L-phenylalanine **99** was of particular interest due to the decreased bond dissociation energy of a benzylic C-H (355 kJ/mol) compared to a phenolic O-H bond (364 kJ/mol). This theoretically increases the feasibility of hydrogen atom abstraction from the methyl group by 5'-dA•. If 5'-dAH were formed with **99**, the analogue deuterated at the methyl position

(103) could easily be investigated to confirm the ‘methyl group’ as the hydrogen abstraction site by detection of deuterated 5'-dAD (Scheme 3.9 B).



Scheme 3.9 Additional tyrosine analogues investigated as HydG substrates.

Table 3.6 HydG dependent AdoMet cleavage in the presence of tyrosine analogues.

Unproductive AdoMet cleavage was quantified as the formation of 5'-dAH and is stated (in decreasing order) as relative percentages to 5'-dAH formed in the presence of L-tyrosine. Assays were carried out in duplicate with less than 0.04% standard deviation.

Substrate analogue	AdoMet cleavage (%)
L-Tyrosine, 3	100.0
3-Amino-L-tyrosine, 100	5.6
<i>p</i> -Hydroxyphenyl- α -hydroxypropionic acid, 91	5.3
<i>p</i> -Hydroxyphenylpropionic acid, 92	1.9
<i>p</i> -Tyramine, 94	1.6
D-Tyrosine, 95	1.3
L-Phenylalanine, 96	1.3
<i>p</i> -Methyl-L-phenylalanine, 99	1.2
Negative (no L-tyrosine)	1.2
<i>p</i> -Amino-L-phenylalanine, 97	1.1
3-Nitro-L-tyrosine, 101^a	0.3
<i>p</i> -Fluoro-L-phenylalanine, 98^a	0.1

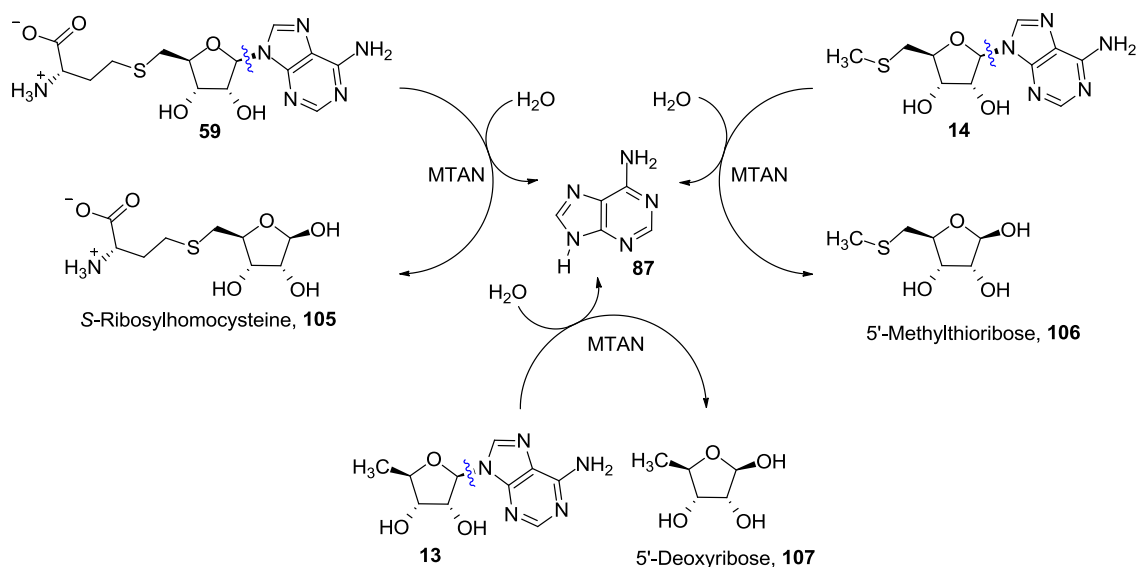
a - These analogues co-eluted with 5'-dAH during HPLC analyses and 5'-dAH formation was instead assessed as adenine formation in the presence of 5'-methylthioadenosine nucleosidase as discussed in the text.

Substitution of L-tyrosine **3** with the D-tyrosine enantiomer **95** did not result in HydG catalysed AdoMet cleavage, suggesting strong stereoselective recognition of the L-tyrosine substrate. This observation is in contrast to

findings by Kuchenreuther and co-workers which showed that D-tyrosine **95** supported *in vitro* activation of *C. pasteurianum* HydA in assays additionally containing a desalted Δ iscR *E. coli* lysate and the purified maturation enzymes HydE, HydF and HydG³⁶. Possible explanations for the apparent HydG activity in the absence of L-tyrosine include that L-tyrosine was not successfully removed from the *E. coli* lysate. This is in fact very likely as Kuchenreuther and co-workers used a PD-10 column for the desalting step, which was shown in section 2.3 to have poor separation efficiency for complete exclusion of the small molecule fraction from the proteins. Alternatively, L-tyrosine may have co-purified with HydG or the presence of the other maturation enzymes selectively 'pressurised' HydG into accepting D-tyrosine **95** as a substrate.

The analogues 3-nitro-L-tyrosine **101** and *p*-fluoro-L-phenylalanine **98** co-eluted with 5'-dAH during HPLC analyses of the assay supernatants, which made accurate 5'-dAH quantification impossible. To nevertheless determine any uncoupled AdoMet cleavage supported by these analogues, the activity assays were repeated in the presence of 5'-methylthioadenosine/*S*-adenosyl-L-homocysteine nucleosidase (MTAN, EC 3.2.2.9). MTAN rapidly cleaves the β -glycosidic bond of adenine derivatives such as AdoHcy **59**, 5'-dAH **13** and MTA **14** to release adenine **87** and the respective ribose^{201,202} (Scheme 3.10). In the presence of MTAN, any *in situ* formed 5'-dAH will be hydrolysed and can thus be quantified as adenine. However, due to the broad substrate specificity of MTAN, any AdoHcy **59** or MTA **14** impurities present in commercial AdoMet preparations would also result in adenine formation. As a consequence, it was imperative to also analyse assays only containing AdoMet. However, the amount of adenine released by AdoMet samples was similar to the adenine quantities detected in assays containing the tyrosine analogues **98** and **101**, suggesting that no uncoupled AdoMet cleavage occurred.

Chapter 3 – Kinetics



Scheme 3.10 Action of 5'-methylthioadenosine nucleosidase.

MTAN catalyses the hydrolysis of β -glycosidic bonds.

3.6.2 HydG catalysed *p*-cresol formation is pH dependent

A nearly 20% decrease in tyrosine cleavage activity was observed for WT HydG in the presence of 250 μ M AdoMet compared to 50 μ M AdoMet (section 3.4.3, Figure 3.11 A). In addition, the former assays were approximately 0.4 pH units more acidic than the latter, suggesting a pH dependent *p*-cresol formation activity by WT HydG. To test this hypothesis, activity assays with an overall pH of 6.90, 7.23 and 7.81 were carried out with WT HydG (20 μ M), AdoMet (0.5 mM), tyrosine (1 mM) and sodium dithionite (1 mM) (Method 23).

Interestingly, the turnover number for *p*-cresol formation (Figure 3.13) increased from $(8.4 \pm 1.3) \times 10^{-4} \text{ s}^{-1}$ over $(17.0 \pm 1.0) \times 10^{-4} \text{ s}^{-1}$ to $(21.5 \pm 2.8) \times 10^{-4} \text{ s}^{-1}$ in pH 6.90, pH 7.23 and pH 7.81 assays, respectively. This nearly threefold activity enhancement over approximately 1 pH unit confirms that the observed decrease in WT HydG activity with increased AdoMet concentrations was likely due to a lowered assay pH. The demonstrated increase in *p*-cresol

formation at elevated pH may be due for a number of reasons. HydG may for example respond to pH with a change in the cluster I coordination environment, increasing the affinity for AdoMet and/or the rates of reductive AdoMet cleavage. This would be analogous to the [NiFe]-hydrogenase maturation enzyme HypA which undergoes ligand substitution at the intrinsic Zn binding site in response to pH changes²⁰³. Alternatively, the affinity for tyrosine may have been increased.

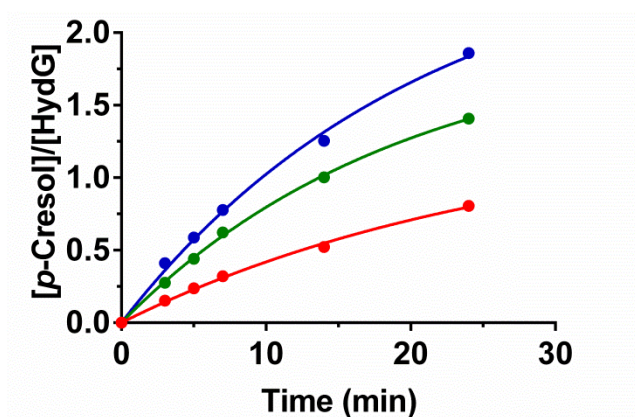


Figure 3.13 HydG catalysed *p*-cresol formation is pH dependent.

Formation of *p*-cresol at 37 °C as catalysed by WT HydG (20 μM) in 50 mM HEPES, 0.5 M KCl, pH 6.90 (—●—), 7.23 (—●—) or 7.81 (—●—) buffer additionally containing AdoMet (0.5 mM), tyrosine (1 mM) and sodium dithionite (1 mM). The data represent single assays fitted to first order kinetics (Equation 3.1). Note that the pH values reflect the final assay pH as measured using a calibrated (25 °C) pH electrode.

It is interesting to note that *p*-cresol formation by the two C-terminal HydG mutants may have been less strongly affected by the decreased assay pH (section 3.4.3, Figure 3.11 A), inferring that the ionisation state of a catalytic amino acid residue in the HydG C-terminus may have changed. Over the small pH range investigated, theoretically only the ionisation state of a histidine

Chapter 3 – Kinetics

residue (side chain $pK_a = 6.4^{204}$) could have been strongly affected, but no conserved histidine is present in the HydG C-terminus (Appendix 5). Bearing in mind the similar K_M^{AdoMet} values across all HydG variants (section 3.4.3, Table 3.3), inferring a similar environment for AdoMet binding, it is unlikely that the coordination of AdoMet was affected by the pH change as suggested earlier. The 5- and 35-fold decreased K_M^{TYR} values for C386S and Δ CTD HydG compared to WT HydG (Table 3.4) may suggest that the C-terminal HydG mutants would be less sensitive to potential ionisation state changes of the tyrosine substrate. However, it cannot be concluded that a functional group of tyrosine was titrated as the true pK_a of tyrosine and/or HydG active site residues may be perturbed due to the immediate protein environment²⁰⁴. Amino acid residues involved in reaction catalysis have for example been found with their side chain pK_a values shifted by an average of 2 pK_a units²⁰⁴. More interestingly, an extreme 4.7 pK_a unit decrease was observed for the ammonium moiety in 2-hydroxy-5-nitrobenzylacetoacetate decarboxylase **110** relative to the 'free' model compound *N*-methyl-2-hydroxy-5-nitrobenzylamine **108** ($pK_{aH} = 10.7$)²⁰⁵ (Figure 3.14). Similarly, the pK_a of the nitrophenolic hydroxyl group shifted from 5.9 in the model compound (**108**) to 2.4 when protein bound (**110**)²⁰⁶.

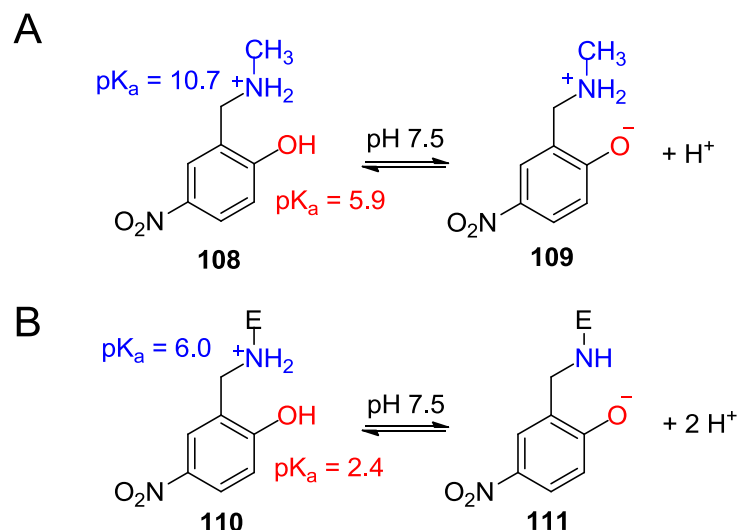


Figure 3.14 Differing pK_a values in an enzyme active site.

(A) Calculated pK_a values of a model *N*-methyl-2-hydroxy-5-nitrobenzylamine compound **108** compared to (B) measured pK_a values in 2-hydroxy-5-nitrobenzyl-acetoacetate decarboxylase **110**^{205,206}. The acetoacetate decarboxylase enzyme is represented by E.

The extreme changes in the acidity constants of acetoacetate decarboxylase amino acid residues were proposed to be due to one or more positively charged groups near the substrate binding site²⁰⁵. A similarly affected HydG active site could be envisioned to decrease the amino pK_{aH} of tyrosine in the HydG-substrate complex from 9.1 to as low as 7.0. This would ensure that a high proportion of anionic tyrosine is present at physiological pH. Possible mechanistic implications include that the N-lone pair is available for direct coordination to cluster II (Figure 2.11). This may result in an increased affinity for tyrosine and thus *p*-cresol formation rates. Alternatively, the availability of the N-lone pair allows electron donation into the tyrosine **3**/tyrosyl radical **32** $C\alpha-C\beta$ σ^* bond to initiate $C\alpha-C\beta$ bond cleavage. Overlap between the N-lone pair orbital and the $C\alpha-C\beta$ antibonding orbital can be

Chapter 3 – Kinetics

achieved in an antiperiplanar arrangement of the tyrosine amino group and the phenolic π -cloud as exemplified in Scheme 3.8.

The exact mechanistic details of pH dependent tyrosine cleavage cannot be inferred from this initial study, but the preliminary observations give scope for further investigations into the pH dependence of WT HydG k_{cat} and K_{M} values. From a plot of *p*-cresol turnover rates against pH, one can infer the pK_{a} of the catalytically important functional group, whereas the pH dependence of the $K_{\text{M}}^{\text{TYR}}$ constant would reflect the involvement of a titratable group during initial substrate binding¹⁵⁸. However, the identity of the important amino acid cannot readily be inferred from the determined pK_{a} value due to the likely effects of the enzyme active site environment on the true pK_{a} value as discussed above. As a result, this study of pH dependent tyrosine cleavage must be interpreted in concert with the available HydG crystal structure (section 4.9) to obtain mechanistic insight into tyrosine cleavage.

Given the current preparation of tyrosine in acidic then basic solution and the varying acidity of enzymatically synthesised AdoMet samples, extra care is required to prepare assays of known overall pH. Due to pK_{a} changes of biologically relevant buffering components with temperature¹⁵⁸, it is also advisable that the buffer pH be measured with a pH electrode calibrated at the assay temperature. This and further precautions have been reviewed in Chapter 7 in 'Enzymes: A practical introduction to structure, mechanism and data analysis'¹⁵⁸.

3.7 Summary and conclusions

Initial kinetic investigations of WT, C386S and Δ CTD HydG demonstrated respective 7- and 30-fold reduced *p*-cresol formation rates by the C-terminal HydG mutants compared to the WT enzyme. To elucidate whether these activity differences were due to decreased affinities of the HydG mutants for the AdoMet and/or tyrosine substrate(s), Michaelis–Menten constants needed to be determined. Due to the inhibitory impurities present in commercial AdoMet preparations, (*S,S*)-AdoMet was enzymatically synthesised and purified by cation exchange chromatography. Although the yield of the synthesis and purification procedure was very poor (5%), enough (*S,S*)-AdoMet for activity assays was obtained. To measure AdoMet and tyrosine dependent initial rates of *p*-cresol formation at low enzyme concentrations, the *p*-cresol quantification procedure employing UV–Vis spectroscopy was modified to exploit the fluorescence properties of *p*-cresol instead. Similarly small K_M^{AdoMet} values ranging from 2.6 μM to 17.4 μM were obtained for all HydG variants, which suggest that the affinity for AdoMet is not strongly affected by the C-terminal mutations. Relative to the K_M^{TYR} constant of 300 μM determined for WT HydG, the apparent affinity of the C386S and Δ CTD HydG enzymes for tyrosine was however 5- and 35-fold decreased, respectively. These differences compare very well to the reduced *p*-cresol formation by C386S and Δ CTD HydG mentioned above, suggesting that it was due to a lowered affinity for tyrosine.

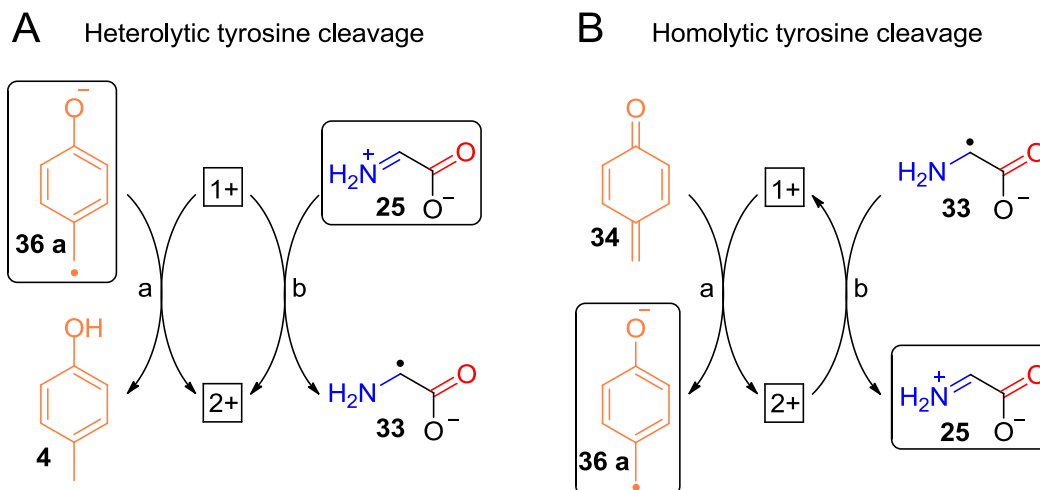
In light of the low 10–14% cluster II population in C386S HydG (section 2.4), the drop in apparent tyrosine affinity compared to WT HydG supports a significant role for the auxiliary [4Fe–4S] cluster in the recognition and/or binding of tyrosine. This function was recently also inferred by the observation

of coupled ^{13}C and ^{15}N features in the HYSORE spectrum of *Sh. oneidensis* WT HydG assays supplemented with ^{13}C , ^{15}N labelled tyrosine¹⁵⁹. The potential involvement of C-terminal residues in tyrosine binding may be inferred from the additional sevenfold affinity decrease of ΔCTD HydG for tyrosine compared to the C386S HydG mutant. The combined EPR and K_M studies of the *C. acetobutylicum* HydG variants are however not sufficient to unambiguously clarify the role of cluster II and C-terminal residues with regard to tyrosine binding.

After determination of the substrate Michaelis–Menten constants, activity assays with *C. acetobutylicum* WT, C386S and ΔCTD HydG were repeated using near saturating substrate concentrations. Bearing in mind that the ΔCTD HydG enzyme cannot totally be saturated with tyrosine due to experimental limitations (the solubility of tyrosine), the observed similarity in the amounts of *p*-cresol formed compared to partially inhibited WT HydG suggests that tyrosine cleavage to *p*-cresol can continue in a manner predominantly independent of the C-terminal domain. This is in accord with the proposal that HydG and ThiH catalysed tyrosine cleavage is initiated inside the TIM barrel³³. For *p*-cresol formation to occur in the absence of the auxiliary [4Fe–4S] cluster and C-terminal residues, some binding contacts to tyrosine must be established with TIM barrel amino acid residues.

In principle, tyrosine can be cleaved homolytically or heterolytically to form a C-centred glycine radical **33** or dehydroglycine **25**, respectively (Scheme 3.11). While formation of the glycine radical **33** is thermodynamically favoured¹²⁴, the in vitro observation that significant amounts of the dehydroglycine **25** hydrolysis product glyoxylate **35** are formed by the C386S and ΔCTD HydG mutants points towards heterolytic cleavage of tyrosine.

Under the reducing assay conditions employed, it appears unlikely that the alternative glycine radical **33** is oxidised to dehydroglycine **25**. Although auxiliary [4Fe–4S] clusters in radical AdoMet enzymes have been postulated to be involved in electron transfer reactions^{68,93} (section 1.2.4), a similar role of the HydG cluster II to catalyse the oxidation of **33** to **25** (Scheme 3.11 B, step b) is excluded on the grounds that cluster II is reduced under assay conditions (section 2.4). Formation of stoichiometric quantities of dehydroglycine **25** (detected as glyoxylate **35**) with respect to *p*-cresol **4** by the Δ CTD HydG mutant is also in agreement with the proposal that cluster II is not involved in electron transfer. Further experimental evidence for heterolytic tyrosine cleavage comes from the EPR characterisation of the *p*-oxidobenzyl radical **36 a** in *Sh. oneidensis* WT HydG assays¹⁵⁹. It can however currently not be excluded that cluster II may catalyse the reversible reduction of dehydroglycine **25** to the C-centred glycine radical **33** (Scheme 3.11 A, step b). Radical **33** could then collapse to cyanide and CO according to the mechanism proposed by Nicolet and co-workers¹³³ (Scheme 3.2). The beauty of this proposal is that the dehydroglycine to glycine radical interconversion leads to an oxidised [4Fe–4S]²⁺ cluster which is required for subsequent reaction with the proposed carbon dioxide radical **69** (Scheme 3.2 C).



Scheme 3.11 Electron transfer roles of the HydG auxiliary [4Fe-4S] cluster.

The reaction products from HydG catalysed (A) heterolytic or (B) homolytic tyrosine cleavage are depicted in the top row of each panel. Interconversion of these cleavage intermediates may require the presence of the HydG cluster II, which is depicted as a square with its corresponding oxidation state. The boxed *p*-oxidobenzoyl radical **36 a** has been directly characterised by EPR¹⁵⁹, while the boxed dehydroglycine intermediate **25** has been inferred by detection of its hydrolysis product glyoxylate **35**³⁴. (De)protonation events have been omitted for clarity.

The C386S HydG mutant was found to coordinate little cluster II and the observation that WT and C386S HydG catalysed cyanide formation with the same relative rates compared to *p*-cresol formation may imply that cluster II is not required for cyanide synthesis. Alternatively, the employed batch of WT HydG coordinated an equally small amount of cluster II. This hypothesis is not unlikely as the ability of WT HydG to form *p*-cresol and cyanide in stoichiometric quantities varied greatly between different batches of reconstituted protein. Firm conclusions regarding the involvement of cluster II

in cyanide formation can as a result not be drawn, unless parallel EPR or Mössbauer spectroscopic characterisations of the coordinated iron–sulfur clusters in the HydG variants are carried out. C-terminal amino acids however seem important for cyanide synthesis as the Δ CTD HydG enzyme formed 100 μ M *p*-cresol but negligible (if any) amounts of cyanide. The *Th. italicus* HydG crystal structure confirms that the unique iron of cluster II is not coordinated by a protein derived residue (section 4.9). As a result, this unique iron atom could ligate three ligands to attain a pseudo–octahedral coordination environment. Assuming that the cyanide and CO ligands coordinate to this iron before transfer to the scaffold maturase enzyme, WT HydG is expected to support formation of 1.5 mol equivalents of cyanide and CO. Less turnover is expected for the C386S HydG mutant because of its decreased cluster II content. While this hypothesis is supported by observation of HydG dependent, iron–sulfur cluster bound cyanide and CO ligands during stopped–flow FTIR investigations on *Sh. oneidensis* WT HydG activity assays^{159,207}, formation of 2.3 mol and 2.8 mol equivalents of cyanide by *C. acetobutylicum* WT and especially C386S HydG (after 60 min) argues against cyanide coordination to cluster II. Both observations would however be in agreement if a cyanide and CO bound auxiliary [4Fe–4S] or [2Fe–2S] cluster is lost during HydG turnover, followed by re–assembly for the next catalytic cycle. More mechanistic studies are required to investigate by which mechanism cyanide and CO are synthesised.

In light of the observation that radical AdoMet enzymes bind their substrates inside the TIM barrel⁶⁵ (section 1.2.2), *p*-cresol formation by Δ CTD HydG may support the hypothesis that HydG shares tyrosine binding residues with ThiH³³. To probe this proposal, HydG catalysed AdoMet cleavage in the presence of various tyrosine analogues has been monitored. For ThiH, the

analogues *p*-hydroxyphenyl- α -hydroxypropionic acid **91** and *p*-hydroxyphenylpropionic acid **92** supported AdoMet cleavage to 50% relative to using the natural substrate L-tyrosine¹³⁰. However, none of the tyrosine analogues investigated stimulated HydG dependent AdoMet cleavage to a significant extent, suggesting that tyrosine binding in HydG may be facilitated by different binding interactions relative to ThiH. This is supported by the *Th. italicus* HydG crystal structure and supplementing sequence alignments (Appendix 5), which highlight that some inward facing TIM barrel residues are conserved among HydG but not ThiH enzymes (discussed in section 4.9).

Preliminary investigations demonstrated that WT HydG catalysed tyrosine cleavage to *p*-cresol is pH dependent, with a nearly threefold enhanced *p*-cresol formation rate at pH 7.8 compared to assays at pH 6.9. More studies are however required to elucidate the cause for this activity increase. At the moment it cannot be distinguished whether a tyrosine functional group or a protein side chain may have been titrated. Based on modelling studies that an antiperiplanar arrangement of the tyrosine amino group to the phenolic π -cloud of the tyrosyl radical **32** elongates the C α -C β bond²⁰⁰, deprotonation of the ammonium functionality is intriguing as it would allow N-lone pair donation into the C α -C β antibonding orbital for heterolytic cleavage of this bond.

Chapter 4

Towards structural characterisation of HydG

4.1 Introduction

Crystallographic information of radical AdoMet enzymes in complex with their substrate(s) is an integral part of establishing reaction mechanisms at the molecular level as exemplified by the high resolution crystal structure of HydE and related QM/MM calculations to model reductive AdoMet cleavage⁵⁵ (see section 1.2.1). With regard to the mechanistic detail of HydG catalysed tyrosine cleavage, it is of particular interest to determine how tyrosine binds in the active site as no conclusive evidence for tyrosine binding to the auxiliary [4Fe-4S] cluster could be gained from EPR spectroscopic studies (Chapter 2). To shed light on the potential transfer of the cyanide and CO ligands from HydG to HydF, co-crystallisation of HydG with HydF would be highly advantageous.

Chapter 4 – Crystallography

Protein crystallisation may be achieved by the sitting or hanging drop vapour diffusion method²⁰⁸, where a protein solution is combined with a precipitant solution in a sealed chamber containing the mother liquor, the unmixed precipitant solution, as outlined in Figure 4.1. Water vapour diffusion from the protein–precipitant drop to the well solution increases the concentration of the protein–precipitant mix and the protein may become supersaturated. Provided nucleation can be achieved, macromolecular crystals may then grow²⁰⁸ (Figure 4.1 C). To improve the reproducibility between crystallisation trials, homogenous and stable protein samples are of great importance²⁰⁹.

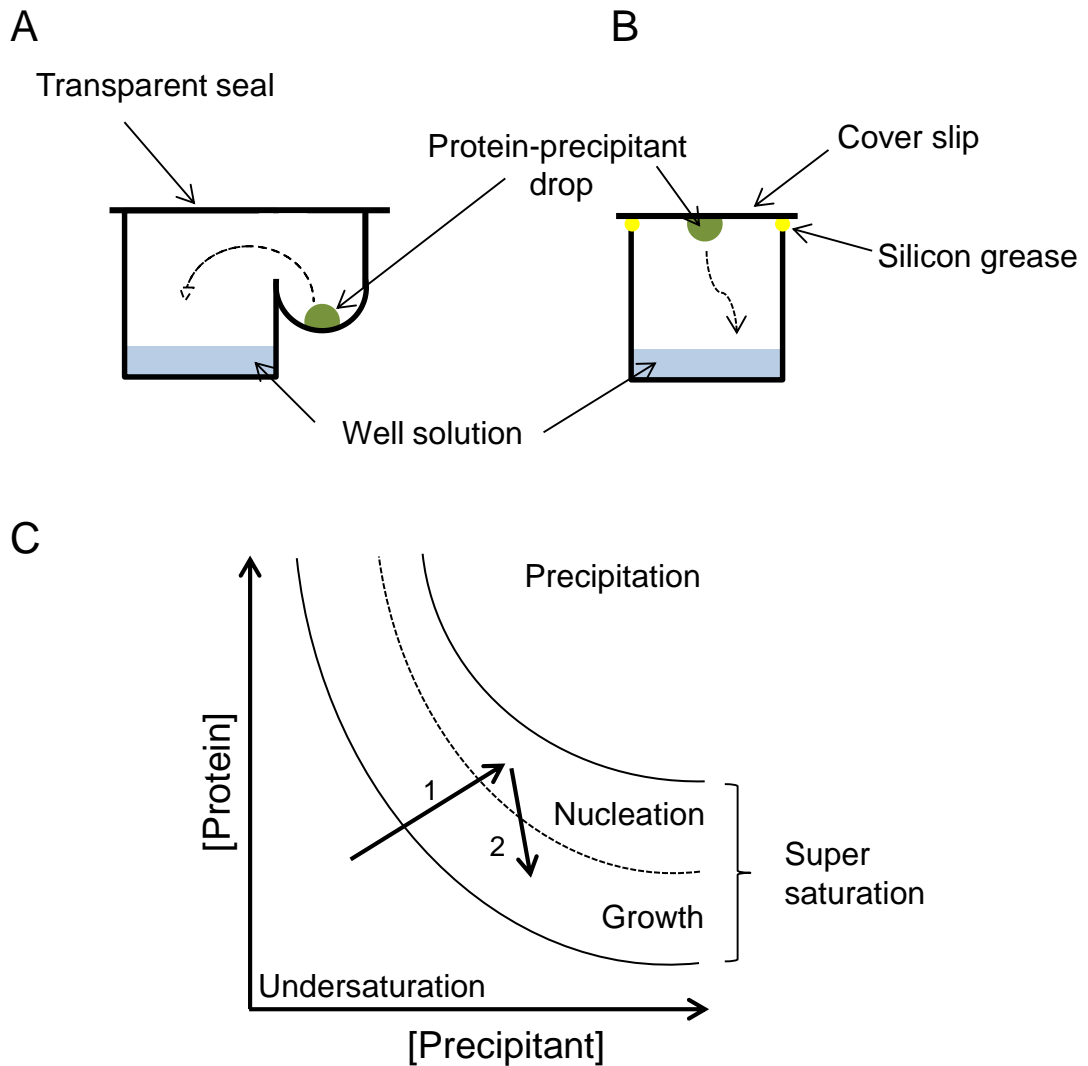


Figure 4.1 Principles of protein crystallisation by vapour diffusion.

Protein crystallisation relies on water vapour diffusion (dashed arrow) from (A) a sitting drop or (B) a hanging drop to the reservoir solution until equilibrium is attained. (C) Dehydration of the protein-precipitant drop decreases its size and leads to increased protein and precipitant concentrations (indicated by arrow 1), which may ultimately lead to nucleation. Any crystal formation and/or protein precipitation initially decreases the protein concentration (arrow 2) but further crystal growth may occur if still in the supersaturation zone. Adapted from Dessau et al.²⁰⁸ and Luft et al.²¹⁰.

4.2 Genetic context of *hydG*

Homogeneous protein solutions are a prerequisite for successful crystallisation experiments²⁰⁹. The extended time periods over which protein crystallisation may take place²¹⁰ could however lead to protein unfolding and degradation, ultimately decreasing the homogeneity of the solution. To increase the likelihood of protein crystallisation, thermostable proteins are therefore often employed. To identify suitable organisms harbouring *hydG*, a protein–protein blast search was carried out on the National Center for Biotechnology Information (NCBI) server using the protein sequence of *C. acetobutylicum* HydG (NP_347984.1) as a reference. Proteins from (hyper)thermophilic organisms with more than 50% similarity were thought suitable. Individual blast searches for the [FeFe]–hydrogenase HydA as well as the remaining maturation proteins were then carried out for the identified organisms using the *C. acetobutylicum* sequences listed in Table 4.1.

Table 4.1 *C. acetobutylicum* hydrogenase genes and protein references.

Protein name	Gene name	NCBI protein reference
HydA	CA_C0028	NP_346675.1
HydE	CA_C1631	NP_348258.1
HydF	CA_C1651	NP_348277.1
HydG	CA_C1356	NP_347984.1

A phylogenetic tree from the sequence alignment of the HydG proteins likely expressed with HydE, HydF and HydA was constructed and identifies two major subgroups, the thermophilic *Thermoanaerobacter* and the hyperthermophilic *Thermotoga* species (Figure 4.2). Surprisingly, HydG from *Thermotoga lettingae* TMO and *Thermotoga thermarum* DSM 5069 cluster separately.

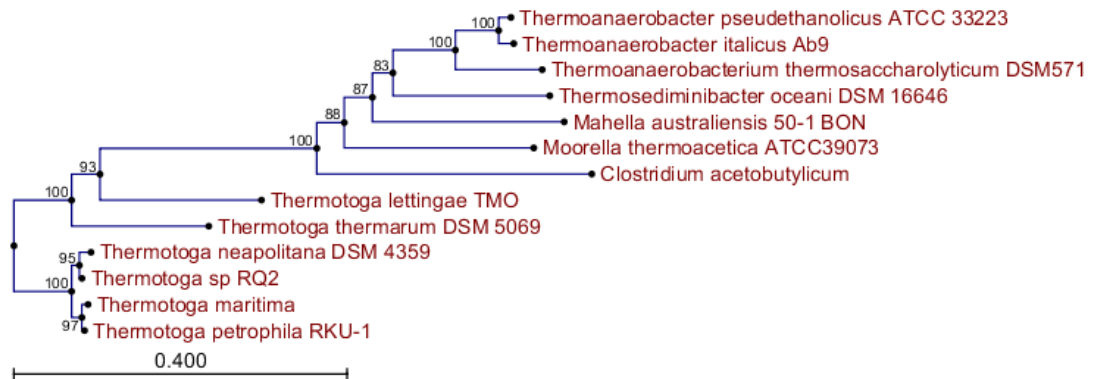


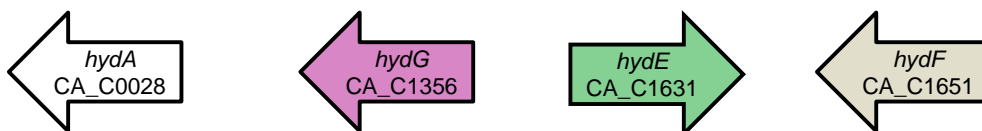
Figure 4.2 Phylogenetic tree based on primary sequences of HydG from different (hyper)thermophilic organisms.

The tree was generated using the CLC Sequence Viewer 6.5.4 software applying the Neighbor Joining algorithm. The numbers at each branch represent the bootstrap value of 100 replicates, while the branch length reflects the genetic change (number of substitutions/sequence length).

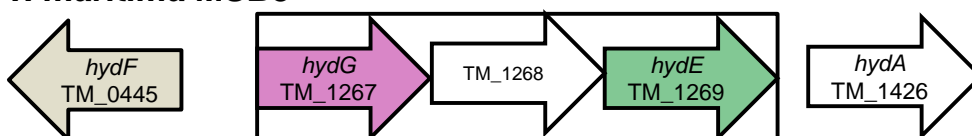
To increase the diversity of the HydG proteins for investigation in crystallisation studies, one organism of each subgroup was chosen. The genetic context of *hydG* in the selected organisms *T. maritima* MSB8, *Thermotoga lettingae* (*T. lettingae*) and *Th. italicus* Ab9 is shown in Figure 4.3 and highlights that the *hyd* maturation genes are not clustered together as one might expect based on the observation of fused *hydE-hydF*²² and *hydG-hydF*²⁸ genes in *Chl. reinhardtii* (CHLREDRAFT_128256) and *Laribacter*

hongkongensis HLHK9 (LHK_02327), respectively. Only the *hydE* and *hydG* genes in the selected *Thermotoga* species group together, separated by a gene encoding a ‘small hypothetical protein’. Blast searches were carried out with the aim of identifying these hypothetical proteins, but were unsuccessful.

***C. acetobutylicum* ATCC 824**



***T. maritima* MSB8**



***T. lettingae* TMO**



***Th. italicus* Ab 9**

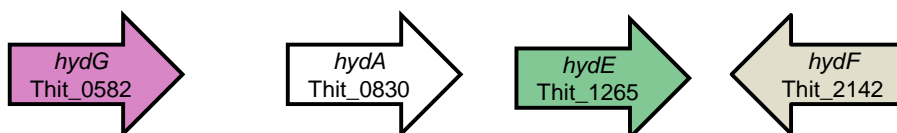


Figure 4.3 Genetic context of *hydG* from selected organisms.

Using the amino acid sequences of the *clostridial* hydrogenase proteins (Table 4.1), blast searches were carried out to identify their (hyper)thermophilic analogues. The genetic context of the associated genes in *T. maritima*, *T. lettingae* and *Th. italicus* is depicted schematically, with the NCBI reference for each gene clearly stated. The size of the arrows does not correlate with gene size and the spacing is arbitrary; only boxed genes are truly clustered.

4.3 Preparation of *hydG* expression plasmids

Filipa Martins previously attempted to express C-terminally 6His tagged *T. maritima* HydG (then thought to be ThiH) in *E. coli*²¹¹. To increase the in vivo assembly of the HydG iron-sulfur cluster, the *T. maritima* HydG encoding plasmid pFM103 (Appendix 2) also contains an *isc* operon for co-expression of *E. coli* iron-sulfur cluster assembly proteins. This plasmid was in turn based on the pFM024 plasmid expressing *Sulfolobus solfataricus* (*S. solfataricus*) LipA²¹¹. However, the obtained yield of cells was poor (1 g/L) and was attributed to the unfavourable codon bias of expressing a *T. maritima* gene in *E. coli* BL21(DE3)²¹¹. To improve expression levels, a related plasmid pRD004 was constructed which contained the codon optimised *T. maritima hydG* gene. Kuchenreuther and co-workers observed that a C-terminally Strep II tagged HydG protein did not function during activation of the [FeFe]-hydrogenase HydA³⁵, pointing to a role of the C-terminal domain in interacting with the maturation partners. With the aim to also crystallise HydG in the catalytically more active form, the plasmid pRD004 was further modified to encode an N-terminal instead of a C-terminal 6His tagged *T. maritima* HydG.

Plasmids encoding *hydG* from *T. lettingae* (pRD002) and *Th. italicus* (pRD003) were constructed similarly to the *T. maritima hydG* expressing plasmid pFM103²¹¹. Both target genes were however codon optimised for expression in *E. coli*¹² and additionally modified to encode an N-terminal 6His tag. Gene synthesis and subcloning into pFM024 between an NcoI and XhoI restriction site was carried out at Life Technologies. The prepared plasmids encoding *hydG* from three different (hyper)thermophilic organisms are summarised in Table 4.2. All plasmid maps and associated nucleotide and protein sequences can be found in Appendix 2.

Table 4.2 Prepared plasmids encoding *hydG*.

All listed plasmids are based on the pFM024 construct²¹¹, contain the target gene between an NcoI and XhoI restriction site and co-express the *isc* operon. Where indicated, genes have been codon optimised for expression in *E. coli*.

Plasmid	Organism	Gene ID	Codon optimised?	Protein ID	6His tag
pFM103	<i>T. maritima</i>	TM_1267	No	NP_229072.1	C-terminal
pRD002	<i>T. lettingae</i>	Tlet_1748	Yes	YP_001471366.1	N-terminal
pRD003	<i>Th. italicus</i>	Thit_0582	Yes	YP_003476445.1	N-terminal
pRD004	<i>T. maritima</i>	TM_1267	Yes	NP_229072.1	N-terminal

All plasmids were transformed into *E. coli* XL10 Gold cells (Method 2) and the presence of the *hydG* gene confirmed by analytical restriction digest (Method 4). As all plasmids are based on plasmid pFM024 and contain a gene of similar length, the restriction digests resulted in nearly identical agarose gels and only a representative analysis is shown in Figure 4.4.

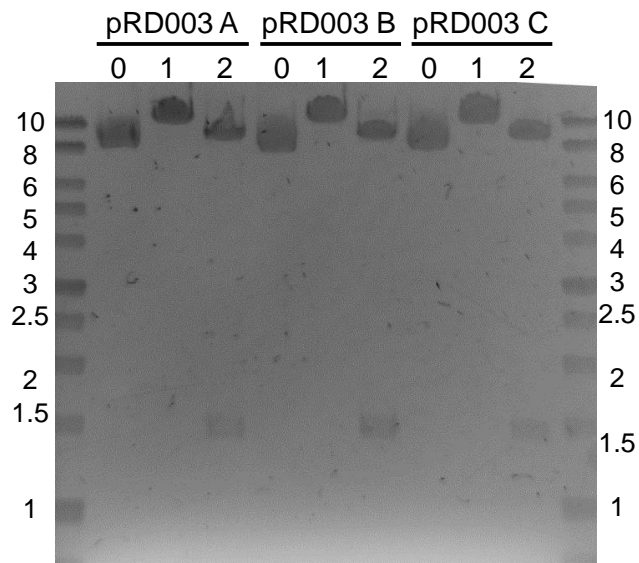


Figure 4.4 Analytical restriction digest of pRD003.

Representative 1% agarose gel of analytical restriction digest of plasmids from three distinct colonies A, B, C. Lanes 1, 11 – DNA ladder (kbp), 0 – unrestrictied plasmid, 1 – single digest with NcoI (linear plasmid – 10.2 kbp), 2 – double digest with NcoI and XhoI (*hydG* – 1.5 kbp, vector backbone – 8.7 kbp).

4.4 Expression and purification of *T. lettingae* HydG

The plasmid pRD002 was transformed into competent *E. coli* BL21(DE3) cells and expression of *T. lettingae* HydG was carried out using a similar method to that used for *C. acetobutylicum* HydG, with the exception that higher yields of soluble protein could be obtained by using a fermenter instead of Erlenmeyer flasks (Method 12). This might be due to the more anaerobic environment provided in the fermenter, which ensures the stability of the oxygen sensitive [4Fe–4S] clusters in HydG. In addition, no overnight incubation as routinely carried out with *C. acetobutylicum* HydG was required, a 4–6 h incubation period after induction was sufficient to give comparable yields of cell pastes (5–6 g/L). The cell paste and cleared lysate appeared dark grey compared to the light beige paste of *C. acetobutylicum* HydG. This may be attributed to expression of *T. lettingae* HydG with higher [4Fe–4S] cluster content and/or high expression of the iron–sulfur cluster containing ISC proteins.

4.4.1 Ni–Affinity purification of *T. lettingae* HydG

Purification of *T. lettingae* HydG was attempted by Ni–affinity chromatography (Figure 4.5, Method 15). To increase the recovery of protein available for crystallisation studies, cell culture experiments were carried out on a 5 L scale and cell pastes from two of these experiments (totalling ~50 g) were combined for purification. On average, 250 mg of protein was routinely purified, which contained two molecular weight impurities of approximately 28 kDa (Figure 4.5 B). These impurities correspond to approximately 30% of the isolated protein and were not observed with *C. acetobutylicum* HydG (Figure 2.3). Assuming negligible protein degradation, these impurities can be excluded to be the co–

expressed ISC proteins based on their molecular weights (Table 4.3). The impurities are less prominent in the lysate supernatant compared to the Ni-eluate, suggesting that they may indeed be HydG degradation products or proteins that tightly associate with *T. lettingae* HydG.

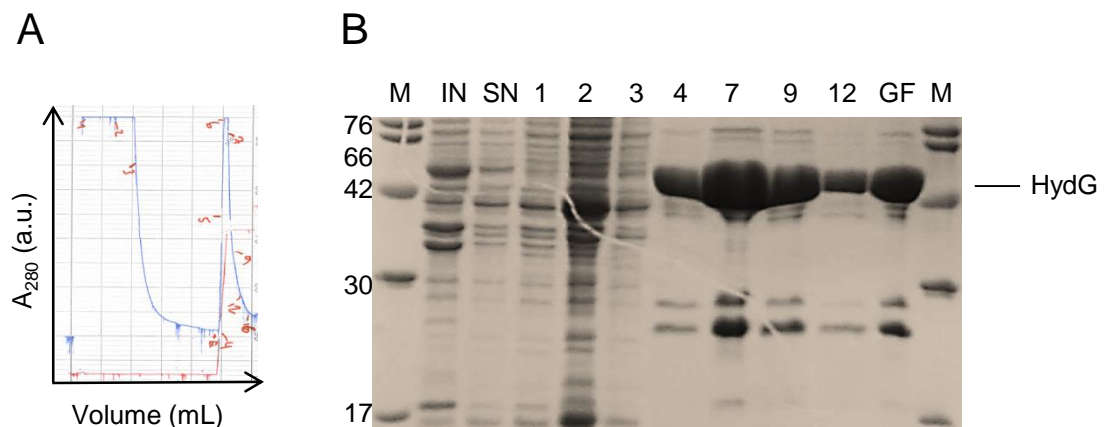


Figure 4.5 Ni-Affinity purification of *T. lettingae* HydG.

Representative (A) elution profile and (B) 15% SDS-PAGE analysis of HydG fractions eluted from a Ni-affinity column. M – molecular weight marker (kDa), IN – insoluble, SN – lysate supernatant, (1–3) – wash fractions, (4–12) – Ni fractions, GF – pooled fractions after buffer exchange by gel filtration chromatography.

Table 4.3 Molecular weights and isoelectric points of ISC proteins.

Protein	Molecular weight (kDa)	pI
HscA	65	5.05
IscS	46	6.04
HscB	20	5.05
IscU	14	4.82
IscA	12	4.75
Fdx	12	4.50

4.4.2 Superdex 75 gel filtration of *T. lettingae* HydG

The Ni-purified *T. lettingae* HydG fractions were buffer exchanged and reconstituted with 8 mol equivalents of iron and sulfide (Method 15). UV-Vis analyses confirmed previous observations that chemically reconstituted HydG shows an increased background absorbance above 500 nm (Figure 4.6 A, solid) compared to as-isolated proteins (Figure 4.6 A, dashed).

Work by Jenny E. Harmer on *S. solfataricus* LipA¹⁵² as well as by Lanz and co-workers¹⁵³ on the radical AdoMet enzymes RlmN and AtsB identified that iron and sulfide bound non-specifically to protein surface residues can trigger protein aggregation. As a consequence, the true amount of catalytically active protein as well as its [4Fe-4S] cluster content may be misjudged as discussed in section 2.3. Partial or complete removal of the aggregated protein can however be achieved by gel filtration chromatography using Superdex 75 or Superdex 200 resin^{152,153}.

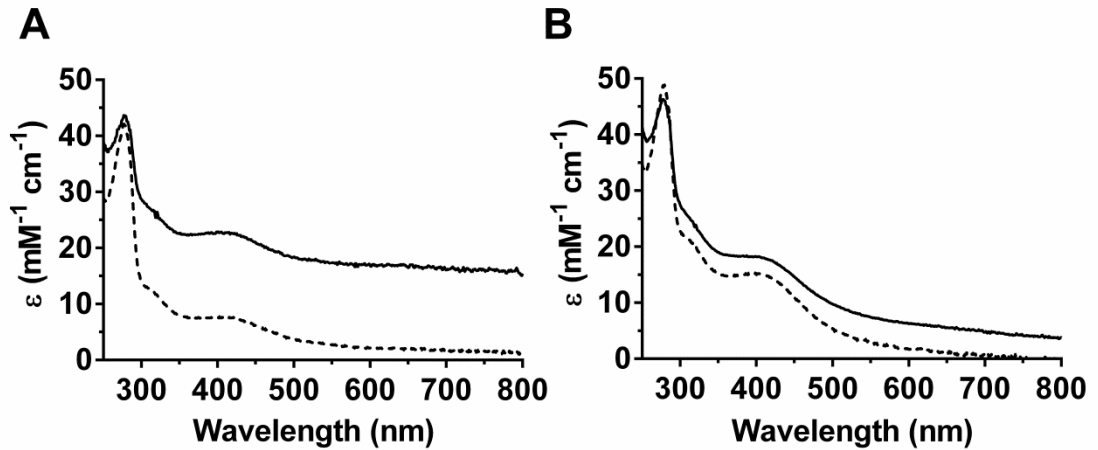


Figure 4.6 UV-Vis characterisation of *T. lettingae* HydG.

(A) As-isolated Ni-purified (---) and chemically reconstituted HydG (—).

(B) Respective Superdex 75 purified HydG before (---) and after the second reconstitution (—).

Ni-purified and reconstituted *T. lettingae* HydG (280 mg) was subjected to Superdex 75 gel filtration chromatography (Method 15), where the first eluting peak was black in colour while the second and proportionally larger peak was golden-green (Figure 4.7 A, B). SDS-PAGE analysis identified the 'black band' as HydG with one high and one low molecular weight impurity, while the 'golden band' corresponded mainly to HydG (Figure 4.7 C). Only 132 mg (47%) of *T. lettingae* HydG was recovered after gel filtration, but UV-Vis spectra confirmed the successful removal of iron-sulfur cluster aggregates by a levelled baseline at higher wavelengths (Figure 4.6 B, dashed). The calculated extinction coefficient at 400 nm suggests the presence of only one [4Fe-4S] cluster and to reconstitute both [4Fe-4S] clusters in *T. lettingae* HydG, the gel filtered protein was re-reconstituted with 5 mol equivalents of iron and sulfide. Only a minor improvement was observed in the UV-Vis spectrum

Chapter 4 – Crystallography

(Figure 4.6 B, solid) but the total amount of pure *T. lettingae* HydG was further reduced to 93 mg (33 %). The recovery of pure and reconstituted *T. lettingae* HydG varied greatly and sometimes as little as 20% was lost at the end of the twofold column/reconstitution protocol.

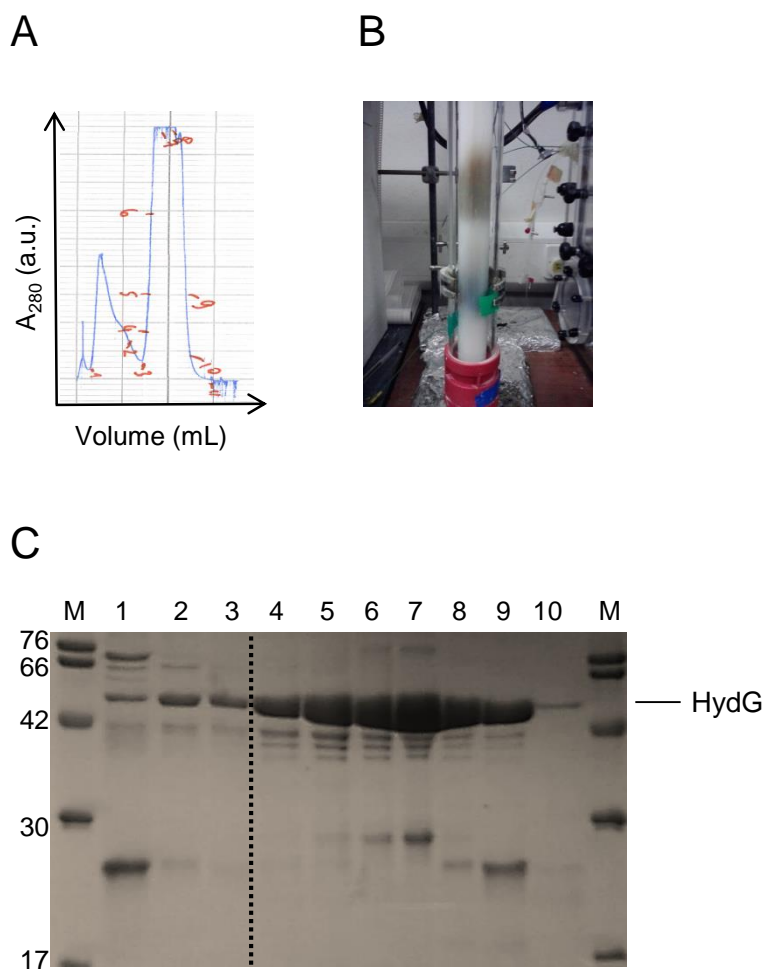


Figure 4.7 Gel filtration of *T. lettingae* HydG.

Representative (A) elution profile and (C) 15% SDS-PAGE analysis of protein fractions eluted from a Superdex 75 column. M – molecular weight marker (kDa), (1-3) – elution fractions corresponding to peak 1 in (A), (4-10) – elution fractions corresponding to peak 2 in (A). A picture of the band separation is shown in (B).

4.5 Expression and purification of *T. maritima* HydG

The N-terminally 6His tagged *T. maritima* HydG encoding plasmid pRD004 was transformed into competent *E. coli* BL21(DE3). The plasmid pFM103 containing C-terminally 6His tagged *T. maritima* HydG was however transformed into Rosetta(DE3)pLysS, a cell strain routinely used for expression of proteins which contain codons rarely used in *E. coli*¹³. Both *T. maritima* HydG variants were expressed in the fermenter (Method 12) and on average 6 g/L of dark grey cell paste was obtained. Protein purification was attempted by Ni-affinity chromatography similar to the procedure outlined for *T. lettingae* HydG. However, independent of the cell strain used, the yield of soluble N- or C-terminally 6His tagged *T. maritima* HydG was poor and small molecular weight impurities were present in near stoichiometric amounts as judged by SDS-PAGE analysis (Figure 4.8 B). This reduced the purity of *T. maritima* HydG to only 35%. As previously discussed for *T. lettingae* HydG, these impurities are unlikely to represent any of the ISC proteins.

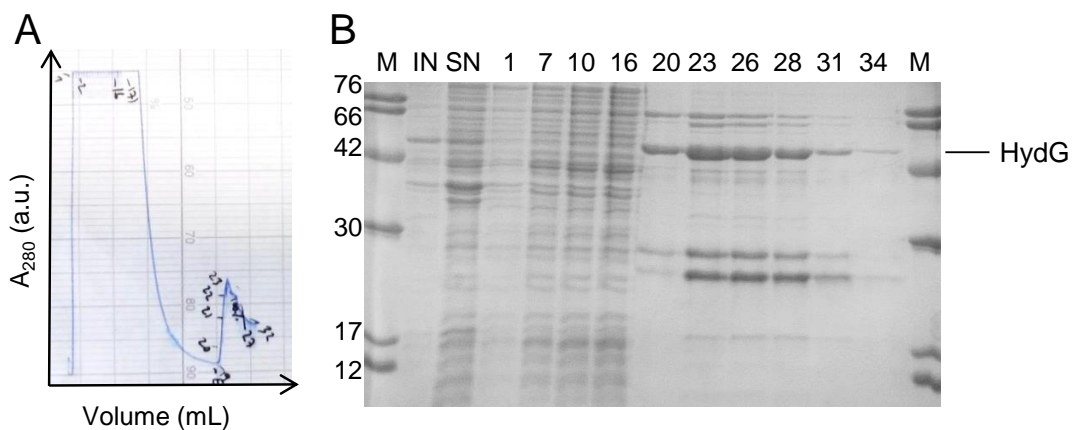


Figure 4.8 Ni-Affinity purification of C-terminally tagged *T. maritima* HydG.

Representative (A) elution profile and (B) 15% SDS-PAGE analysis of HydG fractions eluted from a Ni-affinity column. M – molecular weight marker (kDa), IN – insoluble, SN – lysate supernatant, (1–16) – wash, (20–34) – Ni fractions.

Chapter 4 – Crystallography

With the aim to decrease the amount of impurities in Ni-purified N- and C-terminally 6His tagged *T. maritima* HydG, cell lysates were heated at elevated temperatures ranging between 40 °C and 70 °C for 45 min.

Thermotoga maritima grows optimally at 80 °C and is therefore heat stable²¹⁴, while any *E. coli* proteins should unfold and precipitate at these temperatures. Although protein precipitation was observed during the heating step, SDS-PAGE analysis confirmed that none of the ~28 kDa impurities were removed (Figure 4.9). The identity of these apparently heat stable proteins remains to be established. A survey of heat insensitive *E. coli* proteins²¹⁵ indicates that, based on the molecular weight, only the elongation factor TS (30 kDa), FKBP-type peptidyl-prolyl cis-trans isomerase (29 kDa) or the histidine-binding periplasmic protein (28 kDa) are likely candidates. However, none of these can logically be associated with HydG expression.

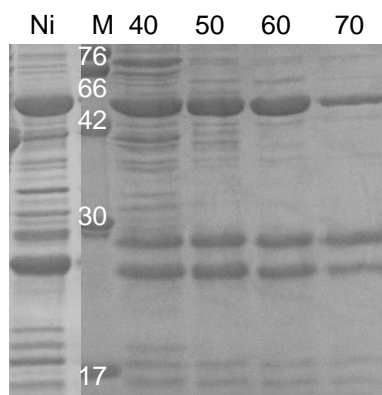


Figure 4.9 SDS-PAGE analysis of heat treated *T. maritima* HydG.

15% SDS-PAGE analysis of Ni-purified C-terminally 6His tagged HydG after anaerobic heat treatment at varying temperatures. Ni – Ni purified HydG fraction, M – molecular weight marker (kDa), numbers – temperature in °C.

4.5.1 Ion exchange chromatography of *T. maritima* HydG

It was attempted to further purify the above Ni-purified C-terminally 6His tagged *T. maritima* HydG fractions by ion exchange chromatography. This chromatography technique exploits the varying charge state (defined by the isoelectric point pI) of different proteins. Depending on the buffer pH, amino acid residues on the protein surface may be neutral, positively or negatively charged. The pI of C-terminally and N-terminally 6His tagged *T. maritima* HydG was calculated²¹⁶ to be 6.98 and 6.78, respectively.

One half of the Ni-purified *T. maritima* HydG fraction was exchanged into buffer containing 20 mM Tris, 5% (w/v) glycerol, 5 mM DTT at pH 8.3 before being applied to a strong anion exchange resin (Q-Sepharose). Protein elution was achieved by applying a gradient to 1 M NaCl (Method 16). While no proteins eluted during the washing step, two poorly resolved peaks eluted between 0.3 M and 0.5 M NaCl (Figure 4.10 A). The first band was golden brown in colour, while the second band was dark green to black. SDS-PAGE analysis identified that *T. maritima* HydG as well as the previously identified impurities corresponded to the earlier eluting band, the proteins eluting as the second peak were too dilute to be identified (Figure 4.10 B).

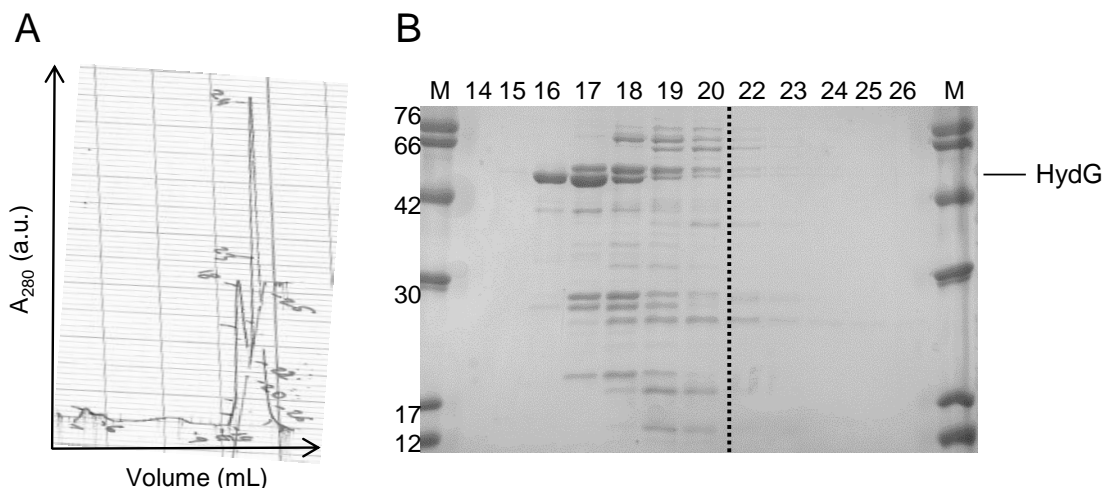


Figure 4.10 Anion exchange purification of C-terminally 6His tagged *T. maritima* HydG.

Representative (A) elution profile and (B) 15% SDS-PAGE analysis of HydG fractions eluted from a Q-Sepharose column. M - molecular weight marker (kDa), (14-20) - elution fractions corresponding to peak 1 in (A), (22-26) - elution fractions corresponding to peak 2 in (A).

As no satisfactory separation of C-terminally 6His tagged *T. maritima* HydG was achieved using the Q-Sepharose resin, a strong cation exchange resin (SP-Sepharose) was employed instead (Method 16). The other half of the Ni-purified *T. maritima* HydG fraction was loaded in 50 mM Mes, 5% (w/v) glycerol, 5 mM DTT, pH 6.0 buffer during which stage a dark green protein was separated (Figure 4.11 A). A protein of light green colour eluted between 0.5 M and 0.6 M NaCl which was identified by SDS-PAGE analysis as HydG. Because an impurity of very similar size to HydG was present in the loading sample, *p*-cresol formation was monitored with protein fractions from peak 1 and 2 in the presence of AdoMet, tyrosine and sodium dithionite (data not shown) to confirm that peak 2 corresponds to *T. maritima* HydG.

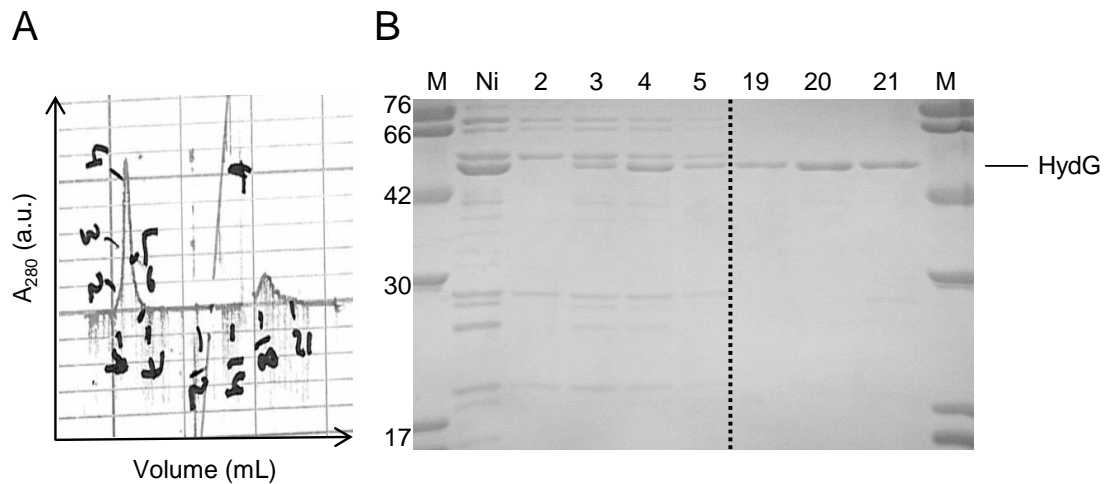


Figure 4.11 Cation exchange purification of C-terminally 6His tagged *T. maritima* HydG.

Representative (A) elution profile and (B) 15% SDS-PAGE analysis of HydG fractions eluted from an SP-Sepharose column. M – molecular weight marker (kDa), Ni – partially Ni-purified HydG, (2-5) – wash fractions corresponding to peak 1 in (A), (19-21) – elution fractions corresponding to peak 2 in (A).

Despite good separation of *T. maritima* HydG using cation exchange chromatography on this small scale, purification of HydG obtained from a 5 L growth was not successful. Only a small proportion of the lower molecular weight impurities could be removed (data not shown).

4.5.2 Superdex 75 gel filtration of *T. maritima* HydG

The discussed ~28 kDa impurities in Ni-purified *T. maritima* HydG were also present in Ni-purified *T. lettingae* HydG, albeit at lower concentrations. Similar to Superdex 75 gel filtration chromatography of *T. lettingae* HydG (section 4.4.2, Figure 4.7 C), chemically reconstituted *T. maritima* HydG was also gel filtered with the aim of removing further impurities. As observed with *T. lettingae* HydG, an earlier eluting black band was followed by a golden-green band, but this time the second peak was proportionally smaller compared to the first peak (Figure 4.12 A). Unfortunately, the purity of *T. maritima* HydG could not be greatly improved, only the high molecular weight impurities were removed completely (Figure 4.12 B). The observed almost inverse relationship between protein aggregate and chemically reconstituted *T. maritima* (Figure 4.12 A) compared to *T. lettingae* HydG (Figure 4.7 A) may account for the poor recovery of *T. maritima* HydG. Lanz and co-workers suggested that the extent of iron-sulfide aggregate associated with iron-sulfur cluster proteins is likely dependent on the amino acid sequence¹⁵³ but given the 69% sequence identity²¹⁷ between *T. lettingae* and *T. maritima* HydG, this hypothesis may not be true in this study.

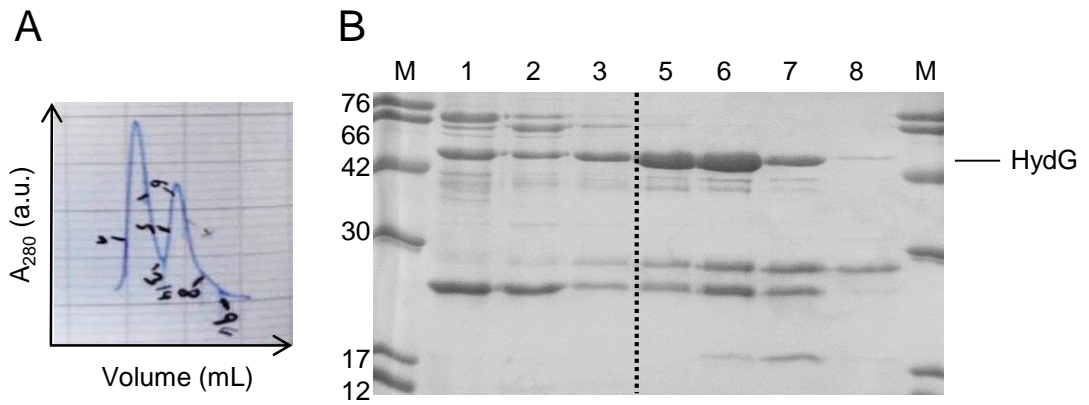


Figure 4.12 Gel filtration purification of C-terminally 6His tagged *T. maritima* HydG.

Representative (A) elution profile and (B) 15% SDS-PAGE analysis of HydG fractions eluted from a Superdex 75 gel filtration column. M – molecular weight marker (kDa), (1–3) – elution fractions corresponding to peak 1 in (A), (5–8) – elution fractions corresponding to peak 2 in (A).

4.6 Expression and purification of *Th. italicus* HydG

The plasmid pRD003 was transformed into *E. coli* BL21(DE3) cells and expression of *Th. italicus* HydG investigated on a small, 100 mL scale. SDS-PAGE analysis of the soluble portion of the cell lysate confirmed expression of *Th. italicus* HydG as a band around 55 kDa (Figure 4.13).

Further large scale manipulations of *Th. italicus* HydG similar to the procedure described for *T. lettingae* HydG (section 4.4) were carried out by Pedro C. Dinis.

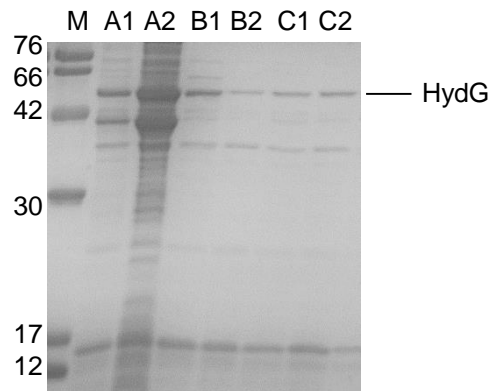


Figure 4.13 Small scale expression of *Th. italicus* HydG.

15% SDS-PAGE analysis of soluble cells obtained from pRD003 expression. M – molecular weight marker (kDa), letters – ‘name’ of plasmid obtained from *E. coli* XL10 Gold cells, numbers – distinct transformations into BL21(DE3).

4.7 Screening crystallisation conditions

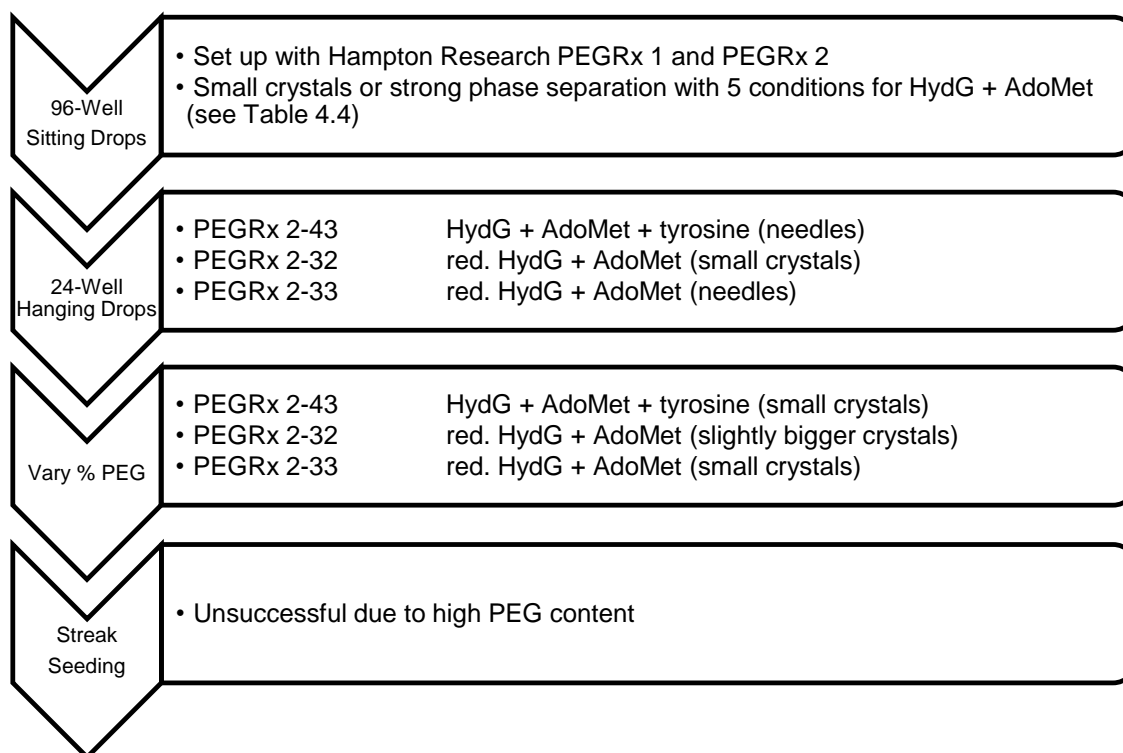
The aim of this project is to crystallise reduced or non-reduced *T. maritima* and *T. lettingae* HydG in the presence of AdoMet, tyrosine or AdoMet and tyrosine. In the presence of sodium dithionite (NaDT), AdoMet in HydG-AdoMet-tyrosine co-crystallisation trials was substituted with AdoHcy to prevent turnover of HydG. All crystal plates were manually set up inside an anaerobic glove box (see section 7.10) and visualised using a microscope mounted inside the glove box. The composition of all commercial and handmade screens used can be found in the electronic appendix.

4.7.1 C-terminally 6His tagged *T. maritima* HydG

Jenny E. Harmer and Pedro C. Dinis previously attempted to crystallise C-terminally 6His tagged *T. maritima* HydG in the presence of AdoMet using the Hampton Research PEGRx 1 and PEGRx 2 screens in sitting drops in 96-well plates. From this initial work, the conditions in Table 4.4 were identified to yield small crystals or strong phase separation. Efforts to reproduce and improve crystal growth are discussed below and summarised in Scheme 4.1. Using the previously identified conditions, 24-well plates with hanging drops containing reduced or non-reduced *T. maritima* HydG with AdoMet, tyrosine or AdoMet (AdoHcy under reducing conditions) and tyrosine were set up (Method 36). Only the conditions PEGRx 2-43 and PEGRx 2-33 yielded reproducible small needles for non-reduced *T. maritima* HydG with AdoMet and tyrosine, or reduced HydG with AdoMet, respectively as outlined in Table 4.5 A2, B2. Condition PEGRx 2-32 on the other hand promoted small crystal formation of reduced *T. maritima* HydG with AdoMet (Table 4.5 B1).

Table 4.4 Initial leads for crystallisation of *T. maritima* HydG with AdoMet.

Screen solution	Condition
PEGRx 1–27	0.1 M Bis–Tris propane pH 9.0, 10% (v/v) Jeffamine ED–2001 pH 7.0
PEGRx 1–47	0.1 M Imidazole pH 7, 12% (w/v) PEG 20000
PEGRx 2–32	0.2 M Na–formate, 0.1 M Bicine pH 8.5, 20% (w/v) PEG monomethyl ether 5000
PEGRx 2–33	4% (v/v) 2–Propanol, 0.1 M Bis–Tris propane pH 9, 20% (w/v) PEG monomethyl ether 5000
PEGRx 2–43	5% (v/v) (±)–2–Methyl–2,4–pentanediol, 0.1 M HEPES pH 7.5, 10% (w/v) PEG 10000



Scheme 4.1 Flow chart summarising the efforts to crystallise *T. maritima* HydG.

Table 4.5 Crystallisation of *T. maritima* HydG.

Crystallisation in 24-well plates was attempted using the vapour diffusion method with hanging drops (varying protein:mother liquor ratios are indicated in μL) and 0.5 mL mother liquor well solution. The period of crystal growth is indicated in days (d).

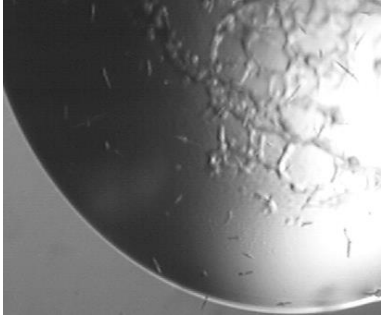
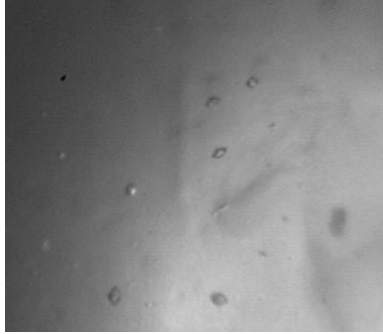
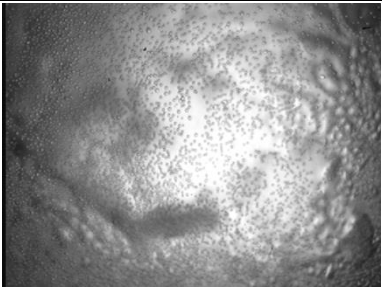
(A) Non-reducing 24-well screen	(A) Optimisation achieved?
<p>(1) </p> <p>1.4 mM HydG, 5 mM AdoMet, 3 mM tyrosine, (1:2), 35 d <u>PEGRx 2-33</u> 4% (v/v) 2-Propanol, 0.1 M Bis-Tris propane pH 9, 20% (w/v) PEG monomethyl ether 5000</p>	No
<p>(2) </p> <p>1.4 mM HydG, 5 mM AdoMet, 3 mM tyrosine, (1:2), 35 d <u>PEGRx 2-43</u> 5% (v/v) (\pm)-2-Methyl-2,4-pentanediol, 0.1 M HEPES pH 7.5, 10% (w/v) PEG 10000</p>	<p>(2') </p> <p>1.4 mM HydG, 5 mM AdoMet, 3 mM tyrosine, (2:1, 1:1, 1:2), 4 d <u>PEGRx 2-43</u> 5% (v/v) (\pm)-2-Methyl-2,4-pentanediol, 0.1 M HEPES pH 7.5, <u>15% or 20%</u> (w/v) PEG 10000</p>

Table 4.5 cont.

(B) Reducing 24-well screen	(B) Optimisation achieved?
<p>(1) </p> <p>1.6 mM HydG, 5 mM AdoMet, 1 mM NaDT, (1:1), 5 d <u>PEGRx 2-32</u> 0.2 M Na-formate, 0.1 M Bicine pH 8.5, 20% (w/v) PEG monomethyl ether 5000</p>	<p>(1') </p> <p>1.6 mM HydG, 5 mM AdoMet, 1 mM NaDT, (1:1), 21 d <u>PEGRx 2-32</u> 0.2 M Na-formate, 0.1 M Bicine pH 8.5, <u>30%</u> (w/v) PEG monomethyl ether 5000</p>
<p>(2) </p> <p>1.6 mM HydG, 5 mM AdoMet, 1 mM NaDT, (1:2), 35 d <u>PEGRx 2-33</u> 4% (v/v) 2-Propanol, 0.1 M Bis-Tris propane pH 9, 20% (w/v) PEG monomethyl ether 5000</p>	<p>(2') </p> <p>1.6 mM HydG, 5 mM AdoMet, 1 mM NaDT, (1:2), 12 d <u>PEGRx 2-33</u> 4% (v/v) 2-Propanol, 0.1 M Bis-Tris propane pH 9, <u>25%</u> (w/v) PEG monomethyl ether 5000</p>

To optimise the crystal growth from fine needles to macromolecular crystals, the percentage PEG of the screen solutions listed in Table 4.5 was varied between 5% and 30%. Over a three week period, non-reduced HydG in the presence of AdoMet and tyrosine yielded small dark crystals with a <10% PEG version of PEGRx 2-43, while a 15% or 20% 'derivative' led to crystal growth after 4 days (Table 4.5 A2'). These crystals were reproducible between

different batches of protein, but stayed very small. Streak seeding was difficult due to the high PEG content and despite providing nucleation points, only crystals of the same shape and size were formed (not shown, similar to Table 4.5 A2'). The crystals obtained of non-reduced HydG with AdoMet and tyrosine using modified PEGRx 2-43 (Table 4.5 A2') were dipped into 75% glycerol as a cryoprotectant, then flash frozen in liquid N₂ and subjected to synchrotron radiation on the Microfocus MX beamline I24 (Figure 4.14). Unfortunately, the crystals did not diffract.

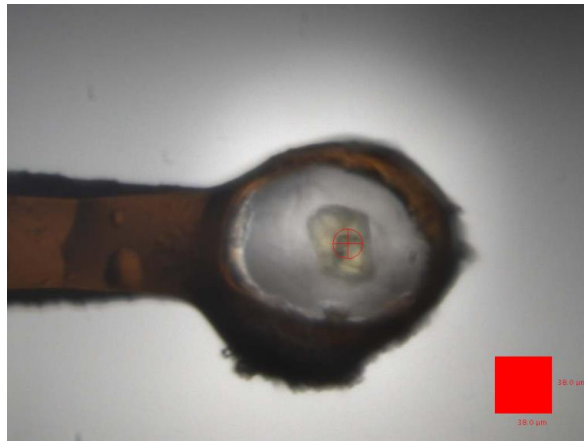


Figure 4.14 Small crystal of non-reduced C-terminally 6His tagged *T. maritima* HydG with AdoMet and tyrosine.

Crystal of non-reduced HydG with AdoMet and tyrosine, dipped into 75% glycerol before being flash frozen in liquid N₂. Loop size – 0.05–0.1 mm, beam size – 20 x 20 μm. Crystals were obtained by vapour diffusion using hanging drops of a protein–substrate mix (1.4 mM HydG, 5 mM AdoMet, 3 mM tyrosine) with modified PEGRx 2-43 (5% (v/v) (±)-2-methyl-2,4-pentanediol, 0.1 M Hepes pH 7.5, 20% (w/v) PEG 10000) mother liquor (2:1, 3 μL total) in a sealed 24-well plate with 0.5 mL well solution.

Chapter 4 – Crystallography

Slightly varying the percentage PEG in the PEGRx 2–32 and PEGRx 2–33 screen solutions also resulted in small and reproducible crystals of reduced *T. maritima* HydG with AdoMet (Table 4.5 B1', B2'). Similar to efforts with PEGRx 2–43 however, crystal growth could not further be improved by streak or direct seeding experiments due to the high PEG content.

The PACT Premier (PP) MD1–29 crystallisation suite from Molecular Dimensions was also screened in a 96–well (sitting drop) format due to the lack of further improvements with the hits from the PEGRx screens. This particular suite screens the pH in different PEG/ion environments, while the previously used PEGRx suit only provided a test for PEGs of differing length. However, no additional leads could be identified and further resources were instead focussed on crystallisation of *T. lettingae* HydG because of its higher purification yield and purity (sections 4.4, 4.5) compared to *T. maritima* HydG, suggesting it may be a better candidate for successful crystallisation.

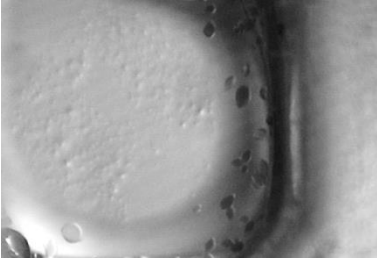
4.7.2 N-terminally 6His tagged *T. lettingae* HydG

Crystallisation of *T. lettingae* HydG was not previously attempted and initial screens were carried out in 96-well plates using the sitting drop vapour diffusion method with commercial Hampton Research PEGRx 1 and PEGRx 2 or Molecular Dimensions PACT Premier MD1–29 screens (Method 36). The following tables summarise initial hits and further crystal growth optimisation studies for reduced and non-reduced *T. lettingae* HydG in the presence of AdoMet (Table 4.6), tyrosine (Table 4.7) or AdoMet and tyrosine (Table 4.9). No crystalline features were observed for reduced *T. lettingae* HydG with AdoHcy and tyrosine.

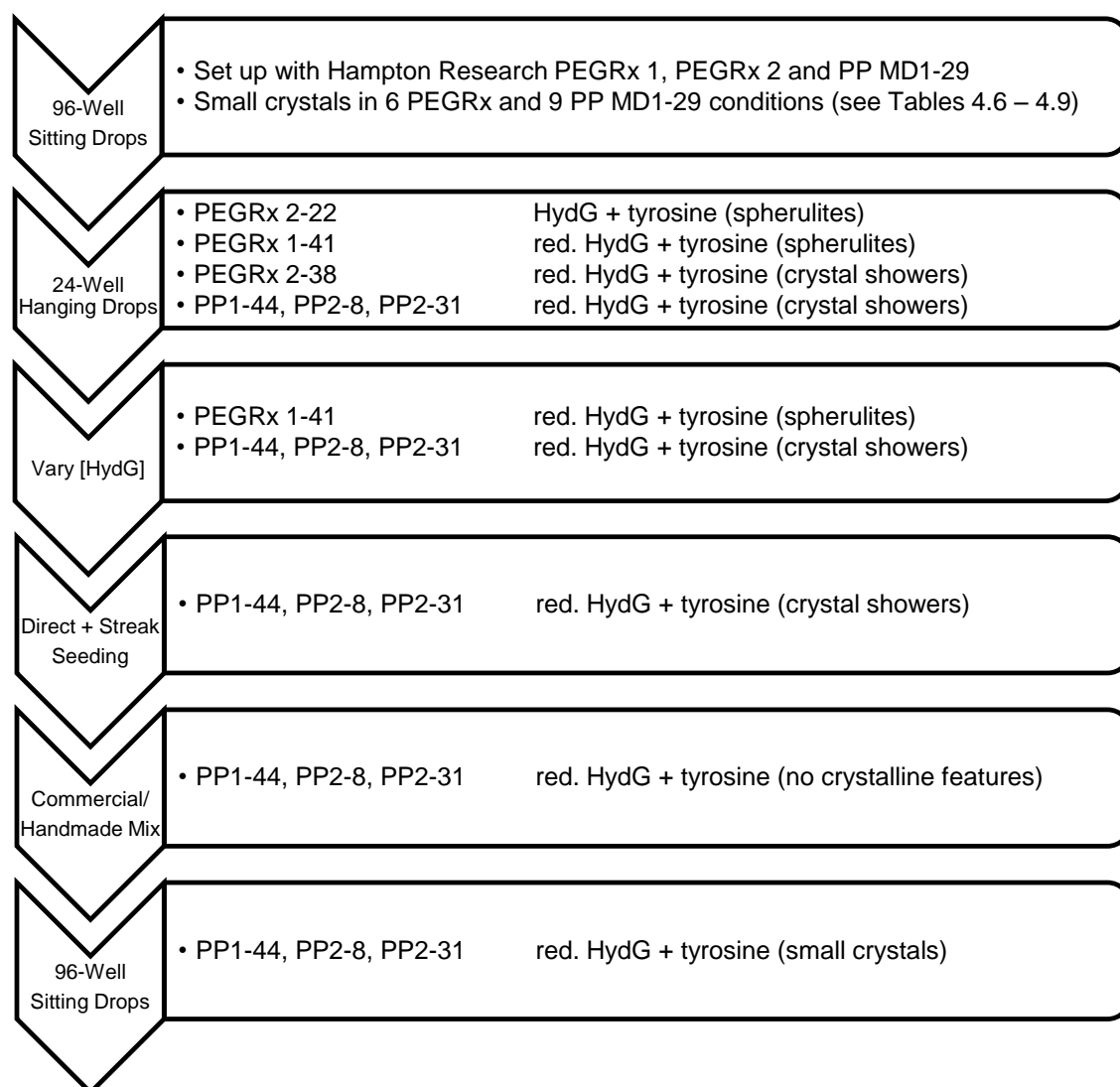
The conditions PEGRx 2–23 and PEGRx 2–36 were initially identified to aid crystallisation of non-reduced and reduced *T. lettingae* HydG with AdoMet, respectively (Table 4.6), but could unfortunately not be reproduced in a 96-well or 24-well format using commercial or handmade screen solutions. Furthermore, the instability of the ‘petal-like’ crystals obtained with PEGRx 2–23 prevented their analysis by synchrotron radiation.

Table 4.6 Crystallisation of *T. lettingae* HydG with AdoMet.

Crystallisation by vapour diffusion was attempted in 96-well plates with sitting drops (1:1 protein:mother liquor, 2 µL total) and 50 µL mother liquor well solution. Indicated concentrations refer to the individual protein and mother liquor solutions, not the final concentrations in the sitting drop. The period of crystal growth is indicated in days (d).

(A) Non-reducing 96-well screen	(A) Reproducible in 24-well format?
(1)	No
	
<p>0.95 mM HydG, 10 mM AdoMet, 18 d <u>PEGRx 2-23</u> 4.0 M K-formate, 0.1 M Bis-Tris propane pH 9.0, 2% PEG monomethyl ether 2000</p>	
(B) Reducing 96-well screen	(B) Reproducible in 24-well format?
(1)	No
	
<p>0.94 mM HydG, 10 mM AdoMet, 2 mM NaDT, 18 d <u>PEGRx 2-36</u> 10% (v/v) 2-Propanol, 0.1 M NaOAc.3H₂O pH 4.0, 22% PEG 6000</p>	

Crystallisation of *T. lettingae* HydG in the presence of tyrosine was more promising as spherulites and small crystals were observed in reducing and non-reducing environments (Table 4.7). Interestingly, nine conditions from the PACT Premier screen resulted in green-brown protein crystals, which were either hexagonal or diamond shaped as shown in Table 4.7 B3, B4 and summarised in Table 4.8. Efforts to reproduce and improve these crystalline features are discussed below and summarised in Scheme 4.2.



Scheme 4.2 Flow chart summarising the efforts to crystallise *T. lettingae* HydG.

Chapter 4 – Crystallography

The observed spherulites could be reproduced in a 24-well format (Method 37) using hanging drops and handmade screen solutions (Table 4.7 A1', B1'). The reduced protein crystals obtained with PEGRx 2-38, PP1-44, PP2-8 and PP2-31 could also somewhat be replicated (Table 4.7 B2', B4'), but independent of using commercial or handmade screen solutions, only showers of crystals were obtained. This was evidence for too many nucleation sites and too little crystal growth. With the aim to separate nucleation from growth²¹⁸, drops with three different HydG concentrations (0.45 mM, 0.75 mM, 1.3 mM) were prepared in the PP1-44, PP2-8 and PP2-31 matrices. Screen solution PEGRx 1-41 was also included with the goal to identify conditions where crystals instead of spherulites would be formed. Although no strong improvements were achieved, it was observed that, independent of HydG concentration, spherulites always formed in protein:PEGRx 1-41 1:2 drops. Crystal showers formed with any of the three PACT Premier solutions in the 1:1 and 2:1 drops. There was no relationship between HydG concentration and the size of the crystal shower.

Direct as well as streak seeding experiments were then carried out with the crystal showers obtained with PP1-44, PP2-8 and PP2-31 solutions (Method 38), but even with up to a millionfold dilution of seed stocks, only similar crystal showers were obtained.

It was furthermore attempted to set up hanging protein drops (in 24-well format) with commercial PP1-44, PP2-8 and PP2-31 screen solutions and respective handmade well solutions, but no crystalline features were observed.

However, by setting up 96-well crystal plates with the above commercial screen solutions (PP1-44, PP2-8, PP2-31), crystals, albeit a little smaller formed (not shown, similar to Table 4.7 B3, B4).

Table 4.7 Crystallisation of *T. lettingae* HydG with tyrosine.

Crystallisation by vapour diffusion was attempted in 96-well plates with sitting drops (1:1 protein:mother liquor, 2 μ L total) and 50 μ L mother liquor well solution while crystallisation in 24-well plates was attempted using hanging drops (varying protein:mother liquor ratios are indicated in μ L) and 0.5 mL mother liquor well solution. Indicated concentrations refer to the individual protein and mother liquor solutions, not the final concentrations in the drop. A different batch of protein and non-commercial screen solutions were employed for 24-well crystallisation trials unless otherwise stated. The period of crystal growth is indicated in days (d).

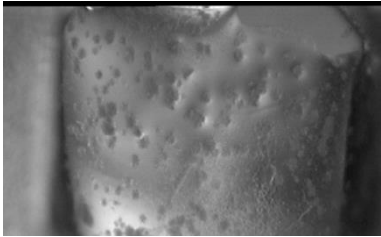
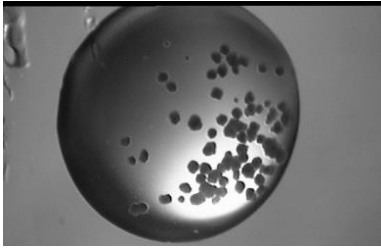
(A) Non-reducing 96-well screen	(A) Reproducible in 24-well format?
<p>(1) </p> <p>0.9 mM HydG, 3 mM tyrosine, 22 d <u>PEGRx 2-22</u> 0.2 M NH₄-citrate tribasic pH 7.0, 0.1 M Imidazole pH 7.0, 20% PEG monomethyl ether 2000</p>	<p>(1') </p> <p>0.4 mM HydG, 3 mM tyrosine, (1:1), 3d <u>Modified PEGRx 2-22</u> 0.2 M Na-citrate pH 7.0, 0.1 M Imidazole pH 7.0, 20% PEG monomethyl ether 2000</p>
<p>(2) </p> <p>0.9 mM HydG, 3 mM tyrosine, 14 d <u>PPI-44</u> 0.2 M NH₄Cl, 0.1 M Tris pH 8, 20% PEG 6000</p>	No

Table 4.7 cont.

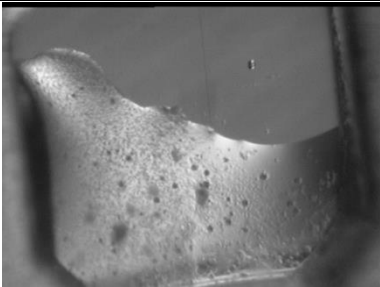
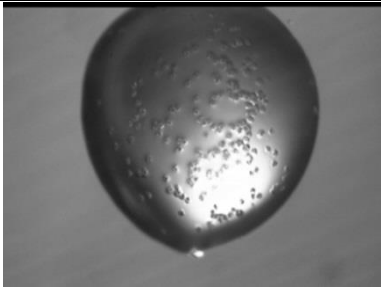
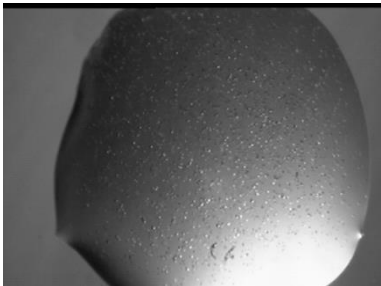
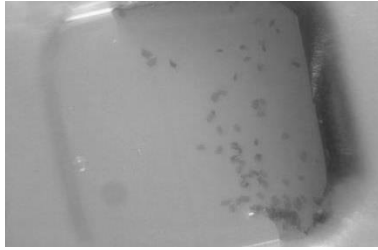
(B) Reducing 96-well screen	(B) Reproducible in 24-well format?
(1)	(1')
	
<p>0.8 mM HydG, 3 mM tyrosine, 2 mM NaDT, 12 d</p>	<p>1.1 mM HydG, 3 mM tyrosine, 2 mM NaDT, (1:1), 1 d</p>
<p><u>PEGRx 1-41</u></p>	<p><u>PEGRx 1-41</u></p>
<p>0.1 M Na-citrate tribasic.2H₂O pH 5.5, 16% PEG 8000</p>	<p>0.1 M Na-citrate tribasic.2H₂O pH 5.5, 16% PEG 8000</p>
(2)	(2')
	
<p>0.8 mM HydG, 3 mM tyrosine, 2 mM NaDT, 12 d</p>	<p>1.1 mM HydG, 3 mM tyrosine, 2 mM NaDT, (1:2), 3 d</p>
<p><u>PEGRx 2-38</u></p>	<p><u>PEGRx 2-38</u></p>
<p>20% (v/v) 2-Propanol, 0.1 M Tris pH 8.0, 5% PEG 8000</p>	<p>20% (v/v) 2-Propanol, 0.1 M Tris pH 8.0, 5% PEG 8000</p>

Table 4.7 cont.

(3)



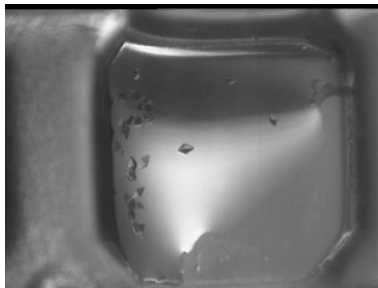
No

0.8 mM HydG, 3 mM tyrosine, 2 mM
NaDT, 4 d

PP1-6

0.1 M SPG buffer pH 7,
25% PEG 1500

(4)

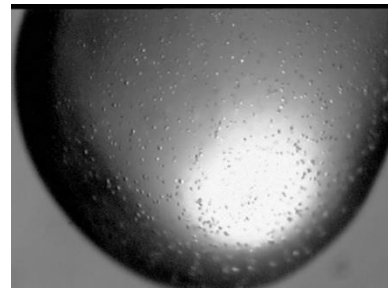


0.8 mM HydG, 3 mM tyrosine, 2 mM
NaDT, 4 d

PP2-8

0.2 M Na₂SO₄,
20% PEG 3350

(4')



0.5 mM HydG, 3 mM tyrosine, 2 mM
NaDT, (1:1), 4 d

PP2-8

0.2 M Na₂SO₄,
20% PEG 3350

Table 4.8 Overview of different crystal forms obtained with reduced *T. lettingae* HydG in the presence of tyrosine.

Screen solution	Condition
<i>Hexagonal</i>	
PP1-6	0.1 M SPG buffer pH 9, 25% (w/v) PEG 1500
PP1-31	0.2 M NaCl, 0.1 M HEPES pH 7, 20% (w/v) PEG 6000
PP1-32	0.2 M NH ₄ Cl, 0.1 M HEPES pH 7, 20% (w/v) PEG 6000
PP2-9	0.2 M LiCl, 0.1 M Tris pH 8, 20% (w/v) PEG 6000
<i>Diamond shaped</i>	
PP1-44	0.2 M NH ₄ Cl, 0.1 M Tris pH 8, 20% (w/v) PEG 6000
PP2-8	0.2 M Na ₂ SO ₄ , 20% (w/v) PEG 3350
PP2-29	0.2 M NaNO ₃ , 0.1 M Bis-Tris propane pH 7.5, 20% (w/v) PEG 3350
PP2-31	0.2 M NaOAc, 0.1 M Bis-Tris propane pH 7.5, 20% (w/v) PEG 3350
<i>Mix of both</i>	
PP1-41	0.1 M MMT buffer pH 8, 25% (w/v) PEG 1500

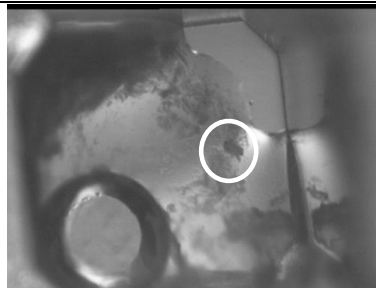
Efforts to crystallise HydG in the presence of AdoMet and tyrosine, or AdoHcy and tyrosine under reducing conditions, were rather unsuccessful. The best lead for AdoMet and tyrosine co-crystallisation was a crystal shower observed with PP1-17 under non-reducing conditions (Table 4.9 A2). Due to time constraints however, this could not further be investigated.

Table 4.9 Crystallisation of *T. lettingae* HydG with AdoMet and tyrosine.

Crystallisation by vapour diffusion was attempted in 96-well plates with sitting drops (1:1 protein:mother liquor, 2 μ L total) and 50 μ L mother liquor well solution. Indicated concentrations refer to the individual protein and mother liquor solutions, not the final concentrations in the drop. The period of crystal growth is indicated in days (d).

(A) Non-reducing 96-well screen

(1)

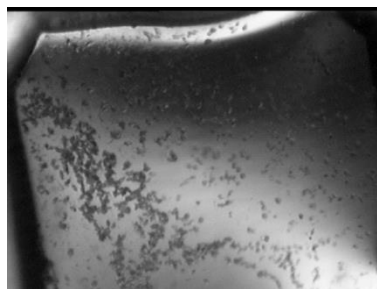


0.95 mM HydG, 10 mM AdoMet,
3 mM tyrosine, 1 d

PEGRx 2-35

0.15 M $\text{Li}_2\text{SO}_4 \cdot \text{H}_2\text{O}$,
0.1 M Citric acid pH 3.5,
18% PEG 6000

(2)



0.8 mM HydG, 10 mM AdoMet, 3 mM
tyrosine, 1 d

PP1-17

0.1 M MIB buffer pH 8,
25 % PEG 1500

4.8 Data collection on *T. lettingae* HydG crystals

4.8.1 Basic theory

Reflection of X-ray radiation of approximately 12 keV ($\sim 1 \text{ \AA}$, see Equation 4.1) from atomic planes in macromolecular crystals is detected by a Pilatus detector resulting in a diffraction pattern of different intensity spots²¹⁹ (Figure 4.15 B, Figure 4.16 B).

$$e \text{ (keV)} = \frac{12.39}{\lambda \text{ (\AA)}} \quad \text{Equation 4.1}$$

The origin of the diffracted wave is described by Miller indices (hkl) , while the associated spot intensity (I_{hkl}) is proportional to the square of the amplitude of the structure factor (F_{hkl}) (Equation 4.2)²²⁰. The structure factor itself is described by the atomic scattering factor (f_j) and the vector x_j (x, y, z) describing the atomic position of the reflected wave (Equation 4.3)²²⁰.

$$I_{hkl} \propto |F_{hkl}|^2 \quad \text{Equation 4.2}$$

$$F_{hkl} = \sum_j^N f_j e^{2\pi i (hx_j + ky_j + lz_j)} \quad \text{Equation 4.3}$$

To calculate the electron density [$\rho(xyz)$] for individual atoms in the unit cell according to Equation 4.4, the phase of the reflected wave (ϕ_{hkl}) must be known. This however cannot be measured during the experiment and is known as the ‘phase problem’²²⁰.

$$\rho(xyz) = \frac{1}{V} \sum_{hkl} |F_{hkl}| e^{-2\pi i (hx+ky+lz) + i\phi_{hkl}} \quad \text{Equation 4.4}$$

There are different methods to obtain initial information about the phase^{220–222}, but for metalloenzymes the use of singlewavelength or multiwavelength anomalous dispersion (SAD, MAD) experiments are most relevant. This method uses X-ray radiation of sufficiently high energy to promote electronic transitions of inner shell electrons of a target metal²²¹. The required energies are atom specific and do not excite electrons in ‘light atoms’ such as carbon, nitrogen or oxygen²²¹. Due to absorption of some of the radiation, the scattered photons have a phase different from a ‘normal scattered’ photon^{220,221}. These phase differences contribute to the atomic scattering factor (f) as a real (f') and an imaginary (f'') component (Equation 4.5). This results in different structure factors and therefore different spot intensities (see Equation 4.2, Equation 4.3) of reflections from the heavy atom(s). These anomalous diffraction centres are thus reference points for solving the protein structure using the high resolution diffraction data acquired with 12 keV X-ray radiation²²⁰.

$$f = f^0 + f' + if'' \quad \text{Equation 4.5}$$

For the crystals discussed in the next section, anomalous data was recorded at the iron K-edge. To determine the individual f' and f'' components, a fluorescence scan at 7.11 keV (1.74 Å)²²³ was carried out.

Automatic processing of the obtained crystallographic data at Diamond outputted an initial working model for the protein structure. A measure for the quality of the obtained atomic model is the R-factor, which reflects the deviation of calculated structure factors (F_{hkl}^{calc}) from a simulated diffraction pattern of the atomic model with structure factors of the experimentally observed diffraction pattern (F_{hkl}^{obs}) (Equation 4.6)²²⁴. A well-defined structure is expected to have an R-factor close to 0.2²²⁵.

$$\text{R-factor, -work or -free} = \frac{\sum | |F_{hkl}^{\text{obs}}| - |F_{hkl}^{\text{calc}}| |}{\sum |F_{hkl}^{\text{obs}}|} \quad \text{Equation 4.6}$$

Further refinement of the structure is automatically carried out on only 90% of the experimentally observed data²²⁶ (the ‘working’ data set) and its quality is described by the R–work value (Equation 4.6). To obtain R–free, the remaining ‘free’ 10% of the reflections are compared to the predicted 10% as modelled using the ‘working’ data set (Equation 4.6). To assess whether a structure has been ‘over–fitted’, likely resulting from incorporation of more degrees of freedom than there are experimental observations^{225,227}, the R–work and R–free values need to be compared. A well refined structure will have a 0.02–0.08 higher R–free than R–work value²²⁵. Once a satisfactorily R–free value has been obtained after several refinement cycles, additional parameters are usually reviewed to further verify the model²²⁵.

4.8.2 Practice

Crystals were flash frozen in liquid N₂ in the presence or absence of a cryoprotectant and then analysed at Diamond Light Source. Only crystals which diffracted are mentioned here as most were too small to be analysed accurately or too fragile to be flash frozen satisfactorily. Only two crystals, both of reduced *T. lettingae* HydG in the presence of tyrosine diffracted and were stable enough to acquire a full data set as summarised below. Finding a solution to both data sets is work in progress by Pedro C. Dinis.

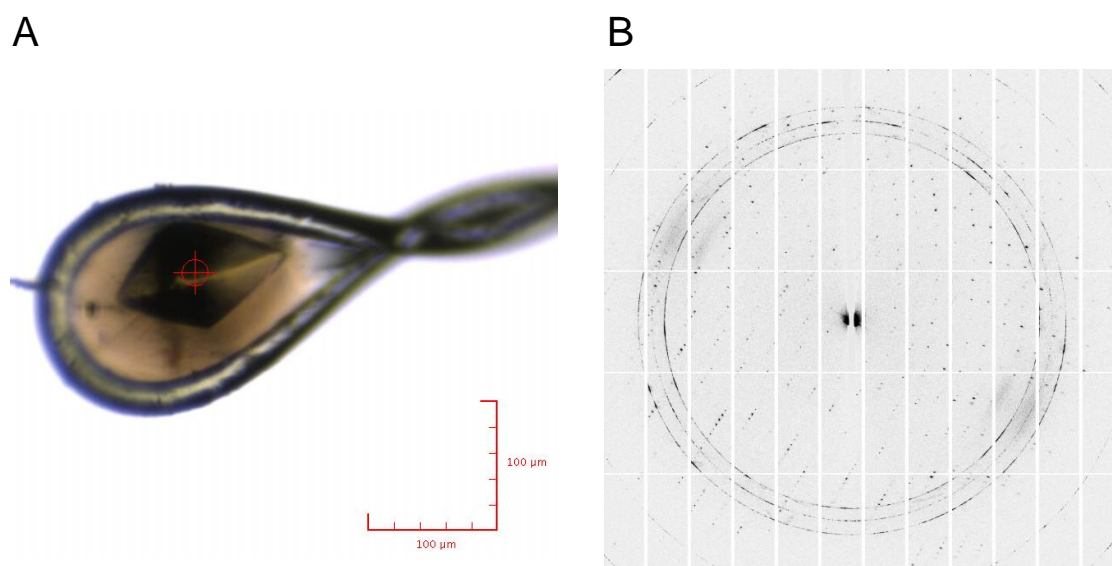


Figure 4.15 Data collection of M7S13.

(A) Crystal of reduced *T. lettingae* HydG with tyrosine, directly flash frozen in liquid N₂. Loop size – 0.1–0.2 mm, beam size – 20 x 20 μm. Crystals were obtained by vapour diffusion using sitting drops of protein (0.8 mM HydG, 3 mM tyrosine, 2 mM sodium dithionite) and PP2–29 (0.2 M NaNO₃, 0.1 M Bis–Tris propane pH 7.5, 20% (w/v) PEG 3350) mother liquor (1:1, 2 μL total) in a sealed 96–well plate with 50 μL well solution. (B) Associated diffraction pattern from 12 keV synchrotron radiation to 2.7 Å resolution.

Table 4.10 Data processing statistics for M7S13.

The highest resolution shell is shown in parentheses.

Parameter	Anomalous Data (3daii-run)	High Resolution Data (3daii-run)
Beamline	I03	I03
Wavelength (Å)	1.73891	0.97625
Space group	P 2 ₁ 2 ₁ 2 ₁	P 2 ₁ 2 ₁ 2 ₁
Cell dimensions		
a, b, c (Å)	61.96, 66.93, 133.53	62.01, 67.03, 133.60
α , β , γ (°)	90.0, 90.0, 90.0	90.0, 90.0, 90.0
Resolution (Å)	2.61–66.93 (2.61–2.68)	2.48–66.80 (2.48–2.54)
I/ σ (I)	18.0 (2.5)	16.0 (2.4)
R-merge	0.089 (0.627)	0.045 (0.249)
Completeness (%)	94.8 (67.5)	92.3 (61.6)
Anomalous completeness (%)	94.5 (66.8)	79.5 (34.3)
Anomalous multiplicity	6.1 (3.2)	1.8 (0.8)
Total reflections	189325	69344
Twinning score	2.35, no twinning	2.47, no twinning

I/ σ (I) – Average intensity divided by its average standard deviation.

R-merge – Measure for intensity deviation from identical reflections.

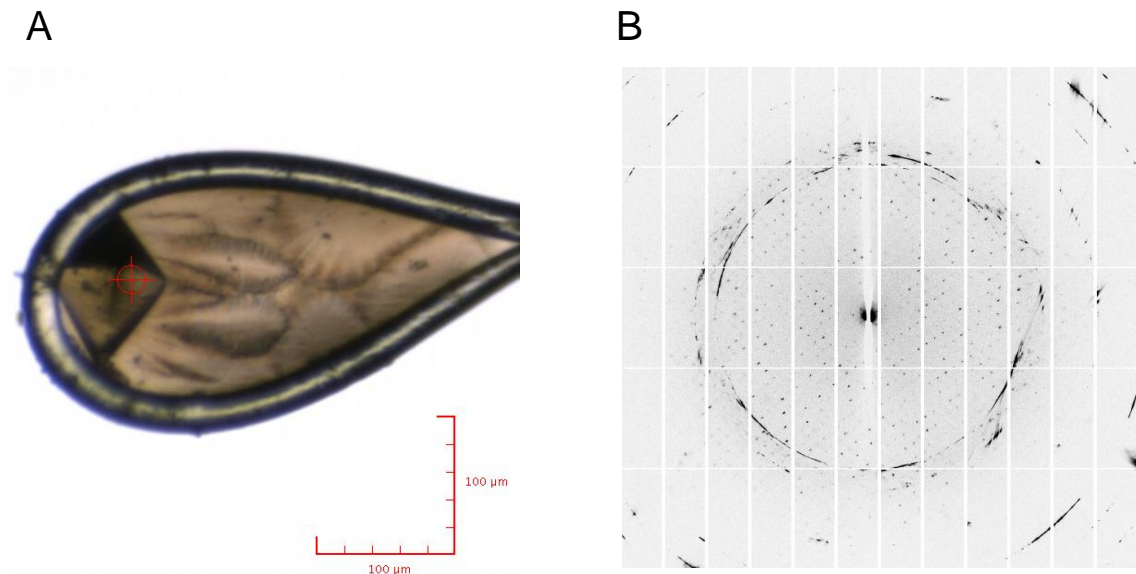


Figure 4.16 Data collection of M8S1.

(A) Crystal of reduced *T. lettingae* HydG with tyrosine, directly flash frozen in liquid N₂. Loop size – 0.1–0.2 mm, beam size – 20 x 20 μm. Crystals were obtained by vapour diffusion using sitting drops of protein (0.8 mM HydG, 3 mM tyrosine, 2 mM sodium dithionite) and PP2–8 (0.2 M Na₂SO₄, 20% (w/v) PEG 3350) mother liquor (1:1, 2 μL total) in a sealed 96–well plate with 50 μL well solution. (B) Associated diffraction pattern from 12 keV synchrotron radiation to 3.2 Å resolution.

Table 4.11 Data processing statistics for M8S1.

The highest resolution shell is shown in parentheses.

Parameter	Anomalous Data (3daii-run)	High Resolution Data (3daii-run)
Beamline	I03	I03
Wavelength (Å)	1.73891	0.97625
Space group	P 1 2 ₁ 1	P 2 ₁ 2 ₁ 2 ₁
Cell dimensions		
a, b, c (Å)	61.85, 133.59, 66.62	62.22, 66.59, 133.46
α , β , γ (°)	90.0, 90.47, 90.0	90.0, 90.0, 90.0
Resolution (Å)	3.10–66.79 (3.10–3.18)	2.72–66.59 (2.72–2.79)
I/ σ (I)	9.4 (2.3)	10.1 (2.1)
R-merge	0.165 (0.740)	0.095 (0.724)
Completeness (%)	98.0 (98.2)	97.7 (99.7)
Anomalous completeness (%)	96.2 (97.5)	89.2 (95.9)
Anomalous multiplicity	3.3 (3.3)	2.0 (2.1)
Total reflections	128285	59827
Twinning score	2.34, no twinning	2.52, no twinning

I/ σ (I) – Average intensity divided by its average standard deviation.

R-merge – Measure for intensity deviation from identical reflections.

4.9 Crystal structure of *Th. italicus* HydG

Pedro C. Dinis crystallised non-reduced *Th. italicus* HydG in the presence of AdoMet and solved the associated crystal structure to 1.8 Å resolution using the Fe-SAD anomalous data (Table 4.12). Although tyrosine was included in the crystallisation conditions, no corresponding electron density was present in the structure. Despite the comparatively small, 52% and 61% sequence identity²¹⁷ of *T. lettingae* and *C. acetobutylicum* HydG to *Th. italicus* HydG, the following discussion assumes that all are structurally comparable.

4.9.1 Overall fold and AdoMet binding

Thermoanaerobacter italicus HydG crystallised as a homodimer and adopts a full $\beta_8\alpha_8$ TIM barrel with a narrow circular opening of 19 Å in diameter (Figure 4.17). Four α -helices before and after the TIM barrel structural elements constitute to the N- and C-terminal domains, respectively (Figure 4.17, wheat, light blue). The C-terminal domain partially closes the 'lower' half of the TIM barrel and makes contact with the N-terminal helices. Interestingly, *Th. italicus* HydG is structurally highly homologous to *T. maritima* HydE³⁷ (Figure 4.17, insert). The average distance between backbone atoms in both structures (the root-mean-square deviation, rmsd) is only 2.15 Å, while it varies between 9 Å and 27 Å when comparing *Th. italicus* HydG to the auxiliary cluster containing radical AdoMet enzymes listed in Table 1.1. Structural differences between HydG and HydE include that HydE lacks the C-terminal domain found in HydG and that the auxiliary iron-sulfur clusters are positioned differently.

Table 4.12 Data processing statistics for *Th. italicus* HydG.

The highest resolution shell is shown in parentheses.

Parameter	Anomalous Data (3daii-run)	High Resolution Data (3daii-run)
Beamline	I03	I03
Wavelength (Å)	1.72921	0.97625
Space group	P 1	P 1
Cell dimensions		
a, b, c (Å)	54.41, 56.92, 85.07	54.34; 56.90; 85.14
α , β , γ (°)	88.74, 83.42, 66.39	88.69; 83.46; 66.33
Resolution (Å)	1.73–52.14 (1.73–1.78)	1.99–84.56 (1.99–2.04)
I/ σ (I)	19.8 (3.0)	5.7 (2.0)
R-merge	0.033 (0.230)	0.125 (0.922)
Completeness (%)	69.1 (6.0)	93.7 (94.1)
Anomalous completeness (%)	60.5 (5.2)	73.0 (71.1)
Anomalous multiplicity	1.5 (1.1)	1.0 (1.0)
Total reflections	215940	139754
Twinning score	2.37, no twinning	2.77, no twinning
No. of refinement cycles		12
R-work (before/after)		0.319/0.224
R-free (before/after)		0.286/0.278

I/ σ (I) – Average intensity divided by its average standard deviation.

R-merge – Measure for intensity deviation from identical reflections.

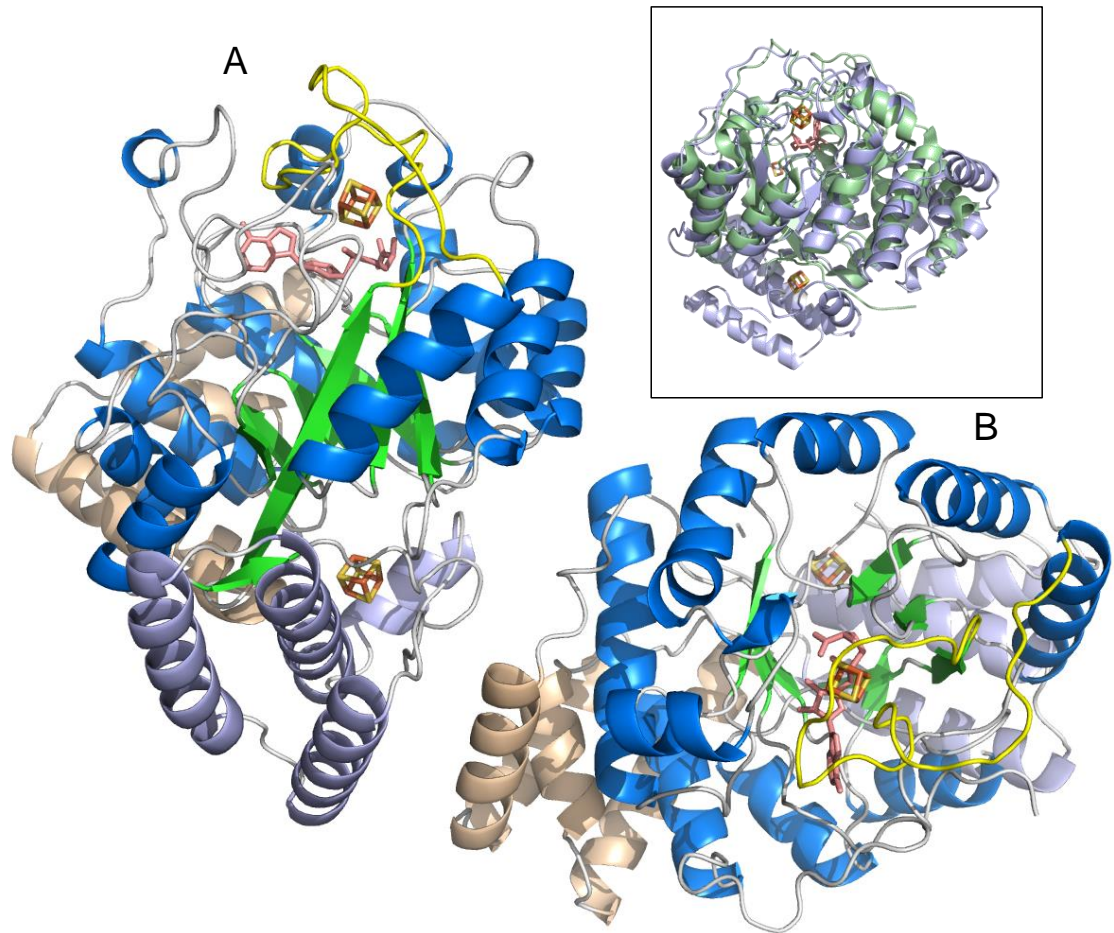


Figure 4.17 Crystal structure of *Th. italicus* HydG homodimer.

Monomer A represents a side view of the TIM barrel, while monomer B represents a top view. AdoMet (salmon) and the [4Fe-4S] clusters (iron, orange; sulfur, yellow) are shown as sticks. The AdoMet binding loop is coloured yellow and the N- and C-terminal helices outside the barrel domain are coloured wheat and light blue, respectively. Remaining secondary structure elements are coloured as follows: helices – blue, sheets – green, loops – grey. The insert shows a structural alignment of HydG (monomer A) with HydE (PDB 3IIZ) in light blue and green, respectively (rmsd – 2.15 Å).

The *Th. italicus* HydG cysteine CX₃CX₂C motif coordinating the radical AdoMet [4Fe–4S] cluster is located on a long loop covering the lateral TIM barrel opening (Figure 4.17, yellow), a detailed view of AdoMet binding is shown in Figure 4.18. Unsurprisingly, AdoMet is coordinated to the unique iron of cluster I via its α -amino and α -carboxy groups as also observed for other radical AdoMet enzymes^{65,66} (see section 1.2.2.2). The distance between the AdoMet sulfonium and the unique iron is 2.8 Å compared to 3.5 Å to the nearest cluster sulfide. Interaction of the aromatic Tyr96 residue in the CX₃CXYC motif provides hydrophobic face to edge interactions to the AdoMet adenine moiety (Figure 4.18, yellow). Backbone hydrogen bonding contacts are established between the AdoMet adenine amine and residues from the AdoMet binding loop and the loop following β 6 (Figure 4.18, yellow, green). The ‘GXIXGXXE’ motif corresponds to ‘GVLYGLYD’ in *Th. italicus* HydG, where the conserved Leu236 holds the adenine ring in place by providing hydrophobic interactions (Figure 4.18, cyan). The glycine rich ‘GGE’ motif is situated on the loop following β 2 and establishes backbone hydrogen bonding interactions with the AdoMet amino group (Figure 4.18, orange). Hydrogen bonds to the ribose hydroxyls are formed by Glu194.

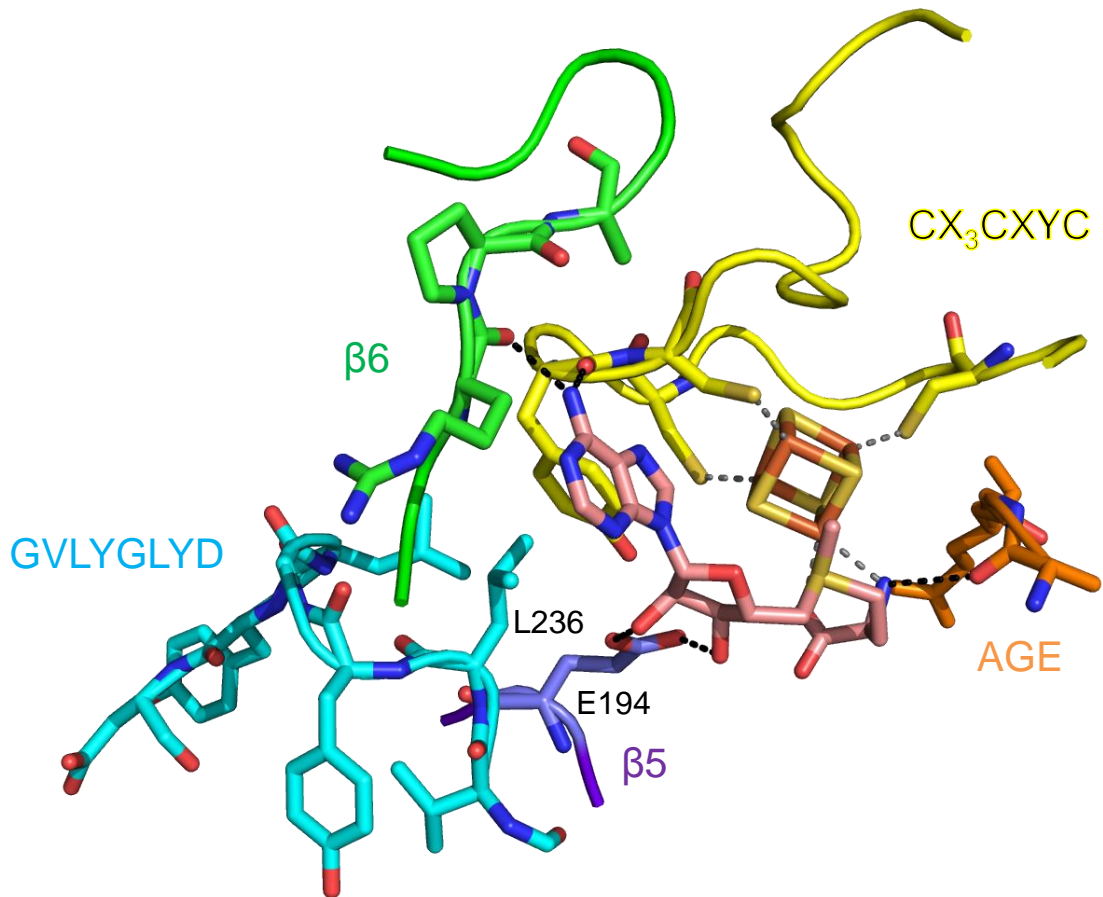


Figure 4.18 AdoMet binding in the *Th. italicus* HydG active site.

HydG active site highlighting identified interactions with AdoMet (salmon) as described in the text. Hydrogen bonding and coordination interactions are depicted as black and grey dashes, respectively.

4.9.2 C-terminal domain and tyrosine binding

The C-terminal domain of *Th. italicus* HydG comprises a short, non-TIM barrel associated β -sheet and four α -helices which partially close the 'lower' half of the TIM barrel (Figure 4.17). As inferred by spectroscopic experiments with *C. acetobutylicum* HydG (Chapter 2), the cysteine residues of the C-terminal CX₂CX₂₂C motif coordinate an auxiliary [4Fe-4S] cluster (Figure 4.19 A). While Cys380 and Cys383 are located on a loop surrounding the cluster, the last cysteine residue, Cys406, is situated on a C-terminal α -helix (Figure 4.19 A). The density of the cluster II binding loop is partially missing in monomer B, suggesting a high degree of flexibility.

The small change in the EPR spectrum of reduced WT *C. acetobutylicum* HydG upon addition of tyrosine or tyrosine and AdoHcy (section 2.4) was cautiously interpreted to indicate tyrosine binding to the auxiliary [4Fe-4S] cluster. Coordination of tyrosine or the dehydroglycine cleavage product is substantiated by the observation that the fourth iron of the C-terminal [4Fe-4S] cluster does not interact with a protein residue and is facing into the TIM barrel active site (Figure 4.19 A). An analogous spatial arrangement has also been observed for the GTP binding auxiliary cluster in MoaA^{86,118}. Unfortunately, and for currently unknown reasons, no electron density corresponding to tyrosine or a related cleavage product could be identified in the *Th. italicus* HydG structure, despite inclusion of tyrosine in the crystallisation conditions.

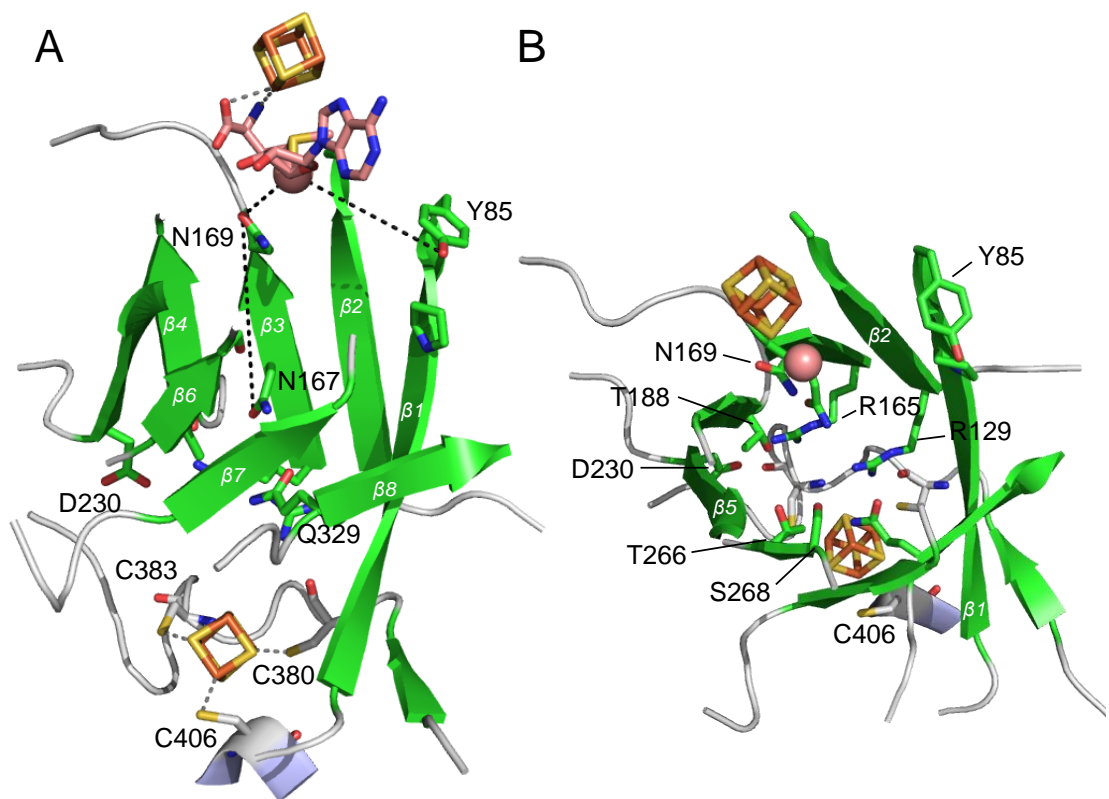


Figure 4.19 A tunnel links both [4Fe–4S] clusters of *Th. italicus* HydG.

(A) Side view of the HydG TIM barrel core, helices and main loops have been omitted for clarity. The 5'–C of AdoMet (salmon) is shown as a sphere while conserved and potentially mechanistically relevant amino acids lining the TIM barrel core are shown as sticks. Initial hypothetical radical transfer from 5'–dA• to nearby amino acids is indicated by black dashes while coordination interactions are shown by grey dashes. (B) Top view of the HydG TIM barrel, for clarity only showing the 5'–C of AdoMet as a sphere. Colour key as in Figure 4.17.

The 27.2 Å distance between the unique irons of cluster I and cluster II is 10 Å longer than the separation between both [4Fe–4S] clusters in MoaA⁸⁶ and nearly twice as long compared to other radical AdoMet enzymes also coordinating an additional [4Fe–4S] cluster (Table 1.1). This large separation somewhat weakens the argument for direct tyrosine coordination to cluster II as electron tunnelling has only been observed over distances ranging between 4 Å and 14 Å¹²⁰. In addition, a close spatial relationship between the position of 5'-dA• formation and hydrogen atom abstraction is required to prevent damaging side reactions as described in section 1.2.3. In fact, the nearby Asp169 and Tyr85 residues (Figure 4.19 A) may be suitable donors for unproductive hydrogen atom abstraction by the 5'-dA•.

However, long distances between radical mediated reaction centres are possible if they are linked by redox active amino acid residues. A prime example is class I ribonucleotide reductase (RNR), where the initiating tyrosyl radical in subunit R2 is separated by approximately 35 Å from the substrate binding site and the catalytically active cysteine residue in subunit R1²²⁸. A proton-coupled electron transfer path via tryptophan and tyrosine residues is proposed to shuffle the radical to the substrate target (Figure 4.20). Based on the *Th. italicus* HydG crystal structure, a similar pathway could be envisioned for HydG, where the radical from 5'-dA• is initially transferred to Asp169 or Tyr85, located 4.1 Å and 8.5 Å away, respectively (Figure 4.19 A). Additional conserved and polar residues line the active site TIM barrel towards cluster II (Figure 4.19 B) and may continue this network.

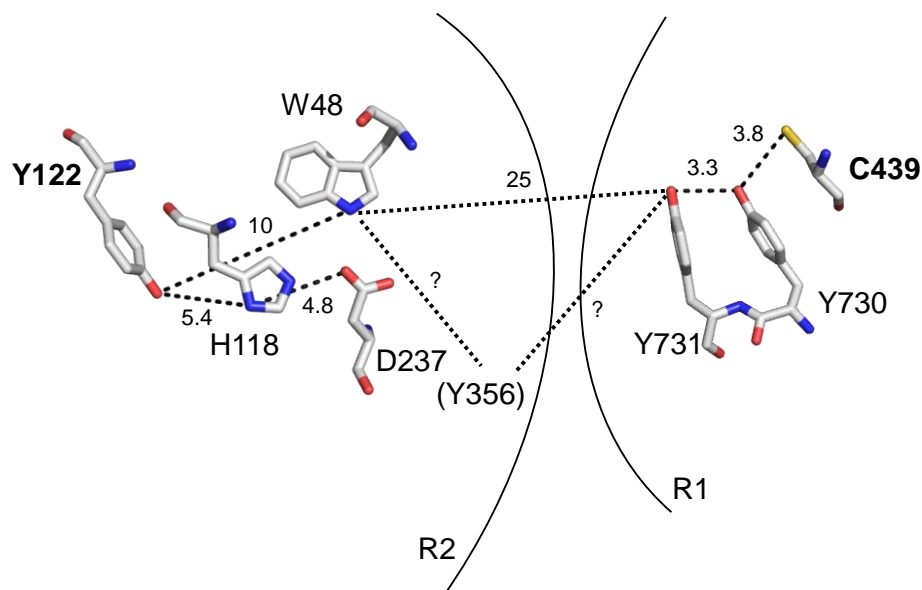


Figure 4.20 Proposed proton-coupled electron transfer pathway in *E. coli* RNR.

Shown are amino acid residues on the class I *E. coli* RNR subunits R2 and R1 proposed to be involved in radical transfer from Tyr122 in R2 to Cys439 in R1.

Small numbers are distances between hydrogen bonding partners in Å.

Adapted from Pizano et al.²²⁸ using PDBs 1RLR (R1) and 1RIB (R2). Tyr356 is a proposed step along the path but could not be modelled accurately due to missing electron density.

Based on the strong secondary structure conservation observed among radical AdoMet enzymes⁶⁹, Pilet and co-workers inferred active site residues which line the TIM barrel β -sheets of ThiH and HydG and may potentially be involved in tyrosine binding and/or catalysis³³. Comparison of four ThiH and HydG sequences and re-analysis with regard to the secondary structure identified in *Th. italicus* HydG highlights that very few β -sheet amino acid residues are conserved (Appendix 5). In fact, only the PXY motif in strand β 1, the last glycine and serine residues of β 5 and β 6, respectively seem completely

Chapter 4 – Crystallography

conserved. The second to last glycine residue in $\beta 5$ and the last serine residue in $\beta 8$ are only partially conserved. Although there are highly conserved ThiH and HydG residues following the β -sheets, these amino acids are predominantly situated at the 'top' of the TIM barrel, close to cluster I and AdoMet and therefore more likely involved in AdoMet binding. The low similarity between proposed active site residues further suggests that tyrosine binding in HydG and ThiH is accomplished by different interactions as already proposed in section 3.6.1.

4.10 Summary and conclusions

Plasmids encoding codon optimised N-terminally 6His tagged HydG from three different (hyper)thermophilic organisms in a genetic background of the *isc* operon have been prepared. Expression and Ni-affinity purification analogous to *C. acetobutylicum* HydG was only successful for *T. lettingae* and *Th. italicus* HydG. All Ni-purified and chemically reconstituted HydG samples contained a protein-iron-sulfur aggregate which was separated from the catalytically active HydG by Superdex 75 gel filtration chromatography to obtain crystallisation grade protein. The N- and C-terminally 6His tagged *T. maritima* HydG proteins co-purified in a near stoichiometric ratio with two impurities of approximately 28 kDa in size and numerous attempts to remove these impurities by strong anion or cation exchange chromatography as well as gel filtration were unsuccessful.

Commercial crystallisation screens were employed to screen for conditions suitable to crystallise N-terminally 6His tagged *T. lettingae* and C-terminally 6His tagged *T. maritima* HydG. Small diamond or hexagonal shaped crystals were obtained with reduced *T. lettingae* HydG in the presence of tyrosine. Two of these crystals diffracted synchrotron radiation to 2.7 Å and 3.2 Å, but determination of the *T. lettinage* HydG crystal structure remains work in progress. These crystals were only reproducible in a 96-well sitting drop format, whereas crystal showers formed in 24-well hanging drops. In both cases, the crystals remained small despite various optimisation efforts. The small crystals of non-reduced *T. maritima* HydG with AdoMet and tyrosine did not diffract.

Pedro C. Dinis successfully crystallised non-reduced *Th. italicus* HydG with AdoMet and tyrosine and solved the crystal structure to 1.8 Å resolution.

Chapter 4 – Crystallography

Coordination of cluster I and AdoMet was found to be very similar to other radical AdoMet enzymes⁶⁵. The auxiliary [4Fe-4S] cluster inferred by spectroscopic studies was confidently modelled into the structure and demonstrates a three cysteine coordination environment. The unique iron is pointing into the active site but tyrosine coordination to this iron could not be confirmed as there was no electron density that could satisfactorily be allocated to tyrosine. The large 27.2 Å separation between the unique iron atoms of cluster I and cluster II questions direct ligation of tyrosine to cluster II because electron transfer from the incipient 5'-dA• to the tyrosine hydroxyl group is unlikely over this distance. Conserved polar residues inside the TIM barrel line the channel which connects both [4Fe-4S] clusters and may provide a radical transfer path, analogous to the reaction catalysis by class I RNR²²⁸. Individual mutations of the conserved active site residues and comparative kinetic analyses of the resulting HydG mutants with regards to tyrosine cleavage may support this hypothesis. A decreased ability to form *p*-cresol is expected if any of these residues is important for tyrosine cleavage. These are elaborate experiments as parallel measurements of tyrosine dissociation constants for these HydG mutants are required to distinguish between catalytic amino acids and residues predominantly involved in tyrosine binding.

It cannot be excluded that tyrosine binds close to the 5'-C of AdoMet and that only the tyrosine derived dehydroglycine is transferred to cluster II for subsequent collapse to cyanide and CO. Further optimisation of conditions to crystallise HydG with tyrosine or AdoMet and tyrosine is required to address this question of tyrosine binding. The solubility of tyrosine¹⁹⁹ somewhat restricts the concentrations achievable in co-crystallisation experiments within the pH 6 to pH 8 range. Alternative strategies^{229,230} towards crystallisation of HydG-substrate complexes include (i) co-expression of HydG with AdoMet or

tyrosine, (ii) the presence of either or both substrates during HydG purification if turnover in the presence of DTT can be excluded and (iii) soaking of the tyrosine substrate into the current *T. lettingae* HydG–AdoMet crystals. An altogether different approach would be to try and crystallise HydG with a non-productive tyrosine analogue or a combination of *p*-cresol and glyoxylate. Activity studies with tyrosine analogues as discussed in section 3.6.1 and/or similar binding studies could guide the selection process for suitable tyrosine derivatives.

The loop surrounding cluster II could not be modelled accurately in *Th. italicus* HydG monomer B due to missing electron density, inferring some flexibility in this region. In addition, the C-terminal domain only partially protects the ‘lower’ TIM barrel region and one could envision binding of another maturation enzyme during potential cluster transfer from HydG to HydF, HydE or HydA after cyanide and CO incorporation into cluster II. This cluster transfer role may also explain the unprecedented long distance between both [4Fe–4S] clusters as conformational changes at the C-terminus are not to interfere with the cluster I and AdoMet coordination environments.

Chapter 5

Investigating cyanide transfer between *C. acetobutylicum* HydG and HydF

5.1 Introduction

HydF is a GTPase²⁶, that is, it cleaves the γ phosphate group of GTP to generate guanosine-5'-diphosphate (GDP) and inorganic phosphate. Its GTPase activity was found to be gated by the size of the monovalent alkali metal cations present in the assay buffer³¹. Potassium ions were found to give the highest activities compared to sodium ions, more commonly employed in buffers³¹.

The primary sequence of HydF contains three C-terminal cysteine residues in a CXHX₄₆₋₅₃HCX₂C motif^{23,26} (Figure 5.1, yellow) which have been implicated in ligating a [4Fe-4S] cluster²⁶⁻²⁸. Coordination of the fourth iron was proposed to occur by one of the conserved histidine residues (Figure 5.1, green), but unambiguous experimental evidence is lacking. For example, no

histidine ligation could be identified for *T. maritima*²⁶ and *Thermotoga neapolitana* (*T. neapolitana*)²³¹ HydF, while the opposite was inferred by HYSORE spectroscopic characterisations³² of reduced, non-reconstituted *C. acetobutylicum* HydF^{EG} or UV-Vis and EPR characterisations²⁸ of HydF expressed on its own. Whether His306²⁸ or His352²³¹ is the fourth ligand to the [4Fe-4S] cluster in *C. acetobutylicum* HydF still requires unambiguous characterisation. However, the observed coordination of imidazole to the *T. maritima*²⁶ and *T. neapolitana*²³¹ HydF [4Fe-4S] cluster suggests an exchangeable coordination site and either histidine ligand may serve as an anchoring point. Evidence for an additional [2Fe-2S] cluster in HydF^{EG} as well as HydF was coming from respective UV-Vis³⁰ and EPR spectroscopic investigations^{28,31}.

```

Clostridium acetobutylicum EACTHHRQS | PP - - NIEDYALIVHCAGCMLNRRSMLH
Thermotoga maritima      EGCTHRPLT | PDLEEIEGAKLI I HCGGCVLNRAAMMR
Thermoanaerobacter italicus EGCTHHRQP | PD - - NLEEYSLIVHCGACMLNRREMMY
Thermoanaerobacter tengcongensis EACTHHRQS | KK - - DLSKYALIVHCGGCMITRREMLY
    
```

Figure 5.1 Partial sequence alignment of HydF from selected organisms.

Shown is the partially conserved CXHX₄₆₋₄₈HCX₂C motif of HydF, with the conserved cysteine and histidine residues highlighted in yellow and green, respectively. The red dotted line indicates the exclusion of 30 amino acids.

The role of HydF as a scaffold protein during [FeFe]-hydrogenase H-cluster assembly is controversial in the literature as described in the introductory chapter. However, whether HydF is the ultimate protein transferring the [2Fe] subcluster to HydA or not, the mentioned functional and spectroscopic observations suggest that HydF coordinates a cyanide and CO ligated subcluster at some point during [FeFe]-hydrogenase activation. The

aim of this project is to identify whether the cyanide and CO ligands synthesised by HydG^{25,34,35} are transferred to HydF on a HydG derived iron–sulfur cluster or whether the ligands are transferred individually to the HydF [2Fe–2S] cluster. These hypotheses can be investigated by incorporating ⁵⁷Fe instead of the natural abundant ⁵⁶Fe into the [4Fe–4S] clusters of HydG, either during protein expression or during in vitro reconstitution. After controlled incubation of HydF with ⁵⁷Fe containing HydG in the presence of identified substrates and additional maturation partners, cyanide incorporation into HydF could be assessed by the established detection method³⁴ (Method 32), while the potential transfer of ⁵⁷Fe from HydG to HydF can be characterised using Mössbauer spectroscopy²³². The conditions for loading of the HydF [2Fe–2S] cluster by individually or co–expressed HydE and HydG maturases in vitro has not yet been identified and forms part of this project.

This chapter describes the experiments carried out to test the hypothetical transfer of (iron–sulfur cluster bound) cyanide from HydG to HydF. To ascertain the in vitro assay conditions for HydF loading, detection of cyanide on HydF after incubation with HydG and/or HydE and the associated substrates will be used as a reporter tool. Isolation of HydF from this complex incubation mixture requires the presence of an orthogonal affinity tag on HydF compared to the HydE and HydG maturation proteins. For reasons discussed in section 5.5, Strep II tagged HydF and 6His tagged HydE and HydG proteins were employed. To further test whether HydE modifies the HydF [2Fe–2S] cluster before insertion of cyanide and CO by HydG^{31,40} (see section 1.1.2), HydF expressed on its own and in a background of HydE (HydF^E) will be investigated.

5.2 Expression and purification of *C. acetobutylicum* HydF and HydF^E

N-terminally Strep II tagged *C. acetobutylicum* HydF (48 kDa) was then expressed in *E. coli* BL21(DE3) as described in Method 11, yielding on average 7 g light beige cell paste per L growth medium. HydF was expressed as a soluble protein and was purified employing the tight interaction between the Strep II peptide tag and streptavidin²³³ immobilised on Strep-Tactin resin (Method 17). Elution of HydF was achieved by competition binding with DTB, an analogue of the natural ligand biotin. Between 60 mg and 100 mg of HydF was obtained from 5 L growths and the purity estimated as 95% by SDS-PAGE analysis (Figure 5.2). To increase the cation dependent activity of HydF³¹ and to decrease oxidation and freeze/thawing induced activity loss, the recommended loading buffer for purification of Strep II tagged proteins (100 mM Tris, 0.15 M NaCl, pH 8)²³⁴ was modified to a 100 mM Tris, 0.3 M KCl, 5% (w/v) glycerol, 1 mM DTT, pH 8 buffer (Table 5.1). During subsequent purifications, the protein yield was however reduced to approximately 20 mg due to loss of HydF in the flow through, despite otherwise similar purification procedures (Table 5.1, 4-5). None of the introduced buffer components are known to interfere with Strep II tag binding²³⁴ and N-terminally Strep II tagged HydF has previously been successfully purified using similar buffers⁴¹, decreasing the likelihood that these components induce conformational changes in HydF which could sequester the Strep II tag.

The observed decreased binding of HydF could be due to inefficient removal of DTB from previous purifications when using 0.5 M NaOH for resin regeneration. However, even after the recommended regeneration procedure employing 2-(4'-hydroxy-benzeneazo)benzoic acid (HABA)²³⁴, low yields of

HydF were still obtained. It is unlikely that HydF binding was hindered by irreversible inactivation of streptavidin by the tightly associating natural ligand biotin ($K_d \sim 10^{-15} \text{ M}$)^{235,236} as the fraction of free biotin at the end of a logarithmic growth phase²³⁷ is not high enough to block all streptavidin binding sites. To prevent other small molecules from potentially interfering with HydF binding to streptavidin, cleared HydF cell lysates were dialysed for 2 h prior to column loading (Table 5.1, 6–7), but yields of purified HydF remained low (2–4 mg/L). Although the Strep–Tactin Superflow resin is quoted to have a limited regeneration life time²³⁴, exhaustion of the resin was excluded as purifications of other Strep II tagged proteins in the laboratory using the same resin were successful. The reasons(s) for limited HydF binding could not be identified.

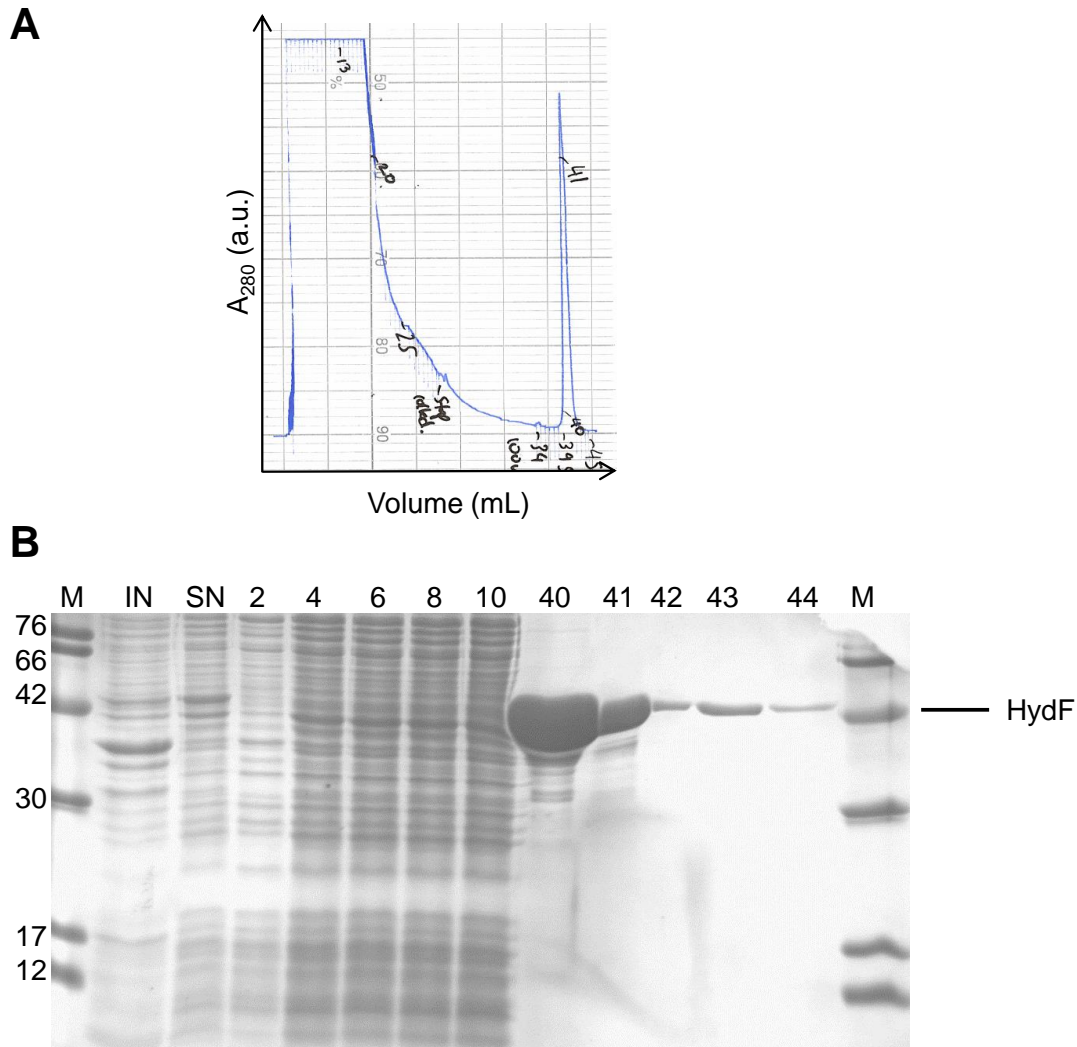


Figure 5.2 Strep-Tactin affinity purification of HydF.

(A) Elution profile and (B) 15% SDS-PAGE analysis of protein fractions eluted from the Strep-Tactin Superflow high capacity column. M - molecular weight marker (kDa), IN - insoluble, SN - lysate supernatant, (2-10) - wash fractions, (40-44) - elution fractions.

Table 5.1 Modifications to Strep II tagged HydF, HydF^E purifications.

	Lysate volume (mL)	Loading/Elution buffers	Flow rates (mL/min)	Yield (mg)
1	120	100 mM Tris, 0.3 M KCl, pH 8, ± 2.5 mM DTB	5.0	100
2	110	100 mM Tris, 0.3 M KCl, 5% (w/v) glycerol, pH 8, ± 2.5 mM DTB	2.5	61
3	50	100 mM Tris, 0.3 M KCl, 5% (w/v) glycerol, 1 mM DTT, pH 8, ± 2.5 mM DTB	2.0	45
4	150	100 mM Tris, 0.3 M KCl, 5% (w/v) glycerol, 1 mM DTT, pH 8, ± 2.5 mM DTB	1.0	18
5	60	100 mM Tris, 0.3 M KCl, 5% (w/v) glycerol, 1 mM DTT, pH 8, ± 5 mM DTB	2.0	10
6	20 ^a	100 mM Tris, 0.3 M KCl, 5% (w/v) glycerol, 1 mM DTT, pH 8, ± 2.5 mM DTB	1.5	20
7	20 ^a	100 mM Tris, 0.3 M KCl, 5% (w/v) glycerol, 1 mM DTT, pH 7.2, ± 2.5 mM DTB	1.5	20

a – Dialysed against 1 L loading buffer over 2 h with two buffer changes.

Co-expression of N-terminally 6His tagged *C. acetobutylicum* HydE (42 kDa) with Strep II tagged HydF was achieved by stepwise transformation of the HydF encoding plasmid into competent *E. coli* BL21(DE3) already containing the HydE encoding plasmid (Method 2). Expression of HydF^E (Method 11) yielded on average 4 g/L cell paste from which 10–20 mg HydF^E could be purified. The low protein yield was due to elution of HydF^E during the column washing step (Figure 5.3 B) as previously observed for HydF. Despite loss of protein, HydE was successfully removed from HydF and HydF^E was judged to be 92% pure.

The initial increase in DTB concentration during HydF or HydF^E (HydF^(E)) purifications resulted on some occasions in early eluting peaks (peak 1, 2) just before elution of the main protein peak (peak 3) as exemplified in Figure 5.4 A for the purification of HydF^E. SDS-PAGE analysis confirmed that each peak corresponds to apparently pure HydF^E (Figure 5.4 B). Decreased HydF^E binding to the Strep-Tactin resin may have been due to a proportion of HydF not being properly folded, such that the Strep II tag is unavailable for binding. To investigate whether this could have been due to the presence of differing iron-sulfur clusters in HydF, elution fractions corresponding to peaks 1 and 2 were pooled and together with the main peak 3 (Figure 5.4) they were analysed by UV-Vis spectroscopy. Surprisingly, a strong absorbance at 260 nm was associated with the initial peaks (Figure 5.5 A, dashed) compared to the main protein peak 3 (data not shown, similar to Figure 5.6 B, solid).

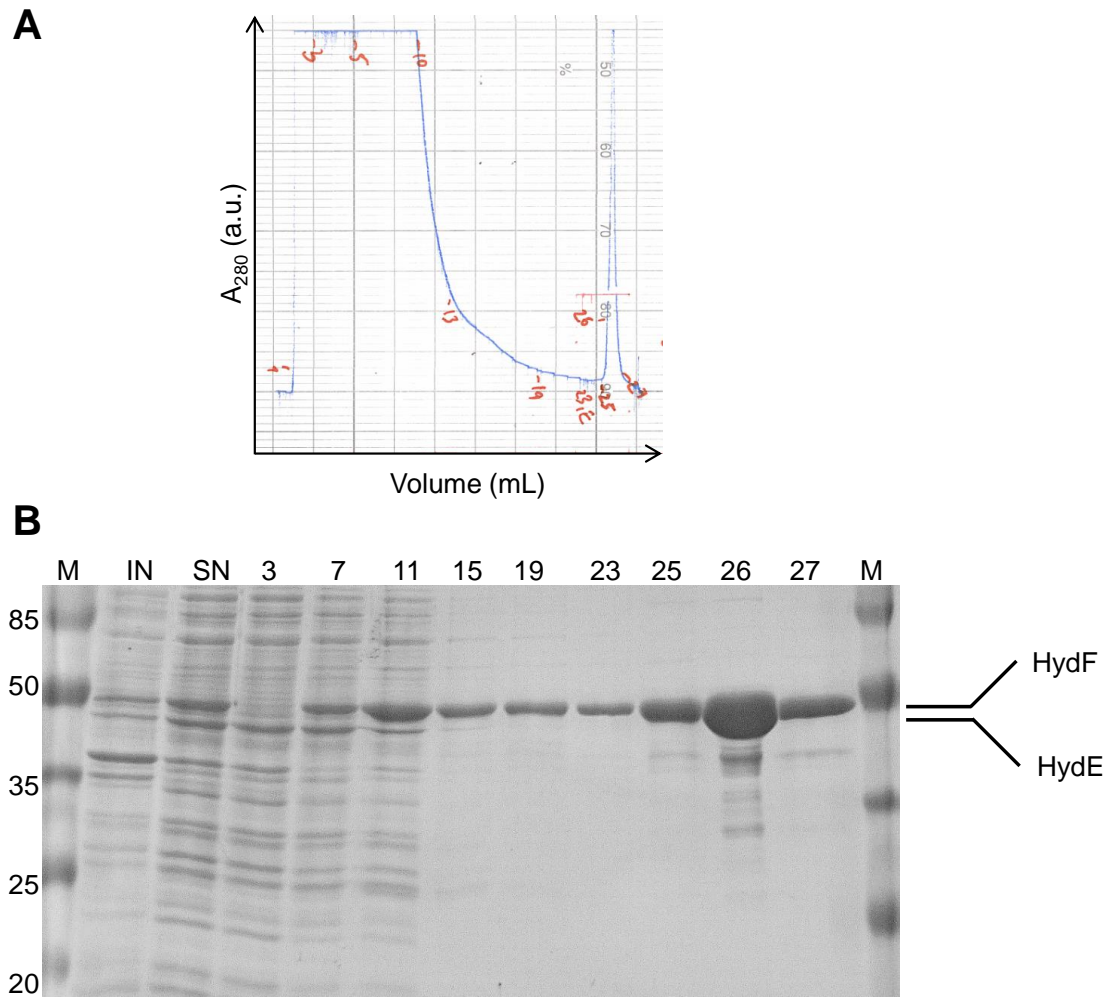


Figure 5.3 Strep-Tactin affinity purification of HydF^E.

(A) Elution profile and (B) 15% SDS-PAGE analysis of protein fractions eluted from the Strep-Tactin Superflow high capacity column. M - molecular weight marker (kDa), IN - insoluble, SN - lysate supernatant, (3-19) - wash fractions, (23-27) - elution fractions.

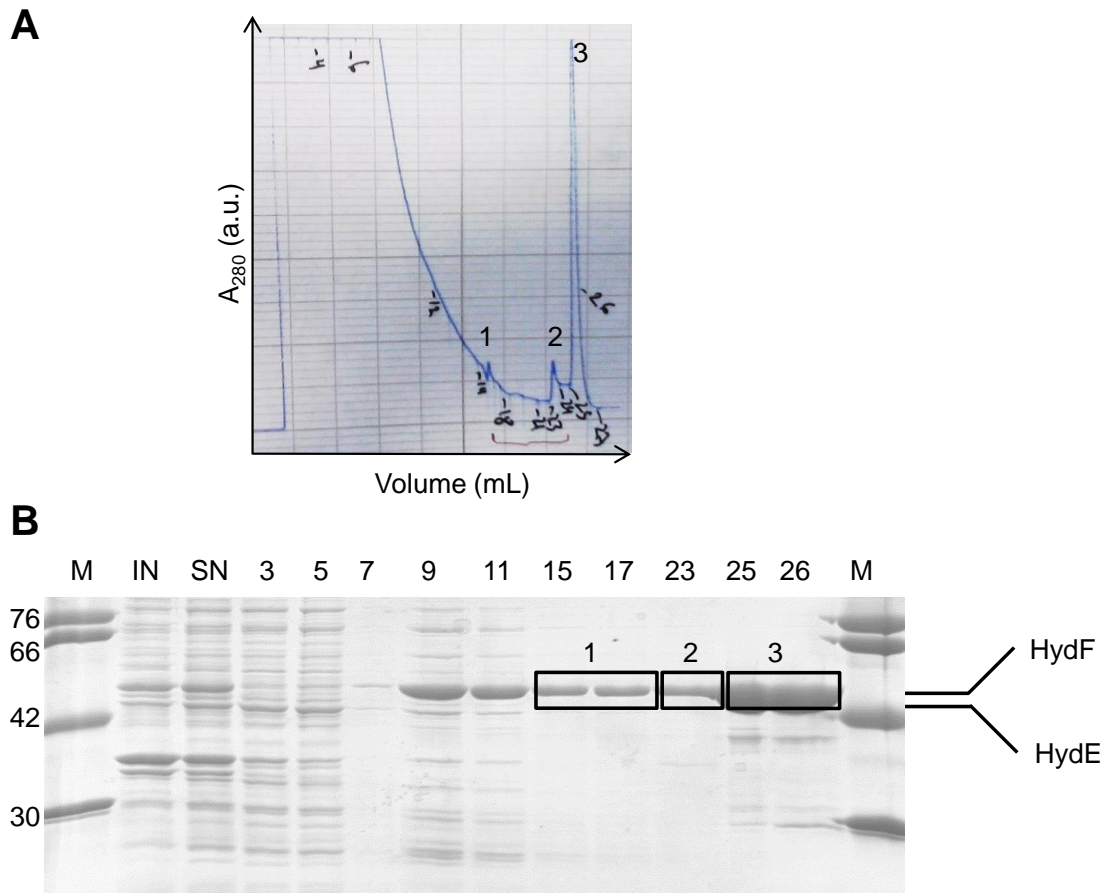


Figure 5.4 Strep-Tactin affinity co-purification of HydF^E.

(A) Elution profile and (B) 15% SDS-PAGE analysis of protein fractions eluted from the Strep-Tactin Superflow high capacity column. M - molecular weight marker (kDa), IN - insoluble, SN - lysate supernatant, (3-17) - wash fractions, (23-26) - elution fractions.

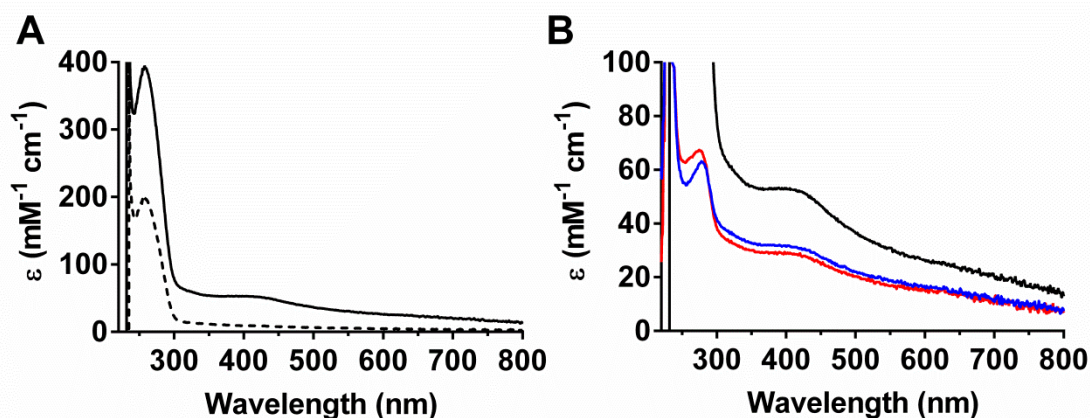


Figure 5.5 UV-Vis analysis of early eluting HydF^E fractions.

(A) As-isolated HydF^E (---) and reconstituted HydF^E (—) from pooled peaks 1, 2.
 (B) Reconstituted HydF^E from pooled peaks 1, 2 (—, as in A) after treatment with RNase A (—) or benzonase (—).

HydF is a GTPase and GTP strongly absorbs at 260 nm ($\epsilon_{260} = 12.1 \text{ mM}^{-1} \text{ cm}^{-1}$)²³⁸. While the intracellular GTP concentration of glucose fed, exponentially growing *E. coli* is estimated at 4.9 mM²³⁹, the observed ϵ_{260} between 200 and 400 mM⁻¹ cm⁻¹ for the early eluting peaks 1, 2 could suggest the presence of approximately 17 to 33 equivalents of GTP per HydF^E monomer. This is however an unlikely high extent of non-specific binding by GTP. Concentration and reconstitution of this sample with iron and sulfide (Method 18) did not decrease the 260 nm absorbance feature (Figure 5.5 A, solid), suggesting that binding of the impurity is independent of the iron-sulfur cluster state. To investigate whether ribonucleic acid (RNA) or deoxyribonucleic acid (DNA) co-purified with these HydF^E fractions, a sample was treated with RNase A or the non-specific nuclease benzonase for 6 h before UV-Vis analysis was repeated (Figure 5.5 B). The observation that the RNase and benzonase treatment of reconstituted HydF^E from peaks 1, 2 resulted in a strongly decreased 260 nm

Chapter 5 – Cyanide transfer

absorbance feature and a UV–Vis spectrum comparable to pure reconstituted HydF^E (Figure 5.6 B) suggests that RNA may have co-purified with HydF^E. This also agrees with the observed high viscosity of cell lysates²⁴⁰ during purification of HydF^E compared to HydG. As a consequence, a benzonase treatment step was included in subsequent HydF^E purifications. Unfortunately, loss of HydF^E in the flow through could nonetheless not be overcome.

5.3 Characterisation of *C. acetobutylicum* HydF and HydF^E

C. acetobutylicum HydF was purified containing $0.5 \pm 0.0(4)$ irons per protein, somewhat lower than the 1 mol of iron per mol of HydF previously described in the literature^{30,31}. The corresponding UV–Vis spectrum (Figure 5.6 A, dashed) showed a weak absorption band around 410 nm, characteristic for $[4\text{Fe–}4\text{S}]^{2+}$ clusters¹³⁴ and a shoulder at 330 nm potentially representing $[2\text{Fe–}2\text{S}]^{2+}$ clusters¹³⁷. After chemical reconstitution with 10 molar equivalents of iron and sulfide (Method 18), HydF contained on average 6.0 ± 0.2 irons per protein. The increased iron content was also confirmed by the increased absorbance at 410 nm (Figure 5.6 A, solid). While no protein precipitate was observed during reconstitution of HydF, precipitation was observed after a single freeze–thaw cycle, accounting for an approximately 50% protein loss. Future activity studies should thus be carried out with freshly reconstituted HydF^(E) samples.

Co-expression of HydE with HydF did not affect the iron–sulfur cluster content of HydF and very similar UV–Vis spectra (Figure 5.6 B) and iron numbers were obtained. The UV–Vis spectra of reconstituted HydF mirror spectra obtained for reconstituted *T. maritima* HydF²⁶ while previously characterised, as-isolated *C. acetobutylicum* HydF showed additional $[2\text{Fe–}2\text{S}]$ cluster characteristic absorbance features at approximately 310 nm and 580 nm³⁰ not observed here. This could indicate that in vitro reconstitution of HydF only assembles the $[4\text{Fe–}4\text{S}]$ cluster, but fails to populate the $[2\text{Fe–}2\text{S}]$ cluster state. This is not too surprising given that the primary sequence of HydF only contains a single conserved cysteine triad²⁶ and that the $[2\text{Fe–}2\text{S}]$ cluster is likely hold in place by coordination to the $[4\text{Fe–}4\text{S}]$ cluster via a protein derived cysteine residue⁴² (Scheme 1.1, 7).

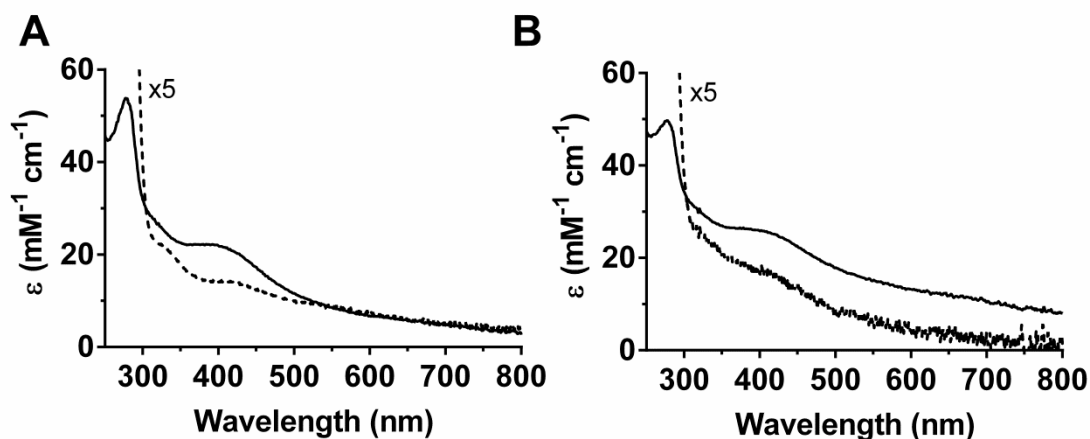


Figure 5.6 UV-Vis characterisation of HydF and HydF^E.

As-isolated HydF (---, 5x enhanced) or reconstituted HydF (—) expressed (A) in the absence or (B) in the presence of HydE.

To confirm the functionality of reconstituted HydF and HydF^E proteins, the GTPase activity was assessed by incubation with 2 mM GTP in the absence or presence of HydG (Method 24). The amounts of GDP formed were quantified using an ion-pair reverse phase HPLC method previously optimised in the laboratory²⁴¹ (Method 34). Irrespective of the genetic background of HydF and the presence of HydG, average turnover numbers for GDP formation of 1.5 min⁻¹ were observed (Figure 5.7 B). This is in the range of the k_{cat} values observed by Shepard and co-workers for as-isolated HydF (1.8–2.1 min⁻¹)³¹. Although the large error associated with the rate data does not allow a comparison between the activity of HydF in the presence or absence of HydG, the GTPase activity of reconstituted HydF and HydF^E was confirmed.

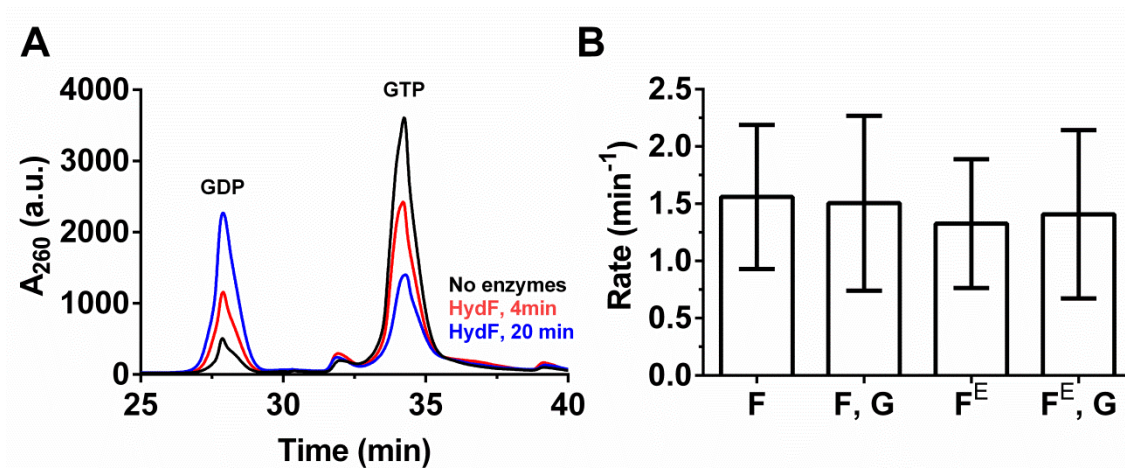


Figure 5.7 GTPase activity of reconstituted HydF and HydF^E.

(A) Representative HPLC chromatograms showing GDP ($R_t = 27.9$ min) formation from GTP ($R_t = 34.3$ min) as catalysed by HydF in 20 mM HEPES, 0.5 M KCl, 5% (w/v) glycerol, pH 7.4 buffer. Activity assays contained HydF^(E) (38 μ M), GTP (2 mM), MgCl₂ (2 mM), DTT (5 mM) and were incubated at 37 °C.

(B) Apparent GDP formation rates by HydF and HydF^E in the absence or presence of HydG (25 μ M), expressed in mol of GDP per mol of HydF per minute. The data represents the average of two time points with error bars as standard deviations.

5.4 Expression, purification and characterisation of *C. acetobutylicum* HydE

HydE is a radical AdoMet enzyme that slowly cleaves AdoMet in the absence of its main substrate ($k_{\text{cat}} \sim 0.008\text{--}0.02 \text{ min}^{-1}$)²⁴. The identity of this substrate is currently unknown, but the observation that HydA activation was achieved by heterologous co-expression with the hydrogenase maturation proteins in *E. coli*²² suggests that all required substrates for H-cluster assembly were present in the *E. coli* metabolic pool, including the HydE substrate.

Similar to HydG, *C. acetobutylicum* and *T. maritima* HydE contain two conserved cysteine motifs (Figure 5.8) and *T. maritima* HydE has been characterised to contain a maximum of eight irons and eight sulfides per monomer²⁴, suggesting the presence of two [4Fe–4S] clusters. However, in the available 1.35 Å resolution X-ray structure of *T. maritima* HydE³⁷, a [2Fe–2S] cluster is coordinated by the C-terminal cysteine triad.



Figure 5.8 Partial sequence alignment of HydE from selected organisms.

(A) Conserved N-terminal radical AdoMet CX₃CX₂C motif and (B) partially conserved C-terminal CX₇CX₂C motif.

Expression of N-terminally 6His tagged *C. acetobutylicum* HydE (42 kDa) was achieved similar to HydG and HydF (Method 11) and yielded on average 5 g/L grey cell paste. Using Ni-affinity chromatography (Method 13), 30 mg of 80% pure protein was isolated. The low expression yield was also observed in the literature⁴¹. Taking into account the sluggish growth rates of *E. coli* during HydE expression, this might suggest accumulation of a toxic product. As observed for as-isolated HydG and HydF, *C. acetobutylicum* HydE was purified containing substoichiometric amounts of iron (Figure 5.10, dashed). After chemical reconstitution with 10 molar equivalents of iron and sulfide (Method 18), HydE contained approximately 5.0 ± 0.2 irons per protein and showed an increased absorbance at 410 nm (Figure 5.10, solid).

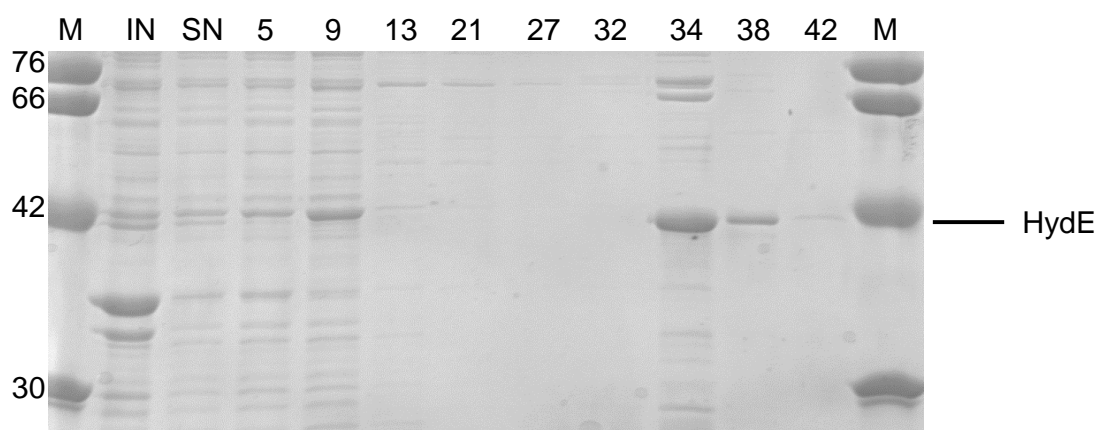


Figure 5.9 Ni-Affinity purification of HydE.

15% SDS-PAGE analysis of fractions eluted from the Ni-affinity column. M – molecular weight marker (kDa), IN – insoluble, SN – lysate supernatant, (5–27) – wash fractions, (32–42) – elution fractions.

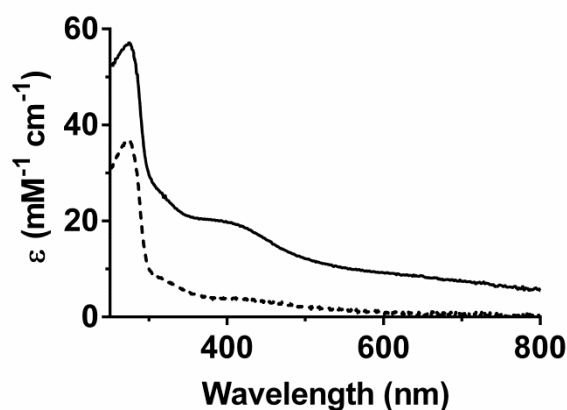


Figure 5.10 UV-Vis characterisation of HydE.

UV-Vis spectra of as-isolated HydE (---, 0.4 ± 0.1 Fe/protein) and reconstituted HydE (—, 5.0 ± 0.2 Fe/protein).

To confirm the AdoMet cleavage activity of reconstituted HydE ($22 \mu\text{M}$, 5.0 ± 0.2 Fe/protein) compared to HydG ($45 \mu\text{M}$, 6.2 ± 0.4 Fe/protein), both enzymes were separately incubated with AdoMet (1 mM), tyrosine (2 mM), MgCl_2 (2 mM) and sodium dithionite (1 mM) in the absence or presence of a cleared HydE lysate (~ 4 mg/mL) (Method 20). Tyrosine was also included in HydE activity assays to investigate the possibility that HydE may catalyse tyrosine cleavage following the mechanism which was originally proposed by Pilet et. al for HydG³³ to form the dithiolate bridge (Scheme 1.10). The formation of 5'-dAH and *p*-cresol was quantified after a 2 h incubation period at 37°C . Unfortunately, 5'-dAH could not accurately be quantified in the presence of the HydE lysate due to co-elution of unknown lysate components (Figure 5.11 A). Purified and reconstituted HydE apparently formed 1.2 equivalents of 5'-dAH and more interestingly, 0.2 equivalents of *p*-cresol compared to 6.6 and 4.3 equivalents, respectively formed by HydG (Figure 5.11 C). The absence of 5'-dAH and *p*-cresol in control assays containing no

maturation enzymes or only a HydE lysate (Figure 5.11 B) suggested that tyrosine cleavage to *p*-cresol was associated with HydE. The observation of slow *p*-cresol formation by HydE was intriguing. However, careful analysis of the purified HydE samples by SDS-PAGE and more importantly by Western blotting analysis employing an anti His tag (Method 9) identified that HydE contained traces of HydG (Figure 5.11 D). Taking into account the 1.5-fold uncoupled turnover observed for HydG (Figure 5.11 C), the HydG contamination in HydE likely accounts for all the *p*-cresol and 0.5 equivalents of the 5'-dAH quantified in HydE assays. As a result, HydE catalysed the formation of approximately 0.7 equivalents of 5'-dAH. This corresponds to an approximated turnover rate of 0.01 min^{-1} , in agreement with the previously mentioned AdoMet cleavage rates observed for *T. maritima* HydE²⁴.

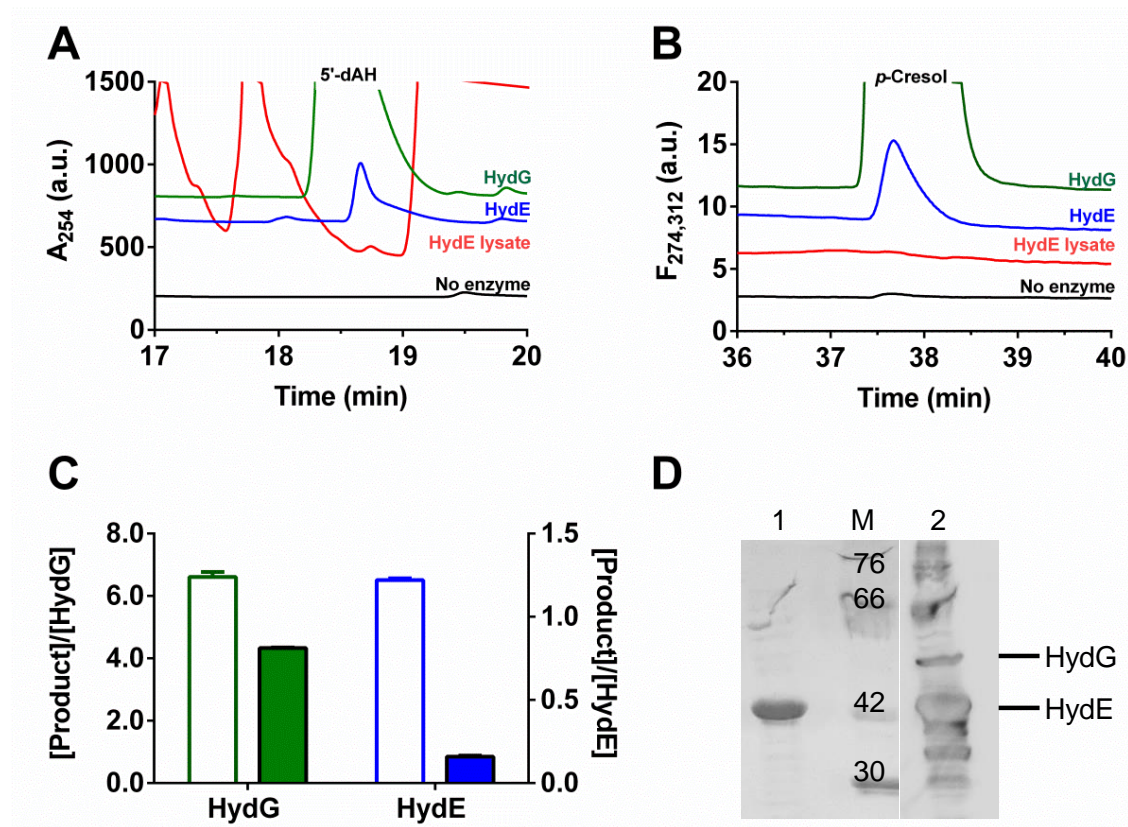


Figure 5.11 Activity studies with HydE.

HPLC chromatograms of (A) 5'-dAH ($R_t = 18.7$ min) and (B) *p*-cresol ($R_t = 37.7$ min) formation in the absence of maturation enzymes and by a cleared HydE lysate (~4 mg/mL), reconstituted HydE (22 μ M, 5.0 ± 0.2 Fe/protein) or HydG (45 μ M, 6.2 ± 0.3 Fe/protein) in the presence of AdoMet (1 mM), tyrosine (2 mM), MgCl₂ (2 mM), DTT (5 mM) and sodium dithionite (1 mM).

(C) Comparative formation of 5'-dAH (no fill) and *p*-cresol (filled) as catalysed by HydG or HydE (plotted on right y-axis). (D) HydG impurity in Ni-affinity purified HydE fraction as analysed by SDS-PAGE (1) and anti His tag Western blotting (2), M - molecular weight marker (kDa).

5.5 Strep tag pull-down assays for characterisation of activated HydF

To facilitate separation of HydF from HydG and/or HydE for characterisation, orthogonal purification tags are required. Both, N-terminally 6His tagged^{28,30,31} and Strep II tagged⁴¹ HydF have been employed in previous studies to evaluate the in vitro biosynthetic pathway towards the hydrogenase H-cluster. During this project, it was observed that the UV-Vis absorbance of reconstituted HydG and HydF proteins at 410 nm is greatly reduced after passage through a Ni-charged affinity column compared to using Strep-Tactin resin (Figure 5.12 A, B), likely reflecting an overall decrease in [4Fe-4S] clusters. The additional observation of a prominent shoulder at 330 nm and a shift from 410 nm to 420 nm suggests the presence of predominantly [2Fe-2S] clusters¹³⁷ rather than [3Fe-4S] clusters²⁴².

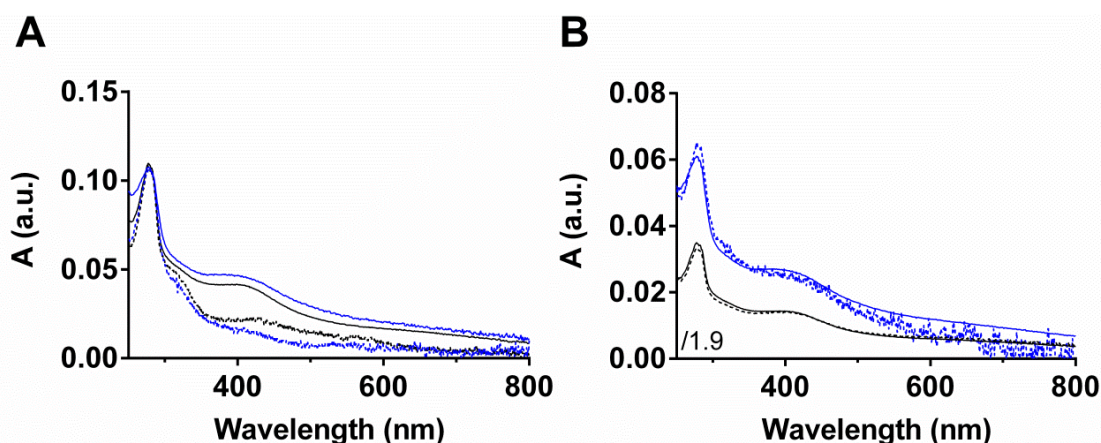


Figure 5.12 UV-Vis spectra of HydG and HydF before and after affinity chromatography.

Reconstituted 6His tagged HydG (black) and Strep II tagged HydF (blue) before (solid) and after (dashed) passage through a (A) Ni-Sephacryl Fast Flow or (B) Strep-Tactin Superflow high capacity column. Spectra are normalised to the protein 280 nm absorbance unless otherwise indicated.

Chapter 5 – Cyanide transfer

Bearing in mind the affinity of Sepharose for metal ions²⁴³, the observed cluster loss during Ni-affinity chromatography might be due to binding of cluster Fe³⁺ to free Sepharose sites. In addition, cluster destabilisation could be due to coordination of imidazole (present in the loading buffer) to a [4Fe–4S] cluster iron. Although imidazole (histidine) ligation to [4Fe–4S] clusters can be found in nature, especially in [NiFe]–²⁴⁴ and [FeFe]–hydrogenases⁶ as well as HydF itself^{28,231}, the unnaturally high concentration of imidazole in the buffer (20 mM) might promote cluster decomposition. Destabilisation of a four cysteine ligated [4Fe–4S] cluster due to imidazole coordination and subsequent conversion to predominantly [3Fe–4S] clusters was observed in a cysteine to histidine mutant of the DNA repair enzyme MutY²⁴⁵ and confirms that unnatural imidazole coordination may have a negative effect. To prevent imidazole induced loss of a potentially modified HydF [2Fe–2S] cluster during separation from the other maturation proteins, N-terminally Strep II tagged HydF was used in future investigations to allow for milder separation conditions.

To investigate the reaction conditions required for potential cyanide transfer from HydG to HydF, two in vitro assays employing reconstituted HydF or HydF^E and HydG were investigated (Table 5.2, Method 24). Assays (300–400 µL) contained an approximate 1:1 ratio of HydF and HydG maturation proteins (100 µM) as well as MgCl₂ (2 mM) and the HydG substrates AdoMet (0.3 mM) and tyrosine (2 mM). Bearing in mind the observation that an *E. coli* lysate was required for HydA activation by the Hyd maturation proteins³⁶, interaction assays were additionally supplemented with HydE and a cleared *E. coli* lysate (Table 5.2). Assays were incubated at 37 °C for 1–2 h in the absence or presence of the HydF substrate GTP (2 mM).

Table 5.2 Overview of activity assays carried out to establish reaction conditions for cyanide transfer from HydG to HydF.

Assays containing the reconstituted maturation proteins HydG (100 μ M), HydF^(E) (100 μ M), HydE (22 μ M) and the additives AdoMet (0.3 mM), tyrosine (2 mM), MgCl₂ (2 mM) and sodium dithionite (1 mM) were carried out at 37 °C, in the absence or presence of a cleared HydE lysate (~4 mg/mL) or GTP (2 mM) as indicated.

Assay	Reconstituted proteins	Substrates	<i>E. coli</i> lysates
1	HydF, HydG	AdoMet, tyrosine, \pm GTP	NA
2	HydF ^E , HydG	AdoMet, tyrosine, \pm GTP	NA
3	HydF, HydG, HydE	AdoMet, tyrosine, \pm GTP	Cleared HydE lysate

Strep II tagged HydF was anaerobically separated from the other proteins and small molecules using Strep-Tactin Superflow high capacity resin. Collected fractions were analysed by SDS-PAGE to confirm the identity and purity of the separated proteins (Figure 5.13 A). Using densitometry it was found that, independent of the presence of GTP, approximately 6% HydG routinely co-purified with HydF^(E) (Figure 5.13 B). All isolated protein fractions were analysed for their cyanide content by acid precipitating the protein and derivatisation of the neutralised supernatant with taurine and NDA (Scheme 1.11, Method 32)³⁴. The apparent recovery of approximately 0.2 equivalents of cyanide with a HydF elution sample from a HydF-HydG interaction assay (Figure 5.13 C, D) is likely to be a false positive due to (i) the inaccuracy of the Bradford method in determining protein concentrations below 2 mg/mL, (ii) the poor signal-to-noise ratio in the HPLC chromatogram for the apparent

cyanide derivative (Figure 5.13 C) and more importantly, (iii) the observation of inconsistent cyanide to HydG ratios in the wash fractions (Figure 5.13 D).

The varying quantities of cyanide detected in the eluted HydG fractions could indicate that cyanide might not be bound to HydG at the point of elution from the Strep–Tactin column. As a result, any cyanide identified with HydF might actually be HydG derived due to insufficient column washing. In future experiments, a prolonged washing period and analysis of intermediate wash fractions for cyanide are required to ensure that detection of cyanide on HydF will be a true observation. Initial UV–Vis analyses of reconstituted HydG after passage through a Strep–Tactin column showed that the [4Fe–4S] clusters stay intact (Figure 5.12 B), suggesting that the detected cyanide might not have been associated with an iron–sulfur cluster, but that it was released into solution during HydG turnover. Alternatively, incorporation of cyanide and CO into the HydG [4Fe–4S] cluster may destabilise the cluster, as required for a facile transfer to HydF, which may thus allow cluster removal by mild Strep–Tactin buffers. Unfortunately, the eluted and turned over HydG fractions were too dilute to obtain accurate UV–Vis spectra for investigation of the HydG [4Fe–4S] cluster content before and after turnover.

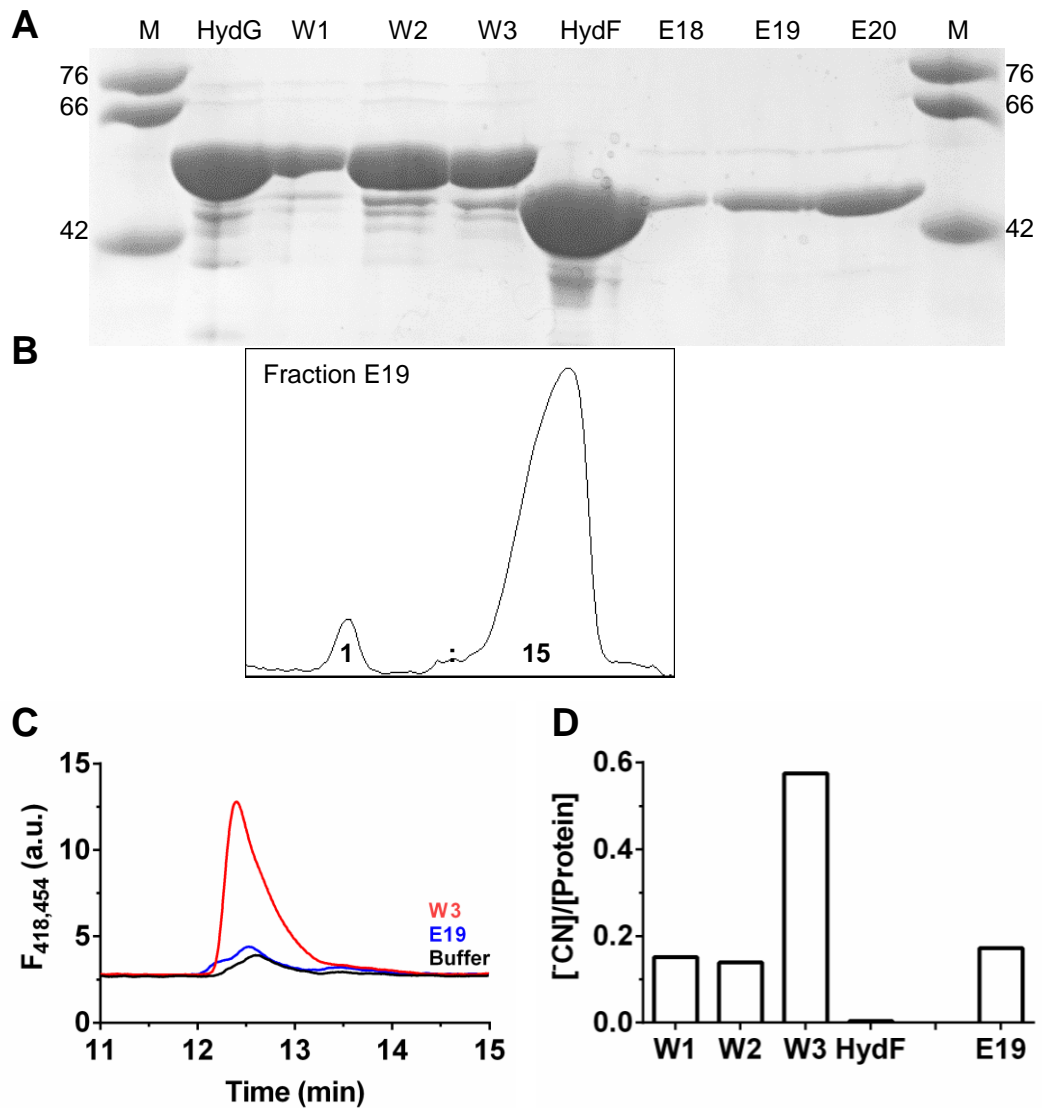


Figure 5.13 Analysis of HydF^(E), HydG and HydE interaction assays.

Representative (A) 15% SDS–PAGE analysis of fractions from HydF and HydG separations using Strep–Tactin Superflow high capacity resin. (B) Densitometry analysis of fraction E19. (C) HPLC analysis of selected fractions after cyanide derivatisation and (D) respective quantification.

The absence of cyanide in HydF samples isolated from HydG–HydF–(HydE) interaction assays could be for a number of reasons, including (i) that only a small amount of cyanide was transferred to HydF, but subsequently lost as hydrogen cyanide ($pK_a = 9.2$, $b.p. = 26\text{ }^\circ\text{C}$)^{246,247} during acid precipitation of the cyanide derivatisation procedure, or (ii) that the small amount of cyanide on HydF was below the cyanide quantification limit of $5\text{ }\mu\text{M}$. The latter scenario is very likely as the eluted HydF fractions only contained between 0.1 mg/mL and 0.3 mg/mL protein ($2\text{--}6\text{ }\mu\text{M}$ HydF), which, assuming two mol of cyanide bind to one mol of HydF leads to only $4\text{--}12\text{ }\mu\text{M}$ cyanide. Furthermore, (iii) the UV–Vis spectrum of reconstituted HydF in this study (Figure 5.6 A, solid) supports the presence of $[4\text{Fe–}4\text{S}]$ but not $[2\text{Fe–}2\text{S}]$ clusters. This supports the hypothesis that any $[2\text{Fe–}2\text{S}]$ clusters potentially present in as-isolated HydF may have been removed during in vitro reconstitution. While the GTPase activity of reconstituted HydF was not abolished (Figure 5.7), the chemically reconstituted iron–sulfur clusters may not reflect the natural protein environment and may, as a result, hamper interactions with the HydG and/or HydE maturation partners, ultimately preventing successful cyanide incorporation. To confirm this hypothesis, it would be interesting to repeat the protein interaction studies by Vallese and co-workers⁴¹ with reconstituted proteins.

The poor signal-to-noise ratio observed in the HPLC chromatogram of the apparent cyanide derivative in eluted HydF fractions (Figure 5.13 C) may be overcome by using a more sensitive cyanide detection method as discussed next.

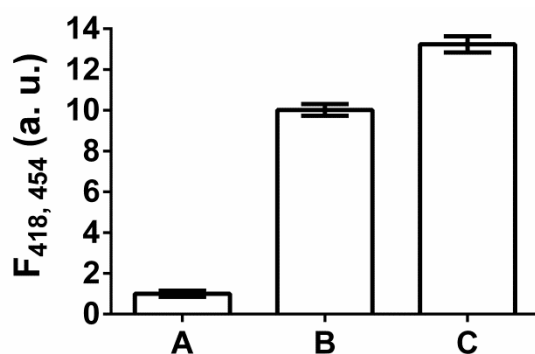
5.6 Modification of the cyanide detection method

The cyanide derivatisation procedure was revisited to improve the cyanide recovery from samples with a low concentration of HydF (<2 mg/mL). Assay samples of interest are routinely acid precipitated, followed by immediate neutralisation and the addition of the derivatisation reagents taurine and NDA³⁴ (Method 32). The high protein concentrations usually employed in HydG activity assays required the addition of acid for accurate and time dependent cyanide quantification. It was thus investigated whether addition of acid is also required for samples containing lower amounts of protein or whether the strongly basic conditions employed during the derivatisation procedure (use of 20% ammonia) would be sufficient for *in situ* protein precipitation. This method would be advantageous as any cyanide released would be immediately captured due to the presence of the derivatisation reagents.

A turned over activity assay containing 10 μ M HydG was derivatised (10 μ L) as usual (Table 5.3 A). The resulting fluorescence response of the cyanide derivatisation product was then compared to derivatisation reactions of a 10-fold diluted assay sample of increased volume (100 μ L). These derivatisations were carried out with and without acid/neutralisation treatment (Table 5.3 B, C). The results confirm a 14-fold enhanced cyanide detection sensitivity by (i) leaving out the acid addition/neutralisation step, (ii) increasing the volume of the derivatisation sample and (iii) leaving out the final twofold water dilution step before HPLC analysis (Figure 5.14). By additionally implementing increased sensitivity settings on the fluorimeter itself, the currently optimised cyanide quantification limit of 0.5 μ M could be improved even further if required.

Table 5.3 Comparative investigations of cyanide derivatisation procedure.

Cyanide containing sample	Treatment	Relative cyanide concentration to sample A (μM)
(A) $x \mu\text{M}$, 200 μL	Addition of acid (15 μL), buffer (20 μL) and base (30 μL)	0.755 x
	Derivatisation of above (10 μL) with 90 μL derivatisation reagents	0.075 x
	1:1 Dilution with water before HPLC injection	0.038 x
(B) 0.1 x μM , 200 μL	Addition of acid (15 μL), buffer (20 μL) and base (30 μL)	0.075 x
	Derivatisation of above (100 μL) with 90 μL derivatisation reagents	0.040 x
	Direct HPLC injection	0.040 x
(C) 0.1 x μM , 200 μL	No acid or neutralisation treatment	0.100 x
	Derivatisation of above (100 μL) with 90 μL derivatisation reagents	0.053 x
	Direct HPLC injection	0.053 x

**Figure 5.14 Optimisation of cyanide derivatisation procedure.**

Cyanide containing samples in Table 5.3 were derivatised in duplicate and are plotted relative to sample A, after correction for initial sample dilution.

5.7 Summary and conclusions

Initial experiments to investigate the cyanide transfer from HydG to HydF employed individually expressed, affinity purified and reconstituted protein samples. The functionality of reconstituted HydF^(E) and HydE enzymes was confirmed by monitoring their GTPase and AdoMet cleavage activity, respectively. No cyanide could however be unambiguously detected on orthogonally tagged HydF or HydF^E isolated from in vitro assays additionally containing HydG and its substrates AdoMet and tyrosine and/or HydE and a cleared *E. coli* lysate. This result is likely a combination of the dilute HydF (and therefore cyanide) samples and the limited cyanide quantification level of 5 μM . In addition, reconstitution of the maturase enzymes could have introduced non-natural iron-sulfur cluster states, potentially preventing essential protein interactions for cyanide transfer.

While the cyanide detection method was modified to allow a 14-fold more sensitive cyanide quantification, the use of protein samples of higher concentrations would be advantageous to ensure a more accurate determination of cyanide to protein ratios. Furthermore, high yielding expression and purification procedures as well as good in vivo iron-sulfur cluster assembly protocols are required to obtain as-isolated HydF and HydF^E proteins with a natural [4Fe-4S]-[2Fe-2S] cluster content. Isolation of acceptable quantities of 6His tagged *C. acetobutylicum* HydG can easily be achieved (section 2.2), but expression of HydE was limited while purification of Strep II tagged HydF and HydF^E was less successful. A substantial amount of HydF and HydF^E was not binding to the Strep-Tactin column and was lost in the flow through. Affinity chromatography using Ni-Sepharose resin is a more robust purification procedure, but substitution of the currently used Strep II

tag with a 6His tag on HydF is not advisable due to the observed iron–sulfur cluster loss upon contact with Ni–chelated Sepharose resin. Alternative protein tags known for mild purification conditions include the maltose/maltodextrin²⁴⁸ and the glutathione S–transferase/glutathione system²⁴⁹. The large size of the protein tag (43 kDa, 26 kDa, respectively) might however interfere with required interactions between the Hyd maturation proteins and makes this strategy less promising.

To aid soluble expression and in vivo assembly of the maturase iron–sulfur clusters, ISC assembly proteins may be co–expressed^{250,251}. Because *E. coli* expresses proteins belonging to the ISC biosynthesis and sulfur mobilisation machinery^{252,253}, the use of a $\Delta iscR$ strain as employed by Kuchenreuther and co–workers²⁵⁴ is more favourable than plasmid based overexpression of the ISC assembly proteins as deletion of *iscR* stimulates synthesis of iron–sulfur containing proteins²⁵⁵. The energy demand to maintain plasmid based ISC protein expression on the other hand may induce a stress response in *E. coli*²⁵⁶, which could ultimately reduce the protein yield. Addition of an iron and/or sulfur source to expressing *E. coli* cells has also been successfully used to improve intrinsic iron–sulfur cluster assembly²⁵⁷ and may be employed in the future.

HydG samples separated from HydG–HydF interaction assays showed inconsistent cyanide to protein ratios, suggesting that cyanide might not be incorporated into the HydG [4Fe–4S] cluster, but instead released into solution. Alternatively, the cyanide and CO associated [4Fe–4S] clusters may be more labile. The potential release of a loaded HydG iron–sulfur cluster was previously discussed in section 3.5.

Chapter 6

Conclusions and future work

6.1 Conclusions

This project was concerned with the mechanistic and structural characterisation of the radical AdoMet enzyme HydG. Particular focus was laid on establishing whether the additional cysteine CX₂CX₂₂C motif at the HydG C-terminus is able to coordinate an auxiliary [4Fe-4S] cluster and whether this cluster functions during L-tyrosine dependent cyanide and CO synthesis. The following paragraphs establish a possible mechanistic model for HydG catalysed tyrosine cleavage by taking into account results obtained in this study as well as very recent advances by Kuchenreuther and co-workers^{159,207}.

Chapter 6 – Outlook

HydG coordinates an auxiliary [4Fe-4S] cluster

UV-Vis and EPR spectroscopic characterisation of a *C. acetobutylicum*

N-terminal C96/100/103A triple HydG mutant which is unable to coordinate the radical AdoMet [4Fe-4S] cluster demonstrated unambiguously that the HydG C-terminal cysteine triad coordinates an auxiliary [4Fe-4S] cluster. This conclusion was also confirmed by the crystal structure of *Th. italicus* WT HydG. EPR analyses further demonstrated that this auxiliary cluster is reducible with 5'-deazaflavin and dithionite in vitro, but that it is unable to coordinate AdoMet.

C-terminal mutations decrease the affinity for tyrosine but not for AdoMet

In this thesis, C-terminal HydG mutants were used to extend previous activity studies^{34,133,160} to distinguish whether C-terminal mutations affect the rate of tyrosine cleavage or whether the subsequent cleavage of dehydroglycine or the related glycine radical is negatively affected. To initially estimate the affinity of the WT, C386S and Δ CTD HydG enzymes for tyrosine and AdoMet, Michaelis-Menten constants were determined. Measuring initial *p*-cresol formation in the presence of very low enzyme concentrations required the detection of *p*-cresol by its fluorescent rather than UV-Vis properties and further necessitated the use of an optimised HPLC elution method to separate *p*-cresol from tyrosine. Similarly small K_M^{AdoMet} constants (3-17 μM) were observed for all protein variants, suggestive of the AdoMet binding region not being perturbed by the introduced C-terminal mutations. This proposal is in agreement with the determined X-ray crystal structure of *Th. italicus* HydG, which shows that the C-terminus forms an individual domain and does not directly interact with AdoMet binding structural elements. The K_M^{TYR} constants for C386S HydG

(1.6 mM) and Δ CTD HydG (10.6 mM) were however 5- and 35- fold higher relative to the WT HydG K_M^{TYR} value. This supports the hypothesis that the auxiliary [4Fe–4S] cluster may be involved in tyrosine binding. Although direct coordination of tyrosine to WT HydG could not be confirmed by EPR analyses in this study, HYSCORE experiments by Kuchenreuther and co-workers¹⁵⁹ suggest that tyrosine itself or the derived dehydroglycine are coordinated to cluster II.

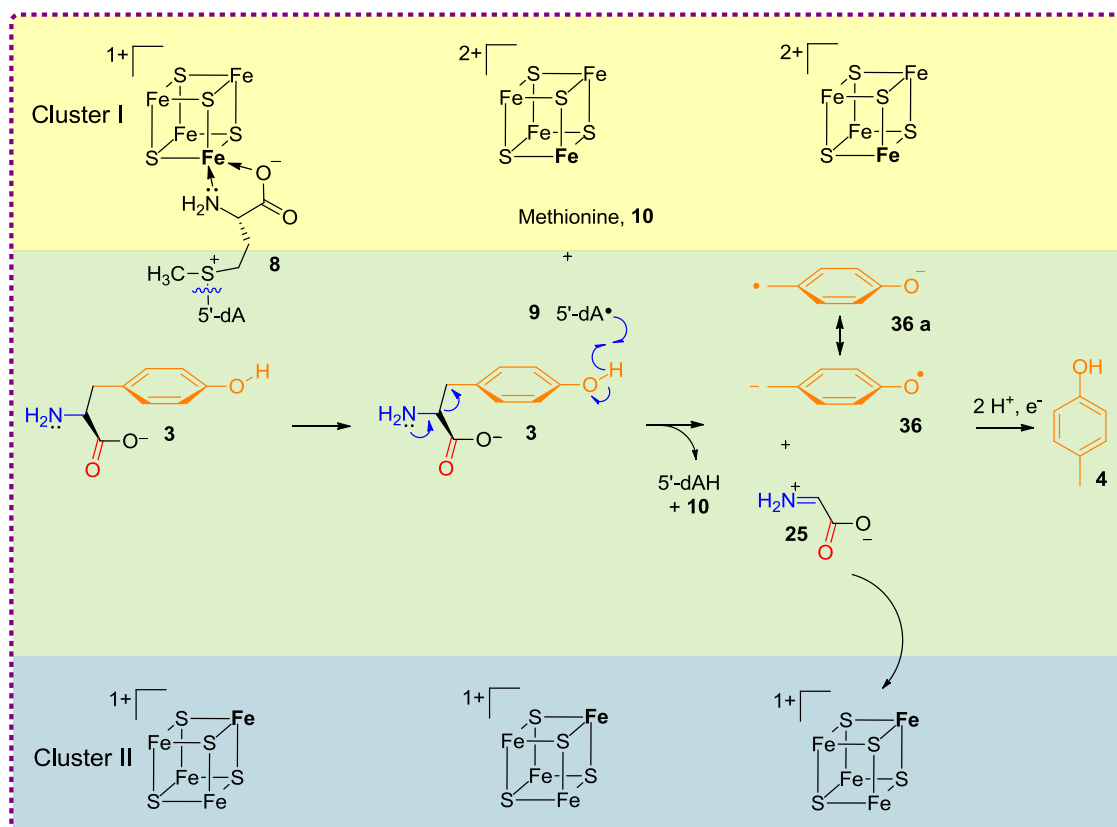
Tyrosine binding likely occurs inside the TIM barrel

To structurally characterise the HydG active site, crystallisation studies with HydG from three different (hyper)thermophilic organisms were carried out. Among other things, this involved large scale gel filtration chromatography to remove protein–iron–sulfur aggregates from the functional enzyme. Numerous crystallisation conditions were screened and optimised and resulted in small crystals of non-reduced *Th. italicus* HydG with AdoMet and tyrosine or reduced *T. lettingae* HydG with tyrosine. Although tyrosine was included in both crystallisation conditions, electron density representing this substrate could not confidently be assigned in the associated crystal structures. The *Th. italicus* HydG structure demonstrated a large 27 Å distance between the unique iron of the radical AdoMet and auxiliary [4Fe–4S] cluster, which weakens the proposal of tyrosine coordinating to cluster II. The AdoMet cleavage product 5'-dA• **9** generated near cluster I would not be closely situated to tyrosine's phenolic hydrogen for efficient hydrogen atom abstraction (Scheme 6.1). For this reason, coordination of dehydroglycine **25** to cluster II for subsequent cyanide and CO formation is more likely (Scheme 6.2, **73**, **77**). Binding of tyrosine **3** deeper inside the TIM barrel is further supported by the ability of the Δ CTD HydG mutant to form *p*-cresol **4**. However, the

Chapter 6 – Outlook

proposal that HydG and ThiH share active site TIM barrel residues for tyrosine binding³³ is not supported by the fact that amino acid residues conserved among HydGs and facing into the barrel are not present in ThiH. Formation of dehydroglycine **25** rather than the C-centred glycy radical has the mechanistic advantage that the former can ‘travel’ from its site of generation, presumably at the upper half of the TIM barrel, to the C-terminal [4Fe-4S] cluster (Scheme 6.1). This would not easily be possible for the highly reactive glycy radical. Heterolytic tyrosine cleavage is supported by detection of stoichiometric quantities of the dehydroglycine hydrolysis product glyoxylate in Δ CTD HydG assays, as well as EPR characterisation of the *p*-oxidobenzyl radical **36 a** in *Sh. oneidensis* WT HydG assays¹⁵⁹.

The preliminary observations that *p*-cresol **4** formation is pH dependent, with higher formation rates under basic conditions, may support the hypothesis that tyrosine **3** does not coordinate to cluster II, at least not via its α -amino group. The alkaline assay conditions may facilitate deprotonation of the tyrosine ammonium to ensure that N-lone pair donation into the C α -C β σ^* bond is possible (Scheme 6.1). If tyrosine were N-chelated to the unique cluster iron, this lone pair would not be available. Whether tyrosine is really bound in an anionic form or not is unclear at this moment and the exact reasons for the pH dependent activity differences require further investigations.



Scheme 6.1 HydG catalyzed tyrosine cleavage to *p*-cresol.

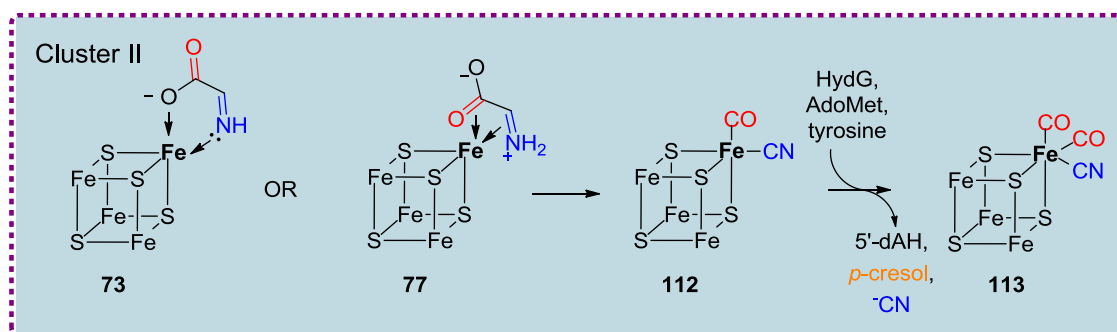
Depicted is a schematic of the reactions postulated to occur in the HydG active site. The AdoMet binding, upper part of the TIM barrel is highlighted in yellow, the main TIM barrel domain in green and the extra C-terminus in blue.

Heterolytic cleavage of tyrosine **3** results in dehydroglycine **25** and a *p*-oxidobenzylradical **36 a**. The former is likely transferred to cluster II. The unique iron atoms of both [4Fe-4S] clusters are shown in bold but cluster coordinating residues have been omitted for clarity.

Generation of a [3Fe-4S]-Fe(CO)₂CN complex on HydG

It was observed that WT and the C386S HydG mutant formed cyanide with similar relative rates compared to *p*-cresol, while the C-terminal truncated Δ CTD mutant yielded insignificant amounts of cyanide. This may suggest that cluster II is not essential for cyanide formation but that C-terminal residues could play a functional role instead. However, the alternative hypothesis, where the auxiliary cluster is required for cyanide synthesis cannot be excluded for the following reasons. (1) The ability of WT HydG to form equimolar equivalents of cyanide with respect to *p*-cresol varied between WT HydG samples from different reconstitution batches. This may have been due to a decreased reconstitution success of cluster II. (2) EPR analyses suggest that the C386S HydG mutant is able to coordinate some auxiliary [4Fe-4S] clusters (10–14%), which could have allowed the reduced synthesis of cyanide. The exact function of cluster II during the synthesis of cyanide and CO is unclear, but iron bound cyanide and CO signatures recently observed in the stopped-flow FTIR spectra of a *Sh. oneidensis* HydG activity assays¹⁵⁹ strongly suggest that cluster II accepts both diatomic ligands. The formation of almost three equivalents of cyanide during six turnovers of C386S HydG suggests that the ligand bound iron-sulfur cluster is released and potentially re-assembled during turnover. Unless the unique iron of each available cluster II uses its three coordination sites to bind cyanide, the reduced cluster II content (10–14%) would not explain the ability to form the observed amount of cyanide. Coordination of three cyanide molecules per cluster II might be possible in the absence of CO coordination. This possibility is supported by the observed lack of C386S HydG catalysed CO formation.

Interestingly, additional time resolved FTIR investigations by Kuchenreuther and co-workers identified that two sequential organometallic complexes are likely formed during turnover of WT HydG²⁰⁷. These include the cyanide and CO coordinated cluster II (112) as suggested above and a modified [3Fe-4S]-Fe(CO)₂CN cluster 113²⁰⁷ (Scheme 6.2). Insertion of atmospheric CO into 112 was excluded and the additional CO ligand is thought to derive from a second turnover of HydG²⁰⁷. Based on the $\sim 20 \times 10^{-4} \text{ s}^{-1}$ turnover rates of *C. acetobutylicum* WT HydG, the estimated 30 s timescale for conversion of 112 to 113 is one order of magnitude faster than expected. This might however be due to slightly different experimental conditions. The fate of the cyanide equivalent resulting from the proposed second turnover was not investigated.



Scheme 6.2 HydG catalysed dehydroglycine cleavage to cyanide and CO.

Depicted is a schematic of the reactions potentially occurring at the C-terminally coordinated cluster II. The unique iron is shown in bold, while cluster coordinating residues have been omitted for clarity.

Investigating HydG catalysed cyanide transfer to HydF

Experimental evidence in the literature suggested that HydF might be a scaffold protein to which the cyanide and CO ligands as well as the dithiolate bridge are transferred by the respective maturation proteins HydG and

Chapter 6 – Outlook

HydE^{30,31}. It was thus attempted to detect the transfer of cyanide from HydG to HydF. After incubation of HydF with HydG, AdoMet, tyrosine and/or HydE in the absence or presence of GTP, HydF was isolated from the assay mix by exploiting its orthogonal Strep II tag compared to 6His tagged HydE and HydG proteins. Unfortunately, no cyanide could confidently be detected on HydF. Instead, cyanide was identified in the wash fractions, suggesting that it may not stay associated with HydG. Although the 410 nm absorbance of the HydG [4Fe–4S] clusters did not change after passage through the Strep–Tactin column in the absence of the other assay components, cyanide release due to iron–sulfur cluster decomposition cannot be excluded as the cyanide and CO loaded [4Fe–4S] cluster may be more labile than the unmodified cluster II.

The ultimate goal of these preliminary experiments was to identify whether the cyanide and CO ligands are transferred on a HydG derived iron–sulfur cluster to HydF. It was planned to incubate ⁵⁷Fe enriched HydG with non–enriched HydF, where detection of a ⁵⁷Fe containing iron–sulfur cluster in the separated HydF sample would confirm transfer of iron from HydG to HydF. Similar experiments have recently been carried out with ⁵⁷Fe enriched HydG and non–enriched HydE, HydF and HydA²⁰⁷. It was identified that in vitro activated HydA coordinated ⁵⁷Fe, suggesting that cluster bound cyanide and CO ligands are transferred during H–cluster assembly. This observation does not clarify whether HydF^{30,31} or HydG³⁶ acts as a scaffold protein but questions previous proposals that the dithiolate bridge is inserted into the HydF [2Fe–2S] cluster before installation of the cyanide and CO ligands^{31,40,41}. Further research is required to address these intriguing ‘missing links’.

6.2 Future experiments

The observed ^{13}C , ^{15}N coupling with reduced cluster II in HYSCORE spectra of *Sh. oneidensis* WT HydG activity assays¹⁵⁹ are likely a result from dehydroglycine coordination. To address the important question of where tyrosine binds, advanced EPR techniques such as electron spin echo envelope modulation (ESEEM) and ENDOR spectroscopy may be applied to WT HydG in the presence of ^2H , ^{15}N , ^{13}C , and/or ^{17}O labelled tyrosine. From the hyperfine coupling constants between the quadrupole nuclei and the electron spins on the reduced [4Fe–4S] clusters, the distance of their separation can be inferred^{136,258–260}. Studies with tyrosine labelled at the hydroxyl, amino and carboxylate group are of particular interest. Although interactions of up to 10 Å are theoretically observable²⁶¹, the large separation between both clusters identified in the HydG crystal structure implies that coupling of tyrosine should only be observed with one cluster, if any at all. Bearing in mind the known radical AdoMet and auxiliary [4Fe–4S] cluster g values determined in Chapter 2, the spectroscopic data may be deconvoluted as to identify this participating cluster and to build a spatial map of tyrosine binding.

The pH dependence of HydG catalysed *p*-cresol formation was intriguing and may suggest that the affinity for tyrosine is enhanced under basic conditions. To investigate this proposal, rapid equilibrium dialysis may be used to determine the dissociation constant of tyrosine at varying pH. If the observed increase in the tyrosine cleavage reaction under basic pH is indeed due to an increased affinity of HydG for tyrosine, crystallisation of HydG in the presence of tyrosine or AdoMet and tyrosine may then be achieved by using more alkaline crystallisation conditions.

Chapter 6 – Outlook

Detailed elucidation of the tyrosine cleavage mechanism is a complex investigation and not easily addressed due to short lived intermediates and the fact that measurable parameters such as the number of transferred electrons are identical in both heterolytic and homolytic cleavage pathways. Experimental observations suggest that the tyrosine hydroxyl hydrogen is abstracted during tyrosine cleavage¹³⁰, but the resulting tyrosyl radical has not yet been experimentally observed. Tomter and co-workers²⁶² comprehensively characterised the protein derived tyrosyl radical of RNR R2 from Epstein-Barr virus using EPR, Raman and UV-Vis spectroscopy and these techniques may also be applied to a HydG assay to follow formation of the tyrosyl radical.

The role of cluster II during a potential electron transfer step may be investigated by reducing WT HydG stoichiometrically with 5'-deazaflavin. Reduction of the radical AdoMet cluster would allow generation of one equivalent of 5'-dA• to initiate formation of the tyrosyl radical. Assuming cluster II is a source for electrons, characterisation of the obtained turnover products (if any) may establish to which intermediate the electron was transferred. Any [4Fe-4S] cluster redox-changes may be observed using freeze-quench EPR. Although the radical AdoMet [4Fe-4S] cluster is oxidised during AdoMet cleavage and would also result in loss of the $S = \frac{1}{2}$ EPR signal, independent oxidation of the auxiliary [4Fe-4S] cluster may be identified due to its slightly different g values. Comparison of the time dependent loss of the auxiliary [4Fe-4S] cluster signal in the EPR spectrum with formation of *p*-cresol and cyanide could establish how many redox changes took place per turnover.

It was postulated that the cyanide and CO bound cluster II is released and a new [4Fe-4S] cluster reassembled during multiple turnovers of HydG. Due to the decrease of the characteristic [4Fe-4S] cluster absorption band around

400 nm in the presence of AdoMet¹⁵⁴ and/or sodium dithionite^{263,264}, UV-Vis spectroscopy cannot easily be used to follow potential [4Fe-4S] cluster release under the current turnover conditions. Ugulava and co-workers were able to characterise spectroscopic changes of the reduced BioB [2Fe-2S] cluster during biotin formation¹⁰⁸. In these experiments, BioB was reduced with a flavodoxin, flavodoxin reductase and NADPH mix¹⁰⁸. By employing the natural electron donor system of *C. acetobutylicum* HydG for turnover, likely to be a ferredoxin²⁶⁵, it may be possible to follow [4Fe-4S] cluster re-assembly spectroscopically.

Chapter 7

Experimental

7.1 Materials

Table 7.1 Overview of materials used in this study.

<i>Chemicals</i>	Source
<ul style="list-style-type: none"> • Reagent grade chemicals 	Sigma Aldrich, Fisher Scientific
<ul style="list-style-type: none"> • DTT • IPTG • Antibiotics 	Melford Laboratories Ltd.
<ul style="list-style-type: none"> • Bacto-tryptone • Yeast extract 	Oxoid
<ul style="list-style-type: none"> • Polyacrylamide-bis polyacrylamide • Bacto agar 	Fisher Scientific

Table 7.1 cont

<i>Consumables</i>	Supplier
<ul style="list-style-type: none"> Wizard® Plus SV Minipreps Plasmid DNA Purification System kit 	
<ul style="list-style-type: none"> Molecular weight markers for DNA electrophoresis 	Promega
<ul style="list-style-type: none"> dNTPs 	
<ul style="list-style-type: none"> PageRuler pre-stained protein ladder 	Thermo Scientific
<ul style="list-style-type: none"> Pierce Western Blotting Substrate 	
<ul style="list-style-type: none"> Nitrocellulose membrane, 0.45 µm 	Bio-Rad
<ul style="list-style-type: none"> EDTA-free protease inhibitor tablets 	Roche
<ul style="list-style-type: none"> Pre-packed Sephadex G-25 Nap-10, PD-10 columns 	
<ul style="list-style-type: none"> Superdex 75, Superdex 200 	GE Healthcare
<ul style="list-style-type: none"> Chelating Sepharose Fast Flow 	
<ul style="list-style-type: none"> Q- and SP-Sepharose 	
<ul style="list-style-type: none"> Source 15S 	
<ul style="list-style-type: none"> Strep-Tactin Superflow high capacity 	IBA
<ul style="list-style-type: none"> PES based membranes, 10 kDa MWCO 	Millipore
<ul style="list-style-type: none"> Sterile 0.22 µm, 0.45 µm filters 	
<ul style="list-style-type: none"> PES based spin filters, 10 kDa MWCO 	Sartorius Stedim Biotech
<ul style="list-style-type: none"> Far UV quartz cuvettes, 1 cm path 	Starna Scientific Ltd.
<ul style="list-style-type: none"> Disposable PMMA UV grade, semi-micro cuvettes, 1 cm path 	Fisher Scientific

Table 7.1 cont

• EPR tubes, Wilmad Quartz (CFQ), 4 mm OD	Sigma Aldrich
• Analytical HPLC columns	Phenomenex
• TLC plates, modified gel 60, RP-18, F254	VWR
• 24- and 96-well crystallisation plates	Greiner Bio-One
<i>Enzymes/Plasmids</i>	
• Benzonase	Sigma Aldrich
• BSA	
• Restriction enzymes	New England Biolabs
• Yeast inorganic pyrophosphatase	
• <i>PfuTurbo</i> polymerase	Stratagene
• pCDFDuet-1_ <i>hydG</i> _WT	J. B. Broderick & J. W. Peters lab (Montana State University)
• pCDFDuet-1_ <i>hydG</i> _C386S	
• pACYCDuet-1_ <i>hydE</i>	
• pCDFDuet-1_ <i>hydF</i>	
• <i>E. coli</i> AdoMet synthetase	
• pFM024_ <i>lipA</i> , pFM103_ <i>hydG</i>	Filipa T. Martins
<i>Antibodies</i>	
• Anti-6His tag, mouse/IgG2b	Thermo Scientific
• Rabbit anti-mouse IgG-HRP	Santa Cruz Biotechnology

Unless otherwise stated, commercial preparations of *S*-adenosyl-*L*-methionine were employed throughout all experiments.

7.2 Equipment

Microbiology

PCR amplifications were carried out in a Progene Thermal Cycler (Techne). Agarose gels and SDS-PAGE gels were run in an electrophoresis apparatus (Bio-Rad), while Western blots were run in a Mini Trans-Blot module (Bio-Rad) inserted into the electrophoresis unit. All gels were visualised using a GeneGenius Bio Imaging System from Syngene.

Bacterial Growth

Heat stable solutions for bacterial growth were sterilised in a PriorClave steam autoclave (PriorClave Ltd.) at 121 °C for 25 min, whereas glucose, arabinose and IPTG solutions were filter sterilised through 0.45 µm filters. Bacterial cultures were incubated in an Innova 4400 Incubator Shaker (New Brunswick, Scientific), an Innova 4230 Refrigerated Incubator Shaker (New Brunswick, Scientific) using 5 L or 250 mL Erlenmeyer flasks or a BioFlo® 110 fermentor with a 7.5 L vessel (Eppendorf UK Ltd). Plated bacterial cultures were grown in an Economy Incubator Size 2 (Gallenkamp). Cells were harvested by centrifugation (Sorvall, Evolution RC, Kendro) using SLC-6000, SLA-1500 or SS-34 rotors. Small scale centrifugations (< 1.5 mL) were performed using an Eppendorf 5415D microcentrifuge at room temperature.

Anaerobic purification, reconstitution and in vitro activity assays

All experiments involving oxygen sensitive proteins were carried out inside an anaerobic glove box (Belle Technology, Portesham, UK, O₂ < 2 ppm) equipped with a Pharmacia Acta FPLC (GE Healthcare, Buckinghamshire, UK) and a VC 130 Sonicator (Sonics and Materials, Newtown, Connecticut, USA) and maintained at 20 °C. Cell lysates were cleared in 250 mL gas tight polycarbonate centrifuge bottles (Beckmann–Coulter, High Wycombe, UK). Unless otherwise stated, purification was carried out with Pharmacia XK columns. Protein solutions (> 1 mL) were concentrated by ultrafiltration using an Amicon pressure–cell or spin filters. Determination of pH was achieved using a Mettler Delta 340 pH meter connected to a Mettler Toledo Inlab 413 Combination electrode.

Spectroscopy

Aerobic absorbance readings were performed using a Lambda 2 spectrophotometer (Perkin–Elmer) or a Tecan Safire² microplate reader. Anaerobic absorbance spectra using far UV quartz cuvettes were recorded with an Ocean Optics USB2000 spectrophotometer (Duiven, The Netherlands) equipped with a Mini–D2–GS light source connected by optical P–400–2–UV/SR fibres to a cuvette holder inside the glove box. Compound concentrations were adjusted as not to exceed 1.0 absorbance units for most accurate results.

NMR spectra

NMR spectra were recorded by Martyn J. Hiscox using a Bruker DPX 400 spectrometer (400 MHz, 100 MHz).

HPLC analyses

Chromatographic separation of compounds was achieved on a workstation (Gilson 321 Pump with H1 Heads and a Gilson 234 Autoinjector) equipped with a dual wavelength Gilson–UV–Vis–155 detector and a Shimadzu RF–10AXL fluorimeter. Chromatograms were analysed using Gilson Unipoint Software (version 5.11).

EPR spectroscopy

EPR measurements were performed by Enrico Salvadori (University College London) on a Bruker EMXplus spectrometer operating at 9.4 GHz (X-band) equipped with a 4122SHQE resonator, with an Oxford Instruments ESR900 cryostat for measurements in the temperature interval 10–40 K. Measurements were performed with a magnetic field sweep from 0 mT to 600 mT, a microwave power of 2 mW, a modulation amplitude of 0.5 mT and a modulation frequency of 100 kHz.

Crystallography

Crystal trays were manually prepared inside the glove box and monitored using a Meiji EMZ–13TR microscope with an Infinity 1 camera situated inside the glove box and connected via a USB cable to a laptop outside the glove box. Images were taken using the associated Infinity Capture or Infinity Analyse software.

Data analysis

EPR data was analysed and simulated using the EasySpin software²⁶⁶ with MATLAB (Release 2013a, The MathWorks, Inc., Natick, Massachusetts, USA).

Kinetic data was analysed and graphs prepared using GraphPad Prism (version 6.00 for Windows, GraphPad Software, La Jolla California USA).

Densometric analysis of SDS–PAGE gels was carried out with ImageJ.

Sequence alignments were carried out using the CLC Sequence Viewer software (version 6.5.4) and phylogenetic trees constructed by the same software using the Neighbor Joining algorithm.

The percentage identity between HydG sequences was determined using LALIGN²¹⁷ on the ExPASy server, while structural similarity was estimated using the ‘align command’ in PyMol²⁶⁷.

Figures of X–ray crystal structures were prepared using PyMol²⁶⁷.

7.3 General microbiology methods

Composition of liquid media can be found in Appendix 3.

Method 1 Preparation of competent cells

Competent cells were prepared using the rubidium chloride method by Hanahan²⁶⁸. A glycerol freeze smear of the required *E. coli* cells [XL-10 Gold, BL21(DE3) or Rosetta(DE3)pLysS] was added to 2YT media (10 mL) containing the appropriate antibiotic and was incubated overnight at 37 °C, 180 rpm. This culture was added as a 1% inoculum to fresh 2YT media (100 mL) supplemented with the appropriate antibiotic and grown at 37 °C, 180 rpm until an OD₆₀₀ between 0.6 and 0.7 was reached, at which point the cells were removed and chilled on ice for 10 min. Cells were harvested by centrifugation (2 x 50 mL, SS-34, 4000 rpm, 4 °C, 10 min). The supernatant was discarded and the pellets resuspended in ice cold TFB I buffer (10 mL, Table 7.2) and centrifuged again for 20 min. The cells were resuspended in TFB II buffer (1.5 mL, Table 7.2) before quickly divided into 100 µL aliquots and flash frozen in liquid N₂. All cells were stored at -80 °C until further use.

Table 7.2 Composition of TFB buffer solutions.

Buffer	Component	Quantity	Final concentration
TFB I	RbCl	12.1 g	100 mM
	MnCl ₂	9.9 g	50 mM
	KOAc	2.9 g	30 mM
	CaCl ₂	1.1 g	10 mM
	Glycerol	150 g	15% (w/v)

Adjust pH to 5.8 with 1% acetic acid, bring to 1 L and filter sterilise.

Table 7.2 cont.

TFB II	MOPS	2.1 g	10 mM
	RbCl	1.2 g	10 mM
	CaCl ₂	8.3 g	75 mM
	Glycerol	150 g	15% (w/v)

Adjust pH to 6.8 with dilute NaOH and filter sterilise. Store both at -80 °C.

Method 2 Transformation of competent *E. coli* cells

Aliquots of competent cells (100 µL) were thawed on ice, purified plasmid DNA (1 µL) added with care and the mix incubated on ice for 30 min before heat shocked at 42 °C for 40 s. The tube was returned to ice and cold SOC medium (250 µL, Table 7.3) added before incubation at 37 °C, 200 rpm for 1 h. Inside a sterile fume hood, the cell suspensions (40 µL) were spread onto 2YT agar plates containing antibiotic dependent on the plasmid used and were then incubated overnight at 37 °C. Plates were sealed and stored at 4 °C for up to two weeks.

For co-transformation experiments of *hydF* and *hydE* into *E. coli* BL21(DE3), positive clones from initial transformation of *hydE* were used to inoculate a 2YT overnight culture (10 mL). This culture was then used to prepare competent cells (Method 1) which were subsequently transformed with *hydF*. The reverse order of transformation was less efficient due to the sluggish growth rates of HydE in BL21(DE3).

Table 7.3 Composition of SOC medium.

Component	Quantity	Final concentration
Bacto-tryptone	20 g	2%
Bacto-yeast extract	5 g	0.5%
NaCl	0.5 g	10 mM
250 mM KCl	10 mL	2.5 mM
2 M MgCl ₂	5 mL	10 mM
Adjust pH to 7.0 with 5 M NaOH, bring to 980 mL and autoclave.		
1 M Sterile glucose	20 mL	20 mM

Method 3 Isolation of plasmid DNA

E. coli cells were harvested from overnight cultures (10 mL, 7500 rpm, 4 °C, 10 min) and plasmid DNA isolated/purified using the Wizard® Plus SV Minipreps Plasmid DNA Purification System Kit (Promega) as per the manufacturer's instructions. Plasmid DNA was eluted from the purification column with sterile deionised water (50 µL) and stored at -20 °C until required.

Method 4 Analytical digest

Purified plasmid DNA was digested with appropriate restriction enzymes and NEBuffer in the presence or absence of BSA at 37 °C for 2 h as summarised in Table 7.4 (optimal conditions were selected using the NEB Double Digest Finder available online at <https://www.neb.com/tools-and-resources/interactive-tools/double-digest-finder>). Digests were analysed by 1% agarose gel electrophoresis with ethidium bromide staining (Method 5).

Table 7.4 Analytical digest mixture.

Component	Quantity	Final concentration
Plasmid DNA (100–500 ng/ μ L)	5 μ L	50–250 ng/ μ L
NEBuffer (10x)	1 μ L	1x
BSA (1 mg/mL)	1 μ L	0.1 mg/mL
Restriction enzyme(s) (10–20 U/ μ L)	1 μ L per enzyme	1 – 2 U/ μ L
Sterile deionised water	To 10 μ L	

Method 5 Agarose gel electrophoresis

6x Gel loading buffer (2 μ L, Table 7.5) was added to each digest (10 μ L) and the samples loaded onto a 1% agarose gel. The gel was run in 1x Tris–Acetate–EDTA (TAE) buffer (Table 7.6) at a constant voltage of 90 V for approximately 45 min before stained in dilute ethidium bromide solution. After 1 min of staining, the gel was washed with water for 30 min, then visualised under UV light.

Table 7.5 Composition of 6x gel–loading buffer.

Component	Quantity
40% (w/v) Sucrose	4 g
0.25% Bromophenol Blue	25 mg
Adjust to 10 mL with deionised water and store at 4 °C.	

Table 7.6 Composition of 50x TAE running buffer.

Component	Quantity
TrisBase	242 g
Acetic acid	57.1 mL
500 mM EDTA, pH 8.0	100 mL
Adjust to 1 L with deionised water.	

Method 6 Preparation of glycerol freezes

Using a sterile loop, well isolated colonies were picked from plates containing the correct plasmid and incubated overnight at 37 °C, 180 rpm in 2YT media (10 mL) containing antibiotic before viciously mixed with an equal amount of filter sterilised 50% (w/v) glycerol. Aliquots were stored at –80 °C until required.

Method 7 Determination of protein concentration

Protein concentrations were determined using the Bradford method¹⁴⁷. In detail, Bradford reagent (1 mL, Table 7.7) was added to an appropriately diluted protein sample (<0.5 mg/mL, 20 µL) and the absorbance at 595 nm read against a buffer/media blank (20 µL) prepared similarly. Three BSA samples (0.13–0.5 mg/mL) were used as calibration standards.

Table 7.7 Composition of Bradford reagent.

Component	Quantity
Coomassie Brilliant Blue G250	100 mg
95% (v/v) EtOH	50 mL
Stir until completely dissolved.	
85% (v/v) Orthophosphoric acid	100 mL
Stir for 2 h, then adjust to 1 L with deionised water and vacuum filter.	

Method 8 SDS–PAGE analysis

The components listed in Table 7.8 were mixed to prepare a 15% resolving gel which was then applied to each of four plates (~5 mL); the surface was covered with isopropanol while the gel was allowed to set for ~45 minutes. The isopropanol layer was carefully removed before the stacking gel (Table 7.8)

applied and a Teflon comb inserted. The gel was set for another 45 minutes after which the comb was removed and the wells washed with deionised water. Gels were stored at 4 °C and used within one week.

Table 7.8 Composition of 15% SDS–PAGE resolving and stacking gel.

Component	Resolving gel	Stacking gel
	Quantity	
Deionised water	4.6 mL	5.5 mL
30% (w/v) Acrylamide	10 mL	1.3 mL
1.5 M Tris (pH 8.8)	5 mL	--
1.5 M Tris (pH 6.8)	--	1 mL
10% (w/v) SDS	200 µL	80 µL
10% (w/v) Ammonium persulfate (freshly prepared)	200 µL	80 µL
TEMED	8 µL	8 µL

Protein samples (~1 mg/mL, 20 µL) were mixed with 2x SDS–PAGE loading buffer (20 µL, Table 7.9) and heated at 95 °C for 5 min before loaded onto the gel as 10 µL aliquots. Electrophoretic separation was achieved at 200 V (~45 min) in 1x SDS–PAGE running buffer (Table 7.9). Gels were stained with Coomassie Brilliant Blue stain (Table 7.10) while heated for 3 x 20 s in a microwave, then destained (Table 7.10) before imaging.

Table 7.9 Composition of SDS–PAGE buffers.

Component	Quantity	Final concentration
<i>2x SDS–PAGE loading buffer</i>		
400 mM Tris.HCl, pH 6.8	25 mL	100 mM
Bromophenol Blue	0.2 g	0.2% (w/v)
SDS	4 g	4% (w/v)
Glycerol	20 g	20% (w/v)
DTT ^a	--	200 mM
Adjust to 100 mL with deionised water, store at 25 °C.		
<i>a</i> – Add DTT (154 mg) shortly before use to 5 mL buffer.		
<i>5x SDS–PAGE running buffer</i>		
TrisBase	15.1 g	125 mM
Glycine	94 g	1.25 M
10% (w/v) SDS	50 mL	0.5% (w/v)
Adjust to 1 L with deionised water.		

Table 7.10 Composition of SDS–PAGE imaging solutions.

Component	Quantity	Final concentration
<i>SDS–PAGE stain solution</i>		
Acetic acid	100 mL	10% (v/v)
MeOH	450 mL	45% (v/v)
Coomassie Brilliant Blue R250	2.5 g	0.25% (w/v)
Adjust to 1 L with deionised water.		
<i>SDS–PAGE destain solution</i>		
Acetic acid	100 mL	10% (v/v)
MeOH	300 mL	30% (v/v)
Adjust to 1 L with deionised water.		

Method 9 Western Blotting

Serial dilutions of the target protein (1–8 µg) was analysed by SDS–PAGE using a PageRuler pre–stained protein ladder as otherwise described in Method 8, but without staining the SDS–PAGE gel. Meanwhile, two filter pads and two blotting pads of a Mini Trans–Blot module as well as a nitrocellulose membrane were soaked with transfer buffer (Table 7.11) for 20 min in previously cleaned containers. The blotting sandwich was prepared by carefully placing a blotting pad and a filter pad onto the black side of the gel cassette, followed by the SDS–PAGE gel and the nitrocellulose membrane. Another layer of filter and blotting pad was added and the cassette carefully closed, paying attention not to disturb the layers, before assembled into the blotting module. A small magnetic stirrer bar, a cooling unit and approximately 1 L transfer buffer were then added, the module placed on a magnetic stirrer and the blot run at constant voltage (100 V) for 1 h with gentle stirring. The membrane was then placed into blocking buffer (TBS buffer + 5% (w/v) milk, Table 7.11) for 1 h at room temperature with gentle agitation, before transferred to a 50 mL Falcon tube containing the monoclonal 1° antibody (anti–6His tag, mouse/IgG2b) at 1 µg/mL in blocking buffer. After overnight incubation at 4 °C, the membrane was thoroughly washed 3–5 times with washing buffer (TBS buffer + 0.05% (v/v) Tween–20, Table 7.11), before transferred to a 2° antibody solution (0.4 µg/mL, rabbit anti–mouse IgG–HRP) in blocking buffer for a 1 h gentle agitation period at room temperature. The membrane was again thoroughly washed, before covered with a 1:1 pre–mixed Pierce Western Blotting Substrate solution (1 mL) in the absence of light. After approximately 30 s, the membrane was quickly covered in cling film and then immediately visualised.

Table 7.11 Composition of Western blotting buffers.

Component	Quantity	Final concentration
<i>Transfer buffer</i>		
TrisBase	6.06 g	25 mM
Glycine	28.8 g	192 mM
MeOH (HPLC grade)	400 mL	20% (v/v)
Adjust to 2 L with deionised water. Do not adjust pH, but check that > 8.0.		
<i>TBS buffer</i>		
TrisBase	2.42 g	20 mM
NaCl	8.78 g	150 mM
Adjust to 1L with deionised water and the pH to 7.4.		

7.4 Preparation of plasmids

The pCDFDuet-1 plasmids containing N-terminally 6His tagged *C. acetobutylicum* ATCC824 *hydG*_{WT}³⁰ or *hydG*_{C386S} as well as the plasmids pACYCDuet-1_*hydE* and pCDFDuet-1_*hydF* were kind gifts from the J. B. Broderick laboratory (Montana State University). Associated plasmid maps can be found in Appendix 2.

Method 10 Site-Directed Mutagenesis

The pCDFDuet-1 plasmid encoding the mutant gene *hydG*_{C96/100/103A} was prepared by Benjamin R. Duffus and Ian R. Bruzas (Montana State University) using a QuikChange Lightning Multi Site-Directed Mutagenesis Kit (Agilent Technologies, La Jolla, CA) and *C. acetobutylicum hydG*_{WT}³⁰ as a template with forward (CTT TCA AAC TAC GCT GTA AAC GGA GCT GTA TAT GCT CCA TAC CAT C) and reverse primers (G ATG GTA TGG AGC ATA TAC AGC TCC GTT TAC AGC GTA GTT TGA AAG) from Integrated DNA Technologies (Coralville, IA). Incorporation of the mutations was confirmed by sequencing (ISU Molecular Research Core Facility, Pocatello, ID). The plasmid encoding *hydG*_{C386S} was prepared similarly by Shawn E. McGlynn (Montana State University). The presence of the C386S mutation (TGT→TCT) and the absence of secondary mutations was confirmed by sequencing (Eurofins, UK).

The plasmid containing the mutant gene *hydG*_{ΔCTD} encodes a STOP codon in place of C386 and was prepared using a QuikChange Site-Directed Mutagenesis Kit (Stratagene) with the *hydG*_{WT} encoding plasmid³⁰ as a template with forward (TAT ATT CCA AGC TTT TAA ACC GCT TGT TAT CGT

Chapter 7 – Experimental

GAA GGA) and reverse primers (TCC TTC ACG ATA ACA AGC GGT TTA AAA GCT TGG AAT ATA) synthesised by Eurofins UK.

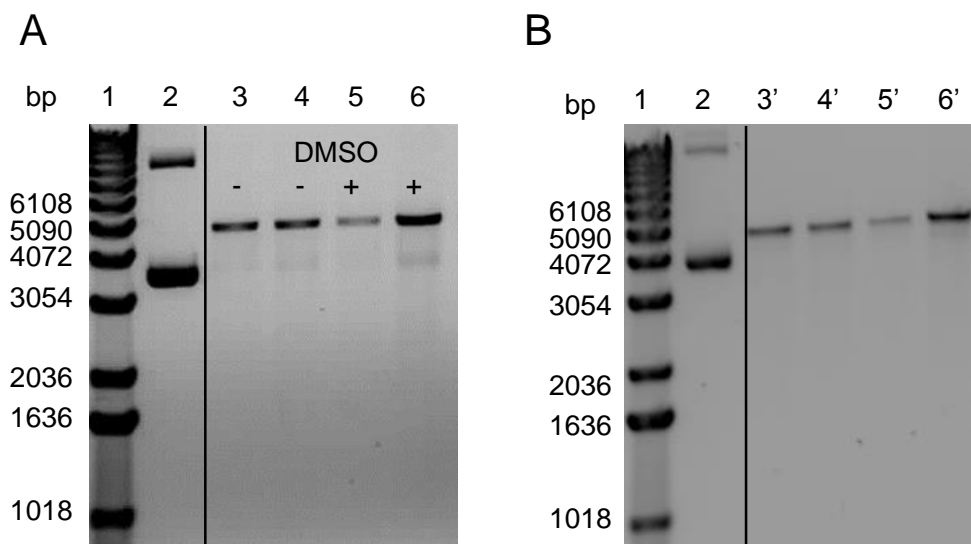
Initial PCR reactions were prepared with *PfuTurbo* polymerase in the presence or absence of dimethyl sulfoxide (DMSO) (Table 7.12) and cycled in a PCR machine as outlined in Table 7.13. The PCR reactions were analysed by 1% agarose gel electrophoresis (Method 5, Figure 7.1 A), before the remainder (~45 μ L) was subjected to DpnI digestion (1 μ L, 10 U/ μ L) for 1.5 h at 37 °C (Figure 7.1 B). These digests were directly transformed into competent *E. coli* XL10–Gold cells (Method 2) and the presence of the pCDFDuet–1 plasmid was confirmed by single and double analytical restriction digests (Method 4) using the restriction enzymes BamHI and Sall (not shown). Incorporation of the mutation and absence of secondary mutations was confirmed by sequencing (Eurofins, UK).

Table 7.12 Components for mutagenesis PCR.

Component	Volume (μ L)	Final Quantity
10x Reaction buffer	5	1x
dsDNA Template (50 ng/ μ L)	0.1–1.0	5–50 ng
Forward oligo	0.97	125 ng
Reverse oligo	0.97	125 ng
dNTP mix (10 mM each)	1	200 μ M
(DMSO)	(2.5)	(5%)
Sterile deionised water	Adjust to 49 μ L	NA
<i>PfuTurbo</i> polymerase (2.5 U/ μ L)	1	2.5 U

Table 7.13 Optimised PCR cycling parameters.

Comment	Number of Cycles	T (°C)	Time (min)
Denature	1	95	1
Denature		95	1
Anneal	15	63	1
Extend		72	8
Final extension	1	72	10
'Storage'	1	4	hold

**Figure 7.1 Analytical 1% agarose gel analyses of mutagenesis PCR mix towards pCDFDuet-1 containing *hydG_ΔCTD*.**

Equal volumes of mutagenesis PCR mix (10 μ L) were loaded onto a 1% agarose gel and stained with ethidium bromide. (A) Lane 1 – DNA ladder (bp), lane 2 – pCDFDuet-1 WT *HydG* template plasmid, lanes (3–6) – mutagenesis PCR products where 10 ng or 20 ng dsDNA template was used in uneven and even numbered lanes, respectively. The presence or absence of DMSO in the PCR mix is indicated. (B) Mutagenesis PCR products after DpnI digest, lanes as in (A).

7.5 Expression and purification of proteins

Note that HydF as well as HydG and HydE proteins required for interaction studies with HydF were purified with buffers containing KCl instead of NaCl. Purification of HydG variants for spectroscopic and kinetic characterisations was carried out with NaCl containing buffers.

Method 11 Large scale expression of proteins from *C. acetobutylicum*

The following protocol is generalised and was used to express the *C. acetobutylicum* proteins used throughout these studies as summarised in Table 7.14. 2YT media (100 mL) containing the appropriate antibiotic was inoculated with a glycerol freeze smear of the target protein in *E. coli* BL21(DE3) and incubated overnight at 37 °C, 180 rpm before used (4 x 12.5 mL) to inoculate fresh 2YT media (4 x 1.25 L) supplemented with antibiotic, glucose (5 g/L) and potassium phosphate (50 mM, pH 7.5). The cells were grown to an OD₆₀₀ between 0.6 and 0.8, which usually took 2–3 h, before protein expression was induced by the addition of IPTG (1 mM). Cells were grown for a further 2 h at 27 °C, then transferred into a sealed 5 L Schott bottle and further stirred at 4 °C overnight. Cells were harvested by centrifugation (SLC–6000, 7500 rpm, 40 min, 4 °C) to give a beige cell paste, which was stored at –80 °C until further use.

Table 7.14 Parameters for expression of proteins from *C. acetobutylicum*.

Target protein	Parent plasmid(s)	Antibiotic ($\mu\text{g}/\text{mL}$)	Yield (g/L)
HydG variants	pCDFDuet-1	Streptomycin (50)	4.5
HydE	pACYCDuet-1	Chloramphenicol (30)	4.5
HydF	pCDFDuet-1	Streptomycin (50)	7.5
HydF ^E	pCDFDuet-1,	Streptomycin (50)	3.5
	pACYCDuet-1	Chloramphenicol (30)	

Method 12 Expression of HydG in a fermenter

Improved yields of HydG (when co-expressed with the ISC proteins) could be obtained through protein expression in the fermenter instead of using Erlenmeyer flasks. Although the yield of cells was reduced from 40–60 g to 25–35 g, the purified proteins contained a higher proportion of assembled iron–sulfur clusters.

An overnight starter culture to express the target (hyper)thermophilic HydG protein was prepared as described in Method 11. This culture (50 mL) was then used to inoculate freshly autoclaved 2YT media (5 L) which additionally contained ampicillin (100 $\mu\text{g}/\text{mL}$), glucose (5 g/L), potassium phosphate (50 mM, pH 7.5) and which had been equilibrated to 37 °C at 50 rpm. The cells were grown to an OD_{600} between 0.6 and 0.8 with dO_2 dependent agitation rates, calibrated to $\text{dO}_2 = 0$ with 0 rpm and $\text{dO}_2 = 100$ with 250 rpm. Reaching the exponential growth phase usually took 2–3 h, at which point protein expression was induced by the addition of arabinose (20% (w/v), 10 mL/L). Cells were grown for a further 4–5 h at 27 °C, before harvested by centrifugation (SLC–6000, 7500 rpm, 40 min, 4 °C) to give a dark grey to black cell paste (~30 g), which was stored at –80 °C until further use.

Method 13 Ni-affinity purification of 6His tagged proteins

Inside an anaerobic glove box, the frozen cell paste of the 6His tagged target protein was resuspended in anaerobic buffer A (20 mM Hepes, 0.5 M NaCl/KCl, 5% (w/v) glycerol, 20 mM imidazole, pH 7.4) and stirred for 30 min in a cooled water bath before addition of lysozyme to 0.1 mg/mL and one EDTA-free protease inhibitor tablet for every 50 mL suspension. After an additional 1 h stirring period, the cells were lysed by sonication (5–6 x 10 min, 2 s bursts, 20 W) to approximately 20 mg/mL and cleared by centrifugation (SLA-1500, 14500 rpm, 40 min, 4 °C). The cleared cell lysate was loaded with respective flow rates of 5 mL/min or 10 mL/min onto a XK26 or XK50 column, packed with chelating Ni-Sepharose Fast Flow resin (30 mL). The UV-Vis absorbance at 280 nm was monitored and the column was washed with buffer A until the absorbance returned to the baseline. A linear gradient to 60% buffer B (20 mM Hepes, 0.5 M NaCl/KCl, 5% (w/v) glycerol, 0.5 M imidazole, pH 7.4) was then applied over 100 mL to elute the target protein. Fractions containing the target protein (as judged by the brown colour) were pooled, concentrated to 20–30 mL by ultrafiltration before loaded at 3 mL/min onto a Superdex 75 column (XK26, 50 mL), previously equilibrated with buffer C (20 mM Hepes, 0.5 M NaCl/KCl, 5% (w/v) glycerol, 5 mM DTT, pH 7.4). The protein was eluted with the same buffer and the most concentrated 10 mL fractions were pooled and further concentrated. Aliquots of 0.5 mL were flash frozen in liquid N₂ and stored at –80 °C until further use. On average, 180–250 mg of pure WT, C386S or Δ CTD HydG and 20–30 mg of pure HydE was obtained from 5 L growths.

Method 14 Analytical gel filtration chromatography

Affinity purified and reconstituted HydG variants (3–5 mg/mL) were individually loaded (0.5 mL, 1 mL/min) onto an Econo Column (Biorad, 1.5 cm x 50 cm, 125 mL) packed with Superdex 200 and pre-equilibrated in buffer C (20 mM Hepes, 0.5 M NaCl, 5% (w/v) glycerol, 5 mM DTT, pH 7.4). The elution volume of each protein fraction was noted. A calibration curve was obtained by plotting the log of the molecular weights of the proteins alcohol dehydrogenase (146.8 kDa), BSA (66.5 kDa) and lysozyme (14 kDa) loaded similarly against their partition coefficient (K_{av}). The partition coefficient was calculated using Equation 7.1, with V_e – elution volume, V_v – column void volume (elution volume of blue dextran, 2000 kDa) and V_c – calculated column volume.

$$K_{av} = \frac{V_e - V_v}{V_c - V_v} \quad \text{Equation 7.1}$$

Method 15 Purification and reconstitution of (hyper)thermophilic HydG

Affinity purification of (hyper)thermophilic HydG proteins was carried out similar to Method 13, but cell pastes from 2 x 5 L growths were used to increase the total yield of protein, as required for more reproducible crystallisation experiments. An additional modification was the addition of benzonase (~370 units) to the resuspended cell pastes. Sonication was found to be inefficient, likely due to the large suspension volume, and was therefore carried out in two separate batches, before recombination and harvesting of the cells. Between 250 mg and 350 mg of *T. lettingae* and *T. maritima* HydG was obtained after Ni-affinity chromatography, with the latter being considerably less pure.

Chapter 7 – Experimental

The affinity purified protein (~3 mg/mL, ~90 mL) in buffer C (20 mM Hepes, 0.5 M NaCl, 5% (w/v) glycerol, 5 mM DTT, pH 7.4) was brown–green in colour. It was not further concentrated but the iron–sulfur clusters immediately reconstituted overnight with 8 molar equivalents of iron and sulfide as described in Method 18. Little (if any) protein precipitate was observed the next day and the now dark green protein gently concentrated to 2 mL, before centrifuged (13000 rpm, 15 min) and loaded at 1 mL/min onto a Superdex 75 column (XK26, 300 mL) previously equilibrated overnight into buffer C. Once the loading was complete, the flow rate was increased to 2 mL/min and the black loading solution was separated into an earlier eluting black band and a later eluting golden band. Separation of both bands varied between HydG from different organisms as described in Chapter 4 and all fractions were collected. After analysis by SDS–PAGE (Method 8), the golden, pure HydG containing fractions were pooled and re–reconstituted with 5 molar equivalents of iron and sulfide overnight (Method 18). Any protein precipitate was removed by centrifugation (SS–34, 14000 rpm, 4 °C, 15 min) before the protein concentrated using a ultrafiltration pressure cell or spin filters to approximately 55 mg/mL. Protein was lost during this multistep purification and reconstitution procedure, 70% and 87% on average for *T. lettingae* and *T. maritima* HydG, respectively. The previously concentrated protein was immediately used to prepare crystallisation trays or stored inside the glove box for a maximum of one week. Storage at –80 °C at this stage was found to result in protein precipitate after thawing. If ‘too much’ protein was purified by Ni–affinity chromatography, non–concentrated protein aliquots after the first reconstitution were stored at –80 °C. When required, these fractions were gently thawed, concentrated and purified by Superdex 75 gel filtration and re–reconstituted as described above.

Method 16 Ion exchange purification of *T. maritima* HydG

Anion exchange purification of *T. maritima* HydG was attempted by initially diluting a Ni-purified HydG fraction 10-fold into buffer D (20 mM Tris, 5% (w/v) glycerol, 5 mM DTT, pH 8.3). This solution (~30 mL) was then applied at 4 mL/min onto a Q-Sepharose column (XK16, 20 mL). After the UV-Vis absorbance returned to the baseline, protein elution was achieved by applying a gradient to 1 M NaCl in buffer D. Two poorly resolved peaks eluted between 0.3 M and 0.5 M NaCl.

Cation exchange purification was similar attempted, with pre-purified HydG diluted into buffer E (50 mM Mes, 5% (w/v) glycerol, 5 mM DTT, pH 6.0), before being loaded onto a SP-Sepharose column (XK16, 20 mL). Protein elution was achieved over a 1 M NaCl gradient in buffer E, where a protein of light green colour eluted between 0.5 M and 0.6 M NaCl.

Method 17 Affinity purification of Strep II tagged HydF and HydF^E

Inside an anaerobic glove box, protein purification was initiated by resuspending the obtained paste (3 mL/g) in buffer F (100 mM Tris, 0.5 M KCl, 5% (w/v) glycerol, 1 mM DTT, pH 8.0), followed by addition of benzonase (~370 units). The suspension was then stirred in a cooled water bath for 30 min before addition of lysozyme (0.1 mg/mL) and EDTA free protease inhibitor tablets (1 tablet/50 mL lysate). After 1 h, cell lysis was achieved by sonication (4–6 x 10 min, 2 s bursts, 20 W) and the lysate (~20 mg/mL) cleared by centrifugation (SLA-1500, 14500 rpm, 40 min, 4 °C). The extract was applied (2 mL/min) to Strep-Tactin High Capacity resin (XK16, 25 mL) equilibrated with buffer F. The column was then washed with buffer F before protein elution was achieved by applying a step to buffer G (100 mM Tris, 0.5 M KCl, 5% (w/v)

Chapter 7 – Experimental

glycerol, 1 mM DTT, pH 8.0, 2.5 mM *d*-dethiobiotin). Collected protein fractions (light brown in colour) were pooled and concentrated to approximately 20 mL before applied (5 mL/min) to a Superdex 75 column (XK26, 50 mL) equilibrated with buffer C (20 mM Hepes, 0.5 M KCl, 5% (w/v) glycerol, 5 mM DTT, pH 7.4). Buffer exchanged fractions were pooled and concentrated to 4–8 mg/mL before stored at –80 °C as 0.5 mL aliquots. Protein concentrations above 10 mg/mL could not be achieved under these conditions due to protein precipitation. Poor and non-reproducible retention of HydF on the Strep–Tactin column was likely the reason for yields ranging between 10 mg and 100 mg from 5 L growths.

7.6 Protein reconstitution and activity assays

Method 18 Reconstitution of iron–sulfur clusters

Inside an anaerobic glove box, as-isolated protein in buffer C (20 mM Hepes, 0.5 M NaCl/KCl, 5% (w/v) glycerol, 5 mM DTT, pH 7.4) was incubated with 5 mM DTT (200 mM stock in H₂O) for 25 min before dropwise addition of FeCl₃ (20 mM stock in buffer C) over a similar time period. For WT, C386S HydG as well as, HydE, HydF and HydF^E, 10 molar equivalents of FeCl₃ with respect to protein concentration were added, while 6 molar equivalents were used for Δ CTD HydG. In each case, the protein solution changed colour from dark beige to reddish–brown. The sulfur source Na₂S₉H₂O was similarly added, in equimolar concentrations to FeCl₃, and the resulting dark brown to black mixture gently stirred for a further 2 h or left to agitate overnight. Precipitated protein and excess iron sulfide was removed by centrifugation (SS–34, 19000 rpm, 15 min, 4 °C) and the protein exchanged into the required buffer via a pre-equilibrated PD–10 column. It was observed that reconstitution of highly concentrated protein solutions readily resulted in protein precipitation. Although the following concentrations were found suitable for minimal precipitation; HydG variants – 500 μ M, HydE – 100 μ M, HydF^(E) – 100 μ M; protein loss of up to 50% was not uncommon during chemical reconstitution but varied between reconstitution batches.

Method 19 Iron content analysis

The iron content of reconstituted and as-isolated protein samples (1 mL) at approximately 10 μ M or up to 80 μ M, respectively was determined using the method of Fish¹⁴⁵. An iron calibration curve was obtained using direct dilutions of a FeSO₄·7H₂O stock solution (50 μ g/mL) in water as outlined in Table 7.15.

Table 7.15 Dilution series for Fe²⁺ calibration curve.

50 µg/mL Fe ²⁺ stock (µL)	H ₂ O (µL)	Fe ²⁺ (nmol)
400	600	72
350	650	63
300	700	54
250	750	45
200	800	36
150	850	27
100	900	18
50	950	9
30	970	5
10	990	2
0	1000	0

Reagent A (0.142 M KMnO₄ in 0.6 M HCl) was freshly prepared and added (500 µL) to all samples before a 2 h incubation period 60 °C in a heating block. Meanwhile, reagent B was prepared by addition of ammonium acetate (5 M), ascorbic acid (2 M), ferrozine (6.5 mM) and neocuproine (13.1 mM) to a known volume of water in the order and final concentrations stated. If the solution is not yellow, it is likely contaminated and should be prepared again. If an old batch of ammonium acetate was used, the total volume of reagent B may vary slightly due to its hygroscopic properties, but was not found to affect the outcome of the analysis. The protein and calibration samples were allowed to cool to room temperature before reagent B was added (100 µL). After the pink colour had developed fully (~10 min), the absorbance at 562 nm was read and the amount of iron in the protein samples estimated from a calibration curve of iron standards prepared and analysed in parallel (Figure 7.2).

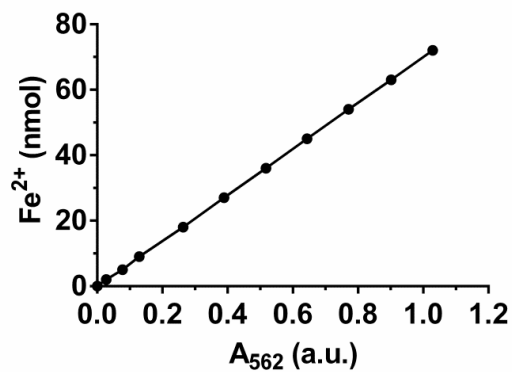


Figure 7.2 Calibration curve of FeSO₄·7H₂O standards.

Method 20 General HydG in vitro activity assays

Unless noted otherwise, all solutions were prepared inside an anaerobic glove box using the deoxygenated assay buffers stated throughout this thesis. If required, previously reconstituted HydG was exchanged into assay buffer via a pre-equilibrated PD-10 column. Tyrosine stock solutions (20 mM) were freshly prepared by addition of a 25.71 mM stock in 200 mM HCl (sonication required, 350 μ L) to a mixture of the appropriate assay buffer (20 μ L) and 1 M NaOH (80 μ L). Further dilutions were achieved using assay buffer as required. Assays (200 μ L) were prepared in duplicate unless stated by addition of AdoMet (10 μ L), HydG (100 μ L) and tyrosine (80 μ L) in the order stated to 1.6 mL Eppendorf tubes at final concentrations as specified in the individual chapters or referred Methods. If the addition of supplements such as MTAN, substrate or product like molecules was required, smaller volumes of HydG at higher concentrations were usually employed, as not to increase the total assay volume beyond 200 μ L. In all cases, sodium dithionite (10 μ L) was added into the cap of each tube and the assays transferred into a water bath outside the glove box for a 5 min temperature equilibration period at 37 °C. Assays were initiated by inverting the Eppendorf tube to mix sodium dithionite with the

Chapter 7 – Experimental

remaining components. Negative control assays were devoid of sodium dithionite unless otherwise stated. All assays were stopped at selected time points by acid precipitating the protein using 20% perchloric acid (15 μ L). When assays were also analysed for cyanide formation, 0.5 M HEPES, pH 7.5 (20 μ L) and 1 M NaOH (30 μ L) were also immediately added. The resulting suspensions were cleared by centrifugation (13000 rpm, 10 min) and the supernatants stored at -80°C before HPLC analyses (section 7.9).

Method 21 Determination of Michaelis–Menten constants

Tyrosine cleavage was assessed by measuring initial rates of *p*-cresol formation as a function of 10 different AdoMet or tyrosine concentration. The AdoMet dependence was measured in assays containing reconstituted HydG (5 μ M), tyrosine (400 μ M for WT, 3 mM for C386S and Δ CTD HydG), sodium dithionite (1 mM) and varying concentrations of enzymatically synthesised AdoMet (5 – 500 μ M) while the rate dependency on tyrosine was determined in similar assays containing enzymatically synthesised AdoMet (100 μ M for WT, 200 μ M for C386S and Δ CTD HydG) and varying concentrations of tyrosine (13 μ M – 4 mM) instead. Assays were carried out in buffer H (50 mM HEPES, 0.5 M KCl, pH 7.4) as outlined in Method 20. Control assays were devoid of sodium dithionite to accurately measure the nanomolar *p*-cresol impurities observed in tyrosine preparations. Reactions were stopped at 4 time points ranging between 1 min and 14 min and the supernatants analysed for *p*-cresol as described in Method 31.

Method 22 AdoMet cleavage in the presence of tyrosine analogues

Previously reconstituted WT HydG in buffer C (20 mM Hepes, 0.5 M NaCl, 5% (w/v) glycerol, 5 mM DTT, pH 7.4) was desalted via a pre-equilibrated PD-10 column into buffer H (50 mM Hepes, 0.5 M KCl, pH 7.4). Activity assays (200 μ L) were prepared similar to Method 20, containing AdoMet (1 mM), WT HydG (25 μ M), tyrosine analogue (1 mM, Table 3.6) and sodium dithionite (1 mM). Tyrosine analogues were dissolved in buffer H, with sonication if required. Due to the limited solubility of D-tyrosine **95**, *p*-hydroxy-phenylpropionic acid **92**, 3-nitro-L-tyrosine **101** and *p*-methyl-L-phenylalanine **99** at neutral pH, these analogues were prepared as described for L-tyrosine in Method 20. Negative control assays were devoid of the tyrosine (analogue) substrate to account for any AdoMet cleavage in the absence of substrate. All assays were stopped after an 80 min incubation period. The analogues 3-nitro-L-phenylalanine **101** and *p*-fluoro-L-phenylalanine **98** co-eluted with 5'-dAH which made accurate quantification of the formed 5'-dAH difficult. These assays were thus repeated as outlined above, but additionally containing MTAN (10 μ M). This allows the quantification of AdoMet cleavage by measuring the formation of adenine as MTAN cleaves any formed 5'-dAH to adenine. To account for any adenine derived from MTA cleavage and AdoMet impurities, negative control assays with AdoMet (1 mM), MTAN (10 μ M) and sodium dithionite (1 mM) were prepared and analysed in parallel (Method 30).

Method 23 HydG activity assays of differing pH

Previously reconstituted WT HydG in buffer C (20 mM Hepes, 0.5 M NaCl, 5% (w/v) glycerol, 5 mM DTT, pH 7.4) was desalted via a pre-equilibrated PD-10 column into buffer H (50 mM Hepes, 0.5 M KCl) of varying pH (6.0, 7.0 or 8.0). Activity assays (0.95 mL) were prepared similar to Method 20, containing AdoMet (0.5 mM), HydG (20 μ M) and tyrosine (1 mM). Inside the glove box, the assay pH was determined using pH paper to ensure significantly different pH values, before a 190 μ L aliquot was removed and initiated with sodium dithionite (10 μ L). The remainder (~700 μ L) was used to accurately measure the assay pH using a pH electrode situated outside the glove box and calibrated at 25 °C. To achieve a broader range of assay pH values, it is recommended that the acidity of AdoMet and the basicity of tyrosine is adjusted before assay initiation. HPLC analysis for *p*-cresol was carried out as described in Method 31.

Method 24 GTPase activity assay

Inside an anaerobic glove box, activity assays (200 μ L) containing reconstituted HydF^(E) (38 μ M), MgCl₂ (2 mM) and GTP (2 mM) in the absence or presence of reconstituted HydG (25 μ M) were prepared in buffer I (20 mM Hepes, 0.5 M KCl, 5% (w/v) glycerol, 5 mM DTT, pH 7.4). Outside the glove box, the assays were pre-equilibrated at 37 °C for 5 min, then incubated for a further 4 min and 20 min, at which points the small molecule assay fraction was separated from the proteins using spin filters. The filtrate was stored at -80 °C or immediately analysed for GTP and GDP by HPLC (Method 34).

7.7 Protein spectroscopy

Method 25 Electron paramagnetic resonance spectroscopy

Reconstituted WT, C386S and Δ CTD HydG proteins (~500 μ M) in buffer C (20 mM Hepes, 0.5 M NaCl, 5% (w/v) glycerol, 5 mM DTT, pH 7.4) were thawed inside an anaerobic glove box before desalted into buffer H (50 mM Hepes, 0.5 M KCl, pH 7.4) via a pre-equilibrated PD-10 column. Proteins were then mixed with freshly prepared substrate(s) (1 mM AdoMet, 1 mM AdoHcy, or 1 mM AdoHcy and 1 mM tyrosine) in buffer H before addition of sodium dithionite (1 mM). Following a 20 min incubation period, the mixture (160 μ L) was transferred into an EPR tube and sealed with a rubber septum before being flash frozen in liquid N₂ outside the glove box. EPR measurements were carried out by Enrico Salvadori with help from Richard Cammack and Christopher W. M. Kay at University College London.

The first derivatives of the acquired EPR spectra were baseline corrected when required using MATLAB²⁶⁹ before plotted using GraphPad Prism²⁷⁰. Simulations of EPR spectra were carried out mostly (80%) by Benjamin R. Duffus and Eric M. Shepard (Montana State University) using the EasySpin software²⁶⁶ in MATLAB. This yielded the g values reported in Chapter 2 and Appendix 4.

7.8 Preparation of enzymatically synthesised AdoMet

Method 26 Expression of AdoMet synthetase and preparation of cell lysates

A glycerol freeze of *E. coli* AdoMet synthetase from the overproducing strain DM22 (pk8) was kindly provided by J. B. Broderick (Montana State University) and was initially constructed by Dr G. D. Markham (FoxChase Cancer Centre)^{188,271}.

Expression of *E. coli* AdoMet synthetase was carried out as described previously⁶¹ with slight modifications. Briefly, an overnight starter culture of *E. coli* DM22 (pk8) in LB media containing oxytetracycline (10 µg/mL) was used as a 1% inoculum into fresh media (5 L). After a 10 h incubation period at 37 °C in an orbital shaker (180 rpm), the cells were isolated by centrifugation (7500 rpm, 30 min, 4 °C) typically yielding 2 g/L of beige, wet cell paste. A crude cell lysate was prepared by resuspending the cell paste (3 mL/g) in buffer I (100 mM Tris, 1 mM EDTA, pH 8.0) supplemented with 50 mg/mL lysozyme. The resulting mixture was stirred at room temperature for 30 min and lysed by 10 x 1 min sonication cycles. The lysate was cleared by centrifugation (7500 rpm, 20 min, 4 °C) and stored as 1 mL aliquots at -80 °C.

Method 27 Enzymatic AdoMet synthesis

Enzymatic AdoMet synthesis was achieved using a previously described method⁶¹ with minor modifications. Briefly, reactions (20 mL) were prepared by dissolving ATP (13 mM) in buffer K (100 mM Tris, 26 mM MgCl₂, 50 mM KCl, 1 mM EDTA, pH 8.0) before addition of acetonitrile (20% (v/v)) and L-methionine (10 mM). An aliquot of the crude AdoMet synthetase cell lysate (1 mL, ~30 mg/mL, Method 26) was then added and the reaction gently stirred at room

temperature. Reaction progress was monitored by reverse phase thin layer chromatography (RP-TLC) (3:1 water:acetonitrile, 0.1% acetic acid; R_f values, AdoMet – 0.25, MTA – 0.40, adenine – 0.55, ATP – 0.93) and HPLC (Method 30). It was found that no further AdoMet was synthesised after 4–5 h, which was equivalent to a 40–60% synthesis yield. The reaction mixture was then adjusted to approximately pH 7 by addition of 1% TFA (~0.5 mL) and the mixture was chilled on ice for 20 min before stored at $-80\text{ }^{\circ}\text{C}$. Acidification below pH 2 increased acid catalysed AdoMet hydrolysis to adenine and prevented successful AdoMet purification.

Method 28 Purification of AdoMet using Amberlite IRC-50 resin

AdoMet purification using a protocol by Farrar et al.¹¹⁵ was attempted. Briefly, an AdoMet synthesis reaction mixture (10 mL) was diluted with deionised water (10 mL), before applied (2 mL/min) onto an Amberlite IRC-50 column (XK-16, 5 mL) previously equilibrated into buffer L (0.2 M sodium acetate, pH 4.4). After the absorbance at 260 nm returned to baseline, a 50 mL gradient to buffer M (1M HCl) was applied, followed by a 20 mL gradient to 30% buffer M and a further 20 mL gradient to 100% buffer M. No UV-Vis changes were observed during any gradients and TLC analysis (Method 27) of the collected fractions confirmed that AdoMet eluted during the washing step.

Method 29 Purification of AdoMet using Source 15S resin

An AdoMet purification protocol by Walsby and co-workers⁶¹ was modified¹⁷⁷, where the AdoMet synthesis reaction mixture was gently thawed and further acidified to pH 5 by addition of 1% TFA (1–1.5 mL) before removal of precipitated polypeptides by centrifugation (7500 rpm, 20 min, $4\text{ }^{\circ}\text{C}$). The

Chapter 7 – Experimental

resulting supernatant was filtered through a 0.22 μm filter and applied (10 mL, 1 mL/min), in 2% buffer O (1 M TFA), to a Source 15S cation exchange column (XK16, 8 mL), previously washed with buffer N (water) and equilibrated with 10% buffer O. The column was further washed with 2% buffer O until the absorbance at 280 nm returned to the baseline. Elution of AdoMet was effected by a 100 mL gradient to 100% buffer O (Figure 3.8). AdoMet typically eluted as a single peak between 70% and 90 % buffer O as indicated by the absorbance increase at 280 nm, but the size of the peak and therefore the amount of AdoMet recovered varied considerably and no strong reproducibility could be obtained. The presence of AdoMet in the selected fractions was confirmed by TLC (AdoMet R_f value of 0.75 under these acidic conditions), before the fractions pooled and lyophilised overnight. The column was then washed extensively with water, before regenerated with 1 M NaOH and stored in water until the next use. The lyophilised white powder was quickly resuspended in the smallest amount of cold water and lyophilised again overnight. From the dry weight, stock solutions of AdoMet (~30 mM) for use in kinetic experiments were prepared outside the glove box using appropriate assay buffers, before being flash frozen as 0.5 mL aliquots for storage at $-80\text{ }^\circ\text{C}$. One aliquot was routinely retained to confirm the purity of AdoMet by HPLC analysis (Method 30) and to more accurately determine its concentration using UV-Vis spectroscopy ($\epsilon_{260} = 15.4\text{ mM}^{-1}\text{ cm}^{-1}$)^{272,273}. It was usually found that the AdoMet sample was half as concentrated as originally prepared based on dry weight measurements and that less than 0.1% adenine and less than 1.5% MTA were present. Higher concentrations of impurities (>5%) were consistently observed in viscous off-white to yellow lyophilisation samples and these batches of AdoMet were discarded. The exact reason for the increased amount

of impurities is unknown, but may be due to lyophilisation periods lasting longer than 3 days.

Initial AdoMet preparations were further analysed by ^1H NMR (Figure 7.3). By integrating the distinct signals of the (*S,S*)- and (*R,S*)-AdoMet methyl groups at 2.96 ppm and 2.92 ppm, respectively¹⁹⁵, it was estimated that the purified AdoMet contained on average 95% of the active (*S,S*)-AdoMet diastereoisomer. High resolution mass spectrometry analysis (Figure 7.4) was kindly carried out by Christianne C. Wicking (Mass Spectrometry Service, University of Southampton) and confirmed the identity of AdoMet ($\text{C}_{15}\text{H}_{23}\text{N}_6\text{O}_5\text{S}^+$) with m/z values of 399.1447 (100%) and 400.1469 (16.7%).

Unfortunately, the retention of AdoMet on the 15S cation exchange column was poor and a low 10–20% purification yield was observed, lowering the overall yield of pure, enzymatically synthesised (*S,S*)-AdoMet to an average of 5%.

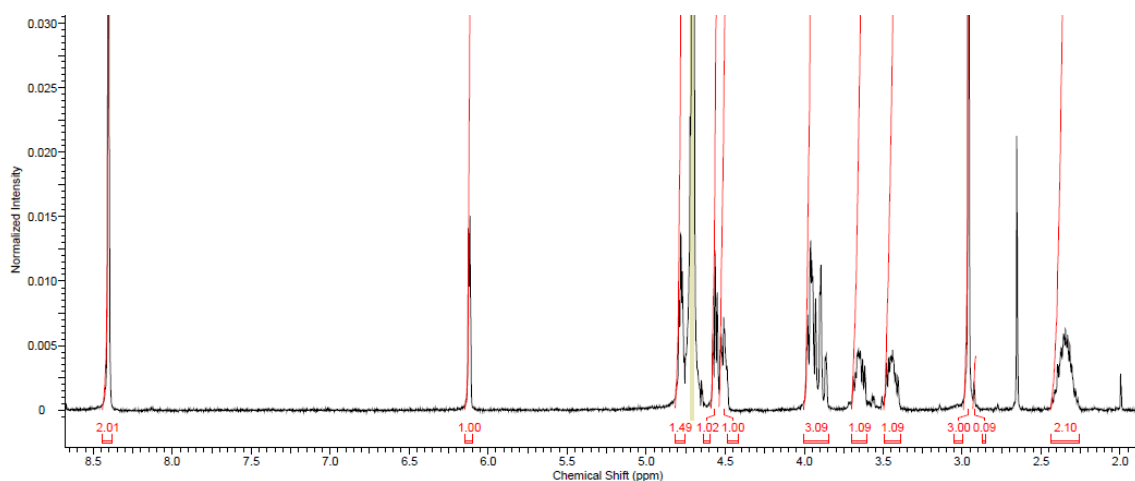
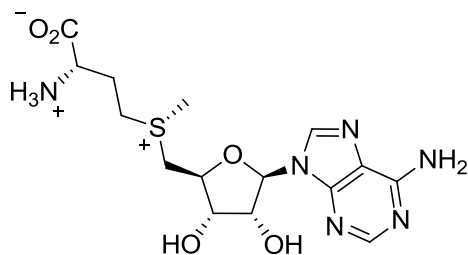


Figure 7.3 ^1H NMR spectrum of enzymatically synthesised and purified AdoMet.

Chapter 7 – Experimental



(D₂O, 400 MHz) δ ppm 2.25–2.44 (m, 2 H, H β), 2.92 (s, 0.1 H, (*R,S*) SMe), 2.96 (s, 3 H, (*S,S*) SMe), 3.40–3.50 (m, 1 H, H γ), 3.60–3.70 (m, 1 H, H γ), 3.85–3.99 (m, 3 H, H α , H5'), 4.48–4.54 (m, 1 H, H4'), 4.54–4.59 (m, 1 H, H3'), 4.78 (t, $J = 4.50$ Hz, 1 H, H2'), 6.12 (d, $J = 4.00$ Hz, 1 H, H1'), 8.40–8.41 (m, 2 H, H2,8). The signal at 2.00 ppm corresponds to acetonitrile while the 2.66 ppm resonance is unidentified.

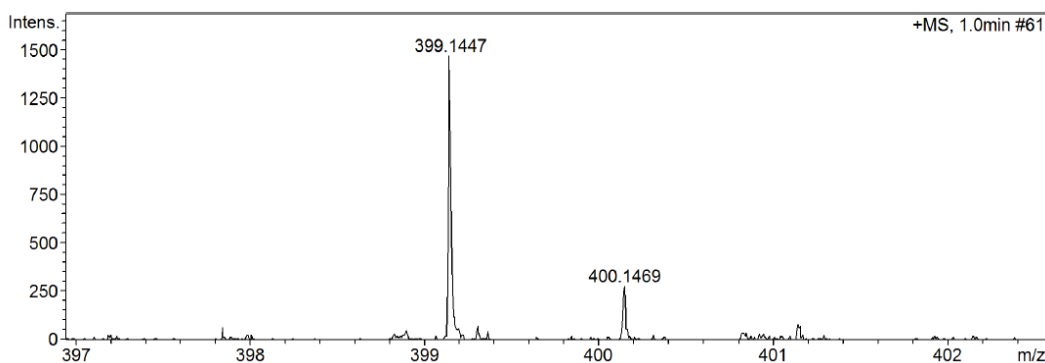


Figure 7.4 High resolution mass spectrum of enzymatically synthesised and purified AdoMet.

AdoMet was resuspended in water (1 $\mu\text{g/mL}$) before immediately analysed by positive ESI mass spectrometry using the following acquisition parameters, capillary voltage – 4 kV, end plate voltage – –0.5 kV, nebulizing gas pressure – 1.0 bar, drying gas temperature – 200 $^{\circ}\text{C}$, drying gas flow rate – 4 L/min.

7.9 HPLC methods

Method 30 Quantification of AdoMet, 5'-dAH and *p*-cresol

To analyse assay supernatants for 5'-dAH **13** and *p*-cresol **4**, the method by Challand et al.¹³⁰ was employed. Assay supernatants were cleared by centrifugation before applied (40 μ L) to a Gemini C₁₈ reverse phase HPLC column (4.6 x 250 mm, 5 μ m, 110 Å) equilibrated with solvent A (0.1% (v/v) acetic acid in water, 0.8 mL/min). After injection, the column was eluted for 8 min with 100% solvent A, followed by a gradient to 50% solvent B (0.1% (v/v) acetic acid in acetonitrile) over 32 min. Over 3 min, the gradient was increased to 100% solvent B, held isocratically for 5 min and returned to 100% solvent A over 2 min. Before the next injection, the column was re-equilibrated with 100% solvent A for 10 min (total sampling time 60 min). The dual wavelength UV-Vis detector monitored the absorbance at 254 nm for detection of 5'-dAH (Figure 7.5 A) and the fluorescence detector monitored elution of *p*-cresol with $\lambda_{\text{ex}} = 274$ nm and $\lambda_{\text{em}} = 312$ nm (Figure 7.5 C). The amounts of 5'-dAH ($R_t = 20.3$ min) and *p*-cresol ($R_t = 38.1$ min) were quantified using a calibration curve of synthetic standards analysed in parallel (Figure 7.5 B, D). The same HPLC method was used to analyse AdoMet samples for impurities (see Figure 3.8), with the following retention times, AdoMet – 3.1 min, adenine – 7.8 min, MTA – 22.9 min.

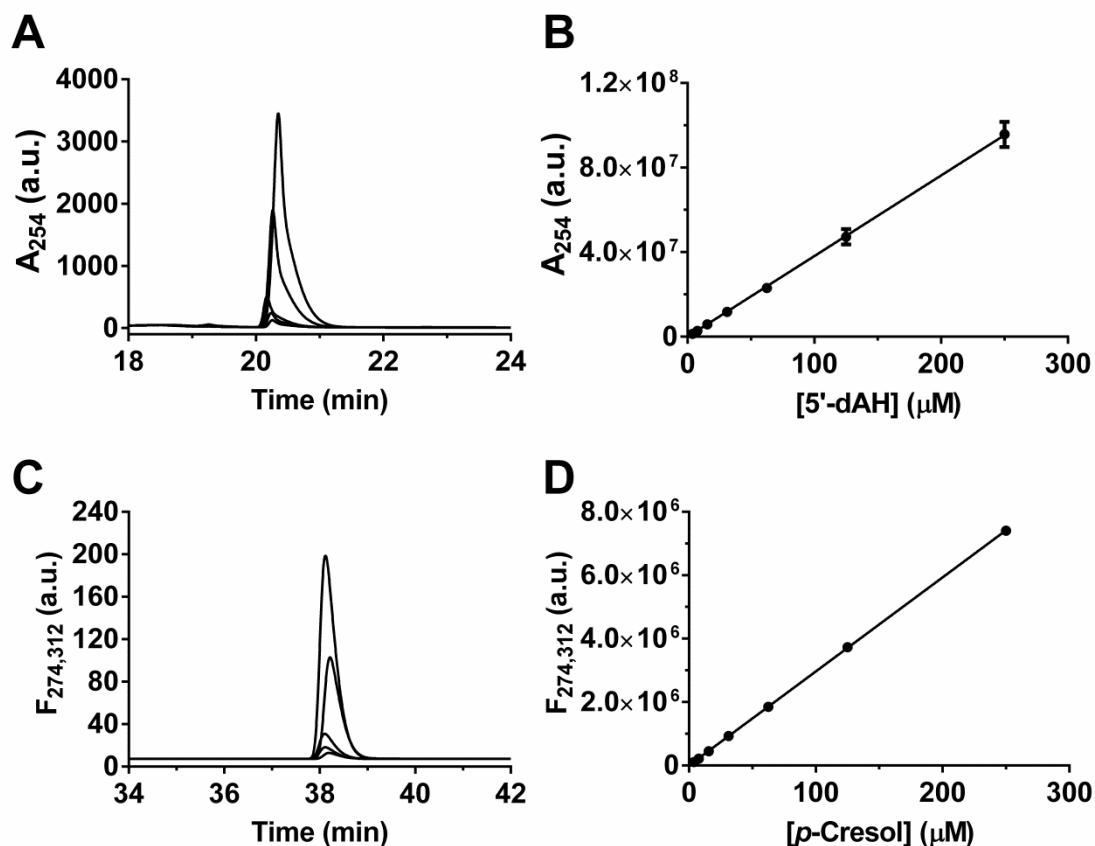


Figure 7.5 HPLC quantification of 5'-dAH and *p*-cresol.

Representative HPLC elution chromatograms of (A) 5'-dAH and (C) *p*-cresol standards ranging between 8 μM and 250 μM and (B, D) respective calibration curves, $R^2 = 0.99$.

Method 31 Quantification of *p*-cresol by HPLC (short run)

If assays were only analysed for *p*-cresol **4**, a modified HPLC procedure to Method 30 was employed, where only the gradient was changed to shorten the run time. Assay supernatants were cleared by centrifugation before applied (40 μL) to a Gemini C_{18} reverse phase HPLC column (4.6 x 250 mm, 5 μm , 110 Å) equilibrated with 70% solvent A (0.1% (v/v) acetic acid in water, 0.8 mL/min). After injection, the column was eluted for 5 min with 70% solvent A, followed by a gradient to 40% solvent B (0.1% (v/v) acetic acid in acetonitrile)

over 3 min. An additional gradient over 7 min to 42% solvent B was applied before a step to 100% solvent B over 1 min where it was held isocratically for 8 min, then returned to 70% solvent A over 1 min. Before the next injection, the column was re-equilibrated with 70% solvent A for 5 min (total sampling time 30 min). The fluorescence detector measured excitation and emission at 274 nm and 312 nm, respectively. The amount of *p*-cresol ($R_t = 15.9$ min) was quantified using a calibration curve of synthetic standards (7.8–125 nM) analysed in parallel. The elution and calibration curve for *p*-cresol were similar to Figure 7.5 C, D and a representative example is shown in Figure 3.5.

Method 32 Quantification of cyanide

Cyanide **5** was quantified as the fluorescent CBI **48** using an adapted derivatisation method³⁴ from Tracqui and co-workers²⁷⁴ (Scheme 1.11). Briefly, a quenched and neutralised assay solution (Method 20) to be analysed (10 μ L) was added to a freshly prepared working solution of MeOH:20% NH_3 :83 mM taurine **46** in water (9:1:3, 65 μ L), before addition of NDA **47** (10 mM in MeOH, 25 μ L). After 30 min incubation at 20 °C the solution was diluted 1:1 with water and immediately injected (40 μ L) onto a pre-equilibrated HyperClone BDS C_{18} reverse phase HPLC column (4.6 x 150 mm, 5 μ m, 130 Å, 0.8 mL/min) for most accurate results. Following sample injection, the column was eluted isocratically for 5 min using 60% solvent C (2 mM ammonium formate buffered to pH 3 with formic acid), before a gradient to 100% solvent D (MeOH) over 10 min was applied and then hold isocratically for another 10 min. The gradient was then reversed to 60% solvent C over 1 min before the column re-equilibrated for 9 min (total sampling time 35 min). Under these conditions, CBI eluted with $R_t = 12.1$ min (Figure 7.6 A) as monitored by fluorescence

detection ($\lambda_{\text{ex}} = 418 \text{ nm}$, $\lambda_{\text{em}} = 454 \text{ nm}$). Cyanide recovery in the presence of protein was found to be reduced^{34,275}, while sodium dithionite affected the fluorescence of the cyanide derivatisation product. To accurately quantify cyanide in activity assays, a calibration curve under assay conditions was employed, where six KCN standards (2.5-fold stock solutions) in 2.5 mM NaOH were added to activity assays lacking AdoMet and tyrosine (Figure 7.6 B). These assays were incubated at 37 °C for two intermediate time periods compared to the activity assays under investigation (eg 20 min and 40 min for 60 min time course assays), before being subjected to the precipitation/neutralisation conditions described in Method 20.

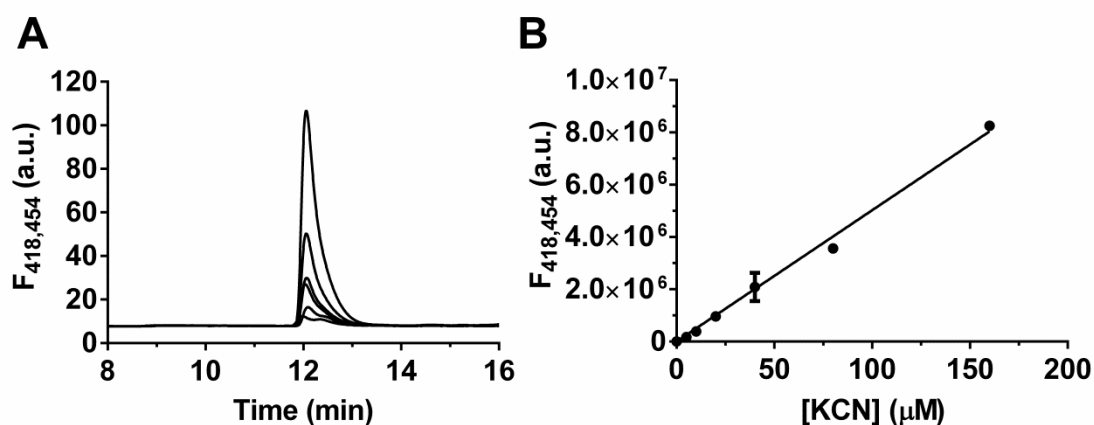


Figure 7.6 HPLC quantification of cyanide.

(A) Representative HPLC elution chromatogram of derivatised cyanide standards ranging between 5 μM and 160 μM . (B) Corresponding calibration curve, $R^2 = 0.99$.

Method 33 Quantification of glyoxylate

Glyoxylate **35** was quantified as the fluorescent 2-quinoxalinol **50** after derivatisation with *o*-phenylene diamine **49** (Scheme 1.11) as described by Kriek et al.¹²⁴, with slight modifications. Briefly, cleared assay supernatants (10 μ L) were diluted with 50 mM HEPES, pH 7.5 to 50 μ L before acidified with 0.5 M HCl (100 μ L) and addition of freshly prepared *o*-phenylene diamine in 0.5 M HCl (10 mg/mL, 50 μ L). Using a PCR machine, all samples were incubated at 25 °C for 1 min, before heated at 95 °C for 10 min, then returned to 25 °C for 10 min before addition of 1.25 M NaOH (120 μ L). After a 5 min period at 4 °C, the samples were stored at -80 °C and only thawed shortly before HPLC analysis. The derivatisation mixture (40 μ L) was applied to an equilibrated HyperClone BDS C₁₈ reverse phase HPLC column (4.6 x 150 mm, 5 μ m, 130 Å) connected to a fluorimeter operating at 350 nm excitation and 420 nm emission wavelengths. After injection, the column was washed with 85% solvent E (100 mM ammonium bicarbonate, 0.8 mL/min) for 5 min, followed by a gradient to 50% solvent F (acetonitrile) over 15 min. The gradient was increased to 100% solvent F over 1 min, hold isocratically for 4 min and returned to 85% solvent E over 0.5 min. Before the next injection, the column was re-equilibrated with 85% solvent E for 9.5 min (total sampling time of 35 min). Under these conditions, 2-quinoxalinol eluted between 6.2min and 6.6 min. Sodium dithionite present in activity assays affected the fluorescence of the 2-quinoxalinol derivative. Quantitative estimates for glyoxylate were thus obtained from a calibration curve of derivatised synthetic glyoxylate standards (3–100 μ M) prepared and incubated like negative control assays lacking AdoMet, HydG and tyrosine.

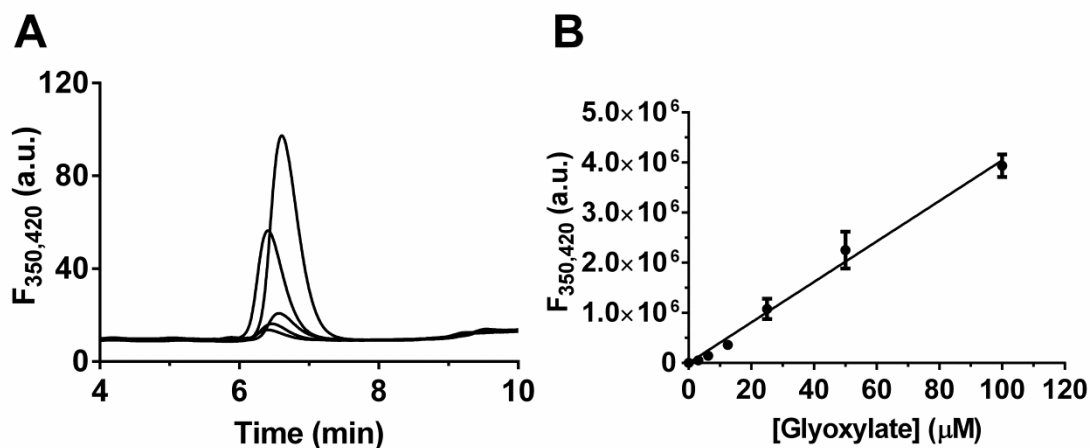


Figure 7.7 HPLC quantification of glyoxylate.

(A) Representative HPLC elution chromatogram of derivatised glyoxylate standards ranging between 6 μM and 100 μM and (B) corresponding calibration curve, $R^2 = 0.98$.

Method 34 Quantification of GTP and GDP

To analyse assay supernatants for GDP, a modified literature method^{241,276} was used. Assay supernatants were cleared by centrifugation before applied (40 μL) to a Gemini C_{18} reverse phase HPLC column (4.6 x 150 mm, 5 μm , 130 \AA) equilibrated with solvent G (5% MeOH, 15 mM N,N -dimethylhexylamine (DMHA), adjusted to pH 7.0 with acetic acid), 0.8 mL/min. After injection, the column was eluted for 5 min with 91% solvent G, followed by a gradient to 51% solvent H (80% MeOH, 15 mM DMHA, adjusted to pH 7.0 with acetic acid) over 32 min. An isocratic phase over 10 min followed, before return to 91% solvent A over 1 min. Before the next injection, the column was re-equilibrated with 91% solvent G for 10 min. Absorbance at 260 nm was monitored for detection of GDP and GTP. Assuming identical extinction coefficients, the amounts of GDP

($R_t = 28.0$ min) and GTP ($R_t = 34.3$ min) were quantified relative to a GTP (2 mM) standard (Figure 7.8).

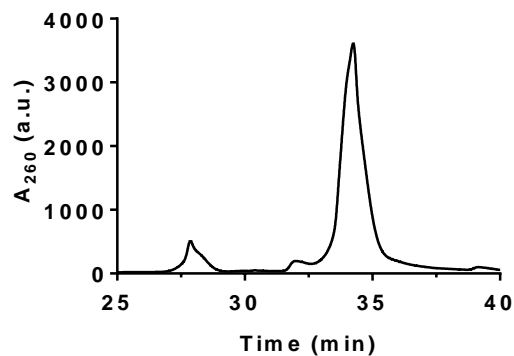


Figure 7.8 HPLC elution chromatogram of GTP.

HPLC elution chromatogram of a synthetic GTP standard ($R_t = 34.3$ min), exemplifying the presence of a GDP impurity ($R_t = 28.0$ min).

7.10 Protein crystallography

HydG proteins, AdoMet and sodium dithionite were prepared in buffer C (20 mM HEPES, 0.5 M NaCl, 5% (w/v) glycerol, 5 mM DTT, pH 7.4). Tyrosine was prepared as detailed in Method 20, while an initial 80 mM AdoHcy stock was prepared in 200 mM HCl. 1 M NaOH was then added (~5–10 μ L) until the AdoHcy was completely dissolved.

Final concentrations of the protein–substrate complexes and the screening conditions used throughout these studies can be found in the electronic appendices. Crystallisation growth was initially monitored every second day over a week, then weekly using a microscope inside the glove box.

Method 35 Preparation of crystallisation buffers

Commercial crystallisation solutions in deep 96–well blocks were transferred into the glove box after being thoroughly purged. Large volume crystallisation solutions (10 mL) were lyophilised before transferred into the glove box and resuspended in sterile deionised water. Individual components of the hand–made crystallisation solutions were prepared in 50 mL Falcon tubes outside the glove box. These solutions were then placed into the glove box and further stirred vigorously for 48 h. Any evaporated water was topped up with sterile deionised water as required and the crystallisation solutions prepared as outlined in the electronic appendix. The MIB, SPG, MMT buffers in the PACT Premier MD1–29 screen were prepared according to the protocol by Newman²⁷⁷.

Method 36 Preparation of 96–well crystallisation trays

Thoroughly purged 96–well crystallisation plates were placed into the glove box at least 48 h before they were required. Protein substrate mixtures (135 μ L) were prepared in a 1.6 mL Eppendorf tube using stock solutions of 200 mM AdoMet, approximately 1 mM HydG, 20 mM tyrosine, 30–50 mM AdoHcy and 200 mM sodium dithionite. These mixtures were then transferred (12 x 10.5 μ L) into 12–strip PCR tubes. Using a multichannel pipette, commercial or hand–made well solutions (50 μ L) were then placed into the main 96 wells. Following this, three different protein–substrate mixtures (1 μ L each) were similarly transferred from the 12–strip PCR tubes into the three sub–wells, followed by well solution (1 μ L) pipetted from the main wells. The plate was then quickly covered with a transparent adhesive film.

Method 37 Preparation of 24–well crystallisation trays

Outside the glove box, the rim of each well was covered with a thin film of silicone grease. The crystallisation plates were then placed thoroughly purged into the glove box at least 48 h before they were required. Protein substrate mixtures were prepared in a 1.6 mL Eppendorf tube assuming a 30% pipetting error and incubated for 10–20 min. Meanwhile, commercial or hand–made well solutions were manually pipetted (0.5 mL) into one well at a time. Well solution (1–2 μ L) from the main well was then pipetted onto a cover slip, before addition of the protein–substrate mixture (1–2 μ L) in 1:1, 2:1 and 1:2 ratios. The cover slip was then gently placed onto the well, ensuring a proper seal with the previously applied grease.

Method 38 Seeding experiments

For 24-well seeding experiments, crystallisation seed stocks were freshly prepared by diluting a grown crystal or crystal shower by serial dilution with mother liquor. These seed stocks were then directly added (0.2 μ L) or directly streaked using the tip of a clean syringe into the well solution-protein-substrate mixture on the cover slip.

Method 39 Crystal freezing

Crystals which have been selected to be tested at Diamond were flash frozen in liquid N₂. This required the removal of crystallisation plates from the glove box. The transparent cover on 96-well plates was cut with a scalpel to expose the target crystal. The crystal was carefully removed using a previously cleaned CryoLoop of a suitable size and directly flash frozen in liquid N₂. Alternatively, it was initially quickly dipped into a sterile 100% (w/v) glycerol solution or mother liquor before flash frozen. For freezing of crystals from 24-well plates, each target cover slip was transferred to a separate plate (with water as mother liquor) before removal from the glove box. This ensured that crystallisation experiments of the target plate were disturbed as little as possible. Frozen crystals were stored in a Dewar containing liquid N₂ until analysis at Diamond, usually within the next day.

References

- (1) Stephenson, M.; Stickland, L. H. *Biochem. J* **1931**, *25*, 205.
- (2) Vignais, P. M.; Billoud, B. *Chem. Rev.* **2007**, *107*, 4206.
- (3) Shima, S.; Pilak, O.; Vogt, S.; Schick, M.; Stagni, M. S.; Meyer-Klaucke, W.; Warkentin, E.; Thauer, R. K.; Ermler, U. *Science* **2008**, *321*, 572.
- (4) Streich, D.; Astuti, Y.; Orlandi, M.; Schwartz, L.; Lomoth, R.; Hammarström, L.; Ott, S. *Chem. Eur. J.* **2010**, *16*, 60.
- (5) Lo, S.-C.; Shih, S.-H.; Chang, J.-J.; Wang, C.-Y.; Huang, V.-C. *Appl. Microbiol. Biotechnol.* **2012**, *95*, 969.
- (6) Peters, J. W.; Lanzilotta, W. N.; Lemon, B. J.; Seefeldt, L. C. *Science* **1998**, *282*, 1853.
- (7) Nicolet, Y.; Piras, C.; Legrand, P.; Hatchikian, C. E.; Fontecilla-Camps, J. C. *Structure* **1999**, *7*, 13.
- (8) Vignais, P. M.; Billoud, B.; Meyer, J. *FEMS Microbiol. Rev.* **2001**, *25*, 455.
- (9) Nicolet, Y.; de Lacey, A. L.; Vernède, X.; Fernandez, V. M.; Hatchikian, E. C.; Fontecilla-Camps, J. C. *J. Am. Chem. Soc.* **2001**, *123*, 1596.
- (10) Lemon, B. J.; Peters, J. W. *Biochemistry* **1999**, *38*, 12969.
- (11) Pandey, A. S.; Harris, T. V.; Giles, L. J.; Peters, J. W.; Szilagyi, R. K. *J. Am. Chem. Soc.* **2008**, *130*, 4533.
- (12) Silakov, A.; Wenk, B.; Reijerse, E.; Lubitz, W. *Phys. Chem. Chem. Phys.* **2009**, *11*, 6592.
- (13) Erdem, Ö. F.; Schwartz, L.; Stein, M.; Silakov, A.; Kaur-Ghumaan, S.; Huang, P.; Ott, S.; Reijerse, E. J.; Lubitz, W. *Angew. Chem. Int. Ed.* **2011**, *50*, 1439.
- (14) Fan, H.-J.; Hall, M. B. *J. Am. Chem. Soc.* **2001**, *123*, 3828.
- (15) Ryde, U.; Greco, C.; De Gioia, L. *J. Am. Chem. Soc.* **2010**, *132*, 4512.

References

- (16) Watanabe, S.; Matsumi, R.; Arai, T.; Atomi, H.; Imanaka, T.; Miki, K. *Mol. Cell* **2007**, *27*, 29.
- (17) Bürstel, I.; Hummel, P.; Siebert, E.; Wisitruangsakul, N.; Zebger, I.; Friedrich, B.; Lenz, O. *J. Biol. Chem.* **2011**, *286*, 44937.
- (18) Soboh, B.; Stripp, S. T.; Muhr, E.; Granich, C.; Brausseman, M.; Herzberg, M.; Heberle, J.; Gary Sawers, R. *FEBS Lett.* **2012**, *586*, 3882.
- (19) Shomura, Y.; Higuchi, Y. *J. Biol. Chem.* **2012**, *287*, 28409.
- (20) Stripp, S. T.; Soboh, B.; Lindenstrauss, U.; Brausseman, M.; Herzberg, M.; Nies, D. H.; Sawers, R. G.; Heberle, J. *Biochemistry* **2013**, *52*, 3289.
- (21) Watanabe, S.; Matsumi, R.; Atomi, H.; Imanaka, T.; Miki, K. *Structure* **2012**, *20*, 2124.
- (22) Posewitz, M. C.; King, P. W.; Smolinski, S. L.; Zhang, L.; Seibert, M.; Ghirardi, M. L. *J. Biol. Chem.* **2004**, *279*, 25711.
- (23) King, P. W.; Posewitz, M. C.; Ghirardi, M. L.; Seibert, M. *J. Bacteriol.* **2006**, *188*, 2163.
- (24) Rubach, J. K.; Brazzolotto, X.; Gaillard, J.; Fontecave, M. *FEBS Lett.* **2005**, *579*, 5055.
- (25) Shepard, E. M.; Duffus, B. R.; George, S. J.; McGlynn, S. E.; Challand, M. R.; Swanson, K. D.; Roach, P. L.; Cramer, S. P.; Peters, J. W.; Broderick, J. B. *J. Am. Chem. Soc.* **2010**, *132*, 9247.
- (26) Brazzolotto, X.; Rubach, J. K.; Gaillard, J.; Gambarelli, S.; Atta, M.; Fontecave, M. *J. Biol. Chem.* **2006**, *281*, 769.
- (27) Cendron, L.; Berto, P.; D'Adamo, S.; Vallese, F.; Govoni, C.; Posewitz, M. C.; Giacometti, G. M.; Costantini, P.; Zanotti, G. *J. Biol. Chem.* **2011**, *286*, 43944.
- (28) Joshi, N.; Shepard, E. M.; Byer, A. S.; Swanson, K. D.; Broderick, J. B.; Peters, J. W. *FEBS Lett.* **2012**, *586*, 3939.
- (29) McGlynn, S. E.; Ruebush, S. S.; Naumov, A.; Nagy, L. E.; Dubini, A.; King, P. W.; Broderick, J. B.; Posewitz, M. C.; Peters, J. W. *J. Biol. Inorg. Chem.* **2007**, *12*, 443.

- (30) McGlynn, S. E.; Shepard, E. M.; Winslow, M. A.; Naumov, A. V.; Duschene, K. S.; Posewitz, M. C.; Broderick, W. E.; Broderick, J. B.; Peters, J. W. *FEBS Lett.* **2008**, *582*, 2183.
- (31) Shepard, E. M.; McGlynn, S. E.; Bueling, A. L.; Grady-Smith, C. S.; George, S. J.; Winslow, M. A.; Cramer, S. P.; Peters, J. W.; Broderick, J. B. *Proc. Natl. Acad. Sci. USA* **2010**, *107*, 10448.
- (32) Czech, I.; Silakov, A.; Lubitz, W.; Happe, T. *FEBS Lett.* **2010**, *584*, 638.
- (33) Pilet, E.; Nicolet, Y.; Mathevon, C.; Douki, T.; Fontecilla-Camps, J. C.; Fontecave, M. *FEBS Lett.* **2009**, *583*, 506.
- (34) Driesener, R. C.; Challand, M. R.; McGlynn, S. E.; Shepard, E. M.; Boyd, E. S.; Broderick, J. B.; Peters, J. W.; Roach, P. L. *Angew. Chem. Int. Ed.* **2010**, *49*, 1687.
- (35) Kuchenreuther, J. M.; George, S. J.; Grady-Smith, C. S.; Cramer, S. P.; Swartz, J. R. *PLoS ONE* **2011**, *6*, e20346.
- (36) Kuchenreuther, J. M.; Britt, R. D.; Swartz, J. R. *PLoS ONE* **2012**, *7*, e45850.
- (37) Nicolet, Y.; Rubach, J. K.; Posewitz, M. C.; Amara, P.; Mathevon, C.; Atta, M.; Fontecave, M.; Fontecilla-Camps, J. C. *J. Biol. Chem.* **2008**, *283*, 18861.
- (38) Glaser, T.; Hedman, B.; Hodgson, K. O.; Solomon, E. I. *Acc. Chem. Res.* **2000**, *33*, 859.
- (39) Dey, A. *Indian J. Chem., Sect A* **2011**, *50*, 498.
- (40) Grigoropoulos, A.; Szilagyi, R. K. *J. Comput. Chem.* **2011**, *32*, 3194.
- (41) Vallese, F.; Berto, P.; Ruzzene, M.; Cendron, L.; Sarno, S.; De Rosa, E.; Giacometti, G. M.; Costantini, P. *J. Biol. Chem.* **2012**, *287*, 36544.
- (42) Czech, I.; Stripp, S.; Sanganas, O.; Leidel, N.; Happe, T.; Haumann, M. *FEBS Lett.* **2011**, *585*, 225.
- (43) Mulder, D. W.; Ortillo, D. O.; Gardenghi, D. J.; Naumov, A. V.; Ruebusch, S. S.; Szilagyi, R. K.; Huynh, B.; Broderick, J. B.; Peters, J. W. *Biochemistry* **2009**, *48*, 64240.

References

- (44) Mulder, D. W.; Boyd, E. S.; Sarma, R.; Lange, R. K.; Endrizzi, J. A.; Broderick, J. B.; Peters, J. W. *Nature* **2010**, *465*, 248.
- (45) Mansure, J. J.; Hallenbeck, P. C. *Biotechnol. Lett.* **2008**, *30*, 1765.
- (46) Booker, S. J. *Biochim. Biophys. Acta: Proteins and Proteomics* **2012**, *1824*, 1151.
- (47) Sofia, H. J.; Chen, G.; Hetzler, B. G.; Reyes–Spindola, J. F.; Miller, N. E. *Nucleic Acids Res.* **2001**, *29*, 1097.
- (48) Krebs, C.; Broderick, W. E.; Henshaw, T. F.; Broderick, J. B.; Huynh, B. H. *J. Am. Chem. Soc.* **2002**, *124*, 912.
- (49) Walsby, C.; Ortillo, D.; Broderick, W. E.; Broderick, J. B.; Hoffman, B. M. *J. Am. Chem. Soc.* **2002**, *124*, 11270.
- (50) Chen, D.; Walsby, C.; Hoffman, B. M.; Frey, P. A. *J. Am. Chem. Soc.* **2003**, *125*, 11788.
- (51) Cospers, M. M.; Cospers, N. J.; Hong, W.; Shokes, J. E.; Broderick, W. E.; Broderick, J. B.; Johnson, M. K.; Scott, R. A. *Protein Sci.* **2003**, *12*, 1573.
- (52) Chatterjee, A.; Li, Y.; Zhang, Y.; Grove, T. L.; Lee, M.; Krebs, C.; Booker, S. J.; Begley, T. P.; Ealick, S. E. *Nat. Chem. Biol.* **2008**, *4*, 758.
- (53) McGlynn, S. E.; Boyd, E. S.; Shepard, E. M.; Lange, R. K.; Gerlach, R.; Broderick, J. B.; Peters, J. W. *J. Bacteriol.* **2010**, *192*, 595.
- (54) Paraskevopoulou, C.; Fairhurst, S. A.; Lowe, D. J.; Brick, P.; Onesti, S. *Mol. Microbiol.* **2006**, *59*, 795.
- (55) Nicolet, Y.; Amara, P.; Mouesca, J.–M.; Fontecilla–Camps, J. C. *Proc. Natl. Acad. Sci. USA* **2009**, *106*, 14867.
- (56) Hioe, J.; Zipse, H. *Chem. Eur. J.* **2012**, *18*, 16463.
- (57) Demick, J. M.; Lanzilotta, W. N. *Biochemistry* **2010**, *50*, 440.
- (58) Zhang, Y.; Zhu, X.; Torelli, A. T.; Lee, M.; Dzikovski, B.; Koralewski, R. M.; Wang, E.; Freed, J.; Krebs, C.; Ealick, S. E.; Lin, H. *Nature* **2010**, *465*, 891.
- (59) Hiscox, M. J.; Driesener, R. C.; Roach, P. L. *Biochim. Biophys. Acta: Proteins and Proteomics* **2012**, *1824*, 1165.

- (60) Cospers, N. J.; Booker, S. J.; Ruzicka, F.; Frey, P. A.; Scott, R. A. *Biochemistry* **2000**, *39*, 15668.
- (61) Walsby, C. J.; Hong, W.; Broderick, W. E.; Cheek, J.; Ortillo, D.; Broderick, J. B.; Hoffman, B. M. *J. Am. Chem. Soc.* **2002**, *124*, 3143.
- (62) Noodleman, L.; Case, D. A. *Adv. Inorg. Chem.* **1992**, *38*, 423.
- (63) Lepore, B. W.; Ruzicka, F. J.; Frey, P. A.; Ringe, D. *Proc. Natl. Acad. Sci. USA* **2005**, *102*, 13819.
- (64) Vey, J. L.; Yang, J.; Li, M.; Broderick, W. E.; Broderick, J. B.; Drennan, C. L. *Proc. Natl. Acad. Sci. USA* **2008**, *105*, 16137.
- (65) Vey, J. L.; Drennan, C. L. *Chem. Rev.* **2011**, *111*, 2487.
- (66) Dowling, D. P.; Vey, J. L.; Croft, A. K.; Drennan, C. L. *Biochim. Biophys. Acta: Proteins and Proteomics* **2012**, *1824*, 1178.
- (67) Berkovitch, F.; Nicolet, Y.; Wan, J. T.; Jarrett, J. T.; Drennan, C. L. *Science* **2004**, *303*, 76.
- (68) Goldman, P. J.; Grove, T. L.; Booker, S. J.; Drennan, C. L. *Proc. Natl. Acad. Sci. USA* **2013**, *110*, 15949.
- (69) Nicolet, Y.; Drennan, C. L. *Nucleic Acids Res.* **2004**, *32*, 4015.
- (70) Martinez-Gomez, N. C.; Downs, D. M. *Biochemistry* **2008**, *47*, 9054.
- (71) Martinez-Gomez, N. C.; Poyner, R. R.; Mansoorabadi, S. O.; Reed, G. H.; Downs, D. M. *Biochemistry* **2009**, *48*, 217.
- (72) Zhu, X.; Dzikovski, B.; Su, X.; Torelli, A. T.; Zhang, Y.; Ealick, S. E.; Freed, J. H.; Lin, H. *Mol. BioSyst.* **2011**, *7*.
- (73) Layer, G.; Moser, J.; Heinz, D. W.; Jahn, D.; Schubert, W. D. *EMBO J.* **2003**, *22*, 6214.
- (74) Farrar, C. E.; Jarrett, J. T. *Biochemistry* **2009**, *48*, 2448.
- (75) Ollagnier, S.; Mulliez, E.; Schmidt, P. P.; Eliasson, R.; Gaillard, J.; Deronzier, C.; Bergman, T.; Gräslund, A.; Reichard, P.; Fontecave, M. *J. Biol. Chem.* **1997**, *272*, 24216.

References

- (76) Padovani, D.; Thomas, F.; Trautwein, A. X.; Mulliez, E.; Fontecave, M. *Biochemistry* **2001**, *40*, 6713.
- (77) Chandor-Proust, A.; Berteau, O.; Douki, T.; Gasparutto, D.; Ollagnier-de-Choudens, S.; Fontecave, M.; Atta, M. *J. Biol. Chem.* **2008**, *283*, 36361.
- (78) Guianvarc'h, D.; Florentin, D.; Bui, B. T. S.; Nunzi, F.; Marquet, A. *Biochem. Biophys. Res. Commun.* **1997**, *236*, 402.
- (79) Wecksler, S. R.; Stoll, S.; Tran, H.; Magnusson, O. T.; Wu, S.-p.; King, D.; Britt, R. D.; Klinman, J. P. *Biochemistry* **2009**, *48*, 10151.
- (80) Ollagnier-de Choudens, S.; Sanakis, Y.; Hewitson, K. S.; Roach, P.; Münck, E.; Fontecave, M. *J. Biol. Chem.* **2002**, *277*, 13449.
- (81) Layer, G.; Grage, K.; Teschner, T.; Schünemann, V.; Breckau, D.; Masoumi, A.; Jahn, M.; Heathcote, P.; Trautwein, A. X.; Jahn, D. *J. Biol. Chem.* **2005**, *280*, 29038.
- (82) Colichman, E. L.; Love, D. L. *J. Org. Chem.* **1953**, *18*, 40.
- (83) Hinckley, G. T.; Frey, P. A. *Anal. Biochem.* **2006**, *349*, 103.
- (84) Hinckley, G. T.; Frey, P. A. *Biochemistry* **2006**, *45*, 3219.
- (85) Wang, S. C.; Frey, P. A. *Biochemistry* **2007**, *46*, 12889.
- (86) Hänzelmann, P.; Schindelin, H. *Proc. Natl. Acad. Sci. USA* **2004**, *101*, 12870.
- (87) Boal, A. K.; Grove, T. L.; McLaughlin, M. I.; Yennawar, N. H.; Booker, S. J.; Rosenzweig, A. C. *Science* **2011**, *332*, 1089.
- (88) Lanz, N. D.; Booker, S. J. *Biochim. Biophys. Acta: Proteins and Proteomics* **2012**, *1824*, 1196.
- (89) Hänzelmann, P.; Hernández, H. L.; Menzel, C.; García-Serres, R.; Huynh, B. H.; Johnson, M. K.; Mendel, R. R.; Schindelin, H. *J. Biol. Chem.* **2004**, *279*, 34721.
- (90) Lees, N. S.; Hänzelmann, P.; Hernandez, H. L.; Subramanian, S.; Schindelin, H.; Johnson, M. K.; Hoffman, B. M. *J. Am. Chem. Soc.* **2009**, *131*, 9184.

- (91) Suzuki, Y.; Noma, A.; Suzuki, T.; Senda, M.; Senda, T.; Ishitani, R.; Nureki, O. *J. Mol. Biol.* **2007**, *372*, 1204.
- (92) Perche-Letuvée, P.; Kathirvelu, V.; Berggren, G.; Clemancey, M.; Latour, J.-M.; Maurel, V.; Douki, T.; Armengaud, J.; Mulliez, E.; Fontecave, M.; Garcia-Serres, R.; Gambarelli, S.; Atta, M. *J. Biol. Chem.* **2012**, *287*, 41174.
- (93) Grove, T. L.; Ahlum, J. H.; Sharma, P.; Krebs, C.; Booker, S. J. *Biochemistry* **2010**, *49*, 3783.
- (94) Grove, T. L.; Ahlum, J. H.; Qin, R. M.; Lanz, N. D.; Radle, M. I.; Krebs, C.; Booker, S. J. *Biochemistry* **2013**, *52*, 2874.
- (95) Hernández, H. L.; Pierrel, F.; Elleingand, E.; García-Serres, R.; Huynh, B. H.; Johnson, M. K.; Fontecave, M.; Atta, M. *Biochemistry* **2007**, *46*, 5140.
- (96) Forouhar, F.; Arragain, S.; Atta, M.; Gambarelli, S.; Mouesca, J.-M.; Hussain, M.; Xiao, R.; Kieffer-Jaquinod, S.; Seetharaman, J.; Acton, T. B.; Montelione, G. T.; Mulliez, E.; Hunt, J. F.; Fontecave, M. *Nat. Chem. Biol.* **2013**, *9*, 333.
- (97) Lee, K.-H.; Saleh, L.; Anton, B. P.; Madinger, C. L.; Benner, J. S.; Iwig, D. F.; Roberts, R. J.; Krebs, C.; Booker, S. J. *Biochemistry* **2009**, *48*, 10162.
- (98) Cicchillo, R. M.; Lee, K.-H.; Baleanu-Gogonea, C.; Nesbitt, N. M.; Krebs, C.; Booker, S. J. *Biochemistry* **2004**, *43*, 11770.
- (99) Douglas, P.; Kriek, M.; Bryant, P.; Roach, P. L. *Angew. Chem. Int. Ed.* **2006**, *45*, 5197.
- (100) Cicchillo, R. M.; Booker, S. J. *J. Am. Chem. Soc.* **2005**, *127*, 2860.
- (101) Ugulava, N. B.; Gibney, B. R.; Jarrett, J. T. *Biochemistry* **2000**, *39*, 5206.
- (102) Ugulava, N. B.; Gibney, B. R.; Jarrett, J. T. *Biochemistry* **2001**, *40*, 8343.
- (103) Ugulava, N. B.; Surerus, K. K.; Jarrett, J. T. *J. Am. Chem. Soc.* **2002**, *124*, 9050.
- (104) Taylor, A. M.; Stoll, S.; Britt, R. D.; Jarrett, J. T. *Biochemistry* **2011**, *50*, 7953.
- (105) Goldman, P. J.; Grove, T. L.; Sites, L. A.; McLaughlin, M. I.; Booker, S. J.; Drennan, C. L. *Proc. Natl. Acad. Sci. USA* **2013**, *110*, 8519.

References

- (106) Harmer, J. E., University of Southampton, Personal Communication, 2013.
- (107) Jameson, G. N. L.; Cosper, M. M.; Hernández, H. L.; Johnson, M. K.; Huynh, B. H. *Biochemistry* **2004**, *43*, 2022.
- (108) Ugulava, N. B.; Sacanell, C. J.; Jarrett, J. T. *Biochemistry* **2001**, *40*, 8352.
- (109) Tse Sum Bui, B.; Mattioli, T. A.; Florentin, D.; Bolbach, G.; Marquet, A. *Biochemistry* **2006**, *45*, 3824.
- (110) Tse Sum Bui, B.; Benda, R.; Schünemann, V.; Florentin, D.; Trautwein, A. X.; Marquet, A. *Biochemistry* **2003**, *42*, 8791.
- (111) Escalettes, F.; Florentin, D.; Tse Sum Bui, B.; Lesage, D.; Marquet, A. *J. Am. Chem. Soc.* **1999**, *121*, 3571.
- (112) Taylor, A. M.; Farrar, C. E.; Jarrett, J. T. *Biochemistry* **2008**, *47*, 9309.
- (113) Fugate, C. J.; Stich, T. A.; Kim, E. G.; Myers, W. K.; Britt, R. D.; Jarrett, J. T. *J. Am. Chem. Soc.* **2012**, *134*, 9042.
- (114) Trainor, D. A.; Parry, R. J.; Gitterman, A. *J. Am. Chem. Soc.* **1980**, *102*, 1467.
- (115) Farrar, C. E.; Siu, K. K. W.; Howell, P. L.; Jarrett, J. T. *Biochemistry* **2010**, *49*, 9985.
- (116) Fugate, C. J.; Jarrett, J. T. *Biochim. Biophys. Acta: Proteins and Proteomics* **2012**, *1824*, 1213.
- (117) Cicchillo, R. M.; Iwig, D. F.; Jones, A. D.; Nesbitt, N. M.; Baleanu-Gogonea, C.; Souder, M. G.; Tu, L.; Booker, S. J. *Biochemistry* **2004**, *43*, 6378.
- (118) Hänzelmann, P.; Schindelin, H. *Proc. Natl. Acad. Sci. USA* **2006**, *103*, 6829.
- (119) Grove, T. L.; Lee, K.-H.; St. Clair, J.; Krebs, C.; Booker, S. J. *Biochemistry* **2008**, *47*, 7523.
- (120) Moser, C. C.; Anderson, J. L. R.; Dutton, P. L. *Biochim. Biophys. Acta: Bioenergetics* **2010**, *1797*, 1573.
- (121) Yokoyama, K.; Numakura, M.; Kudo, F.; Ohmori, D.; Eguchi, T. *J. Am. Chem. Soc.* **2007**, *129*, 15147.

- (122) Zhang, Q.; Chen, D.; Lin, J.; Liao, R.; Tong, W.; Xu, Z.; Liu, W. *J. Biol. Chem.* **2011**, *286*, 21287.
- (123) Kriek, M.; Martins, F.; Leonardi, R.; Fairhurst, S. A.; Lowe, D. J.; Roach, P. L. *J. Biol. Chem.* **2007**, *282*, 17413.
- (124) Kriek, M.; Martins, F.; Challand, M. R.; Croft, A.; Roach, P. L. *Angew. Chem. Int. Ed.* **2007**, *46*, 9223.
- (125) Zhang, Q.; Li, Y.; Chen, D.; Yu, Y.; Duan, L.; Shen, B.; Liu, W. *Nat. Chem. Biol.* **2011**, *7*, 154.
- (126) Yu, Y.; Duan, L.; Zhang, Q.; Liao, R.; Ding, Y.; Pan, H.; Wendt-Pienkowski, E.; Tang, G.; Shen, B.; Liu, W. *ACS Chem. Biol.* **2009**, *4*, 855.
- (127) Decamps, L.; Philmus, B.; Benjdia, A.; White, R.; Begley, T. P.; Berteau, O. *J. Am. Chem. Soc.* **2012**, *134*, 18173.
- (128) Duffus, B. R.; Hamilton, T. L.; Shepard, E. M.; Boyd, E. S.; Peters, J. W.; Broderick, J. B. *Biochim. Biophys. Acta: Proteins and Proteomics* **2012**, *1824*, 1254.
- (129) Fossey, J.; Lefort, D.; Sorba, J. *Free radicals in organic chemistry*, John Wiley and Sons Ltd.: Chichester, 1995.
- (130) Challand, M. R.; Martins, F. T.; Roach, P. L. *J. Biol. Chem.* **2010**, *285*, 5240.
- (131) Batsanov, S. S. *Inorg. Mater.* **2001**, *37*, 871.
- (132) Antonini, E.; Brunori, M. *Hemoglobin and myoglobin in their reactions with ligands*; North Holland Publishing: Amsterdam, 1971; Vol. 21.
- (133) Nicolet, Y.; Martin, L.; Tron, C.; Fontecilla-Camps, J. C. *FEBS Lett.* **2010**, *584*, 4197.
- (134) Sweeney, W. V.; Rabinowitz, J. C. *Annu. Rev. Biochem.* **1980**, *49*, 139.
- (135) Lippard, S. J.; Berg, J. M. In *Principles of Bioinorganic Chemistry*, 1st ed.; University Science Books: Mill Valley, California, 1994.
- (136) Cammack, R.; MacMillan, F. In *Chapter 2, Electron magnetic resonance of iron-sulfur proteins in electron-transfer chains: Resolving complexity*, Hanson, G., Berliner, L., Eds.; Springer: New York, 2010; Vol. 29.

References

- (137) Dailey, H. A.; Finnegan, M. G.; Johnson, M. K. *Biochemistry* **1994**, *33*, 403.
- (138) Lippard, S. J.; Berg, J. M. *Principles of bioinorganic chemistry*, University Science Books: Mill Valley, California, 1994.
- (139) Brückner, A. *Chem. Soc. Rev.* **2010**, *39*, 4673.
- (140) Posewitz, M. C.; King, P. W.; Smolinski, S. L.; Smith, R. D.; Ginley, A. R.; Ghirardi, M. L.; Seibert, M. *Biochem. Soc. Trans.* **2005**, *33*, 102.
- (141) Duschene, K. S.; Broderick, J. B. *FEBS Lett.* **2010**, *584*, 1263.
- (142) McCarty, R. M.; Krebs, C.; Bandarian, V. *Biochemistry* **2012**, *52*, 188.
- (143) Cammack, R. *Appl. Magn. Reson.* **2010**, *37*, 257.
- (144) Sweeney, W. V.; McIntosh, B. A. *J. Biol. Chem.* **1979**, *254*, 4499.
- (145) Fish, W. W. *Methods Enzymol.* **1988**, *158*, 357.
- (146) Jarrett, J. T. *Curr. Opin. Chem. Biol.* **2003**, *7*, 174.
- (147) Bradford, M. M. *Anal. Biochem.* **1976**, *72*, 248.
- (148) Brereton, P. S.; Duderstadt, R. E.; Staples, C. R.; Johnson, M. K.; Adams, M. W. W. *Biochemistry* **1999**, *38*, 10594.
- (149) Mansy, S. S.; Xiong, Y.; Hemann, C.; Hille, R.; Sundaralingam, M.; Cowan, J. A. *Biochemistry* **2001**, *41*, 1195.
- (150) Xiao, Z.; Lavery, M. J.; Ayhan, M.; Scrofani, S. D. B.; Wilce, M. C. J.; Guss, J. M.; Tregloan, P. A.; George, G. N.; Wedd, A. G. *J. Am. Chem. Soc.* **1998**, *120*, 4135.
- (151) Yokoyama, K.; Ohmori, D.; Kudo, F.; Eguchi, T. *Biochemistry* **2008**, *47*, 8950.
- (152) Harmer, J. E., University of Southampton, Personal Communication, 2012.
- (153) Lanz, N. D.; Grove, T. L.; Gogonea, C. B.; Lee, K.-H.; Krebs, C.; Booker, S. J. In *Methods Enzymol.*; David, A. H., Ed.; Academic Press: 2012; Vol. Volume 516, p 125.

- (154) Ugulava, N. B.; Frederick, K. K.; Jarrett, J. T. *Biochemistry* **2003**, *42*, 2708.
- (155) Fang, Q.; Peng, J.; Dierks, T. *J. Biol. Chem.* **2004**, *279*, 14570.
- (156) Werth, M. T.; Cecchini, G.; Manodori, A.; Ackrell, B. A. C.; Schröder, I.; Gunsalus, R. P.; Johnson, M. K. *Proc. Natl. Acad. Sci. USA* **1990**, *87*, 8965.
- (157) Freyer, M. W.; Lewis, E. A. In *Methods in Cell Biology*, Dr. John, J. C., Dr. H. William Detrich, III, Eds.; Academic Press: 2008; Vol. Volume 84, p 79.
- (158) Copeland, R. A. *Enzymes: A practical introduction to structure, mechanism, and data analysis*; 2nd ed.; John Wiley & Sons, Inc.: New York, 2000.
- (159) Kuchenreuther, J. M.; Myers, W. K.; Stich, T. A.; George, S. J.; Nejatyjahromy, Y.; Swartz, J. R.; Britt, R. D. *Science* **2013**, *342*, 472.
- (160) Tron, C.; Cherrier, M. V.; Amara, P.; Martin, L.; Fauth, F.; Fraga, E.; Correard, M.; Fontecave, M.; Nicolet, Y.; Fontecilla-Camps, J. C. *Eur. J. Inorg. Chem.* **2011**, *2011*, 1121.
- (161) Bonifačić, M.; Štefanić, I.; Hug, G. L.; Armstrong, D. A.; Asmus, K.-D. *J. Am. Chem. Soc.* **1998**, *120*, 9930.
- (162) Johnson, W. R.; Kan, J. C. *J. Org. Chem.* **1971**, *36*, 189.
- (163) Grodkowski, J.; Neta, P. *J. Phys. Chem. B* **2001**, *105*, 4967.
- (164) Bach, R. D.; Evans, J. C. *J. Am. Chem. Soc.* **1985**, *108*, 1374.
- (165) Patil, R. D.; Adimurthy, S. *Asian J. Org. Chem.* **2013**, *2*, 726.
- (166) Giambastiani, G.; Campora, J. *Olefin upgrading catalysis by nitrogen-based metal complexes II*; Springer: Netherlands, 2011; Vol. 36.
- (167) Haas, K. L.; Franz, K. J. *Chem. Rev.* **2009**, *109*, 4921.
- (168) Grotjahn, D. B.; Joubran, C. *Inorg. Chim. Acta* **2004**, *357*, 3047.
- (169) Coalter, J. N.; Huffman, J. C.; Caulton, K. G. *Organometallics* **2000**, *19*, 3569.
- (170) Bauer, I.; Knölker, H.-J. In *Iron catalysis in organic chemistry, reactions and applications*; Plietker, B., Ed.; Wiley-VCH: Weinheim, 2008.

References

- (171) Challand, M. R.; Driesener, R. C.; Roach, P. L. *Nat. Prod. Rep.* **2011**, *28*, 1696.
- (172) Duffus, B. R., Montana State University, Personal communication, 2012.
- (173) Welch, K. D.; Davis, T. Z.; Aust, S. D. *Arch. Biochem. Biophys.* **2002**, *397*, 360.
- (174) Hicks, M.; Gebicki, J. M. *FEBS Lett.* **1986**, *199*, 92.
- (175) Rozanas, C.; Fulper, J. *Life Science News* **1999**, *2*, 1.
- (176) Wu, X.; Diao, Y.; Sun, C.; Yang, J.; Wang, Y.; Sun, S. *Talanta* **2003**, *59*, 95.
- (177) Challand, M. R.; Salvadori, E.; Driesener, R. C.; Kay, C. W. M.; Roach, P. L.; Spencer, J. *PLoS ONE* **2013**, *8*, e67979.
- (178) Crain, A. V.; Broderick, J. B. *J. Biol. Chem.* **2013**.
- (179) Iwig, D. F.; Booker, S. J. *Biochemistry* **2004**, *43*, 13496.
- (180) Wong, K. K.; Murray, B. W.; Lewisch, S. A.; Baxter, M. K.; Ridky, T. W.; Ulissi-DeMario, L.; Kozarich, J. W. *Biochemistry* **1993**, *32*, 14102.
- (181) Szu, P.-H.; Rusczycky, M. W.; Choi, S.-h.; Yan, F.; Liu, H.-W. *J. Am. Chem. Soc.* **2009**, *131*, 14030.
- (182) Fersht, A. *Enzyme structure and mechanism*; 2nd ed.; W. H. Freeman and Company: New York, 1985.
- (183) Michaelis, L.; Menten, M. *Biochemistry Zeitung* **1913**, *49*, 333.
- (184) Johnson, K. A.; Goody, R. S. *Biochemistry* **2011**, *50*, 8264.
- (185) Fersht, A. *Structure and mechanism in protein science: A guide to enzyme catalysis and protein folding*; Freeman: New York, 1999.
- (186) Hoffman, J. L. *Biochemistry* **1986**, *25*, 4444.
- (187) Del Olmo, M.; Díez, C.; Molina, A.; de Orbe, I.; Vílchez, J. L. *Anal. Chim. Acta* **1996**, *335*, 23.
- (188) Markham, G. D.; Hafner, E. W.; Tabor, C. W.; Tabor, H. *J. Biol. Chem.* **1980**, *255*, 9082.

- (189) Jaffe, E. K.; Cohn, M. *J. Biol. Chem.* **1978**, *253*, 4823.
- (190) Park, J.; Tai, J.; Roessner, C. A.; Scott, A. I. *Biorg. Med. Chem.* **1996**, *4*, 2179.
- (191) Yan, F.; LaMarre, J. M.; Röhrich, R.; Wiesner, J.; Jomaa, H.; Mankin, A. S.; Fujimori, D. G. *J. Am. Chem. Soc.* **2010**, *132*, 3953.
- (192) Gross, A.; Geresh, S.; Whitesides, G. M. *Appl. Biochem. Biotechnol.* **1983**, *8*, 415.
- (193) Schlenk, F.; DePalma, R. E. *J. Biol. Chem.* **1957**, *229*, 1051.
- (194) *Rohm and Haas Company PDS 0504 A – Apr. 97.*
- (195) Stolowitz, M. L.; Minch, M. J. *J. Am. Chem. Soc.* **1981**, *103*, 6015.
- (196) Kemeny, D. M.; Challacombe, S. J. *ELISA and other solid phase immunoassays, Theoretical and practical aspects*; John Wiley & Sons Ltd., 1988.
- (197) Cospers, M. M.; Jameson, G. N. L.; Davydov, R.; Eidsness, M. K.; Hoffman, B. M.; Huynh, B. H.; Johnson, M. K. *J. Am. Chem. Soc.* **2002**, *124*, 14006.
- (198) Amador-Noguez, D.; Brasg, I. A.; Feng, X.-J.; Roquet, N.; Rabinowitz, J. D. *Appl. Environ. Microbiol.* **2011**, *77*, 7984.
- (199) Hitchcock, D. I. *J. Gen. Physiol.* **1924**, *6*, 747.
- (200) Challand, M. R., PhD Thesis, University of Southampton, 2010.
- (201) Duerre, J. A. *J. Biol. Chem.* **1962**, *237*, 3737.
- (202) Ferro, A. J.; Barrett, A.; Shapiro, S. K. *Biochim. Biophys. Acta: Enzymology* **1976**, *438*, 487.
- (203) Herbst, R. W.; Perovic, I.; Martin-Diaconescu, V.; O'Brien, K.; Chivers, P. T.; Pochapsky, S. S.; Pochapsky, T. C.; Maroney, M. J. *J. Am. Chem. Soc.* **2010**, *132*, 10338.
- (204) Harris, T. K.; Turner, G. J. *IUBMB Life* **2002**, *53*, 85.
- (205) Kokesh, F. C.; Westheimer, F. H. *J. Am. Chem. Soc.* **1971**, *93*, 7270.

References

- (206) Frey, P. A.; Kokesh, F. C.; Westheimer, F. H. *J. Am. Chem. Soc.* **1971**, *93*, 7266.
- (207) Kuchenreuther, J. M.; Myers, W. K.; Suess, D. L. M.; Stich, T. A.; Pelmeshnikov, V.; Shiigi, S. A.; Cramer, S. P.; Swartz, J. R.; Britt, R. D.; George, S. J. *Science* **2014**, *343*, 424.
- (208) Dessau, M. A.; Modis, Y. *J. Vis. Exp.* **2011**, e2285.
- (209) Dale, G. E.; Oefner, C.; D'Arcy, A. *J. Struct. Biol.* **2003**, *142*, 88.
- (210) Luft, J. R.; Wolfey, J. R.; Snell, E. H. *Cryst. Growth Des.* **2011**, *11*, 651.
- (211) Martins, F. T., PhD Thesis, University of Southampton, **2009**.
- (212) Kane, J. F. *Curr. Opin. Biotechnol.* **1995**, *6*, 494.
- (213) Novy, R.; Drott, D.; Yaeger, K.; Mierendorf, R. *inNovations* **2001**, *12*, 1.
- (214) Takahata, Y.; Nishijima, M.; Hoaki, T.; Maruyama, T. *Int. J. Syst. Evol. Microbiol.* **2001**, *51*, 1901.
- (215) Kwon, S.; Jung, Y.; Lim, D. *BMB Rep* **2007**, *41*, 108.
- (216) Gasteiger E.; Hoogland C.; Gattiker A.; Duvaud S.; Wilkins M. R.; Appel R. D.; Bairoch A. In *The Proteomics Protocols Handbook*; Walker, J. M., Ed.; Humana Press: 2005, p 571.
- (217) Huang, X.; Miller, W. *Adv. Appl. Math.* **1991**, *12*, 337.
- (218) Chayen, N. E. *Prog. Biophys. Mol. Biol.* **2005**, *88*, 329.
- (219) Mitchell, E.; Kuhn, P.; Garman, E. *Structure* **1999**, *7*, R111.
- (220) Helliwell, J. R. *Rep. Prog. Phys.* **1984**, *47*, 1403.
- (221) Hendrickson, W. A. *Science* **1991**, *254*, 51.
- (222) Liu, Z.-C.; Xu, R.; Dong, Y.-H. *Acta Crystallogr. Sect. A: Found. Crystallogr.* **2011**, *68*, 256.
- (223) Okube, M.; Sasaki, S. *J. Phys. Conf. Ser.* **2013**, *425*, 202002.
- (224) Brünger, A. T.; Rice, L. M. *Methods Enzymol.* **1997**, *277*, 243.
- (225) Kleywegt, G. J.; Alwyn Jones, T. *Methods Enzymol.* **1997**, *277*, 208.

- (226) Brünger, A. T. *Nature* **1992**, *355*, 472.
- (227) Kleywegt, G. J.; Jones, T. A. *Structure* **1995**, *3*, 535.
- (228) Pizano, A. A.; Lutterman, D. A.; Holder, P. G.; Teets, T. S.; Stubbe, J.; Nocera, D. G. *Proc. Natl. Acad. Sci. USA* **2012**, *109*, 39.
- (229) Danley, D. E. *Acta Crystallogr. Sect. D. Biol. Crystallogr.* **2006**, *62*, 569.
- (230) Hassell, A. M.; An, G.; Bledsoe, R. K.; Bynum, J. M.; Carter, H. L., III; Deng, S.-J. J.; Gampe, R. T.; Grisard, T. E.; Madauss, K. P.; Nolte, R. T.; Rocque, W. J.; Wang, L.; Weaver, K. L.; Williams, S. P.; Wisely, G. B.; Xu, R.; Shewchuk, L. M. *Acta Crystallographica Section D* **2007**, *63*, 72.
- (231) Berto, P.; Di Valentin, M.; Cendron, L.; Vallese, F.; Albertini, M.; Salvadori, E.; Giacometti, G. M.; Carbonera, D.; Costantini, P. *Biochim. Biophys. Acta: Bioenergetics* **2012**, *1817*, 2149.
- (232) Wu, S.-p.; Wu, G.; Surerus, K. K.; Cowan, J. A. *Biochemistry* **2002**, *41*, 8876.
- (233) Schmidt, T. G. M.; Koepke, J.; Frank, R.; Skerra, A. *J. Mol. Biol.* **1996**, *255*, 753.
- (234) Expression and purification of proteins using Strep-tag or Twin-Strep-tag, Ed.; IBA GmbH: 2012.
- (235) Chaiet, L.; Wolf, F. J. *Arch. Biochem. Biophys.* **1964**, *106*, 1.
- (236) Taylor, A. L.; Trotter, C. D. *Bacteriol. Rev.* **1972**, *36*, 504.
- (237) Pai, C. H.; Lichstein, H. C. *Biochim. Biophys. Acta: General Subjects* **1965**, *100*, 28.
- (238) Cavaluzzi, M. J.; Borer, P. N. *Nucleic Acids Res.* **2004**, *32*, e13.
- (239) Bennett, B. D.; Kimball, E. H.; Gao, M.; Osterhout, R.; Van Dien, S. J.; Rabinowitz, J. D. *Nat. Chem. Biol.* **2009**, *5*, 593.
- (240) Scopes, R. K.; Smith, J. A. In *Current Protocols in Molecular Biology*, John Wiley & Sons, Inc.: 1998.
- (241) Batten, L. E., PhD Thesis, University of Southampton, **2013**.

References

- (242) Takagi, T.; Habe, H.; Yoshida, T.; Yamane, H.; Omori, T.; Nojiri, H. *Appl. Microbiol. Biotechnol.* **2005**, *68*, 336.
- (243) Porath, J.; Olin, B. *Biochemistry* **1983**, *22*, 1621.
- (244) Volbeda, A.; Charon, M.-H.; Piras, C.; Hatchikian, E. C.; Frey, M.; Fontecilla-Camps, J. C. *Nature* **1995**, *373*, 580.
- (245) Messick, T. E.; Chmiel, N. H.; Golinelli, M.-P.; Langer, M. R.; Joshua-Tor, L.; David, S. S. *Biochemistry* **2002**, *41*, 3931.
- (246) Beck, M. T. *Pure Appl. Chem.* **1987**, *59*, 1703.
- (247) MDHS 56/2, Hydrogen cyanide in air. [Online Early Access]. Published Online: 1990.
- (248) Lebendiker, M.; Danieli, T. In *Protein Chromatography*, Walls, D., Loughran, S. T., Eds.; Humana Press: 2011; Vol. 681, p 281.
- (249) Harper, S.; Speicher, D. In *Protein Chromatography*, Walls, D., Loughran, S. T., Eds.; Humana Press: 2011; Vol. 681, p 259.
- (250) Kriek, M.; Peters, L.; Takahashi, Y.; Roach, P. L. *Protein Expression Purif.* **2003**, *28*, 241.
- (251) Nakamura, M.; Saeki, K.; Takahashi, Y. *J. Biochem.* **1999**, *126*, 10.
- (252) Keseler, I. M.; Collado-Vides, J.; Santos-Zavaleta, A.; Peralta-Gil, M.; Gama-Castro, S.; Muñiz-Rascado, L.; Bonavides-Martinez, C.; Paley, S.; Krummenacker, M.; Altman, T.; Kaipa, P.; Spaulding, A.; Pacheco, J.; Latendresse, M.; Fulcher, C.; Sarker, M.; Shearer, A. G.; Mackie, A.; Paulsen, I.; Gunsalus, R. P.; Karp, P. D. *Nucleic Acids Res.* **2011**, *39*, D583.
- (253) Py, B.; Barras, F. *Nat. Rev. Microbiol.* **2010**, *8*, 436.
- (254) Kuchenreuther, J. M.; Grady-Smith, C. S.; Bingham, A. S.; George, S. J.; Cramer, S. P.; Swartz, J. R. *PLoS ONE* **2010**, *5*, e15491.
- (255) Akhtar, M. K.; Jones, P. *Appl. Microbiol. Biotechnol.* **2008**, *78*, 853.
- (256) Sørensen, H. P.; Mortensen, K. K. *J. Biotechnol.* **2005**, *115*, 113.
- (257) Jaganaman, S.; Pinto, A.; Tarasev, M.; Ballou, D. P. *Protein Expression Purif.* **2007**, *52*, 273.

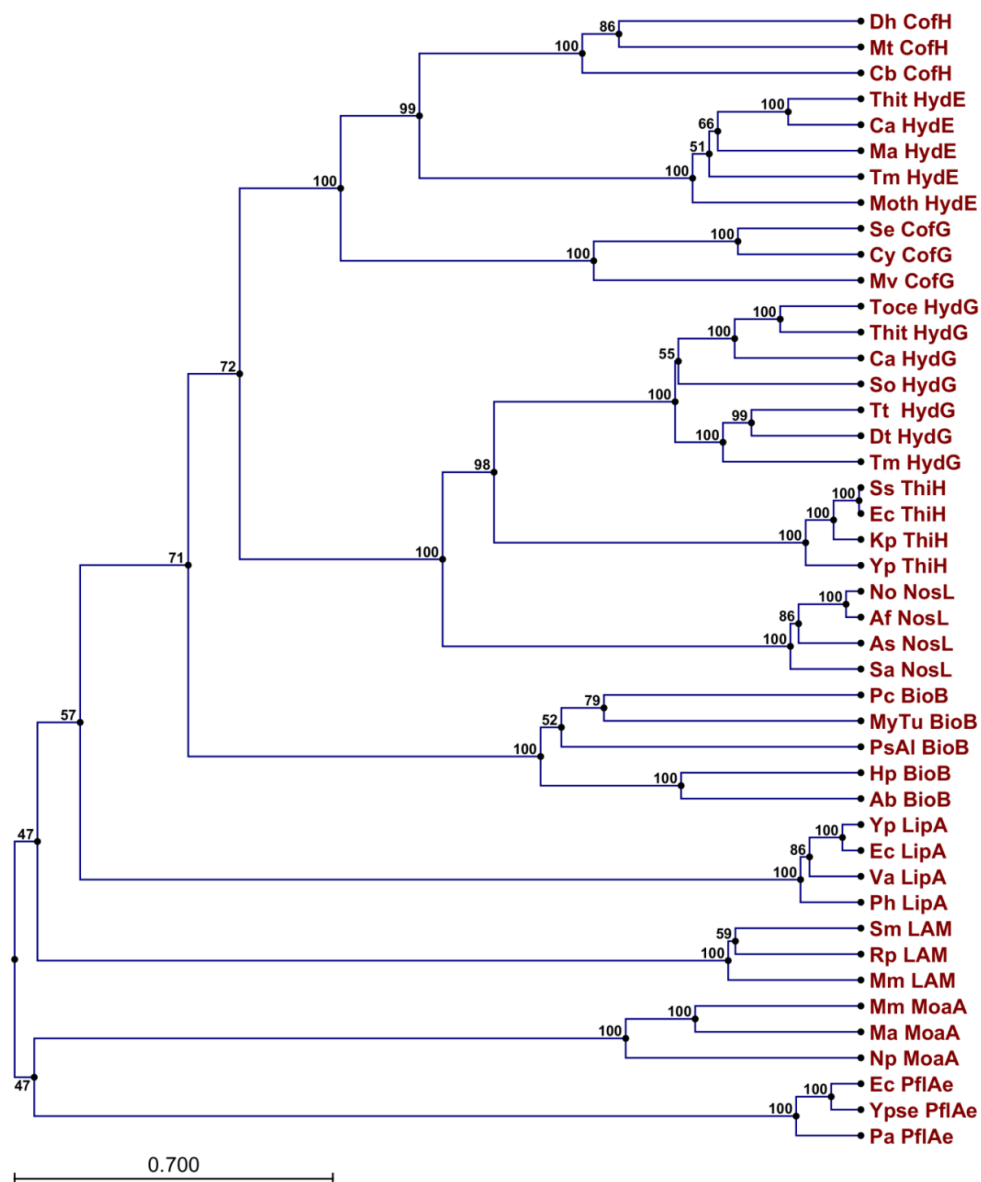
- (258) Muthukumaran, R. B.; Grzyska, P. K.; Hausinger, R. P.; McCracken, J. *Biochemistry* **2007**, *46*, 5951.
- (259) Lin, M. T.; Baldansuren, A.; Hart, R.; Samoilova, R. I.; Narasimhulu, K. V.; Yap, L. L.; Choi, S. K.; O'Malley, P. J.; Gennis, R. B.; Dikanov, S. A. *Biochemistry* **2012**, *51*, 3827.
- (260) Enemark, J. H.; Astashkin, A. V.; Raitsimring, A. M. *Biochem. Soc. Trans.* **2008**, *36*, 1129.
- (261) Harmer, J.; Mitrikas, G.; Schweiger, A. In *High Resolution EPR, Applications to Metalloenzymes and Metals in Medicine*; Berliner, L., Hanson, G., Eds.; Springer New York: New York, 2009, p 13.
- (262) Tomter, A. B.; Zoppellaro, G.; Schmitzberger, F.; Andersen, N. H.; Barra, A.-L.; Engman, H.; Nordlund, P.; Andersson, K. K. *PLoS ONE* **2011**, *6*, e25022.
- (263) Sanyal, I.; Cohen, G.; Flint, D. H. *Biochemistry* **1994**, *33*, 3625.
- (264) Svetlitchnyi, V.; Dobbek, H.; Meyer-Klaucke, W.; Meins, T.; Thiele, B.; Römer, P.; Huber, R.; Meyer, O. *Proc. Natl. Acad. Sci. USA* **2003**, *101*, 446.
- (265) Guerrini, O.; Burlat, B.; Léger, C.; Guigliarelli, B.; Soucaille, P.; Girbal, L. *Curr. Microbiol.* **2008**, *56*, 261.
- (266) Stoll, S.; Schweiger, A. *J. Magn. Reson.* **2006**, *178*, 42.
- (267) The PyMOL Molecular Graphics System, Version 1.3r1. Schrödinger, LLC, Portland, **2010**.
- (268) Douglas, H. *J. Mol. Biol.* **1983**, *166*, 557.
- (269) MATLAB Release 2013a, The MathWorks, Inc., Natick, Massachusetts, US.
- (270) GraphPad Prism (version 6.00 for Windows, GraphPad Software, La Jolla California USA).
- (271) Markham, G. D.; DeParasis, J.; Gatmaitan, J. *J. Biol. Chem.* **1984**, *259*, 14505.
- (272) Schluckebier, G.; Kozak, M.; Bleimling, N.; Weinhold, E.; Saenger, W. *J. Mol. Biol.* **1997**, *265*, 56.
- (273) Shapiro, S. K.; Ehninger, D. J. *Anal. Biochem.* **1966**, *15*, 323.

References

- (274) Tracqui, A.; Raul, J. S.; Geraut, A.; Berthelon, L.; Ludes, B. *J. Anal. Toxicol.* **2002**, *26*, 144.
- (275) Pierik, A. J.; Roseboom, W.; Happe, R. P.; Bagley, K. A.; Albracht, S. P. J. *J. Biol. Chem.* **1999**, *274*, 3331.
- (276) Cordell, R. L.; Hill, S. J.; Ortori, C. A.; Barrett, D. A. *J. Chromatogr. B* **2008**, *871*, 115.
- (277) Newman, J. *Acta Crystallogr. Sect. D. Biol. Crystallogr.* **2003**, *60*, 610.

Appendices

Appendix 1 – Phylogenetic analyses



Phylogenetic tree of selected radical AdoMet enzymes.

Primary sequences were aligned using the CLC Sequence Viewer v6.5.4.

Distances and branching of the resulting phylogenetic tree were inferred using the unweighted-pair group method with arithmetic means (UPGMA) algorithm and bootstrap values determined from 100 replicates using the above software.

Appendix 1

The following organisms (in order of appearance) have been used in the alignment:

CofH; *Dh* – *Desulfovibrio hydrothermalis* AM13 (YP_007327332.1), *Mt* – *Methanothermobacter thermautotrophicus* CaT2 (AP011952.1), *Cb* – *Chlamydiaceae bacterium* 10-1398/6 (APJW01000001.1); **HydE**; *Thit* – *Thermoanaerobacter italicus* Ab9 (YP_003477090.1), *Ca* – *Clostridium acetobutylicum* ATCC 824 (NP_348258.1), *Ma* – *Mahella australiensis* 50-1 BON (YP_004462471.1), *Tm* – *Thermotoga maritima* MSB8 (NP_229074.1), *Moth* – *Moorella thermoacetica* ATCC 39073 (YP_430579.1); **CofG**; *Se* – *Synechococcus elongatus* PCC 6301 (YP_171358.1), *Cy* – *Cyanothece* sp. ATCC 51142 (YP_001804131.1), *Mv* – *Methanocaldococcus villosus* (WP_004590739); **HydG**; *Toce* – *Thermosediminibacter oceani* DSM 16646 (YP_003826605.1), *Thit* – *Thermoanaerobacter italicus* Ab9 (YP_003476445.1), *Ca* – *Clostridium acetobutylicum* ATCC 824, *So* – *Shewanella oneidensis* MR-1 (NP_719454.1), *Tt* – *Thermoanaerobacter tengcongensis* MB4 (NP_623168.1), *Dt* – *Desulfurobacterium thermolithotrophum* DSM 11699 (YP_004280861.1), *Tm* – *Thermotoga maritima* MSB8 (NP_229072.1); **ThiH**; *Ss* – *Shigella sonnei* Ss046 (YP_312902.1), *Ec* – *Escherichia coli* str. K-12 substr. MG1655 (NP_418417.1), *Kp* – *Klebsiella pneumoniae* KP-1 (AVNZ01000016.1), *Yp* – *Yersinia pestis* KIM10+ (NP_667825.1); **NosL**; *No* – *Nocardia* sp. ATCC 202099 (ADR01087.1), *Af* – *Actinokineospora fastidiosa* (ADH93698.1), *As* – *Actinoalloteichus spitiensis* (WP_016697820.1), *Sa* – *Streptomyces actuosus* (ACR48341.1); **BioB**; *Pc* – *Pelobacter carbinolicus* DSM 2380 (YP_356874.1), *MyTu* – *Mycobacterium tuberculosis* str. Haarlem (CP001664.1), *PsAl* – *Pseudomonas alcaligenes* NBRC 14159 (BATI01000002.1), *Hp* – *Helicobacter pylori* P12 (YP_002302007.1), *Ab* – *Arcobacter butzleri* RM4018 (YP_001491120.1); **LipA**; *Yp* – *Yersinia pseudotuberculosis* IP 32953 (YP_069629.1), *Ec* – *Escherichia coli* 83972

(ZP_04002198.1), *Va* - *Vibrio alginolyticus* NBRC 15630 = ATCC 17749
(BATK01000040.1), *Ph* - *Pseudoalteromonas haloplanktis* TAC125
(YP_339540.1); **LAM**; *Sm* - *Sinorhizobium medicae* WSM419 (YP_001329129.1),
Rp - *Rhodopseudomonas palustris* CGA009 (NP_947857.1), *Mm* -
Magnetospirillum magnetotacticum MS-1 (ZP_00051632.2); **MoaA**; *Mm* -
Methanoculleus marisnigri JR1 (YP_001047376.1), *Ma* - *Methanosarcina*
acetivorans C2A (AAM03559.1), *Np* - *Natronomonas pharaonis* DSM 2160
(YP_327061.1); **PFL-Ae**; *Ec* - *Escherichia coli* O157:H7 str. EDL933
(NP_286777.1), *Ypse* - *Yersinia pseudotuberculosis* IP 31758
(YP_001401556.1), *Pa* - *Photobacterium angustum* S14 (ZP_01235149.1).

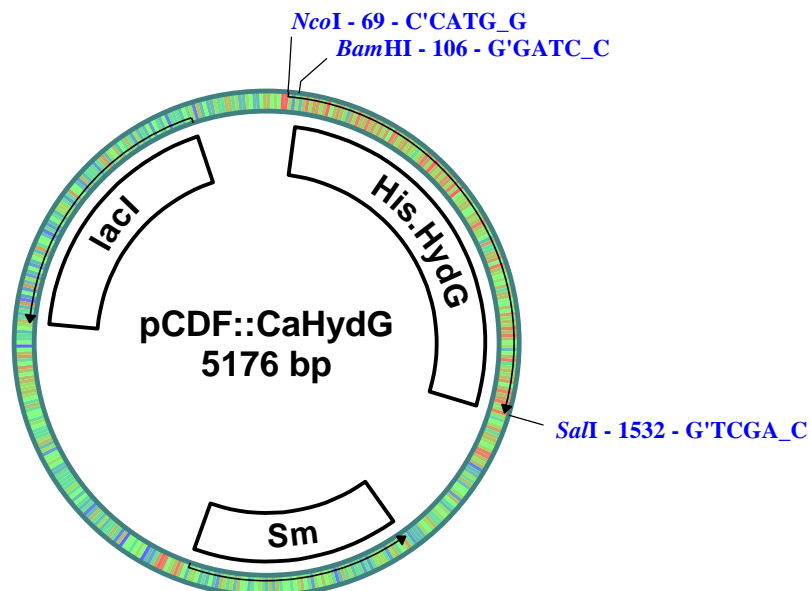
Appendix 2 – Plasmid maps

Shown below are plasmid maps for constructs used throughout this project (in order of appearance). Unique restriction sites are indicated in blue while resistance markers are designated as Sm – streptomycin, Cm – chloramphenicol and Amp – ampicillin.

Nucleotide sequences are only listed when the parent sequence has been modified by codon optimisation. Associated protein sequences are presented with the iron–sulfur cluster coordinating cysteine residues highlighted in red.

Expression of proteins encoded in pRD001, pCDFDuet-1 and pACYCDuet-1 vectors is inducible with IPTG while expression of pFM103 and pRD002 – pRD004 encoded proteins must be induced with arabinose.

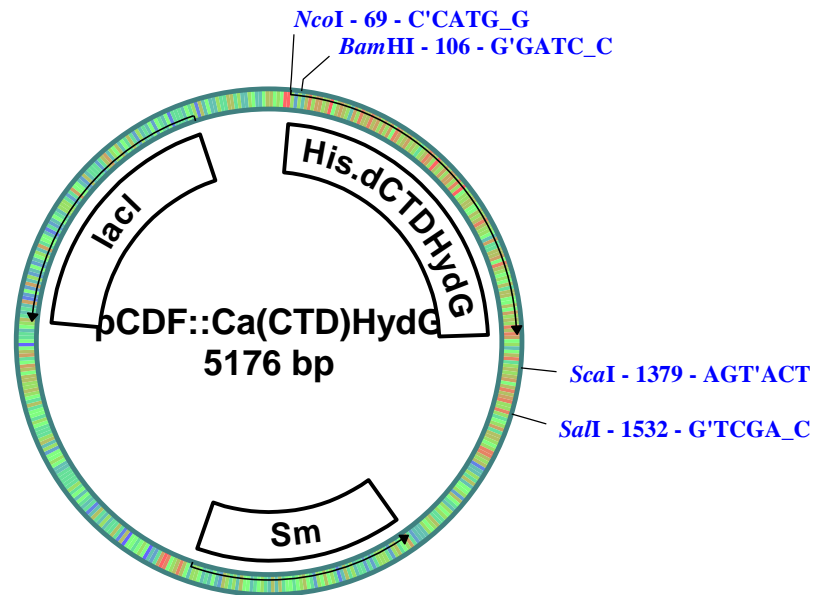
pCDFDuet-1 containing N-terminally 6His tagged *C. acetobutylicum* WT or C386S HydG



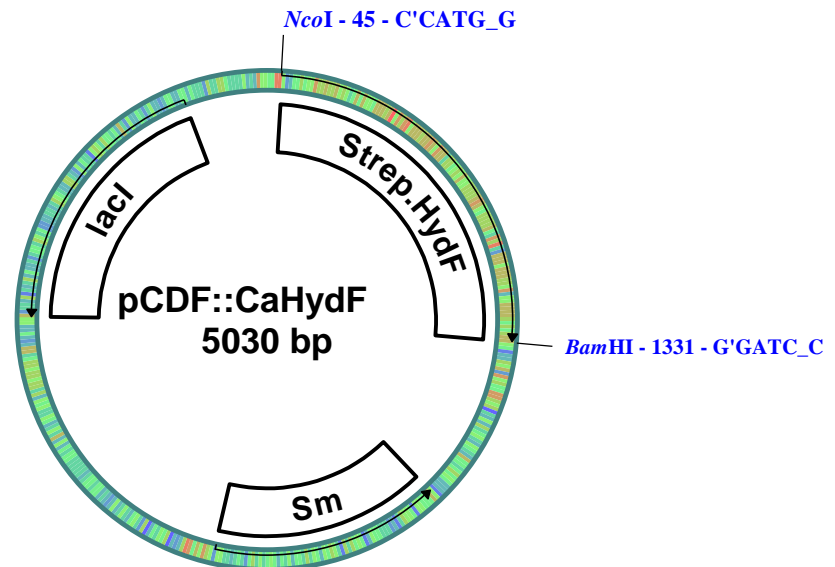
MGSSHHHHHSQDPMYNVKSQVATEFISDEEIIIDSLEYAKQNKSNRELIDSIIEKAKECKGLT
 HRDAAVLLECDLEDENEKMFKLAREIKQKFGNRIVMFAPLYLSNYCVNGCVYCPYHHKN
 KHIARKKLSQEDVKRETIALQDMGHKRLALEAGEDPVNNPIEYILDCKTIYSIKHKNGAIRR
 VNVNIAATTVENYKCLKDAGIGTYILFQETYNNKSYEELHPTGPKHDYAYHTEAMDRAME
 GGIDDVGIGVLFGLNMYKYDFVGLLMHAEHLEAAMGVGPHTISVPRIRPADDIDPENFSNA
 ISDEIFEKIVAIIRIAVPYTGMIIVSTRESKTRERVLGLISQISGGSSTSVGGYVESEPEEDNSSQ
 FEVNDNRTLDEIVNWLLEMNYIPSF(CS)TACYREGRTGDRFMSLVKSGQIANCCQPNALM
 TLKEYLEDYASSNTQKNGEALIASVEKIPNEKVKSIKKHLTELKEGQRDFRF

Appendix 2

pRD001 containing N-terminally 6His tagged *C. acetobutylicum* ΔCTD HydG



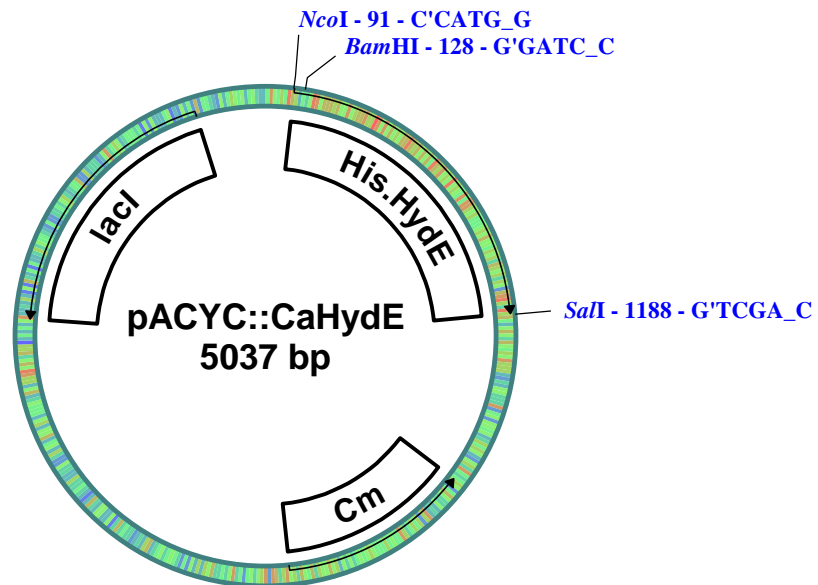
MGSSHHHHHSQDPMYNVKSKVATEFISDEEIIDSLLEYAKQNKSNRELIDSIIEKAKECKGLT
HRDAAVLLECDLEDENEKMFKLAREIKQKFYGNRIVMFAPLYLSNYCVNGCVYCPYHHKN
KHIARKKLSQEDVKRETIALQDMGHKRLALEAGEDPVNNPIEYILDCKIYTIYSIKHKNGAIRR
VNVNIAATTVENYKCLKDAGIGTYILFQETYNKKSYEELHPTGPKHDYAYHTEAMDRAME
GGIDDVGIGVLFGLNMYKYDFVGLLMHAEHLEAAMGVGPHTISVPRIRPADDIDPENFSNA
ISDEIFEKIVAIIRIAPYTGMIIVSTRESKKTREVRVLELGISQISGGSSTSVGGYVESEPEEDNSSQ
FEVNDNRTLDEIVNWLLEMNYIPSF

pCDFDuet-1 containing N-terminally Strep II tagged *C. acetobutylicum* HydF

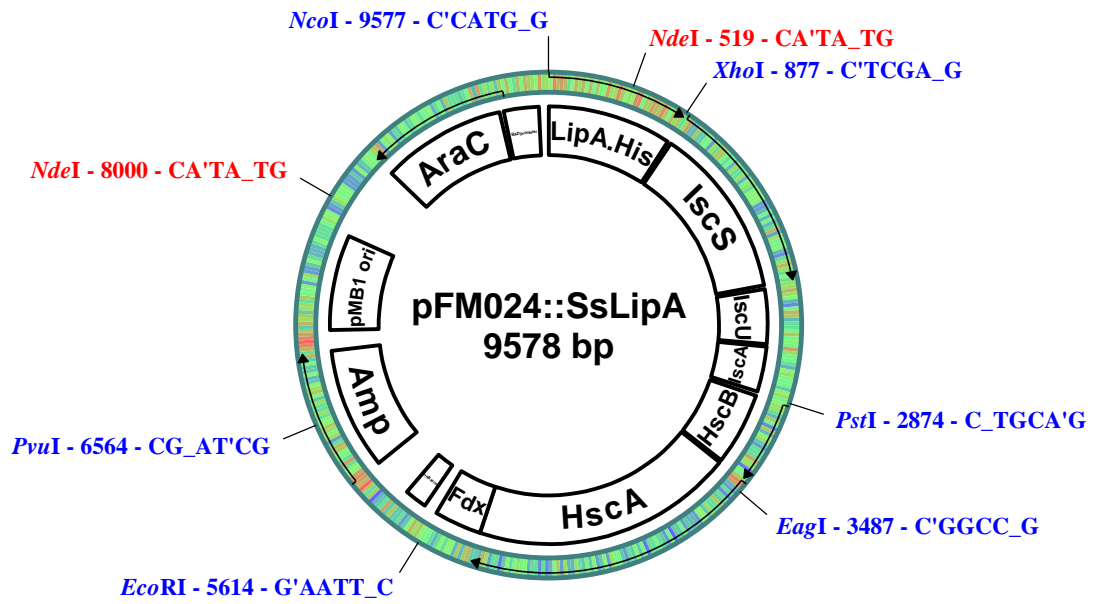
MAWSPQFEKENLYFQGNELNSTPKGERLHIALFGKTNVGKSSVINALTSQEIALVSNVKG
 TTTDPVYKAMELLPLGPVMLIDTAGLDDISDLGELRRGKTLEVLSTKTDVAILVFDVESGITEY
 DKNIYSLLEKKIPLIGVLNKIDKKDYKLEDYTSQFKIPIVPISALNNKGINNLKDELIRLAPEN
 DDKFKIVGDLLSPGDIAVLVTPIDKAAPKGRLILPQQQTIRDILESDAIAMVTKEFELRETLDS
 LRKKPKIVITDSQVFLKVAADTPKDILMTSFSILMARHKGDIELARGARAIEDLKDGDKILIA
 EAC^TTHHRQSDDIGKVKIPRWLRQKTGKKLEFD^FSSGFSFPPNIEDYALIVH^CAG^CM^LNRRS
 MLHRIESSVKKQIPIVNYGVLIAYVQGILPRALKPF^PYADRIFN^QSSRN

Appendix 2

pACYCDuet-1 containing N-terminally 6His tagged *C. acetobutylicum* HydE

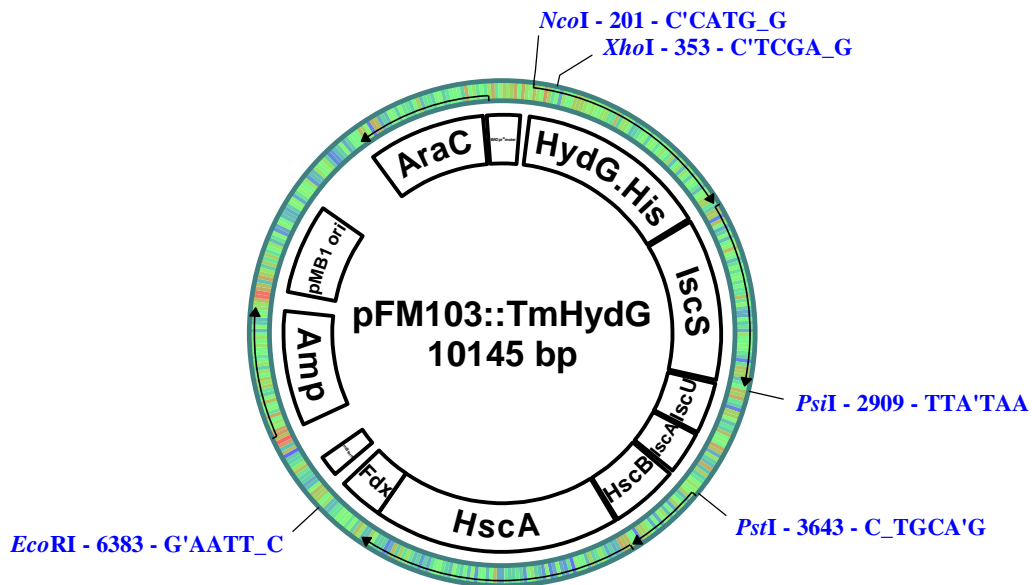


MGSSHHHHHSQDPMDNIIKLINKAEVTHDLTKDELVTLLKDDTHNEEIYKAADRVREKY
VGEEVHLRGLIEFSNICKRNCMYCGLRRDNKNIKRYRLEPDEIIHLAKSAKNYGYQTVVLQS
GEDDYTVKMKYIVSEIKKLNMAITLSIGEKTFFEEYEEYRKSGADRYLIRIETTDKELYEKLD
PKMSHENRINCLKNLRKLGVEVSGCLVGLPNQTIESLADDILFFKEIDADMIGVGPFPINED
TPLGEEKGGEFFMSVKVTALIRLLLDPINIPATTAMESLYPNGRSIALTSGANVVMNVTEGE
YRKLYALYPGKICVNDTPGHCRQCISLKINKINRKVSATKGFRKKSYSKESIG

pFM024 containing C-terminally 6His tagged *S. solfataricus* LipA

Appendix 2

pFM103 containing C-terminally 6His tagged *T. maritima* HydG



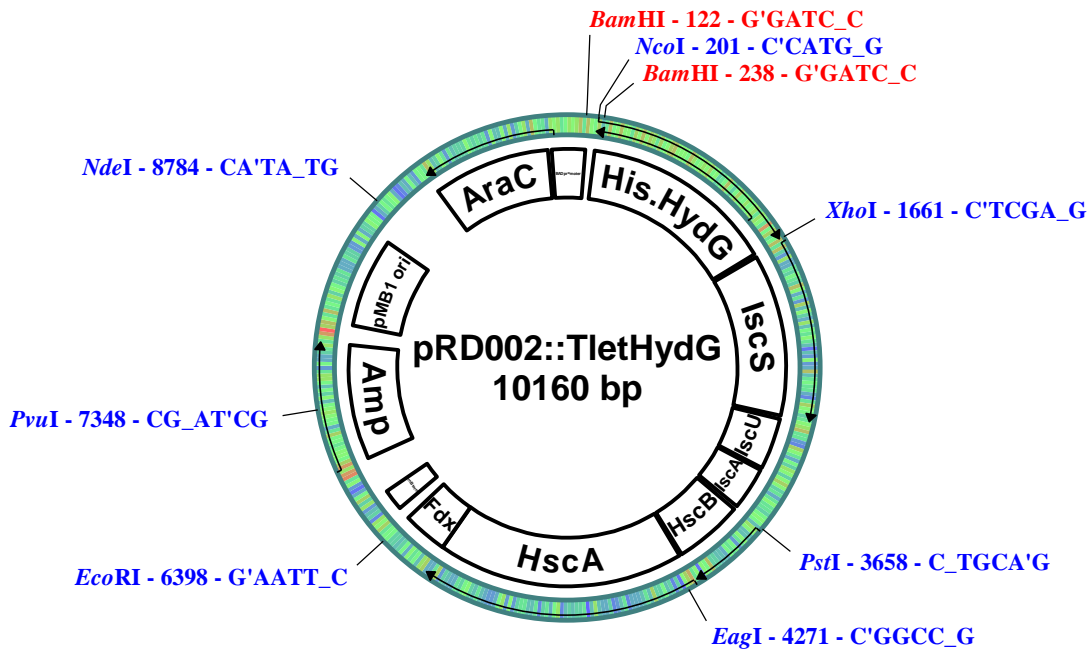
MGCMYVFKERVESRSFIPEEKIFELLEKTKNPDPARVREIIQKSLDKNRLEPEETATLLNVED
 PELLEEIFEAARTLKERIYGNRIVLFAPLYIGND**C**IND**C**VY**C**GFRVSNKVVERRTLTEEQLKEE
 VKALVSQGHKRLIVVYGEHPNYSPEFIARTIDIVYNTKYGNGEIRRVNVNAAPQTIEGYKIIKS
 VGIGTFQIFQETYHRETYLKLHPRGPKSNYNWRLYGLDRAMMAGIDDVGIGALFGLYDWK
 FEVMGLLYHTIHLEERFGVGPHTISFPRIKPAINTPYSQKEHVVSDEDFKLLVAIIRLSVPYTG
 MILTAREPAKLRDEVIKLGVSQIDAGSRIGIGAYSHKEDDEDKRKRQFTLEDPRPLDQVMRSL
 LKEGFVPSF**C**TAC**C**YRAGRTGEHFMEFAIPGFVKNF**C**TPNALFTLQEYLCDYATEETRKVGEE
 VIERELQKMNPKIRERVREGLEKIKRGERDVRFHSHHHHH

pRD002 containing codon optimised N-terminally 6His tagged *T. lettingae***HydG**

CACTATAGGGCGAATTGGCGGAAGGCCGTCAAGGCCGCATCCATGGGCAGCAGCC
ATCACCATCATCACCACAGCCAGGATCCGATGTATACCTTTGTGAAAAAATCCTG
GATAGCGAAAGCTTTATCCCGCATGAAGAAATTAATCGTCTGCTGAGCCTGACCAA
AAACCCGGACAAAAAATACATTGAAGAGATCCTGGAAAAAGCCTGAATAAAGAAC
GTCTGGATCTGAGCGAAACCGCAGCACTGCTGAATGCAGAAAATCCGGAACTGGTT
GAAATGATTTTTACCGCAGCAAATCCCTGAAAGAGAAAATTTACGGTAATCGCAT
TGTTCTGTTTGCACCGCTGTATATTGGTAACGAATGCATTAACAATTGCAGCTATTG
TGGTTTTCGCAGCGAGAATAAACAGGTGATTCGTAAAACCCTGACCGATGAAGAAC
TGACCAATGAACTGTTTGCCTGACCAGCAAAGGTCATAAACGTCTGATTGTTGTG
TTTGGTGAACATCCGGTTTATAGCCCTGAATATATTGCCAAAACCATCGAAAAAAT
CTATAGCTATCGCAATGGCAATGGTGAATTCGTCTGTTAATGTTAATGCCGCAC
CGCAGACCGTTGAAGTTATAAAACCATTTCGTAATGCAGGCATTGGCACCTTTCAG
ATTTTTCAAGAAACCTATCATCTGCCGACCTACAAAAAATACCATAAAGCAGGTCC
GAAAAGCAGCTATACCTATCGTCTGTTTGGTCTGGATCGTGCAATGATTGCAGGTA
TTGATGATGTTGGTATTGGTGCACCTGTTTGGCCTGTATGATTGGAAATTTGAAGTTA
TGGGTCTGATGTGTCATACCCGTCATCTGGAAGAACGTTTTGGTGTGGTCCGCAT
ACCATTAGCTTTCCGCGTATTGAACCGGCAGTTGGTACACCGCTGACAGAAAAACC
GCCTTATGCAGTTAGCGATTATGATTTTAAACGCCTGGTTGCCATTATTCGTCTGAG
CGTTCCGTATACCGGTCTGATTCTGACCGCACGTGAAAAAGTTCAGCTGCGTGATG
AAGTTATTAACCTGGGTGTTAGCCAGATTGATGCAGGTAGCAGCATTGGTGTGGGT
AGCTATGCACAGAAAGATCAAGAAATTGTTCCGAAAAGCCAGTTTATTCTGGGTGA
TACCCGTACCCTGGATGAAGTGATCAAAGAACTGGCAATGGAAGGCTATATTCCGA
GCTTTTGTACCGCATGTTATCGTGCAGGTCGTACCGGTCAGCATTTTATGGAATTTG
CAATTCCGGGTTTCGTGAAAGAATTTTGTACCCCGAATGCCCTGCTGACCTTTAAA
GAATATCTGATTGATTACGCCACCAACGAAACCAAACCTGATTGGTGAAAAACTGAT

Appendix 2

CGAAAAGAACTGCTGAAAATTCCGGATAGCCGTCGTGAAACCGTGCGCAAATGC
 TGGTAAATATTGAAAAGGTGAACGTGATGTGCGCCTGTAACCTCGAGCTGGGCCTC
 ATGGGCCTTCCGCTCACTGCCCGCTTTCCAG



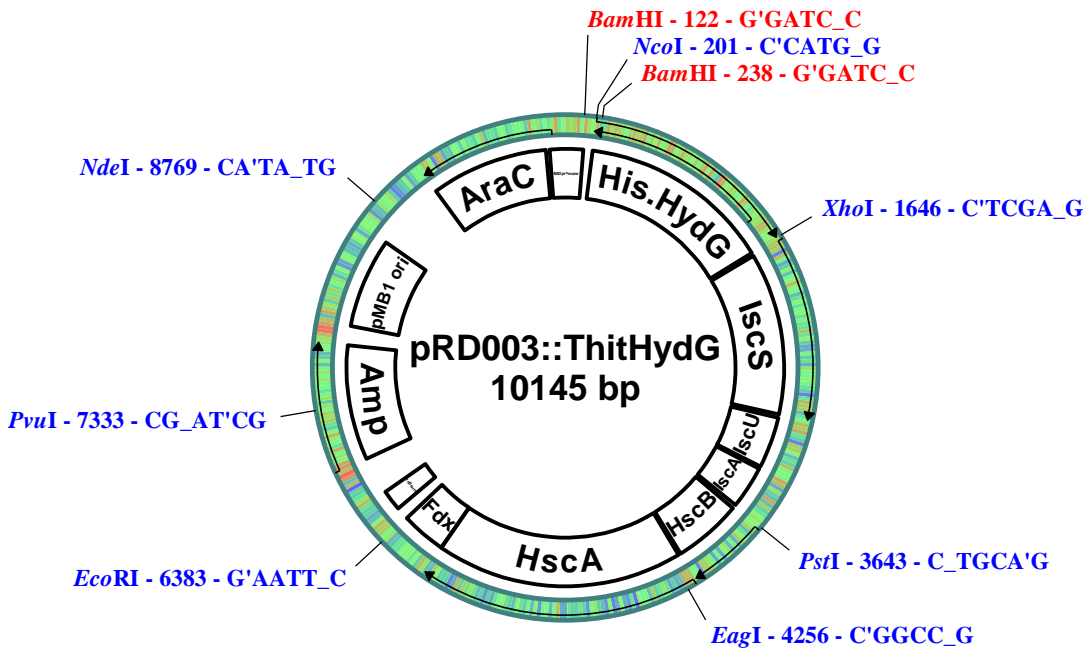
MGSSHHHHHSQDPMYTFVKKILDESFPHEEINRLLSLTKNPKKYIEEILEKSLNKERLDL
 SETAALLNAENPELVEMIFTAAKSLKEKIYGNRIVLFAPLYIGNECINNCSYCGFRSENKQVIR
 KTLTDEELTNELFALTSKGHKRLIVVFGHEPVVSPEYIAKTIEKIYSYRNGNGEIRRVNVNAAP
 QTVEGYKTIRNAGIGTFQIFQETYHLPTYKKYHKAGPKSSYTYRLFGLDRAMIAAGIDDVGIG
 ALFGLYDWKFEVMGLMCHTRHLEERFGVGPHTISFPRIEPAVGTPLTEKPPYAVSDYDFKRL
 VAIIRLSVPYTGLILTAREKVQLRDEVIKLGVSQIDAGSSIGVGSYAQKDQEI VRKSQFILGDT
 RTLDEVIKELAMEGYIPSFCTACYRAGRTGQHFMFAIPGFVKEFC TPNALLTFKEYLIDYAT
 NETKLIGEKLIEKELLKIPDSRRETVRKMLVNIKGERDVRL

pRD003 containing codon optimised N-terminally 6His tagged *Th. italicus***HydG**

CACTATAGGGCGAATTGGCGGAAGGCCGTCAAGGCCGCATCCATGGGCAGCAGCC
ATCACCATCATCACCACAGCCAGGATCCGATGGTTAAAGAAAAAGCCGATTTTCATC
AACGACGAAAAAATTCGTCAGGATCTGGAAAAAGCCAAAAAGCAACCAGCAAAG
ATGCCCTGGAAATTATCGAGAAAGCGAAAAATCTGAAAGGCATCACACCGGAAGAA
GCAGCAGTTCTGCTGAATGTTGAAGATGAAGATCTGCTGAACGAGATGTTTAAAGT
TGCCCGTTATATCAAAGAAGAGATCTACGGTAATCGCATCGTTATTTTTGCACCGC
TGTATGTGAGCAATTATTGCGTGAATAATTGCCGCTATTGCGGTTATCGTCATAGCA
ATGAACAGCAGCGTAAAAAACTGACAATGGAAGAAGTTCGTCGCGAAGTTGAAATT
CTGGAAGAAATGGGTCATAAACGTCTGGCAGTTGAAGCCGGTGAAGATCCGGTTAA
TTGTCCGATTGATTATATCGTGGATGTGATCAAACCATCTACGATACCAAACCTGA
AAAATGGTAGCATTTCGTCGCGTGAATGTTAATATTGCAGCAACCACCGTGGAAAAC
TACAAAAAACTGAAAAAAGTGGGCATCGGCACCTATGTTCTGTTTCAAGAAACCTA
TCATCGTCCGACCTATGAATATATGCATCCGCAGGGTCCGAAACACGATTATGATT
ATCATCTGACCGCAATGGATCGTGCAATGGAAGCAGGTATTGATGATGTTGGTCTG
GGTGTCTGTATGGTCTGTATGATTACAAATATGAAACCGTGGCCATGCTGTATCAT
GCAAATCATCTGGAAGAGAAATTTGGTGTGGTCCGCATACCATTAGCGTTCCGCG
TCTGCGTCCGGCACTGAATATTAGCATTGATAAATTTCCGTACATCGTGAGCGATA
AAGATTTCAAAAAACTGGTTGCCGTTATTCGTATGGCAGTTCCGTATACCGGCATG
ATTCTGAGCACCCGTGAAAAACCTAAATTTCCGGAAGAAGTGATTAGCATCGGTAT
TAGCCAGATTAGCGCAGGTAGCTGTACCGGTGTTGGTGGTTATCATGAAGAAATTA
GCAAAAAAGGTGGTAGCAAACCGCAGTTTGAAGTGGAAGATAAACGTAGCCCGAA
CGAAATTCTGCGTACCCTGTGTGAACAGGGTTATCTGCCGAGCTATTGTACCGCAT
GTTATCGTATGGGTCGTACCGGTGATCGTTTTATGAGCTTTGCAAAAAGTGGCCAG
ATCCATAACTTTTGTCTGCCGAATGCAATCCTGACCTTCAAAGAATTTCTGATCGAT
TATGGTGATGAGAAAACCAAAAAAATCGGCGAAAAAGCGATTGCCGTTAACCTGGA

Appendix 2

AAAAATCCCGAGCCGTACCGTTCGTGAAGAAACCAACGTCGTCTGACCCGTATTG
 AAAATGGTGAACGTGATCTGTACTTTTAACTCGAGCTGGGCCTCATGGGCCTTCCG
 CTCACTGCCCGCTTTCCAG



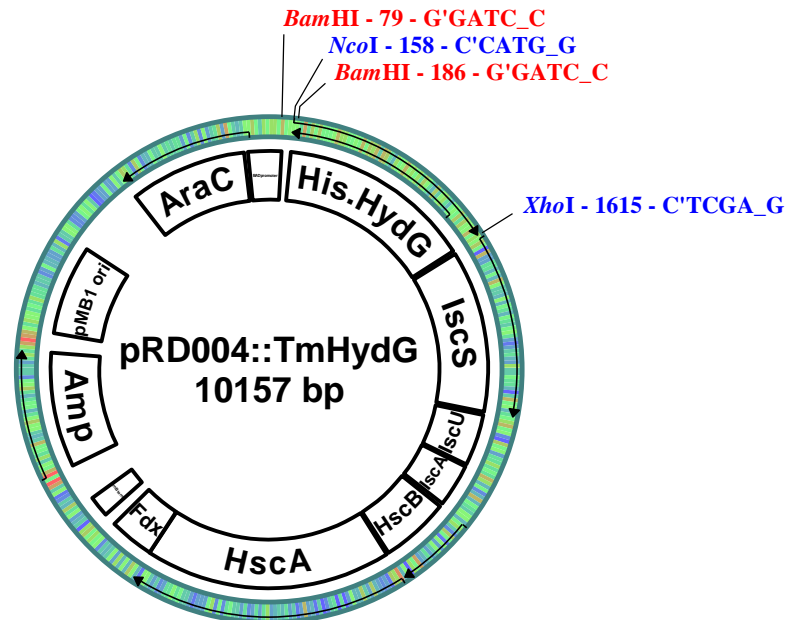
MGSSHHHHHSQDPMVKEKADFINDKIRQDLEKAKKATSKDALEIIEKAKNLKGITPEEA
 AVLLNVEDEDLLNEMFKVARYIKEEYGNRIVIFAPLYVSNYCVNNCRYCGYRHSNEQQRKK
 LTMEEVRREVEILEEMGHKRLAVEAGEDPVNCPIDYIVDVIKTIYDTKLKNGSIRRVNVNIAA
 TTVENYKLLKKVGIGTYVLFQETYHRPTYEYMHPQGPKHDYDYHLTAMDRAMEAGIDDV
 GLGVLYGLYDYKYETVAMLYHANHLEEKFGVGPHTISVPRLRPALNISIDKFPYIVSDKDFKK
 LVAVIRMAVPYTG MILSTREKPKFREEVISIGISQISAGSCTGVGGYHEEISKKGGSKPQFEVE
 DKRSPNEILRTLCEQGYLPSYCTACYRMGRTGDRFMSFAKSGQIHNFCLPNAILTFKEFLID
 YGDEKTKKIGEKAI AVNLEKIPSRTVREETKRRLTRIENGERDLYF

pRD004 containing codon optimised N-terminally 6His tagged *T. maritima***HydG**

CACTATAGGGCGAATTGAAGGAAGGCCGTCAAGGCCGCATCCATGGGGCATCATC
ATCACCATCATCAGGATCCGATGTGCATGTATGTTTTTGTAAAGAACGTGTGGAA
AGCCGCAGCTTTATTCCGGAAGAAAAATCTTTGAGCTGCTGGAAAAACCAAAAA
TCCTGATCCGGCACGTGTGCGTGAAATTATTCAGAAAAGCCTGGATAAAAATCGCC
TGGAACCTGAAGAAACCGCAACCCTGCTGAATGTTGAAGATCCGGAACCTGCTGGAA
GAAATTTTTGAAGCAGCACGTACCCTGAAAGAACGCATTTATGGTAATCGTATTGT
TCTGTTTGCACCGCTGTATATTGGCAACGATTGTATTAATGATTGCGTGTATTGCGG
TTTTCGCGTGAGCAATAAAGTTGTTGAACGTGCGACCCTGACCGAAGAACAGCTGA
AAGAAGAAGTTAAAGCACTGGTTAGCCAGGGTCATAAACGTCTGATTGTTGTTTAT
GGTGAACACCCGAATTACAGCCCTGAATTTATTGCACGTACCATCGATATTGTGTA
TAACACCAAATATGGCAACGGTGAAATTCGTCGTGTTAATGTTAATGCAGCACCCG
AGACCATTGAAGGCTATAAAATCATTAAAAGCGTGGGCATTGGCACCTTTCAGATT
TTTCAAGAAACCTATCACCGCGAACGTACCTGAAACTGCATCCGCGTGGTCCGAA
AAGCAATTATAACTGGCGTCTGTATGGTCTGGATCGTGCAATGATGGCAGGTATTG
ATGATGTTGGTATTGGTGCACCTGTTTGGTCTGTATGATTGGAAATTTGAAGTTATGG
GCCTGCTGTATCATACCATTCTGGAAGAACGTTTTGGTGTGGTCCGCATACC
ATTAGCTTTCGCGTATTAAACCGGCAATTAATACCCCGTATAGCCAGAAACCGGA
ACATGTTGTTAGTGATGAGGACTTCAAAAAACTGGTGGCAATTATTCGTCTGAGCG
TTCCGTATACCGGCATGATTCTGACCGCACGTGAACCGGCAAACTGCGTGATGAA
GTTATTAACCTGGGTGTGAGCCAGATTGATGCAGGTAGCCGTATTGGCATTGGTGC
CTATAGCCATAAAGAAGATGACGAAGATCGTAAACGTCAGTTTACCCTGGAAGATC
CGCGTCCGCTGGATCAGGTTATGCGTAGCCTGCTGAAAGAGGGTTTTGTTCCGAGC
TTTTGTACCGCATGTTATCGTGCAGGTTCGTACCGGTGAACATTTTATGGAATTTGCA
ATTCCGGGTTTTGTGAAAACTTTTGCACCCCGAATGCCCTGTTTACACTGCAAGA
ATATCTGTGTGATTATGCCACCGAAGAAACCCGTAAAGTTGGTGAAGAAGTGATTG

Appendix 2

AACGCGAACTGCAAAAAATGAATCCGAAAATTCGTGAACGTGTTTCGTGAAGGTCTG
 GAAAAAATCAAACGTGGTGAACGTGATGTGCGCTTTTAACTCGAGCTGGGCCTCAT
 GGGCCTTCCTTTCCTGCCCCGCTTCCAG



MGHHHHHHQDPMCMYVFKERVESRSFIPEEKIFELLEKTKNPDPARVREIIQKSLDKNRLE
 PEETATLLNVEDPELLEEIFEARTLKERIYGNRIVLFAPLYIGNDCINDCVYCGFRVSNKVVE
 RRTLTEEQLKEEVKALVSQGHKRLIVVYGEHPNYSPEFIARTIDIVYNTKYGNGEIRRVNVA
 APQTIEGYKIIKSVGIGTFQIFQETYHRETYLKLHPRGPKSNYNWRLYGLDRAMMAGIDDVG
 IGALFGLYDWKFEVMGLLYHTIHLEERFGVGPHTISFPRIKPAINTPYSQKPEHVVSDEDFKK
 LVAIIRLSVPYTG MILTAREPAKLRDEVIKLGVSQIDAGSRIGIGAYSHKEDDED RKRQFTLED
 PRPLDQVMRSLLKEGFVPSFC TAC YRAGR TGEHFMEFAIPGFVKNFC TPNALFTLQEYLCD
 YATEETRKVGEEVIERELQKMNPKIRERVREGLEKIKRGERDVRF

Appendix 3 – Liquid media

Composition of media

Component	Quantity (g)	
	2YT	LB
Bacto-tryptone	16	10
Bacto-yeast extract	10	5
NaCl	5	10
Adjust to 1 L with deionised water and autoclave.		

Thousandfold antibiotic stock solutions were prepared in sterile water or ethanol and added to the cooled media (~50 °C) at the working concentrations listed below.

Antibiotic	Working concentration (µg/mL)
Tetracycline (in EtOH)	50
Oxytetracycline (in EtOH)	10
Streptomycin	50
Chloramphenicol (in EtOH)	30
Ampicillin	100

Agar plates

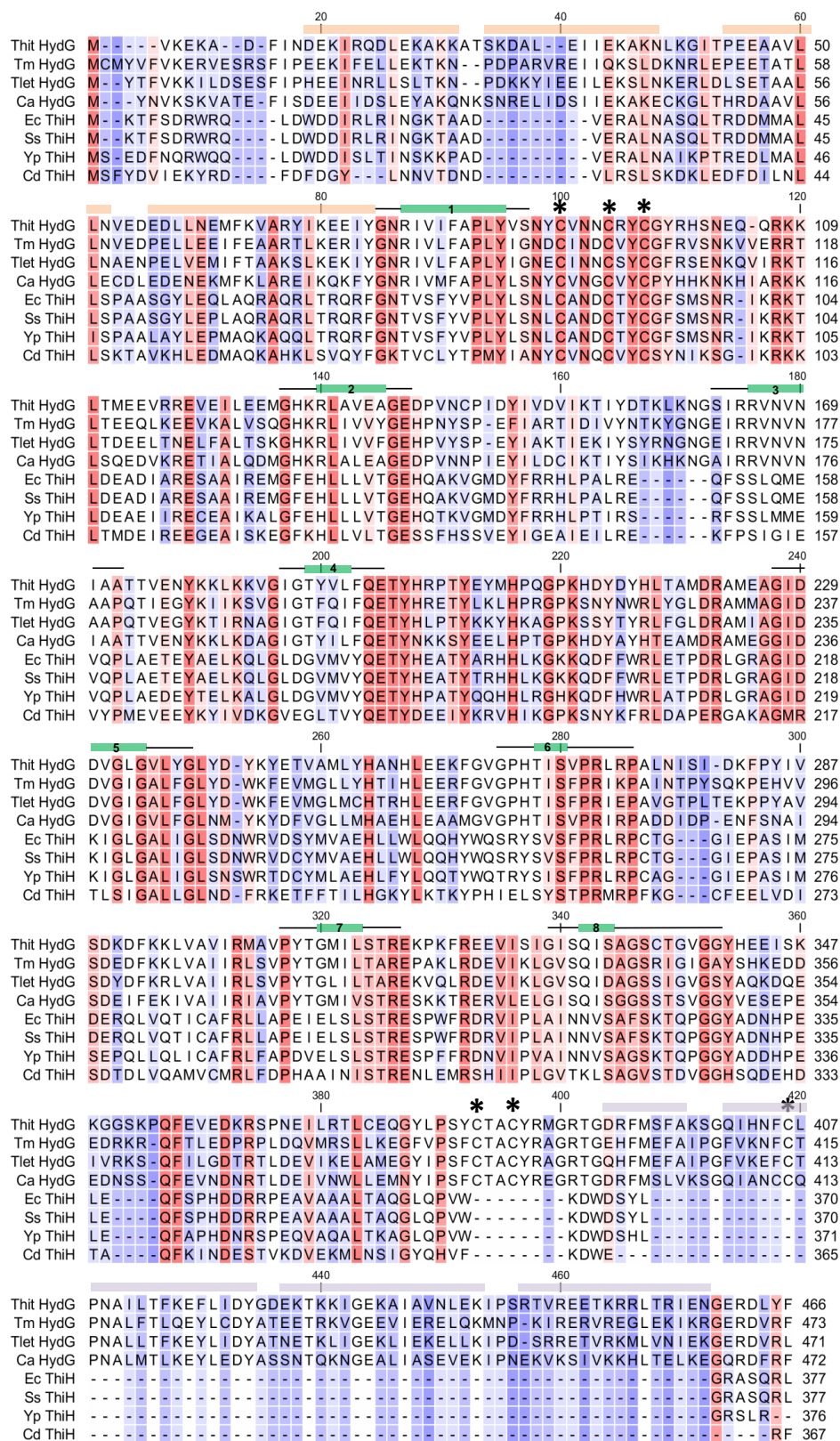
2YT media was supplemented with 15 g/L bacto agar, then autoclaved before transferred to a microbiological safety cabinet. Once cooled to approximately 50 °C, antibiotic was added as required and the viscous solution poured (~20 mL) into petri dishes. Fully cooled petri dishes were stored at 4 °C.

Appendix 4 – EPR simulations

X-band EPR characterisation of dithionite and photoreduced* HydG variants.

Sample	g ₁		g ₂		g ₃		% spin
	g-value	g-strain	g-value	g-strain	g-value	g-strain	
<i>(I) N-Terminal Reduced</i>							
WT*	2.0292	0.03019	1.9100	0.02796	1.8933	0.05680	54.3
WT.AdoMet*	2.0310	0.03020	1.9199	0.02319	1.9053	0.04987	18.0
WT	2.0318	0.04000	1.9122	0.04000	1.8788	0.07000	60.0
WT.AdoMet	2.0318	0.05000	1.9122	0.05000	1.8788	0.10000	4.5
C386S	2.0331	0.03979	1.9272	0.05415	1.8868	0.06359	86.4
ΔCTD	2.0303	0.03539	1.9250	0.03962	1.8850	0.05859	69.6
<i>(II) N-Terminal Reduced, AdoMet-Bound</i>							
WT.AdoMet*	1.9984	0.02607	1.8791	0.02252	1.8393	0.5526	52.0
WT.AdoMet	1.9976	0.02500	1.8897	0.02200	1.8302	0.04000	56.1
C386S.AdoMet	1.9988	0.01957	1.8919	0.02109	1.8352	0.03543	89.7
ΔCTD	1.9988	0.01674	1.8919	0.01847	1.8352	0.03360	30.4
ΔCTD.AdoMet	1.9988	0.01674	1.8919	0.01847	1.8652	0.03360	100.0
<i>(III) C-Terminal Reduced</i>							
WT*	2.0328	0.05492	1.9198	0.03305	1.8803	0.07190	45.7
WT.AdoMet*	2.0309	0.06251	1.9224	0.02617	1.8793	0.07174	30.0
WT	2.0319	0.06000	1.9269	0.04000	1.8696	0.06000	40.0
WT.AdoMet	2.0319	0.05000	1.9269	0.04000	1.8696	0.06000	39.4
C386S	2.0167	0.04356	1.9312	0.02607	1.8595	0.06176	13.6
C386S.AdoMet	2.0387	0.06018	1.9325	0.02172	1.8693	0.07669	10.3
C96/100/103A*	2.0266	0.05651	1.9224	0.03594	1.8795	0.07371	100.0

Appendix 5 – HydG, ThiH sequence alignment



Sequence alignment of HydG and ThiH from selected organisms.

Appendix 5

Secondary structure elements as identified in *Th. italicus* HydG (section 4.9) are displayed as coloured boxes above the sequences as follows; N-terminal domain α -helices, wheat; TIM barrel β -sheets, green; C-terminal domain α -helices, light blue. The residues originally identified by Pilet and co-workers to contribute to TIM barrel β -sheets are marked with black lines³³. The cysteine residues coordinating either [4Fe-4S] cluster are indicated by asterisks.
